Functionalized Materials Based on the Clay Mineral Kaolinite

By

Jonathan Fafard

A thesis submitted to the

Faculty of Science

University of Ottawa

in partial fulfillment of the requirements for the

Ph.D. degree in Chemistry

in the

Ottawa-Carleton Chemistry Institute

Ottawa, Ontario

March 2018

Ph.D. Candidate

Jonathan Fafard

Research Supervisor

Professor Christian Detellier

Acknowledgements

The fruits of the research projects which are contained in this thesis would not have been attained without the help, guidance and support of a great number of people.

I would like to first and foremost thank my supervisor Christian Detellier for his great knowledge, support, patience, and for his full confidence in my work and aptitudes as a researcher during our many years working together. It is thanks to him that I was allowed to grow into the scientist and person that I am today.

During my time as a student in the Detellier research group at the University of Ottawa, I have had the pleasure of working with a great number of wonderful and talented individuals, many of which I would consider my friends as well as colleagues. I would like to thank Gustave Kenne Dedzo, Sadok Letaief, Rola Mansa, Guy Ngassa, Roger Pitre, and many others.

I am also grateful to the support staff at the Centre for Catalysis Research and Innovation: Wendy Pell, Rola Mansa, and Yun Liu; at the University of Ottawa's Chemistry Department: Josée Rouleau, and Annette Campeau; at the University of Ottawa's NMR facility: Glenn Facey, Eric Ye; at the National Ultrahigh-field NMR Facility for Solids: Victor Terskikh; at the University

of Ottawa X-ray Core Facility: Tara Kell and Bulat Gabidullin; at the G.G. Hatch Stable Isotope Laboratory: Paul Middlestead; and at undergraduate teaching labs: Sadok Letaief, Daniel Lafleur, and Robert Nadon for always being there to help with matters related to my research and teaching duties.

And finally, I would like to extend an extra special thanks to the love of my life, Natasha Oickle for always being there for me and giving me the encouragement and motivation I needed to see this thesis through to the end. It is to her that I dedicate this work.

Abstract

The use of kaolinite for preparing functionalized materials for specialized applications is still a relatively niche research subject. This is in spite of its low cost, high availability, and the potential for covalently grafting organic functional groups to its inner and outer surfaces. These grafted compounds have been shown to be highly resistant to heat and solvents, making them very useful for certain applications, for example in polymer nanocomposite materials that require high thermal resistance during polymer processing.

Solid state NMR has been shown to play an essential role in solving the structure of functionalized kaolinite materials, however the current knowledge base for these functionalized kaolinites is notably lacking for some nuclei such as ^{1}H, ^{27}Al and ^{17}O.

Research was undertaken to address these concerns by developing new synthetic strategies for preparing kaolinite based materials for use as nanocomposites and to examine commonly prepared modified kaolinite precursors materials by ^{1}H and ^{27}Al MAS NMR in an attempt to demonstrate their utility for characterizing kaolinite intercalated and grafted complexes.

Solid state ^{1}H NMR of a natural kaolinite, kGa-1b, identified two main proton signals attributed to inner and inner surface hydroxyl protons. The different affinity of these two types of hydroxyl groups towards exchange with deuterium was used to differentiate between the two. The ^{1}H NMR spectra of a DMSO intercalated kaolinite, kDMSO, and a methanol grafted kaolinite, kmethoxy, were fitted with high accuracy using models consistent with the known structures of these materials.

The ^{27}Al MAS NMR spectra of a natural kaolinite, kGa-1b, a DMSO intercalated kaolinite, kDMSO, and a methanol grafted kaolinite, kmethoxy measured at 21.1T showed little difference between one another, while noticeable differences could be seen at 4.7T. ^{27}Al MQMAS experiments found almost no difference between these materials in the multiple quantum dimension, suggesting the differences that were observed are a result of differences in quadrupolar parameters rather than chemical shifts. The ^{27}Al NMR spectra of kGa-1b, kDMSO and kmethoxy were fitted with good accuracy using models consistent with known structures of these materials. Different Al(III) sites with C_Q values varying by up to 0.6MHz were found. The ^{27}Al NMR spectra of two different methanol grafted kaolinites were also compared and it was found that the intensities of the sites with lower values of C_Q were dependent on the quantity of grafted aluminum sites.

The interlayer space of kaolinite was functionalized with a block copolymer: poly(ethylene)-block-poly(ethylene glycol) using a kaolinite pre-intercalated with DMSO, kDMSO, and with a

biodegradable polymer: poly(lactide) using a kaolinite pre-intercalated with urea, kurea, both by using melts of the polymer. The polymers were found to completely displace their precursors from the interlayer space giving a monolayer type arrangement of the polymer.

Attempts were made to graft compounds containing polymerizable functional groups: 3-allyloxy-1,2-propanediol and ethylene glycol vinyl ether to kaolinite's inner surfaces using a kaolinite pre-intercalated and grafted with methanol, kmethoxy, and a kaolinite pre-intercalated with DMSO, kDMSO, respectively. Both compounds were found to displace their precursors from the interlayer space, adopting a monolayer type arrangement. ^{13}C and ^{29}Si NMR results suggest 3-allyloxy-1,2-propanediol's allyl group remains intact and partially keys into the clay mineral's siloxane rings. Ethylene glycol vinyl ether was found to undergo intramolecular cyclization to form an acetal product, consuming its vinyl group in the process. This reaction was observed using an unmodified kaolinite, kGa-1b, suggesting that the clay mineral's surfaces, both inner and outer, act as an acid catalyst.

Table of contents

ACKNOWLEDGEMENTS ..... **II**

ABSTRACT ..... **IV**

TABLE OF CONTENTS ..... **VII**

LIST OF FIGURES ..... **XI**

LIST OF TABLES ..... **XVI**

LIST OF ABBREVIATIONS ..... **XVII**

1 GENERAL INTRODUCTION **1**

1.1 Clays & clay minerals and human activity **1**

***1.2* Classification of clays and clay minerals in soil science** **2**

1.3 Structure and nomenclature of clay minerals **4**

1.4 Layer stacking sequences and polytypism **8**

1.5 Layer charge and cation exchange capacity **10**

1.6 Kaolinite structure and nomenclature **13**

1.7 Hydroxyl groups **14**

1.8 Defect structure **15**

***1.9* Interlayer chemistry of kaolinite** **17**

1.10 Intercalation mechanism **19**

1.11 Displacement reaction **21**

1.12 Grafting reactions **22**

1.13 Kaolinite structural characterization using solid state NMR **23**

1.14 Industrial uses and current trends **24**

1.15 Polymer clay nanocomposites 25

1.16 Aim and purpose of research 28

2 SOLID STATE ^{1}H AND ^{27}AL NMR STUDIES OF MODIFIED KAOLINITE PRECURSOR MATERIALS 31

2.1 Solid state ^{1}H NMR study of natural and modified kaolinites 31

2.1.1 Introduction 31

2.1.2 Description of samples 38

2.1.3 ^{1}H MAS NMR results & discussion 40

2.1.4 Summary of the experiments and conclusions 59

2.2 Solid state ^{1}H NMR study of deuterium exchanged natural and modified kaolinites 61

2.2.1 Introduction 61

2.2.2 Description of samples 62

2.2.3 IR Results & discussion 62

2.2.4 TGA and %CHNS elemental analysis results & discussion 68

2.2.5 ^{1}H MAS NMR analysis & discussion 72

2.2.6 Summary and conclusions 79

2.3 ^{27}Al solid state NMR study of natural and modified kaolinites 81

2.3.1 Introduction 81

2.3.2 Description of samples 87

2.3.3 ^{27}Al MAS NMR results & discussion 88

2.3.4 Simulation and fitting of ^{27}Al NMR experimental spectra 98

2.3.5 ^{27}Al MQMAS NMR results & discussion 124

2.3.6 Summary and conclusions 126

3 NEW KAOLINITE POLYMER:CLAY NANOCOMPOSITES FORMED BY MELT INTERCALATION 129

3.1 Kaolinite functionalized with ethylene glycol based block-copolymers 129

3.1.1 Introduction 129

3.1.2 Description of samples 131

3.1.3 XRD results & discussion 131

3.1.4 TGA results & discussion 136

3.1.5 IR results & discussion 140

3.1.6 ^{13}C CPMAS NMR results & discussion 144

3.1.7 ^{13}C CPMAS NMR with dipolar dephasing results & discussion 147

3.1.8 Summary of results and conclusions 153

3.2 Kaolinite intercalated with poly(lactide) 155

3.2.1 Introduction 155

3.2.2 Description of samples 157

3.2.3 XRD results & discussion 158
3.2.4 IR results & discussion 161
3.2.5 TGA results & discussion 165
3.2.6 ^{13}C CPMAS NMR results & discussion 167
3.2.7 Summary of results and conclusions 170

4 COVALENT GRAFTING OF GLYCOLS AND GLYCOL ETHERS CONTAINING POLYMERIZABLE GROUPS TO KAOLINITE 172

4.1 Introduction 172

4.2 Kaolinite functionalized with 3-allyloxy-1,2-propanediol 176
4.2.1 Description of samples 176
4.2.2 XRD results & discussion 177
4.2.3 IR results & discussion 180
4.2.4 TGA results & discussion 183
4.2.5 ^{13}C CPMAS NMR results & discussion 185
4.2.6 ^{13}C CPMAS with dipolar dephasing NMR results & discussion 189
4.2.7 ^{29}Si CPMAS NMR results & discussion 195
4.2.8 Summary of experiments and conclusions 198

4.3 Kaolinite functionalized with ethylene glycol vinyl ether 200
4.3.1 Description of samples 200
4.3.2 XRD results & discussion 201
4.3.3 IR results & discussion 203
4.3.4 TGA results & discussion 205
4.3.5 ^{13}C CPMAS NMR results & discussion 206
4.3.6 Liquid ^{13}C NMR analysis of kaolinite catalyzed acetalization of ethylene glycol vinyl ether 211
4.3.7 Summary of experiments and conclusions 216

5 EXPERIMENTAL DETAILS AND SUPPLEMENTARY RESULTS 218

5.1 Procedures for material characterisation 218
5.1.1 Solid state ^{1}H nuclear magnetic resonance 218
5.1.2 Solid state ^{29}Si cross polarization magic angle spinning nuclear magnetic resonance (^{29}Si CPMAS NMR) 219
5.1.3 Solid state ^{13}C cross polarization magic angle spinning nuclear magnetic resonance (^{13}C CPMAS NMR) 219
5.1.4 ^{13}C CPMAS NMR with dipolar dephasing 220
5.1.5 Low field, Solid state ^{27}Al MAS NMR 223
5.1.6 High field, Solid state ^{27}Al magic angle spinning nuclear magnetic resonance (^{27}Al MAS NMR) 223
5.1.7 High field Solid state 27Al MQMAS NMR 224
5.1.8 Low field Solid state ^{27}Al MQMAS NMR 224
5.1.9 ^{13}C NMR with proton decoupling and ^{13}C DEPT 135/DEPT 90 experiments 225
5.1.10 Attenuated total reflectance Fourier transfer infrared analysis (ATR-FTIR) 226
5.1.11 Powder X-ray diffraction (XRD) 226

5.1.12 Thermal gravimetric analysis 227
5.1.13 %CHNS Elemental analysis 227
5.1.14 Spectral deconvolution and curve fitting ^{1}H NMR spectra 229
5.1.15 Curve fitting ^{27}Al NMR spectra 229

5.2 Procedures for sample preparation and material characterisation results 231
5.2.1 kGa-1b 231
5.2.2 kDMSO 233
5.2.3 kmethoxy 234
5.2.4 kmethoxy(ht) 236
5.2.5 kGa-1b-d 237
5.2.6 kDMSO-d 238
5.2.7 kmethoxy-d 239
5.2.8 kPEPEG2250 240
5.2.9 kPEPEG920 241
5.2.10 kPEPEG575 242
5.2.11 kPEPEG2250(w) 243
5.2.12 kurea 244
5.2.13 kPLA(u) 245
5.2.14 kPLA 246
5.2.15 kallyloxy 247
5.2.16 kallyloxy(w) 249
5.2.17 kallyloxy(lowT) 250
5.2.18 kallyloxy(lowT)(w) 250
5.2.19 allyloxy (on kGa-1b) 251
5.2.20 kvinyloxy 252
5.2.21 kvinyloxy(w) 253
5.2.22 kvinyloxy(lowT) 254
5.2.23 Thermally induced cyclization of ethylene glycol vinyl ether (i.e. vinyloxy(c)) 254
5.2.24 Kaolinite catalyzed cyclization of ethylene glycol vinyl ether (i.e. vinyloxy(c-KGa-1b) 255

6 GENERAL CONCLUSIONS AND SUGGESTION FOR FUTURE WORK 256

7 BIBLIOGRAPHY 259

List of figures

Figure 1: Commonly used particle size scales used to classify soil fractions in North America. The commonly used USDA scale classifies clay fractions in soils as the sub 2µm fraction. Adapted from: (U.S. Department of Agriculture National soil survey handbook, title 430-VI). 3
Figure 2: Representation of idealized octahedral and tetrahedral sheets in phyllosilicates and their combined, stacked structure. The idealized sheet structures are slightly distorted in the combined tetrahedral-octahedral structure. 5
Figure 3: Representation of idealized 1:1 and 2:1 layered structures in phyllosilicates. Adapted from: (Bailey, 1988a). 6
Figure 4: Diagram outlining individual layers (A), stacks of layers as particles (B) aggregates of particles (C) and assemblies of aggregates (D) in phyllosilicates. Adapted from: (Bergaya and Lagaly, 2013). 7
Figure 5: Schematic representation of the 12 standard polytypes for 1:1 phyllosilicates. Adapted from (Bailey 1988b). 9
Figure 6: Schematic outlining the layered structure found in kaolinite. 14
Figure 7: Schematic outlining the hydroxyl groups in kaolinite. 15
Figure 8: Hinckley index calculation for a low defect, Cornwall, U.K., kaolinite sample. Adapted from (Plançon et al., 1988). 16
Figure 9: Schematic outlining a general intercalation reaction in kaolinite. 20
Figure 10: Schematic outlining the covalent grafting of methanol on kaolinite as methoxy (OCH_3) groups. 22
Figure 11: Schematic showing: (A) a conventional composite, (B) an intercalated and (C+D) a disordered and ordered exfoliated polymer clay nanocomposite material. Materials C and D show a significant increase in the thermal and mechanical properties compared to the neat polymer. Adapted from (LeBaron et al., 1999). 27
Figure 12: Number of documents containing the keyword "nanocomposite" from the period of 1977-2015. Data was retrieved from the Scopus search engine (July 2nd, 2015): https://www.elsevier.com/solutions/scopus. 28
Figure 13: ^{1}H MAS NMR spectrum of kGa-1b and curve fitting results using a three site model. An expanded scale spectrum is shown as an inset. Rotational artifacts resulting from MAS are denoted with an asterisk. 42
Figure 14: Schematic outlining the ^{1}H NMR signals observed for the different hydroxyl groups in kaolinite. 43
Figure 15: ^{1}H MAS NMR of KDMSO and curve fitting results using a four site model. An expanded scale spectrum is shown as an inset. Rotational artifacts resulting from MAS are denoted with an asterisk. 45
Figure 16: ^{1}H MAS NMR of KDMSO and curve fitting results using a five site model where there are two sites for the DMSO CH_3 groups. An expanded scale spectrum is shown as an inset. Rotational artifacts resulting from MAS are denoted with an asterisk. 46
Figure 17: Schematic outlining the ^{1}H NMR signals observed in kDMSO. This summary uses the results in Figure 16 for the five site model used for fitting the experimental spectrum where there are two distinct DMSO methyl species. The surface water present in the material is not shown in this schematic. 47
Figure 18: ^{1}H MAS NMR of kmethoxy and curve fitting results using a seven site model. The interlayer water present in this material was included as a single peak with a chemical shift value of 1.38ppm. An expanded scale spectrum is shown as an inset. Fitting was done using the same parameters used for analysis of kGa-1b for the 2.68ppm and 1.70ppm peaks. Rotational artifacts resulting from MAS are denoted with an asterisk. 51
Figure 19: ^{1}H MAS NMR of kmethoxy and curve fitting results using an eight site model. The interlayer water present in this material was included as one single peak with a chemical shift value of 4.82ppm and the inner

surface hydroxyls as two peaks with chemical shift values of 2.68 and 2.13ppm. These latter values are attributed to clay mineral's inner surface hydroxyls in the 7.2Å and 8.4Å XRD fractions respectively. An expanded scale spectrum is shown as an inset. Fitting was done using the same parameters used for analysis of kGa-1b for the 2.68ppm and 1.70ppm peaks. Rotational artifacts resulting from MAS are denoted with an asterisk. _____ 52
Figure 20: Schematic outlining the ^{1}H NMR signals observed in kmethoxy. This schematic uses the results for the eight site model used for fitting to the experimental spectrum where the clay mineral's inner surface hydroxyls in the 8.4Å and 7.2Å fractions have different chemical shift values _____ 54
Figure 21: ^{1}H MAS NMR of kmethoxy(ht) and curve fitting results using a six site model where the clay mineral's inner surface hydroxyls in the 8.4Å and 7.2Å fractions have different chemical shift values. An expanded scale spectrum is shown as an inset. Fitting was done using the same parameters used for analysis of kGa-1b for the 2.68ppm and 1.64ppm peaks. Rotational artifacts resulting from MAS are denoted with an asterisk. _____ 56
Figure 22: Schematic outlining the ^{1}H NMR signals observed in kmethoxy(ht). This schematic uses the results for the six site model used for fitting the experimental spectrum. _____ 58
Figure 23: ATR-FTIR spectrum of deuterated kaolinites. A close-up of the 2800-2500cm^{-1} region is shown. _____ 66
Figure 24: ATR-FTIR spectrum of deuterated kaolinites. A close-up of the 3750-3500cm^{-1} region is shown. _____ 67
Figure 25: TGA weight loss curves of deuterated kaolinites. The 1st derivative plots and the weight loss curves for the undeuterated materials are included as insets. The weight loss values at 300°C and 650°C are marked on their respective curves. _____ 71
Figure 26: ^{1}H MAS NMR of spectra kDMSO-d and curve fitting results using a three site model. An expanded scale spectrum is shown as an inset showing the entire spinning sideband manifold. Rotational artifacts resulting from MAS are denoted with an asterisk._____ 73
Figure 27: ^{1}H MAS NMR of spectra kmethoxy-d and curve fitting results using a 4 site model. An expanded scale spectrum is shown as an inset showing the entire spinning sideband manifold. Rotational artifacts resulting from MAS are denoted with an asterisk._____ 77
Figure 28: ^{1}H MAS NMR of spectra kmethoxy-d and curve fitting results using a five site model. An expanded scale spectrum is shown as an inset showing the entire spinning sideband manifold. Rotational artifacts resulting from MAS are denoted with an asterisk._____ 78
Figure 29: Nuclear charge distribution in a spin ½ nucleus compared to a spin >½ nucleus. The non-spherical charge distribution in a spin >½nucleus generates a nuclear quadrupole moment. _____ 82
Figure 30: First order quadrupolar spectra of powder samples simulated for a spin quantum number I=5/2 nucleus with different values of η_Q. Adapted from: (Vega, 2012). _____ 84
Figure 31: ^{27}Al MAS NMR spectra of kGa-1b, kDMSO, kmethoxy, and kmethoxy(ht) measured at 4.7T and 21.1T._ 88
Figure 32: Close-up of ^{27}Al MAS NMR spectra of the kGa-1b measured at 21.1T shown in Figure 31. The spectrum is zoomed in to show the line shape of the 1st spinning sideband pair and the tetrahedral aluminum species present.91
Figure 33: ^{27}Al MAS NMR spectra of kGa-2 compared to kGa-1b, measured at 4.7T. A close up of the central peak is shown as an insets. _____ 92
Figure 34: Superposition of the ^{27}Al NMR spectra of kGa-1b and kDMSO. The broadening towards lower chemical shift values in kDMSO is attributed to higher values of C_Q._____ 94
Figure 35: ^{27}Al MAS NMR spectra of kDMSO-d compared to kDMSO and kGa-1b. _____ 95
Figure 36: ^{27}Al MAS NMR spectra of kmethoxy(ht) compared to kmethoxy. These spectra were obtained on a 4.7T magnet. There is a notable shift of the weight of the central transition in kmethoxy(ht) towards higher frequencies. _____ 97
Figure 37: ^{27}Al MAS NMR spectra of kGa-1b at 4.7T fitted to a simulated spectrum using one unique Al(III) site. The chemical shift value and quadrupolar parameters of the site are summarized in Table 10. _____ 98

Figure 38: ^{27}Al MAS NMR spectra of kGa-1b at 4.7T fitted to a simulated spectrum using two unique Al(III) sites. A close up of the central peak is shown as an inset. The chemical shift value and quadrupolar parameters of the each site are summarized in Table 11. _____ *101*
Figure 39: ^{27}Al MAS NMR spectra of kGa-1b at 21.1T fitted to a simulated spectrum using two unique Al(III) sites. A close up of the central peak and its simulated components are shown as insets. The chemical shift value and quadrupolar parameters of the each site are summarized in Table 11. _____ *102*
Figure 40: Summary of the two different ^{27}Al(III) octahedral sites identified for kGa-1b. This uses the parameters identified for the two site model. _____ *103*
Figure 41: ^{27}Al MAS NMR spectra of kDMSO at 4.7T fitted to a simulated spectrum using one unique Al(III) site for the DMSO modified and two sites for the unmodified fraction in the material. The chemical shift value and quadrupolar parameters of the each site are summarized in Table 13. _____ *105*
Figure 42: ^{27}Al MAS NMR spectra of kDMSO at 4.7T fitted to a simulated spectrum using two unique Al(III) sites each for the DMSO modified and unmodified fractions in the material. A close up of the central peak is shown as an inset. The chemical shift value and quadrupolar parameters of the each site are summarized in Table 13. _____ *108*
Figure 43: ^{27}Al MAS NMR spectra of kDMSO at 21.1T fitted to a simulated spectrum using two unique Al(III) sites each for the DMSO modified and unmodified fractions in the material. A close up of the central peak and its components are shown as insets. The chemical shift value and quadrupolar parameters of the each site are summarized in Table 13. _____ *109*
Figure 44: Summary of the different ^{27}Al NMR sites identified for kDMSO. This schematic uses the parameters identified for the four site model. _____ *110*
Figure 45: ^{27}Al MAS NMR spectra of kmethoxy at 4.7T fitted to a simulated spectrum using one unique Al(III) site for the methoxy modified fraction and two sites for the unmodified fraction in the material. The chemical shift value and quadrupolar parameters of the each site are summarized in Table 14. _____ *111*
Figure 46: ^{27}Al MAS NMR spectra of kmethoxy at 4.7T fitted to a simulated spectrum using four unique Al(III) sites for the methoxy modified and two sites for the unmodified fraction in the material. A close up of the central peak is shown as an inset. The chemical shift value and quadrupolar parameters of the each site are summarized in___ *115*
Figure 47: ^{27}Al MAS NMR spectra of kmethoxy at 21.1T fitted to a simulated spectrum using four unique Al(III) sites for the methoxy modified and two sites for the unmodified fraction in the material. A close up of the central peak and its components are shown as insets. The chemical shift value and quadrupolar parameters of the each site are summarized in _____ *116*
Figure 48: Summary of the different ^{27}Al sites identified for kmethoxy. This schematic uses the parameters identified for the six site model. _____ *118*
Figure 49: ^{27}Al MAS NMR spectra of kmethoxy(ht) at 4.7T fitted to a simulated spectrum using four unique aluminum sites each for the methoxy modified and two sites for the unmodified fraction in the material. A close up of the central peak is shown as an inset. The chemical shift value and quadrupolar parameters of the each site are summarized in Table 16. _____ *120*
Figure 50: ^{27}Al MAS NMR spectra of kmethoxy(ht) at 21.1T fitted to a simulated spectrum using four unique Al(III) sites for the methoxy modified and two sites for the unmodified fraction in the material. A close up of the central peak and its components are shown as insets. The chemical shift value and quadrupolar parameters of the each site are summarized in _____ *121*
Figure 51: Summary of the different ^{27}Al sites identified for kmethoxy(ht). This schematic uses the parameters identified for the six site model. _____ *123*
Figure 52: ^{27}Al 3QMAS NMR spectra of kGa-1b, kDMSO, kmethoxy, and kmethoxy(ht) obtained at 4.7T and 21.1T. 1D slices are shown using the coordinates highlighted. _____ *125*
Figure 53: XRD trace and 001 d-spacing values for kPEPEG2250 compared to kDMSO. The water washed material kPEPEG2250 is shown as an inset. The abundance of each 001 reflection is shown in parentheses. _____ *133*

Figure 54: XRD trace and 001 d-spacing values for various kPEPEG materials. The relative abundance of each 001 reflection is shown in parentheses. 134
Figure 55: Side view schematic showing the interlayer space of kaolinite in the prepared kPEPEG materials. 135
Figure 56: TGA weight loss of kPEPEG2250 compared to kDMSO. 1st derivative weight loss curves are shown as insets. 138
Figure 57: TGA weight loss of kPEPEG2250 the water washed material kPEPEG2250(w). 1st derivative weight loss curves are shown as insets. 139
Figure 58: ATR-FTIR of the 3750-2750cm-1 region of kPEPEG2250 compared to kDMSO. Close ups of the 3720-3580cm-1 region are shown as insets. 141
Figure 59: ATR-FTIR of the 2000-650cm-1 region of kPEPEG2250 region compared to kDMSO. Close ups of the 2000-1200cm-1 region are shown as insets. 142
Figure 60: ATR-FTIR spectra of kPEPEG2250 comparing the neat polymer and the water washed product kPEPEG2250(w). 142
Figure 61: 13C CPMAS NMR spectrum of kPEPEG2250 compared to the neat polymer PEPEG and kDMSO. Expanded scale spectra are shown as insets. Rotational artifacts resulting from MAS are denoted with an asterisk. 145
Figure 62: 13C CPMAS NMR spectrum of kPEPEG2250 compared to kPEPEG2250(w). An expanded scale spectra of both materials are shown as insets. Rotational artifacts resulting from MAS are denoted with an asterisk. 146
Figure 63: 13C CPMAS NMR with dipolar dephasing spectra of kPEPEG2250. Shown are the spectra using t_1 times of 0, 10, 20, 30, and 40µs. A close up of the 80-60ppm region is shown as an inset. 149
Figure 64: 13C CPMAS NMR with dipolar dephasing spectra of PEPEG2250. Shown are the spectra using t_1 times of 0, 10, 20, 30, and 40µs. A close up of the 60-80ppm region is shown as an inset. 150
Figure 65: 13C CPMAS NMR with dipolar dephasing spectra of kPEPEG2250(w). Shown are the spectra using t_1 times of 0, 2, 5, 10, 20, 30, and 40µs. 151
Figure 66: Plots of 13C NMR signal decay as a function of t_1 times for kPEPEG compared to the washed and pyrolyzed product kPEPEG2250(w), and the neat polymer (PEPEG). The slope of these plots was used to calculate T_2 values. 152
Figure 67: XRD trace of kPLA compared to its kurea precursor. 159
Figure 68: XRD trace of kPLA compared to the unwashed product kPLA(u). The washing procedure did not remove the reflection attributed to the kaolinite 12.1Å 001 d-spacing. 160
Figure 69: Schematic outlining the 001 spacing of an individual layer in kPLA compared to kurea. 160
Figure 70: ATR-FTIR spectra of kPLA compared to its kurea precursor, showing the 3800-2800cm-1 region. Close ups of the 3720-3600cm-1 region are shown as insets. 162
Figure 71: ATR-FTIR spectra of kPLA compared to its kurea precursor, showing the 2000-650cm-1 region. A close up of the 2000-1100cm-1 region for kPLA is shown as an inset. 163
Figure 72: TGA weight loss curve of kPLA compared to kurea. The 1st derivative plots of the weight loss curves are shown as insets. 166
Figure 73: 13C CPMAS spectrum of kPLA compared to kurea. An expanded scale spectrum of kPLA is shown as an inset. Rotational artifacts resulting from MAS are denoted with an asterisk. 168
Figure 74: 13C CPMAS spectrum of kPLA compared to the neat polymer. Rotational artifacts are denoted with asterisks. Expanded scale spectra for both materials are shown as insets. Rotational artifacts resulting from MAS are denoted with an asterisk. 169
Figure 75: Structure of 3-allyloxy-1,2-propanediol 177
Figure 76: XRD trace of kallyloxy compared to kmethoxy. The water washed material, kallyloxy(w), is shown as an inset. Washing the material in water did not regenerate a kmethoxy fraction. 179
Figure 77: Side view schematic showing the interlayer space of kaolinite in the prepared kallyloxy material. 179

Figure 78: XRD trace of kallyloxy(low T), compared to kmethoxy. The water washed material, kallyloxy(low T)(w), is shown as an inset. Washing the material in water collapsed the 11.4Å fraction, partially regenerating the starting kmethoxy 001 d-spacing. _____ *180*
Figure 79: ATR-FTIR of kallyloxy compared to kmethoxy. The 4000-2500 cm^{-1} region is shown with close ups of the 3700-3600 cm^{-1} region shown as insets. _____ *182*
Figure 80: TGA weight loss curve for the pyrolysis of the kmethoxy starting material (A) compared to kallyloxy (B). The 1st derivative weight loss curves are shown as insets. _____ *184*
Figure 81: ^{13}C CPMAS NMR of kallyloxy compared to the high resolution liquid ^{13}C spectrum of neat allyloxy. ___ *187*
Figure 82: ^{13}C CPMAS NMR of kallyloxy compared to allyoxy adsorbed on the surface of kGa-1b, allyloxy (on kGa-1b). The peaks attributed to interlayer allyloxy were not observed in allyloxy (on kGa-1b). _____ *188*
Figure 83: ^{13}C CPMAS NMR of kallyloxy compared to the high resolution liquid ^{13}C NMR spectrum of neat allyloxy. The 80-0ppm region is shown, with details in the 76-70ppm region as insets. _____ *189*
Figure 84: ^{13}C CPMAS NMR with dipolar dephasing of kallyloxy (80-40ppm region) using different dephasing times (µs). The constrained environment of the clay interlayer causes the carbons inside the clay interlayer to fully relax after 40µs, while those that are absorbed on the surface are much less affected. _____ *191*
Figure 85: ^{13}C CPMAS NMR with dipolar dephasing of kallyloxy (180-80ppm region) using different dephasing times (µs). The constrained environment of the clay interlayer causes the carbons inside the clay interlayer to fully relax after 40µs, while those that are absorbed on the surface are much less affected. _____ *192*
Figure 86: Plots of ^{13}C CPMAS NMR with dipolar dephasing signal as a function of dephasing time (t_1) for kallyloxy. These plots were used to extrapolate T_2 values for each carbon species in the sample. _____ *193*
Figure 87: ^{29}Si CPMAS NMR of kallyloxy compared with other natural and modified kaolinites. _____ *196*
Figure 88: Proposed arrangement of the allyloxy compound in the kaolinite interlayer space. ^{29}Si and ^{13}C data suggest partial keying of the terminal allyl group carbon into the siloxane rings in the clay mineral. _____ *197*
*Figure 89: Structure of ethylene glycol vinyl ether*_____ *201*
Figure 90: XRD results of kvinyloxy compared to starting kDMSO material. _____ *202*
*Figure 91: Oriented slide XRD of the washed material, kvinyloxy(w) compared to kvinyloxy.*_____ *203*
Figure 92: ATR-FTIR of kvinyloxy compared to starting kDMSO precursor. _____ *204*
*Figure 93: TGA weight loss curve for the pyrolysis of the kDMSO starting material (A) compared to kvinyloxy (B). The 1st derivative weight loss curves are shown as insets.*_____ *206*
Figure 94: ^{13}C CPMAS NMR spectra of kvinyloxy compared to the water washed material kvinyloxy(w) and kDMSO. Rotational artifacts resulting from MAS are denoted with an asterisk. _____ *208*
Figure 95: ^{13}C CPMAS NMR spectra of kvinyloxy compared to kvinyloxy prepared at room temperature using a kmethoxy precursor, kvinyloxy (lowT). A high resolution ^{13}C liquid NMR spectrum of the unmodified vinyloxy compound used to prepare kvinyloxy is shown as an inset. Rotational artifacts resulting from MAS are denoted with an asterisk. _____ *209*
Figure 96: Attribution of the ^{13}C NMR chemical shifts observed in kvinyloxy. _____ *210*
Figure 97: Side view schematic showing the interlayer space of kaolinite in the prepared kvinyloxy material. ___ *210*
Figure 98: High resolution ^{13}C NMR refluxed solutions of neat vinyloxy (i.e. vinyloxy(c)), and kGa-1b dispersed in vinyloxy, (i.e. vinyloxy(c-kGa-1b)). _____ *213*
Figure 99: High resolution ^{13}C NMR DEPT experiments of vinyloxy (c-kGa-1b). In DEPT 90, only CH carbons give a positive signal, and in DEPT 135 only CH_2 carbons give a positive signal. _____ *214*
*Figure 100: Proposed mechanism for the clay catalyzed acetalization of vinyloxy.*_____ *215*

List of tables

Table 1: Chemical composition of some dioctahedral and trioctahedral clays and their net charge per formula unit. In species with a non-zero charge, interlayer cations balance out the negative charge. M represents a generic metal cation. Adapted from: (Bergaya and Lagaly, 2013). 11
Table 2: CEC values for different clay minerals. A short explanation on the origin of the clay mineral's CEC is included in the far right column. Adapted from: (Carroll, 1959). 12
Table 3: Summary of compounds that can directly intercalate inside kaolinite 18
Table 4: Summary of ^{1}H NMR peaks identified for kDMSO using a five site model. 47
Table 5: Summary of ^{1}H NMR peaks identified for kmethoxy. 53
Table 6: ^{1}H MAS NMR peaks identified in kmethoxy(ht). 58
Table 7: %CHNS elemental analysis of natural and modified kaolinites 71
Table 8: ^{1}H MAS NMR of kDMSO-d curve fitting results shown in Figure 26. 74
Table 9: Summary of ^{1}H NMR peaks identified for kmethoxy-d 78
Table 10: ^{27}Al MAS NMR parameters of kGa-1b identified from fitting the 4.7T experimental spectra in Figure 37. 99
Table 11: ^{27}Al MAS NMR parameters of kGa-1b identified from fitting the 4.7T and 21.1T experimental spectra in Figure 38 and Figure 39. 102
Table 12: ^{27}Al MAS NMR parameters of kDMSO identified from fitting the 4.7T experimental spectra in Figure 41. 105
Table 13: ^{27}Al MAS NMR parameters of kDMSO identified from fitting the 4.7T and 21.1T experimental spectra in Figure 42 and Figure 43. 109
Table 14: ^{27}Al MAS NMR parameters of kmethoxy identified from fitting the 4.7T experimental spectra in Figure 45. 112
Table 15: ^{27}Al MAS NMR parameters of kmethoxy identified from fitting the 4.7T experimental spectra in Figure 46. 117
Table 16: ^{27}Al MAS NMR parameters of kmethoxy(ht) identified from fitting the 4.7T experimental spectra in Figure 49. 122
Table 17: Modified 001 d-spacing of kPEPEG materials prepared compared to kDMSO. These values are based on XRD data in Figure 54. 135
Table 18: Summary of IR bands identified in the spectrum of kPEPEG2250 shown in Figure 58 and Figure 59. 143
Table 19: Summary of the ^{13}C CPMAS NMR peaks observed for kPEPEG2250. 146
Table 20: Summary of T2 values calculated for kPEPEG compared to the washed and pyrolyzed product kPEPEG2250(w), and the neat polymer (PEPEG). 151
Table 21: Summary of the IR bands identified in kPLA. 164
Table 22: Summary of the ^{13}C CPMAS NMR peaks observed for kPLA. 169
Table 23: Literature review of diol compounds grafted in kaolinite. 175
Table 24: ^{13}C T_2 transverse relaxation times calculated for the carbons in kallyloxy using the plots in Figure 86. T_2 values below 20µs are attributed to carbons inside the clay interlayer space. The T_2 value for the 117.4ppm carbon was not calculated due to the data's poor fit to the linear regression plot. 194

List of abbreviations

3Q – triple quantum

%(v/v) – volume percentage

%(w/w) – weight percentage

%CHNS – Percent carbon, hydrogen, nitrogen, sulfur elemental analysis

allyloxy – 3-allyloxy-1,2-propanediol

ATR-FTIR– attenuated total reflection fourier-transform infrared

br – broad (IR intensity)

$CDCl_3$ – deuterated chloroform

CPMAS – cross-polarization magic angle spinning

CRAMPS – combined rotation and multiple pulse spectroscopy

CT – central transition

d1 – recycle delay

d6 – echo delay

dd – dipolar dephasing

D_2O – deuterium oxide

Da – Dalton

DEPT – distortionless enhanced polarization transfer

DMSO – dimethylsulfoxide

DUMBO – Decoupling Uses Mind Boggling Optimization

h – hour

IR – infrared

I.R. – intercalation ratio

m – medium

M_n – number average molar mass

MAS – magic angle spinning

MQMAS – multiple quantum magic angle spinning

NMR – nuclear magnetic resonance

NMF – N-methyl formamide

OD, O-D – deuterium exchanged hydroxyl group

p1 –pulse length (1^{st} pulse)

p2 – pulse length (2^{nd} pulse)

p3 – pulse length (proton 90° pulse in CPMAS experiment)

p15 – contact time

PEG – poly(ethylene glycol)

PEPEG – poly(ethylene)-block-poly(ethylene glycol)

PLA – poly(lactide)

PMLG – Phase Modulated Lee Goldburg

R^2 – correlation coefficient

REAPDOR – (rotational echo adiabatic passage double resonance)

RF – radio frequency

RT – room temperature

s – strong (IR intensity)

SEM – scanning electron microscope

ST – satellite transition

t_1 – dipolar dephasing time

T_2 – transverse relaxation time

TMS – tetramethylsilane

TMSS – Tetrakis(trimethylsilyl)silane

TGA – thermal gravimetric analysis

U.S.A. – United States of America

U.K. – United Kingdom

vinyloxy – ethylene glycol vinyl ether

vs – very strong (IR intensity)

vw – very weak (IR intensity)

w – weak (IR intensity)

XRD – X-ray diffraction

1 General Introduction

1.1 Clays & clay minerals and human activity

It is hard to imagine life without clay minerals. Clays have played a key role in the geochemistry of this planet, and their genesis has been implicated with that of life on this planet (Bernal, 1949; Brack, 2013; Cairns-Smith, 1987; Weiss, 1981). Clays and clay minerals have also played an important role in human activity since the dawn of civilization. Classically, they have been used as materials in ceramics and pottery, and in construction for making bricks and cement (Manning, 1995; Van Damme and Gmira, 2006). They are still used for many of these classical applications today, especially in construction where they are used to make floor and wall tiles, bricks, and cement. They are also important materials for use as domestic pet waste adsorbents, as ceramics used in sanitary ware, as lubricants in mud drilling, as refractory products in the iron and steel industry, and as fillers and coatings for a variety of commercial products (U.S. Geological Survey, 2017). Today mining and production of clays is a multimillion dollar industry, where they are used as inexpensive, abundant and environmentally friendly materials. Annual production in the United States alone was estimated to be 25.7 million metric tonnes and valued at $1.43 billion in 2016 (U.S. Geological Survey, 2017).

There has also been growing interest in using clay minerals in more specialized applications. For example, research has been done on using clay minerals for use as specialized absorbents for environmental remediation (Yuan *et al.*, 2013; Sanchez-Martin *et al.*, 2006). They have also been used as materials for modifying the surface of electrodes for use as high efficiency sensors (Dedzo and Detellier, 2013; Mousty, 2004; Ngassa *et al.*, 2016; Tonlé *et al.,* 2011). They are also used as catalysts and support materials for catalysis (Mccabe and Adams, 2013; Dedzo *et al.*, 2016; Letaief *et al.*, 2011; Molina *et al.*, 2014).

More research and growth is anticipated in these traditional and specialized applications in the coming years, with some calling them the materials of the 21st century (Bergaya and Lagaly, 2013).

1.2 Classification of clays and clay minerals in soil science

While the terms clays and clay minerals are often used interchangeably, the two terms are in fact not identical. While clay minerals describe a well-defined class of minerals, the term “clays” describes something much more complex and a non-uniform substance. Since their first classification by Agricola in 1546 (Bandy and Bandy, 2004), there has been no uniform nomenclature for describing clays. The most commonly accepted, modern definition of clays was outlined by Guggenheim (Guggenheim and Martin, 1995) as follows:

"The term 'clay' refers to a naturally occurring material composed primarily of fine-grained minerals, which is generally plastic at appropriate water contents and will harden with[sic] dried or fired. Although clay usually contains phyllosilicates, it may contain other materials that impart plasticity and harden when dried or fired. Associated phases in clay may include materials that do not impart plasticity and organic matter"

These fine grained minerals typically refer to micron and sub-micron sized particles, however there is no universally agreed upon value as a cut-off point (see Figure 1). The commonly used USDA limit of <2µm will be used in the context of this work.

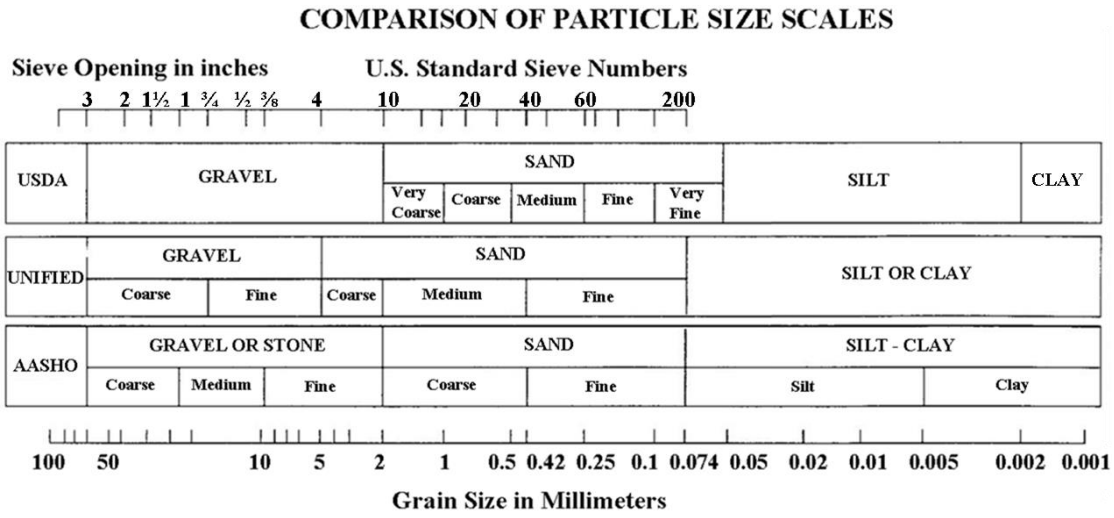

Figure 1: Commonly used particle size scales used to classify soil fractions in North America. The commonly used USDA scale classifies clay fractions in soils as the sub 2µm fraction. Adapted from: (U.S. Department of Agriculture National soil survey handbook, title 430-VI).

1.3 Structure and nomenclature of clay minerals

Clay minerals are the main constituents of clays and responsible for most of their chemical and physical properties. They are part of the phyllosilicate class of minerals, a broad family that also includes micas, chlorites, serpentine and talc. Their ideal structure is a continuous two-dimensional sheet of linked tetrahedral and octahedral coordinated metal oxides (Figure 2).

The tetrahedral sheets can be represented by the base structural formula T_2O_5, where T is a cation, usually Si^{4+}, Al^{3+}, or Fe^{3+}, and much less commonly Be^{2+} or B^{3+} (Bailey, 1988a). Each individual tetrahedron shares 3 of their oxygens with 3 other tetrahedron, forming a planar, hexagonal mesh like structure (Figure 2). The fourth, apical oxygen is shared with an octahedral coordinated metal cation in the octahedral sheet, linking the tetrahedral and octahedral sheets together. These octahedral metal cations are primarily Mg^{2+}, Al^{3+}, Fe^{2+}, and Fe^{3+}, but Li, Ti, V, Cr, Mn, Co, Ni, Cu, and Zn are also possible (Bailey, 1988a).

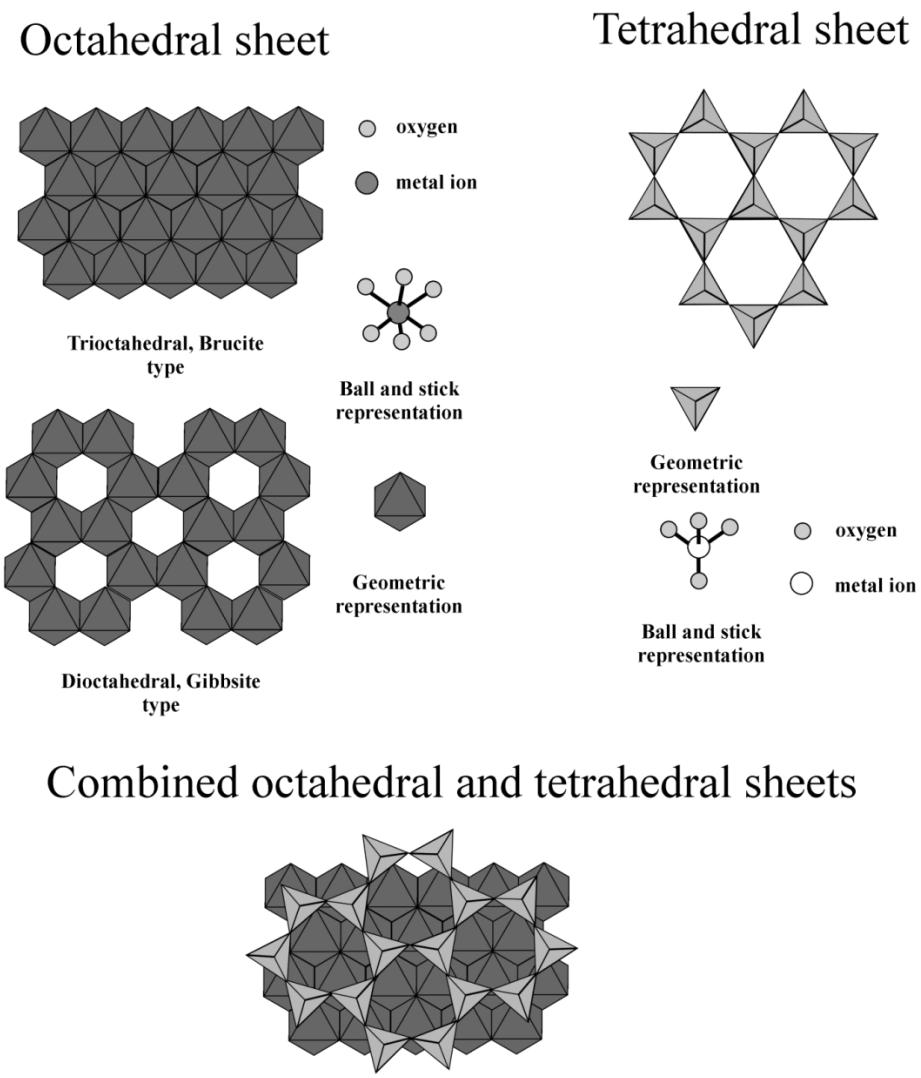

Figure 2: Representation of idealized octahedral and tetrahedral sheets in phyllosilicates and their combined, stacked structure. The idealized sheet structures are slightly distorted in the combined tetrahedral-octahedral structure.

The oxygens in the octahedral sheet are coordinated to either 3 metal centers in the case of a divalent cation, or 2 metal centers in the case of a trivalent one. These types of sheet structures are termed trioctahedral and dioctahedral respectively. In the dioctahedral sheet, this difference in coordination leads to the formation of regularly spaced cavities in the sheet (Figure 2).

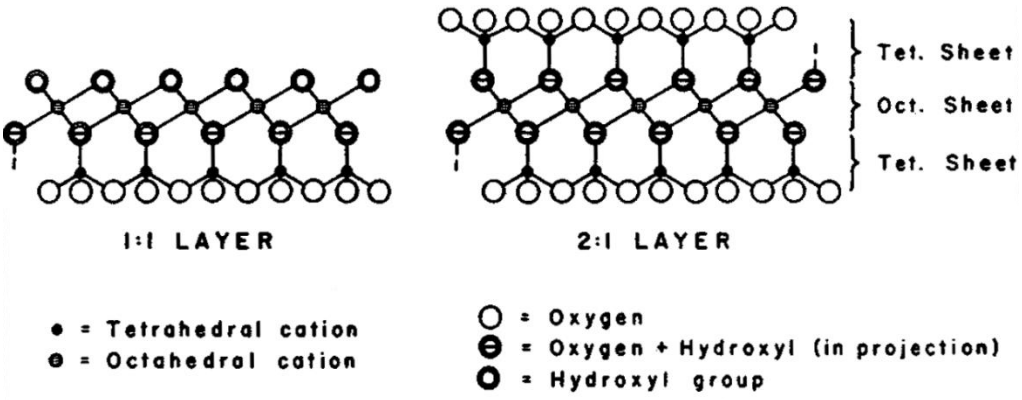

Figure 3: Representation of idealized 1:1 and 2:1 layered structures in phyllosilicates. Adapted from: (Bailey, 1988a).

Each octahedral sheet can form a link through shared oxygens with one or two tetrahedral sheets. This gives rise to two possible arrangements, termed 1:1 and 2:1 layers (see Figure 3). These layers form a vertical stacking structure with a characteristic gap between each layer termed the interlayer space. There is a slight mismatch between the two sheets in the combined structure. As a result, these linked octahedra and tetrahedra in both sheets are slightly distorted from their ideal geometry (Brigatti *et al.*, 2013). These stacked layers form individual particles, which in turn can aggregate together in the bulk material (Figure 4).

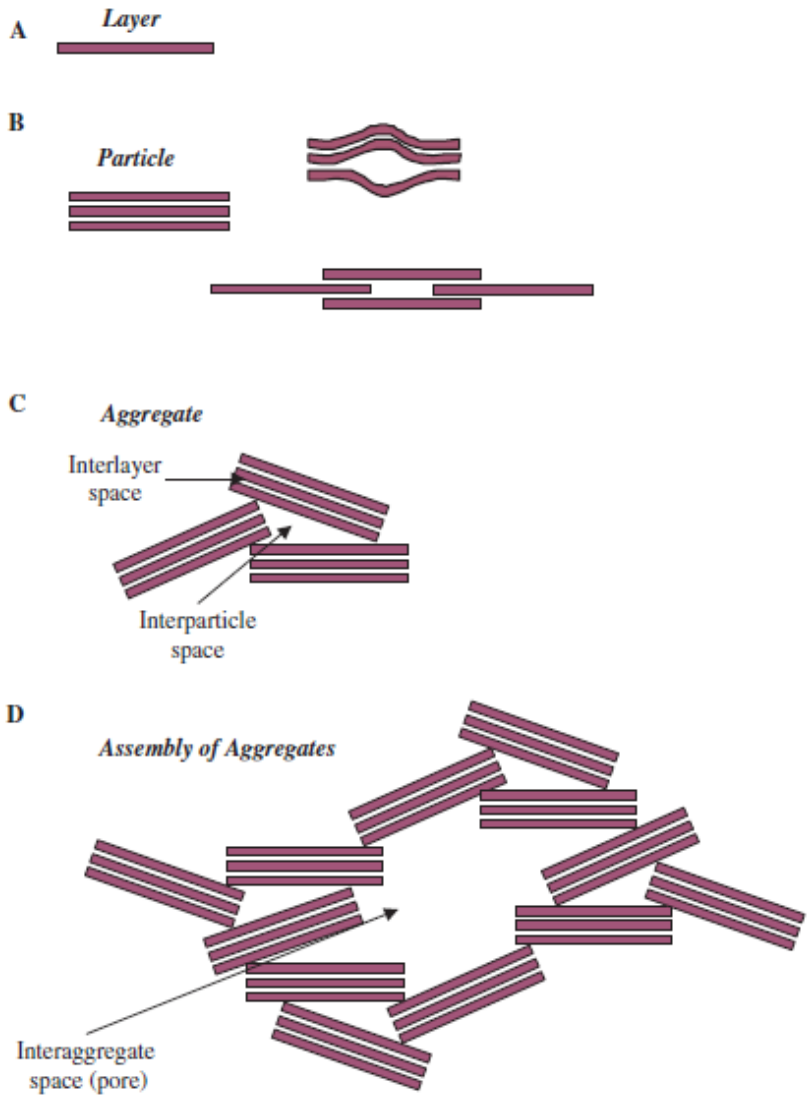

Figure 4: Diagram outlining individual layers (A), stacks of layers as particles (B) aggregates of particles (C) and assemblies of aggregates (D) in phyllosilicates. Adapted from: (Bergaya and Lagaly, 2013).

1.4 Layer stacking sequences and polytypism

Polymorphism refers to be ability of a compound to exist in more than one form or crystal structure. In layered materials such as phyllosilicates, the stacking of individual layers can also give rise to a special type of polymorphism known as polytypism. Polytypes are polymorphs that have identical sheet structures in the horizontal plane but differ in their layer stacking sequences. In clay minerals, this arises as a result of the octahedral cations occupying different sets of positions between two adjacent layers, and as a consequence different hydrogen bonding pairs are possible between adjacent layers (Bailey 1988b). Bailey (Bailey 1988b) describes 12 standard polytypes possible for 1:1 phyllosilicates, and these are outlined in Figure 5.

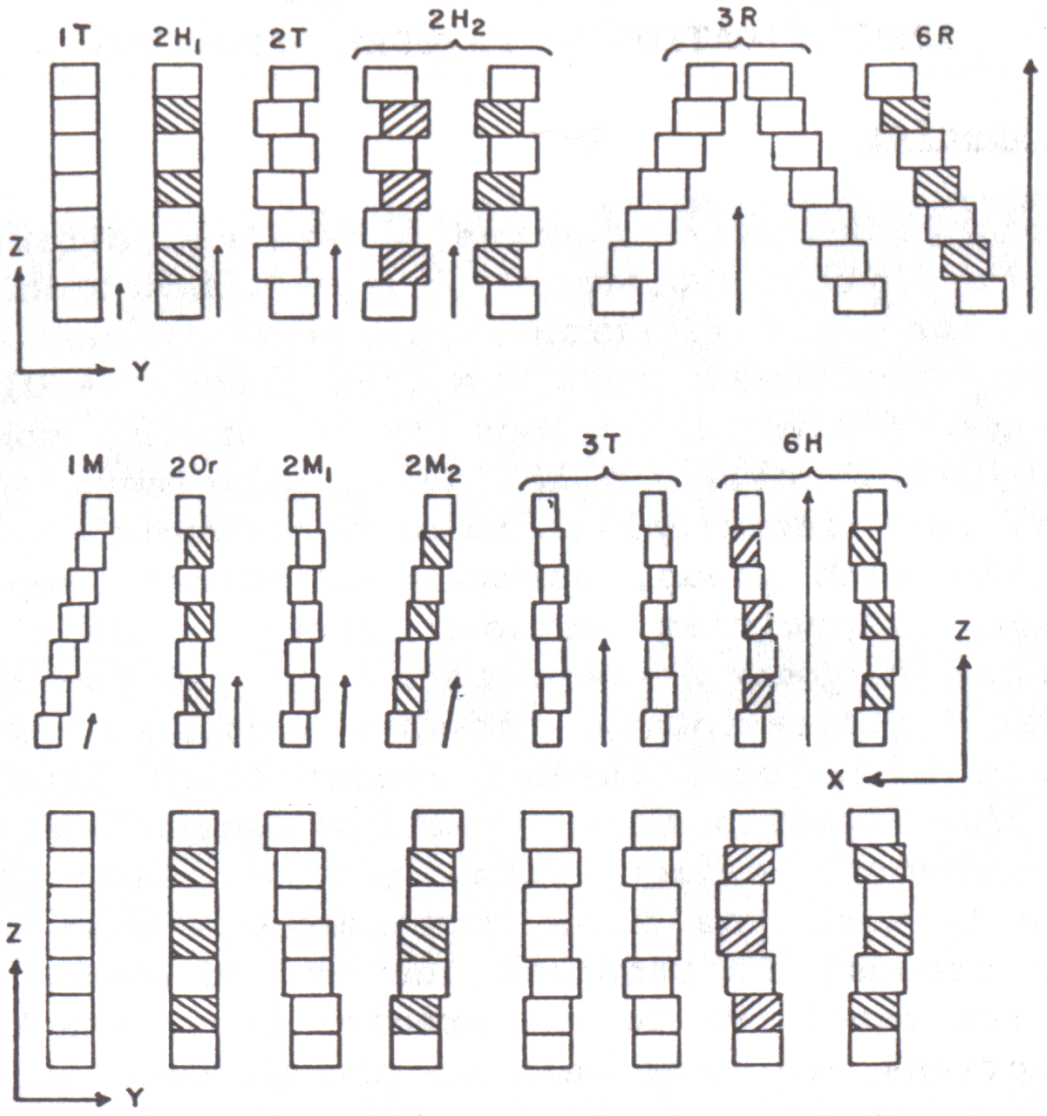

Figure 5: Schematic representation of the 12 standard polytypes for 1:1 phyllosilicates. Adapted from (Bailey 1988b).

1.5 Layer charge and cation exchange capacity

It is possible to have a net negative charge in a given layer. This occurs primarily due to substitution of the metal ions in the structure with lower valence ions; however vacancies in the structure and dehydroxylation are also possible sources (Bailey, 1988a). This substitution can occur in the tetrahedral sheet through substitution of 4^+ ions for 3^+ or 2^+ ions, or in the octahedral sheet through substitution of 3^+ or 2^+ ions with 2^+ or 1^+ ions. Examples of different clay minerals and their respective structure and their net charge per formula unit are shown in Table 1.

To compensate for the negative charge resulting from the isomorphous replacement of the structural cations, a balancing positive charge in the form of hydrated metal cations is integrated into the interlayer space. These interlayer cations are fully exchangeable and this ability to act as cation exchangers is an important property of these clays minerals. Their overall capacity for cation exchange is expressed in a value known as the cation exchange capacity (Carroll, 1959). This value is typically shown in equivalents of H^+ per unit of mass. Table 2 shows examples of CEC values for different types of clay minerals.

Table 1: Chemical composition of some dioctahedral and trioctahedral clays and their net charge per formula unit. In species with a non-zero charge, interlayer cations balance out the negative charge. M represents a generic metal cation. Adapted from: (Bergaya and Lagaly, 2013).

Charge/ formula unit	Dioctahedral species	Trioctahedral species
Serpentine-kaolin group		
~0	Kaolinite $(Si_2)^{IV}(Al_2)^{VI}\ O_5\ (OH)_4$	Serpentine $(Si_2)^{IV}(Mg_3)^{VI}\ O_5\ (OH)_4$
Talc-pyrophyllite group		
~0	Pyrophyllite $(Si_4)^{IV}(Al_2)^{VI}\ O_{10}\ (OH)_2$	Talc $(Si_4)^{IV}(Mg_3)^{VI}\ O_{10}\ (OH)_2$
Smectite group		
~0.2–0.6	Montmorillonite $(Si_4)^{IV}(Al_{2-y}\ Mg_y)^{VI}\ O_{10}\ (OH)_2$, $yM^+.nH_2O$ Beidellite $(Si_{4-x}\ Al_x)^{IV}(Al_2)^{VI}\ O_{10}\ (OH)_2$, $xM^+.nH_2O$	Hectorite $(Si_4)^{IV}(Mg_{3-y}\ Li_y)^{VI}\ O_{10}\ (OH)_2$, $yM^+.nH_2O$ Saponite $(Si_{4-x}\ Al_x)^{IV}(Mg_3)^{VI}\ O_{10}\ (OH)_2$, $xM^+.nH_2O$
Vermiculite group		
~0.6–0.9	Vermiculite $(Si_{4-x}\ Al_x)^{IV}(Al_{2-y}Mg_y)^{VI}\ O_{10}\ (OH)_2$, $(x+y)M^+$	Vermiculite $(Si_{4-x}\ Al_x)^{IV}(Mg_{3-y}M_y{}^{3+})^{VI}\ O_{10}\ (OH)_2$, $(x-y)/2\ Mg^{2+}$
True (flexible) mica group[a]		
~0.9–1.0	Celadonite $(Si_{4-x}\ Al_x)^{IV}(Fe_{2-y}Mg_y)^{VI}\ O_{10}\ (OH)_2$, $(x+y)K^+$ Muscovite $(Si_3\ Al)^{IV}(Al_2)^{VI}\ O_{10}\ (OH)_2$, K^+	Lepidolite $(Si_{4-x}\ Al_x)^{IV}(Mg_{3-y}Li_y)^{VI}\ O_{10}\ (OH)_2$, $(x+y)K^+$ Phlogopite $(Si_3\ Al)^{IV}(Mg_3)^{VI}\ O_{10}\ (OH)_2$, K^+
Brittle mica group		
2.0	Margarite $(Si_2\ Al_2)^{IV}(Al_2)^{VI}\ O_{10}\ (OH)_2$, Ca^{2+}	Clintonite $(Si\ Al_3)^{IV}(Mg_2\ Al)^{VI}\ O_{10}\ (OH)_2$, Ca^{2+}

Table 2: CEC values for different clay minerals. A short explanation on the origin of the clay mineral's CEC is included in the far right column. Adapted from: (Carroll, 1959).

Mineral	Exchange capacity (meq/100g; pH 7)	Structural control
Kaolinite	3-15	Unsatisfied valences on edges of structural units
Halloysite ($2H_2O$)	5-10	Unsatisfied valences on edges of structural units
Halloysite ($4H_2O$)	40-50	Unsatisfied valences on edges of structural units and on internal surface between the layers
Montmorillonite	70-100	Substitutions in the octahedral and tetrahedral units giving excess negative charge; unsatisfied valences on edges of units
Illite	10-40	As in Montmorillonite, plus deficiency of K^+ between the layers
Vermiculite	100-150	Replacement of interlayer cations, substitution within the units, and unsatisfied valences on edges of units
Palygorskite	20-30	Substitution of Al^{+3} for Si^{+4} in structural units, unsatisfied exchange sites structure within channels in the structure

1.6 Kaolinite structure and nomenclature

Kaolinite is the most abundant mineral in the kaolin sub-group of phyllosilicates. The clay minerals in this sub-group are characterized as dioctahedral clays minerals with 1:1 layered structures (Brigatti *et al.*, 2013), and include kaolinite, its two polytypes dickite and nacrite, and its tubular polymorph halloysite. The kaolin sub-group of minerals are part a greater group known as the serpentine-kaolin group, which are characterised by their ~0 charge per formula unit (Bailey, 1980). Kaolinite has a base chemical formula $Al_2Si_2O_5(OH)_4$. Trace amounts of iron, titanium, potassium and magnesium are also sometimes found in its structure (Giese, 1988), however its chemical composition typically deviates little from the base formula. Like other kaolin minerals, its genesis occurs primarily through the weathering of minerals such as feldspars and muscovite in a mechanism similar to the one shown below for potassium feldspar (Murray, 1988):

$$2KAlSi_3O_8 + 3H_2O \rightarrow Al_2Si_2O_5(OH)_4 + 4SiO_2 + 2K(OH) \qquad (1.1)$$

It forms a 1:1 layered stacking structure with an interlayer space of 7.2Å. This is outlined in Figure 6. The individual layers stack in a 1M style stacking sequence (Figure 5). Interlayer cohesion occurs from a combination of van-der-Waals forces, electrostatic and hydrogen bonding interaction between each adjacent layer (Cruz *et al.*, 1973; Theng, 1979) . This

interaction energy is calculated to be 210 kJ per formula unit, making the individual layers very tightly bound, and cohesive (Cruz *et al.*, 1973).

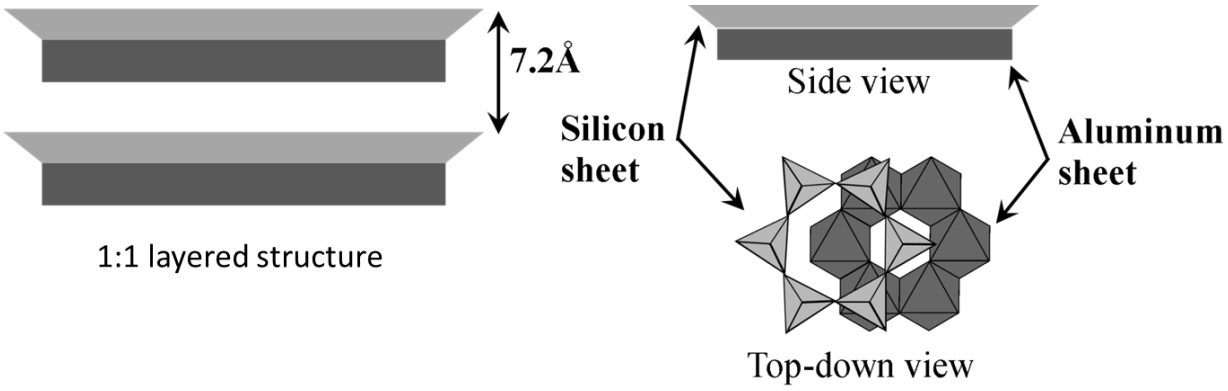

Figure 6: Schematic outlining the layered structure found in kaolinite.

1.7 Hydroxyl groups

The dioctahedral aluminum sheet is capped with hydroxyl groups. These are present as two distinct types (Figure 7) as a result of the gap in the gibbsite type dioctahedral sheet. The hydroxyl groups at the surfaces of the sheet are termed inner surface hydroxyls. They play a key role in the cohesion between individual layers through hydrogen bonding interactions and are highly sensitive to changes occurring to the interlayer environment (Frost *et al.*, 1993; Frost *et al.*, 2000). The hydroxyls inside the octahedral gaps are termed inner hydroxyls. Unlike the inner surface hydroxyls, they are mostly inert to any changes occurring to the interlayer

environment (Frost *et al.*, 1993; Frost *et al.*, 2001). These two types of hydroxyls are present in a 3:1 ratio in the idealized kaolinite structure.

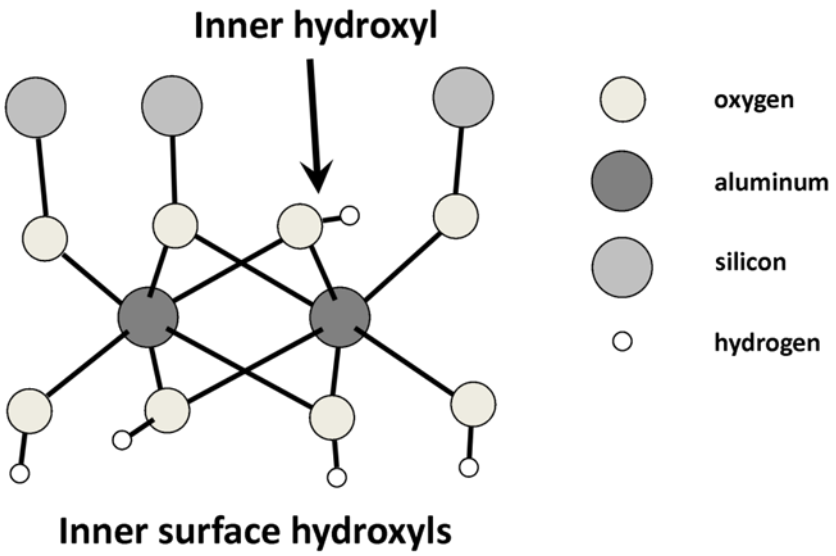

Figure 7: Schematic outlining the hydroxyl groups in kaolinite.

1.8 Defect structure

Zero charge layer phyllosilicates such as kaolinite will often contain a variety of structural defects. These defects mostly arise from slight variations in their stacking sequence (Plançon *et al.*, 1989), and can significantly affect the sharpness of peaks in the mineral's diffraction patterns. Considerable variations in defect structures can be seen across kaolinites obtained

from different localities (Giese, 1988), and these variations are believed to be a source of some of the observed differences in the material properties for these different kaolinites (Murray and Lyons, 1956). Kaolinite's crystallinity is commonly described by an empirical value known as the Hinckley Index (Plançon *et al.*, 1988). This estimates a kaolinite's crystallinity by taking the summed intensities of the $1\bar{1}0$ and $11\bar{1}$ XRD reflections measured from the inter-peak background and dividing it by the intensity of the $1\bar{1}0$ reflection measured from the general background (Figure 8). This yields a dimensionless number, typically between 0.2-1.7 where the larger this number is, the greater the crystallinity of the mineral.

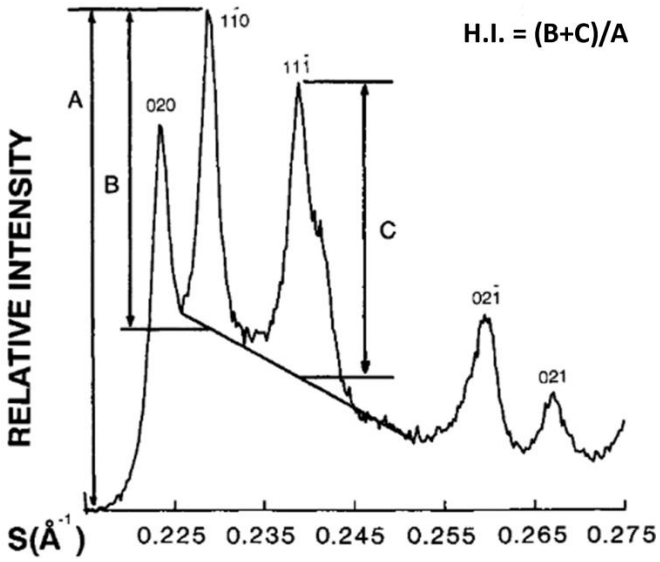

Figure 8: Hinckley index calculation for a low defect, Cornwall, U.K., kaolinite sample. Adapted from (Plançon *et al.*, 1988).

1.9 Interlayer chemistry of kaolinite

Due to the high available surface area in kaolinite confined to the interlayer spaces (Figure 4), chemical modification of kaolinite for specialized applications requires access to these interlayer surfaces. Kaolinite's very cohesive interlayer structure and low CEC values makes this a significant challenge, and strategies typically employed for modifying other commonly used clay minerals in the smectite group cannot be used. Currently, the only known strategy for expanding kaolinite's interlayer space uses small, highly polar molecules capable of disrupting its strong interlayer forces. This was first developed in the early 1960s when it was discovered that some acetate salts such as potassium acetate could be inserted in the kaolinite interlayer space (Wada, 1961). Since then, a number of intercalated complexes have been prepared directly from neat kaolinite; however the list remains limited to a very small number of compounds (Table 3).

Table 3: Summary of compounds that can directly intercalate inside kaolinite

Intercalated compound	Structure	001 d-spacing (Å)
acetamide	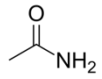	10.9[a]
dimethyl acetamide		12.3[a]
N-methyl acetamide	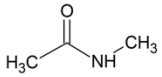	11.3[a]
potassium acetate	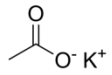	11.4[b]
rubidium acetate	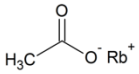	14.4[a]
cesium acetate	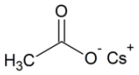	14.7[a]
ammonium acetate	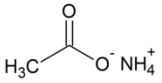	14.0[a]
potassium cyanoacetate	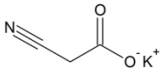	13.0[a]
formamide	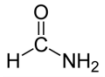	10.1[c]
dimethyl formamide		12.1[c]
N-methyl formamide		10.7[c]
hydrazine		11.0[d]
potassium propionate	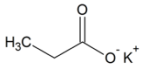	14.0[a]
pyridine N-oxide	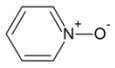	12.5[c]
dimethyl sulfoxide	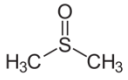	11.2[e]
urea	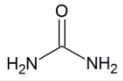	10.7[f]

[a] Weiss *et al.*, 1963a; [b] Wada, 1961; [c] Olejnik, 1970; [d] Weiss *et al.*, 1963b ; [e] Olejnik *et al.*, 1968; [f] Weiss, 1961.

Intercalation will usually produce well defined shifts in kaolinite's x-ray diffraction pattern. This can be readily observed for the *001* reflection, which will shift to lower diffraction angles due its characteristic d-spacing value of 7.2Å expanding to accommodate the intercalated material. The extent of the reaction is usually reported as a ratio called the intercalation ratio which is estimated using the peak ratio intensities of the modified *001* reflection compared to the intensity of the residual, unmodified kaolinite. This is expressed in the following equation (Wiewióra and Brindley, 1969):

$$Intercalation\ ratio = \frac{I_{001\ modified}}{I_{001\ modified} + I_{001\ unmodified}} \qquad (1.2)$$

1.10 Intercalation mechanism

According to Weiss *et al.* (1969), the kinetics of these intercalation reactions can be represented as a logarithmic equation as follows:

$$\sqrt{-\ln(1-\alpha)} = kt \qquad (1.3)$$

where α describes the extent of the reaction as a fractional quantity less than or equal to one, k is a constant, and t represents the reaction time. This will take the form of an s-shaped curve where the reaction proceeds through 3 general stages. First, there is a slow induction period where guest molecules adsorbed on the edge of the layers induce the re-orientation of the hydroxyl groups or the migration of protons (Weiss *et al.*, 1981). This results in the elastic

deformation of the clay layers (Lipsicas *et al.*, 1986). For smaller particles sizes, this can only occur on one side at a time to minimize the deformation energy, while for larger particles this can occur on different sides of the particles simultaneously (Weiss *et al.*, 1981; Lagaly, 1984). This results in faster intercalation reactions for larger particle sizes. Once the layers have been opened up, the reaction proceeds much faster as the space is filled progressively towards the particle's interior. Weiss *et al.* (1969) claimed that structural defects will hamper this, with faster rates observed in more crystalline kaolinites. This continues until the interlayer space approaches saturation with the guest molecules, whereupon it slows down again. This is represented schematically in Figure 9.

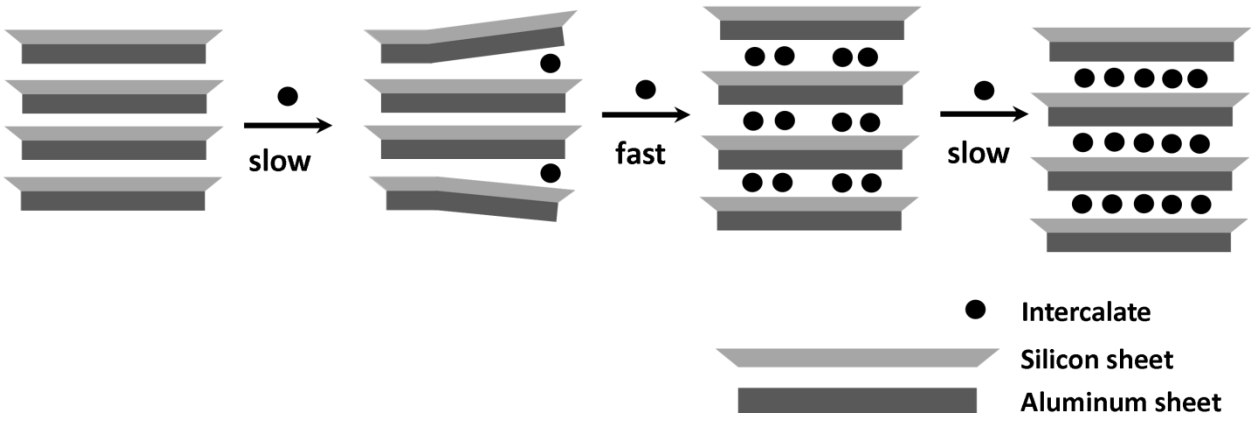

Figure 9: Schematic outlining a general intercalation reaction in kaolinite.

1.11 Displacement reaction

The displacement strategy is commonly used to get around kaolinite's limited reactivity. This first involves the intercalation of a molecule known to insert in the interlayer space of unmodified kaolinite. Once inserted, the interlayer cohesion energy is much weaker and this intercalated compound can then be replaced in a subsequent step by dispersion in an excess of another molecule. This method has been used to prepare a wide variety of kaolinite intercalated complexes using small polar organic molecules like acetone and acetonitrile (Sanchez-Camazano, 1966), various alkyl amines and aromatic amines such as purines and pyridines (Weiss *et al.*, 1966), various organic and inorganic salts like potassium oxalate, alkali halides(Weiss *et al.*, 1963a; Weiss *et al.*, 1966), pyridinium or imidazolium based ionic liquids; (Letaief *et al.*, 2006), various organic polymers such as poly(acrylamide) and poly(ethylene glycol) (Sugahara *et al.*, 1988; Tunney and Detellier, 1996a), and various metal and metal oxide nanoparticles such as Ag and ZnO (Patakfalvi *et al.*, 2003; Németh *et al.*, 2004)[7].

1.12 Grafting reactions

One key advantage offered by kaolinite compared to other commonly used clay minerals is the abundant hydroxyl groups on its inner and outer surfaces. These hydroxyl groups can undergo condensation reactions to yield covalently grafted moieties on the clay mineral's surfaces (Figure 10). This chemistry was first explored in 1993 by Tunney and Detellier (1993) with the covalent grafting of ethylene glycol on kaolinite's inner and outer surfaces. This chemistry has since been expanded to include other polyols (Brandt *et al.*, 2003; Gardolinski and Lagaly, 2005a), simple alcohols (Tunney and Detellier, 1996b), amino alcohols (Tunney and Detellier, 1997), oxysilanes (Tonlé *et al.*, 2007), and a variety of hydroxyl terminated ionic liquids (Dedzo *et al.*, 2012).

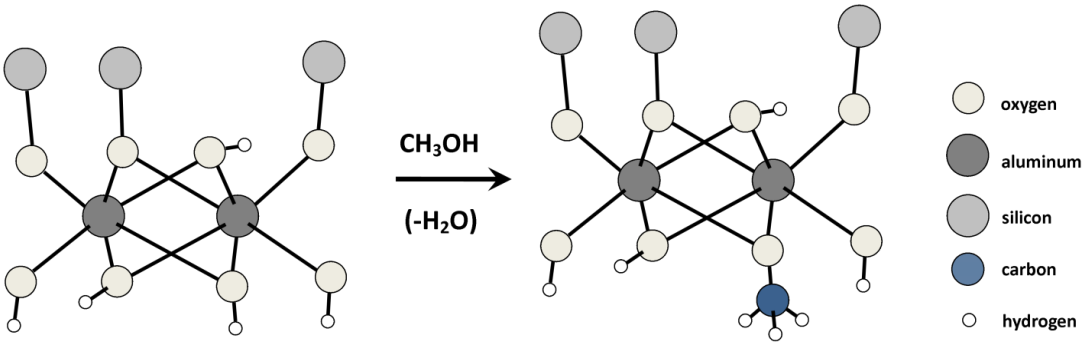

Figure 10: Schematic outlining the covalent grafting of methanol on kaolinite as methoxy (OCH_3) groups.

These grafted kaolinites show a much greater stability compared to intercalated complexes. Most intercalated matter can be easily removed by washing the modified kaolinite in water or by heating to temperatures around 200°C. Grafted compounds, on the other hand, are much more resistant to water washing and are stable up to temperatures of around 400-500°C where the clay mineral irreversibly loses its interlayer hydroxyls as water (Tunney and Detellier, 1996b). This increased thermal stability and resistance to washing in water can be used to distinguish simple intercalated material from grafted ones (Letaief and Detellier, 2011). These properties make grafted kaolinites very attractive for applications requiring a functional material that remains stable after exposure to water or high temperatures. In spite of the clear utility of these grafted kaolinites, this remains a highly underdeveloped field of study.

1.13 Kaolinite structural characterization using solid state NMR

Elucidating the crystal structure of kaolinite samples has proven to be a fairly significant challenge for researchers for many years. This is mostly owing to the great difficulty of obtaining large single crystals for crystallographic analysis and pinpointing the exact positions of hydrogen atoms in the structure (Giese, 1988). As a result, a number of different techniques have been employed for solving their structures. For example, infrared spectroscopy was used to infer the position of H atoms in the kaolinite crystal structure (Wada, 1967).

Nuclear magnetic resonance is a powerful tool for describing local nuclear environments in the solid state and it is a useful complement to other techniques. Kaolinite's elemental composition allows it to be studied using a variety of NMR nuclei, namely ^{29}Si, ^{27}Al, ^{17}O, and ^{1}H. In kaolinites modified with organic material, ^{13}C can also be studied. Solid state NMR has been shown to be an invaluable tool for structural characterisation of kaolinite. For example, early studies by Barron (Barron *et al.*, 1983) showed two inequivalent Si sites in the ^{29}Si NMR spectra of kaolinites, which confirmed the asymmetric nature of the kaolinite layers.

With the exception of ^{13}C and to a lesser extent ^{29}Si, solid state NMR of modified kaolinites is underused as a characterization technique. The current knowledge base available in the literature on the characterization of functionalized kaolinites, even for commonly used precursors such as kaolinite-DMSO intercalates, is notably lacking, especially for less commonly studied nuclei in the solid state such as ^{1}H, ^{27}Al, and ^{17}O. This is probably owing to the fact that most of the early work done in developing the interlayer chemistry of kaolinite was in the 1960s, before high resolution NMR in the solid state was possible. The studies that have been done have, however, been very enlightening. For example, a combination of ^{13}C and ^{29}Si NMR studies on kaolinite-DMSO intercalates identified new peaks in the ^{29}Si NMR spectrum of the clay mineral and in the ^{13}C NMR spectrum of DMSO (Thompson, 1985). This was used to infer the position of the DMSO molecules in the interlayer space of kaolinite-DMSO intercalates, where one methyl group keys into the siloxane ring in the silicon sheet.

1.14 Industrial uses and current trends

Kaolinite and other kaolin sub-group minerals are important as industrial minerals. In 2017, 37 million metric tons of kaolins were mined and produced worldwide, where 43% was used as coatings and fillers, mostly in the pulp and paper industry (U.S. Geological Survey, 2017). Demand for kaolins has stagnated in recent years, attributed primarily to declining sales of paper products. Because of this and the high worldwide abundance of kaolins, there is an interest to investigate possible new applications for kaolinite, especially in regions containing abundant reserves of the clay mineral such as in the U.S.A., the U.K., Brazil, and China.

1.15 Polymer clay nanocomposites

Composites are multicomponent materials that are made up of several component materials that have very different chemical properties and which remain separate and distinct from one another in the final material. Inorganic materials such as clay minerals are widely used in the polymer industry to fabricate composites, where they can serve as reinforcing agents to improve some of its physical properties, such as rigidity and thermal resistance (Elias, 2000). These inorganics can make up as much as 60%(w/w) in polymer composites (Elias, 2000). High quantities of inorganics, however, increase the density of the final material which can be undesirable, for example in lightweight materials. It can also lead to incompatibility between the inorganic and the polymer components, diminishing some of the final material's physical

properties (LeBaron *et al.*, 1999). These issues are minimized in nanocomposite materials. Nanocomposites are a composite material where at least one of its components has dimensions that are <100nm. For polymer clay composites, a nanocomposite material would be obtained when the clay mineral's individual layers are separated from one another (Figure 11). Complete exfoliation and distribution of the clay mineral's separated layers throughout the polymer matrix results in significant improvements to the thermal and mechanical properties of the final material compared to the neat polymer or a simple composite (LeBaron *et al.*, 1999).

The first of these polymer clay nanocomposites was reported as early as 1961 where the in-situ polymerization of vinyl monomers was achieved in the smectite clay mineral montmorillonite (Blumstein, 1961). However, it was not until the 1980s when Toyota patented a process for preparing a nylon-6 nanocomposite by in-situ polymerization inside an organically modified montmorillonite, that these materials attracted much research interest (Okada *et al*., 1986; Okada *et al.*, 1988). This particular nanocomposite showed superior strength, modulus, and heat distortion temperature using <5% (w/w) in clay minerals (Okada and Usuki, 1995). These techniques have been since extended to include epoxys, poly(urethanes), poly(imides), poly(esters), poly(propylene), poly(styrene), poly(siloxanes) and nitrile rubbers (LeBaron et al., 1999). These have been prepared by intercalative in-situ polymerization and by direct intercalation using concentrated solutions or viscous melts of the polymer (Hussain *et al.*, 2006). Both academic (Figure 12) and industrial interest in these polymer clay nanocomposites

continues to grow, with the polymer nanocomposites market forecasted to exceed 5.1 billion USD by 2020 (MarketsandMarkets, 2015).

Polymer clay nanocomposite materials are predominantly prepared using smectite clay minerals, such as montmorillonite, that have been intercalated with bulky organic cations. One important drawback is that some of these intercalates decompose at temperatures used in polymer processing (Chang, 2014). This creates voids in the material and reduces the compatibility between the clay mineral and the polymer matrix, significantly impacting the properties of the final material. Other volatiles such as water can also be problematic and lead to polymer degradation during processing (Davis *et al.*, 2003). As such, there is some interest in recent years to develop new polymer clay nanocomposites that don't use organically modified smectites.

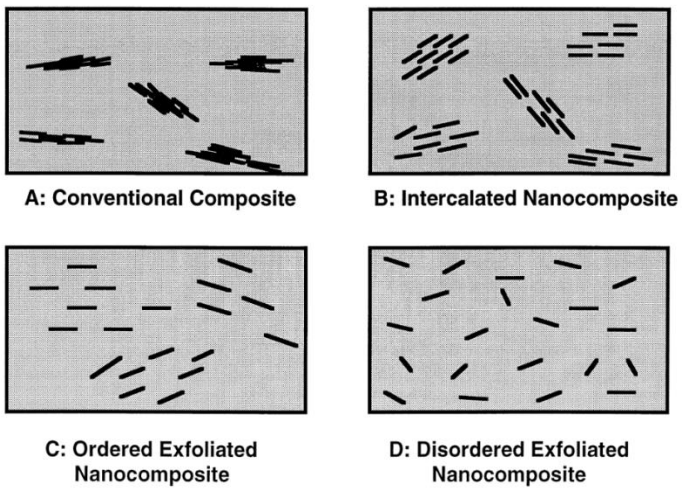

Figure 11: Schematic showing: (A) a conventional composite, (B) an intercalated and (C+D) a disordered and ordered exfoliated polymer clay nanocomposite material. Materials C and D

show a significant increase in the thermal and mechanical properties compared to the neat polymer. Adapted from (LeBaron *et al.*, 1999).

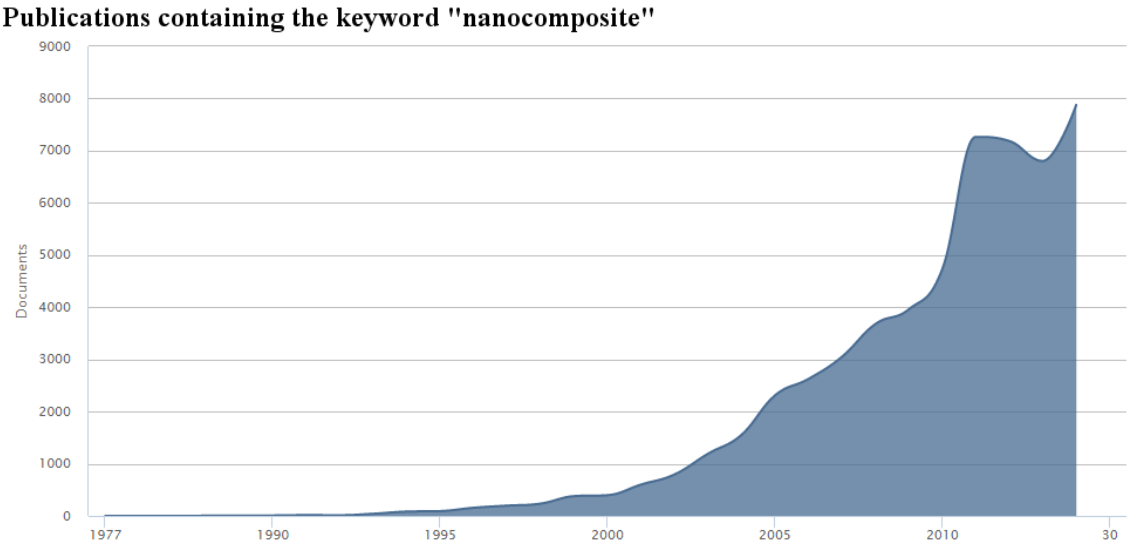

Figure 12: Number of documents containing the keyword “nanocomposite” from the period of 1977-2015. Data was retrieved from the Scopus search engine (July 2nd, 2015): https://www.elsevier.com/solutions/scopus.

1.16 Aim and purpose of research

Using kaolinite to prepare functionalized materials is still a relatively niche subject. This is in spite of the low cost, high availability, and industrial interests in finding new uses for the clay mineral. Despite the challenges with accessing the kaolinite interlayer space, using well developed methods for expanding kaolinite with precursors such as DMSO, NMF or urea then allows the interlayer space to be modified with a wide variety of organic compounds for many applications. Kaolinite also offers a key advantage over other commonly used clay minerals such as smectites, due to the abundant hydroxyl groups available on its internal surfaces for

grafting organic functional groups, making them resistant to heat and to washing in water. These properties could make them very useful for certain applications, for example in polymer nanocomposite materials that require high thermal resistance during polymer processing, or as electrode modifiers for sensing applications (Dedzo and Detellier, 2016).

Solid state NMR has been shown to play an essential role in solving the structure of modified kaolinites such as kaolinite-DMSO. Unfortunately, the knowledge base available on the characterization of functionalized kaolinites, even commonly used precursors such as the aforementioned kaolinite-DMSO, is notably lacking for some nuclei in the solid state such as ^{1}H, ^{27}Al and ^{17}O.

The aim of this research project is to attempt to address these points, by developing new synthetic strategies for preparing kaolinite based materials for use as nanocomposites and to examine commonly prepared modified kaolinite precursors materials by ^{1}H and ^{27}Al NMR in an attempt to demonstrate their utility for characterizing kaolinite intercalated and grafted complexes.

In Chapter 2, solid state ^{1}H and ^{27}Al NMR of various kaolinite precursors commonly used will be studied to demonstrate the utility for differentiating between unmodified kaolinite, and grafted and intercalated complexes.

In Chapters 3 and 4, new synthetic strategies will be investigated for preparing kaolinite nanocomposites. In Chapter 3, the intercalation of polymers using viscous melts will be investigated, while in Chapter 4 the covalent grafting of polymerizable groups will be investigated.

Experimental details related to sample preparation and characterization will be described in Chapter 5.

2 Solid State ^{1}H and ^{27}Al NMR studies of modified kaolinite precursor materials

2.1 Solid state ^{1}H NMR study of natural and modified kaolinites

2.1.1 Introduction

^{1}H is by far the most commonly studied NMR nucleus. This isotope is 99.988% abundant and has a high gyromagnetic ratio, making it very sensitive to NMR. Despite this, ^{1}H NMR is mostly limited to studying liquid phase samples due to the challenges with obtaining high resolution ^{1}H spectra in the solid state.

In NMR, the interaction energy, E, between a nucleus and an applied magnetic field, B_0, is described in the following equation:

$$E = -\gamma \hbar \underset{\sim}{I} \cdot \underset{\sim}{B}_0 \qquad (2.1)$$

Where γ is the gyromagnetic ratio and I is the spin quantum number for a given nucleus and ħ is the Reduced Planck constant. The electron density surrounding a nucleus will alter the magnetic field experienced by it in a phenomenon referred to as chemical shielding. This chemical shielding can yield some very crucial information regarding the chemical environment of a nucleus and transformed NMR from a physical phenomenon into a powerful tool for analytical sciences (Mackenzie and Smith, 2002). This modifies equation 2.1 as follows:

$$E = \frac{\mu_0}{2\pi}\gamma h \underset{\sim}{I} \cdot (\underset{\approx}{1} - \underset{\sim}{\sigma} - \underset{\sim}{\chi}) \cdot B_0 \qquad (2.2)$$

Where μ_0 is the permeability constant, h is the Planck constant, χ is the magnetic susceptibility, and σ represents a second rank tensor describing the chemical shielding interaction. The corresponding Hamiltonian can be written as follows:

$$H_{CS} = \gamma h \underset{\sim}{I} \cdot \underset{\sim}{\sigma} \cdot \underset{\sim}{B}_0 \qquad (2.3)$$

The chemical shielding tensor can be represented in the laboratory frame ($\underset{\sim}{\sigma}$) and in its own principal axis system ($\underset{\sim}{\sigma}^{PAS}$) as follows:

$$\underset{\approx}{\sigma} = \begin{bmatrix} \sigma_{xx} & \sigma_{xy} & \sigma_{xz} \\ \sigma_{yx} & \sigma_{yy} & \sigma_{yz} \\ \sigma_{zx} & \sigma_{zy} & \sigma_{zz} \end{bmatrix} \qquad \underset{\sim}{\sigma}^{PAS} = \begin{bmatrix} \sigma_{XX} & 0 & 0 \\ 0 & \sigma_{YY} & 0 \\ 0 & 0 & \sigma_{ZZ} \end{bmatrix} \qquad (2.4)$$

Taking into account the main magnetic field (B_0), the field at the nucleus, B, can be described as follows:

$$\underset{\sim}{B} = \left(\underset{\approx}{1} - \underset{\approx}{\sigma}\right) \cdot \underset{\sim}{B}_0 = \begin{pmatrix} 1-\sigma_{xx} & -\sigma_{xy} & -\sigma_{xz} \\ -\sigma_{yx} & 1-\sigma_{yy} & -\sigma_{yz} \\ -\sigma_{zx} & -\sigma_{zy} & 1-\sigma_{zz} \end{pmatrix} \begin{pmatrix} 0 \\ 0 \\ B_0 \end{pmatrix} = \begin{pmatrix} -\sigma_{xz} & B_0 \\ -\sigma_{yz} & B_0 \\ (1-\sigma_{zz}) & B_0 \end{pmatrix} \qquad (2.5)$$

Since only the components aligned with the magnetic field, B_0, are of interest, this reduces the chemical shielding Hamiltonian as follows:

$$H_{CS} = \gamma_1 h I_z \cdot \sigma_{zz} \cdot B_0 \qquad (2.6)$$

The chemical shielding tensor element in this expression, σ_{zz}, can be expressed as follows:

$$\sigma_{zz} = \sigma_{iso} + \frac{\sigma_{zz} - \sigma_{iso}}{2}\left[(3\cos^2\theta - 1) + \frac{\sigma_{XX} - \sigma_{YY}}{\sigma_{zz} - \sigma_{iso}}(\sin^2\theta \cos 2\phi)\right] \qquad (2.7)$$

Where the angles θ and ϕ refer to the polar angle of the laboratory frame and the principal axis system of the tensor. The terms $\sigma_{zz} - \sigma_{iso}$ and $\frac{\sigma_{XX} - \sigma_{YY}}{\sigma_{zz} - \sigma_{iso}}$ are sometimes called the shielding anisotropy and asymmetry respectively. These are often quoted together along with the isotropic value, σ_{iso} when describing chemical shielding. Rapid molecular motion in the liquid state and simulation of these conditions in the solid state using magic angle spinning (MAS) will average out the anisotropic components, leaving only the isotropic one.

The chemical shielding of a sample (σ_{sample}) cannot be directly measured, but it can be compared to that of a reference compound (σ_{ref}) giving a value known as the chemical shift, δ. This is expressed as follows:

$$\delta = \frac{\sigma_{ref} - \sigma_{sample}}{1 - \sigma_{ref}} \qquad (2.8)$$

For $|\sigma_{ref}| \ll 1$ this becomes:

$$\delta = \sigma_{ref} - \sigma_{sample} \qquad (2.9)$$

Two nuclei in proximity to one another will also affect the magnetic field they experience by one another through dipolar coupling. Classically this is represented for two dipoles μ_1 and μ_2 separated by a distance *r* as follows:

$$E_D = \frac{\mu_0}{4\pi}\left[\frac{\underset{\sim}{\mu}_1 \cdot \underset{\sim}{\mu}_2}{r^3} - \frac{3\left(\underset{\sim}{\mu}_1 \cdot r\right)\left(\underset{\sim}{\mu}_2 \cdot r\right)}{r^5}\right] \tag{2.10}$$

Where μ_0 is the permeability constant. Substituting $\underset{\sim}{\mu}_1 = \gamma_1 \hbar \underset{\sim}{I}_1$, and $\underset{\sim}{\mu}_2 = \gamma_2 \hbar \underset{\sim}{I}_2$ gives rise to the following quantum mechanical Hamiltonian:

$$H_D = \frac{\mu_0}{4\pi}\frac{\gamma_1\gamma_2\hbar^2}{r^3}\left[\underset{\sim}{I}_1 \cdot \underset{\sim}{I}_2 - \frac{3(\underset{\sim}{I}_1 \cdot r)(\underset{\sim}{I}_2 \cdot \underset{\sim}{r})}{r^2}\right] \tag{2.11}$$

Where I refers to the spin quantum number for a given magnetic dipole. This expression can be rewritten in polar coordinates such that:

$$x = r\sin\theta\cos\phi\,, \qquad y = r\sin\theta\cos\phi\,, \qquad z = r\cos\phi \tag{2.12}$$

This leads to the following expression for the dipolar Hamiltonian:

$$H_D = \frac{\mu_0}{4\pi}\frac{\gamma_1\gamma_2\hbar^2}{r^3}(A + B + C + D + E + F) \tag{2.13}$$

Where the terms A–F represent:

$$A = I_{1z}I_{2z}(3\cos^2\theta - 1)$$

$$B = -\frac{1}{4}[I_{1+}I_{2-} + I_{1-}I_{2+}](3\cos^2\theta - 1)$$

$$C = -\frac{3}{2}[I_{1+}I_{2z} + I_{1z}I_{2+}](\sin\theta\cos\theta)exp(-i\phi) \tag{2.14}$$

$$D = -\frac{3}{2}[I_{1-}I_{2z} + I_{1z}I_{2-}](\sin\theta\cos\theta)exp(+i\phi)$$

$$E = -\frac{3}{4}[I_{1+}I_{2+}]\sin^2\theta\, exp(-2i\phi)$$

$$F = -\frac{3}{4}[I_{1-}I_{2-}](\sin^2\theta)exp(+2i\phi)$$

Only the terms A and B commute with I_z and this represents the secular part of dipolar Hamiltonian, H_D^{Sec}, which is independent of time. This gives the following expression:

$$H_D^{Sec} = \frac{\mu_0}{4\pi}\frac{\gamma_1\gamma_2\hbar^2}{r^3}(A+B) = \frac{\mu_0}{8\pi}\frac{\gamma_1\gamma_2\hbar^2}{r^3}\left[2I_{1z}I_{2z} - \frac{1}{2}[I_{1+}I_{2-} + I_{1-}I_{2+}]\right](3\cos^2\theta - 1) \quad (2.15)$$

In the liquid phase, rapid molecular motion will average out this dipolar interaction. However, in the solid state this is no longer the case and the magnitude of this interaction can typically exceed the magnitude of chemical shielding interaction, leading to significant spectral line broadening (Mackenzie and Smith, 2002). This is the case for ^{1}H which has a low chemical shielding range, so line broadening from dipolar coupling can completely mask any fine details in solid state ^{1}H NMR spectra.

A number of strategies are employed to enhance the resolution of ^{1}H NMR spectra, each having their own sets of drawbacks. Enriching the sample in deuterium can improve spectral resolution, by reducing ^{1}H dipolar interactions simply by dilution (Chevelkov *et al.*, 2006). This method is limited to proton species that are accessible to the enriching reagents in order to be exchanged. MAS alone can average out some of the dipolar interaction, especially for materials

where the protons are well segregated. Yesinowski *et al.* (1987) demonstrated high resolution spectra of hydrated minerals can be achieved with mass rates of 8 kHz. For minerals containing high densities of OH groups, however, this was insufficient (Yesinowski *et al.*, 1988). Modern MAS technologies can now afford MAS rates up to 111 kHz (Andreas *et al.*, 2015), however this rapid spinning can generate considerable amounts of heat through friction and require specialized probes and temperature control measures. NMR pulse sequences using multiple decoupling pulses such as CRAMPS (Ryan *et al.*, 1980), DUMBO (Sakellariou *et al.*, 2000), and PMLG (Vinogradov *et al.*, 1999) can reduce the proton dipolar interaction through experimental design, though these are very sensitive to experimental parameters and require a high level of technical expertise to set up.

^{1}H NMR study of kaolinite was pioneered by Hayashi *et al.* (1992a), where they studied the static and CRAMPS spectra of a number of different kaolinites. In the static spectra, two components with different shapes were deconvoluted into broad and narrow components. These were assigned respectively to water molecules adsorbed on the external surfaces and to the hydroxyl groups in the kaolinite structure. The ^{1}H CRAMPS NMR spectra gave one broad line centered at 2.8 ppm. Spin-lattice relaxation times were also measured (Hayashi *et al.*, 1992b), and the relaxation curves were deconvoluted into two components, one long and one short, which were similarly attributed to external water molecules and interlayer hydroxyl groups.

A number of later studies reported being able to distinguish between kaolinite's inner and inner

surface hydroxyl groups. Wang *et al.* (2002) observed two peaks in the ^{1}H NMR spectra of two Chinese kaolinites which they attributed to inner surface (between 2.4 and 3.0 ppm) and inner (between -1.3 and -0.9 ppm) hydroxyls. Zhu *et al.* (2016) observed two peaks with chemical shifts in the range of 2.8-3.1 ppm and 1.7-1.9 ppm, which they attributed respectively to inner surface and inner hydroxyls. The relative areas of these peaks, however, did not correspond to the 3:1 ratio expected from its structure.

^{1}H NMR studies of modified kaolinites are virtually non-existent in the literature. Cheng *et al.* (2015) examined the ^{1}H NMR spectra of methanol grafted kaolinites and identified two sets of peaks which they attributed to the interlayer organic matter (3.0-3.1ppm) and the kaolinite hydroxyls (1.3-1.4ppm). No other ^{1}H NMR studies of modified kaolinites in the literature are currently known.

Kaolinite's hydroxyl groups have been shown for example in IR spectroscopy to be very sensitive to changes occurring to the interlayer environment during intercalation and grafting reactions. Examining the proton signals of these hydroxyls in kaolinite and modified kaolinite could similarly provide some evidence of interlayer modification and grafting. The goal of this study is to examine the ^{1}H NMR spectra of natural kaolinite, and kaolinites chemically modified by intercalation and by covalently grafting compounds on its inner surfaces in order to gain a better understanding of the spectral features of these materials and evaluate the suitability of ^{1}H NMR as a method for confirming intercalation and grafting reactions in kaolinite.

2.1.2 Description of samples

2.1.2.1 kGa-1b

Samples of kaolinite were prepared and analysed using kGa-1b, a highly crystalline and pure kaolin obtained from the Clay Mineral Society's Source Clay Repository (The Clay Minerals Society, 3635 Concorde Pkwy Suite 500, Chantilly VA 20151-1110, USA). Samples of the >2µm fraction were isolated by sedimentation, and the resulting material was labelled as kGa-1b. Details of the sampling procedure used and the material characterisation results can be found in section 5.2.

2.1.2.2 kDMSO

Kaolinite-dimethylsulfoxide intercalates have been extensively studied and described in the literature (Olejnik *et al.*, 1968; Johnston *et al.*, 1984; Thompson, 1985; Frost *et al.*, 1998). DMSO's very high dipole moment allows it to disrupt interlayer forces holding the individual kaolinite sheets together, making it one of the few compounds known that can intercalate inside a natural, unexpanded kaolinite (Lagaly *et al.*, 2013). Because DMSO is less hazardous than other known compounds that can intercalate directly inside kaolinite such as formamides and hydrazine, kaolinite-DMSO intercalates are a very popular precursor material used for preparing more complex organo-kaolinite materials.

Samples of a DMSO intercalated kaolinite (kDMSO) were prepared in a manner similar to the procedure described by Olejnik *et al.* (1968). Details of the experimental procedure used and the material characterisation results can be found in section 5.2.2.

2.1.2.3 Kmethoxy and kmethoxy(ht)

Methanol was one of the first compounds discovered that could be covalently grafted to kaolinite's inner surfaces (Tunney and Detellier, 1996b). In addition to being one of the most common used grafted kaolinites, it is also the simplest example of a grafted kaolinite making it an excellent candidate for study. The first reports of a methanol grafted kaolinite used a method where the material was prepared at temperatures well above methanol's boiling point inside a pressurized reactor (Tunney and Detellier, 1996b). Later studies (Komori *et al.*, 1998; Komori *et al.*, 2000) reported that a methanol grafted kaolinite could be prepared at room temperature by repeatedly dispersing a kaolinite pre-intercalated with NMF in fresh methanol. These two materials were very similar; however, the material prepared under milder conditions yielded less grafted methoxy groups than the former prepared at high temperatures. Materials prepared using these two methods were analysed in this study to see if any differences between them could be identified.

Samples of a methanol grafted kaolinite prepared at room temperature (kmethoxy) and one prepared at high temperatures (kmethoxy(ht)) was prepared using the methods described by

Komori *et al.* (1998) and Tunney and Detellier (1996b) respectively. Details of the experimental procedure used and the material characterisation results can be found in section 5.2**.**

2.1.3 ^{1}H MAS NMR results & discussion

2.1.3.1 kGa-1b

Two distinct peaks can be identified in the ^{1}H NMR spectrum of kGa-1b (Figure 13) at 1.70 ppm and 2.68 ppm. These are attributed to kaolinite's inner and inner surface hydroxyl protons respectively. The position and relative areas of these peaks was determined by spectral deconvolution and curve fitting using three peaks. Fitting was done using a peak area ratio of 3:1 expected for the inner surface and inner hydroxyls respectively. This ratio was chosen based on kaolinite's base chemical structure: $Al_2Si_2O_5(OH_4)$, which contain 3 inner surface hydroxyls and one inner hydroxyl. A third peak was included to account for the surface adsorbed water in the material. TGA weight loss analysis indicates there is 0.46% (w/w) water adsorbed on the surface of this material (see chapter 5), which gives a peak area of 0.16 relative to the inner hydroxyls. A best fit was obtained when this water peak was centered at 4.92ppm. A summary of these results is shown schematically in Figure 14.

A best fit to the experimental spectrum was found when the inner surface hydroxyl peak at 2.68 ppm was broader and had a more Gaussian character than inner hydroxyl peak at 1.70 ppm. This can be attributed to the inner surface hydroxyls experiencing more ^{1}H-^{1}H dipolar interactions due to their closeness to other hydroxyl groups compared to the segregated inner hydroxyls. Since dipolar interactions in NMR result in Gaussian broadening, this will result in broader peaks with a more Gaussian profile.

The chemical shift values of these peaks agree best with those reported by Zhu *et al.* (2016). The authors rationalized that the inner surface hydroxyls experience a stronger de-shielding from the inductive effects and the hydrogen bonding interactions holding the kaolinite sheets together, resulting in higher ^{1}H chemical shift values.

The chemical shift value for the surface adsorbed water is much lower than what was reported by Zhu *et al.* (2016). However, according to Svishchev and Kusalik (1993), the chemical shift value for water is highly dependent on its abundance in a given sample. Zhu et *al.* (2016) used kaolinite samples that had much greater water content than kGa-1b, and so this could explain the apparent discrepancy in chemical shift values.

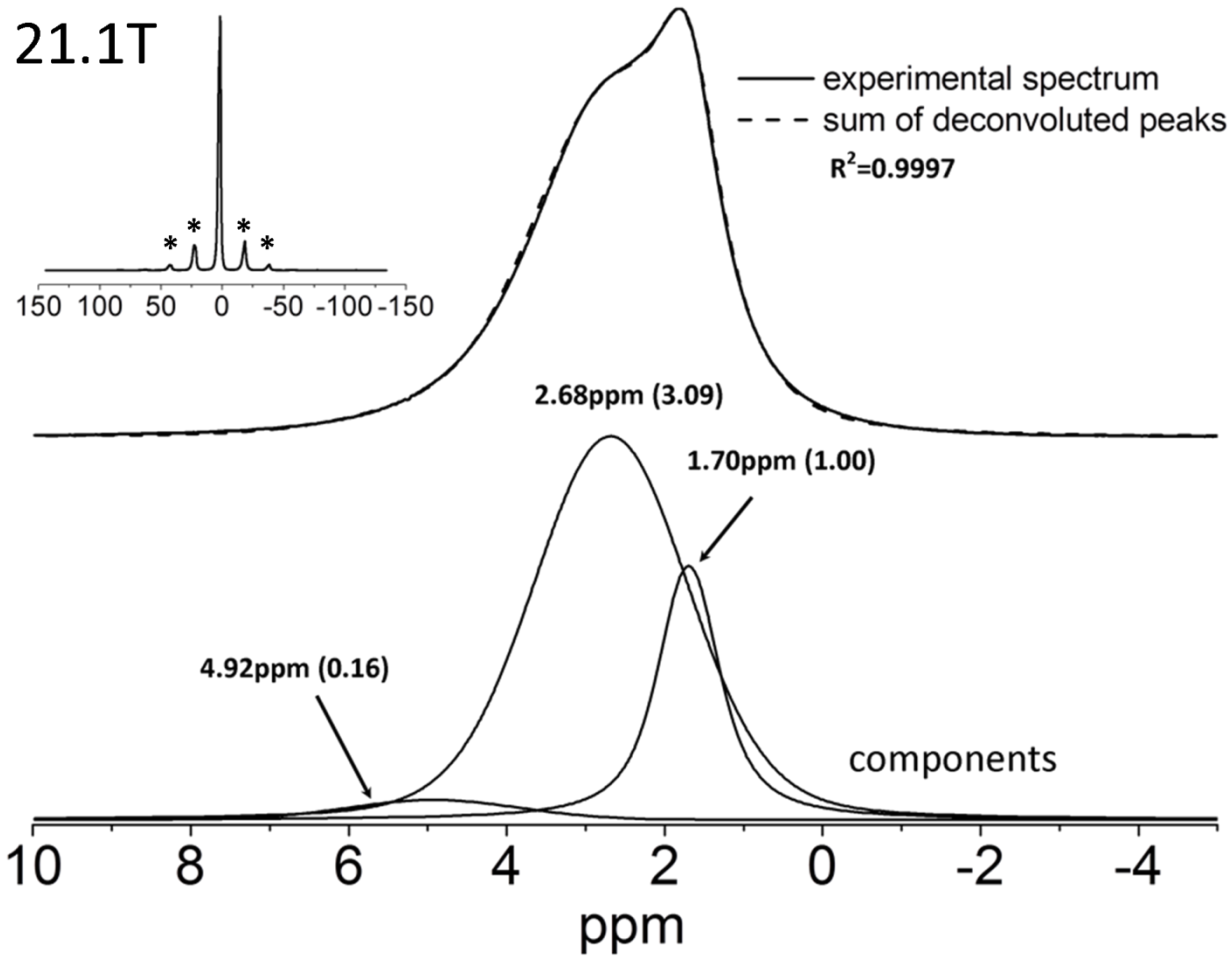

Figure 13: ^{1}H MAS NMR spectrum of kGa-1b and curve fitting results using a three site model. An expanded scale spectrum is shown as an inset. Rotational artifacts resulting from MAS are denoted with an asterisk.

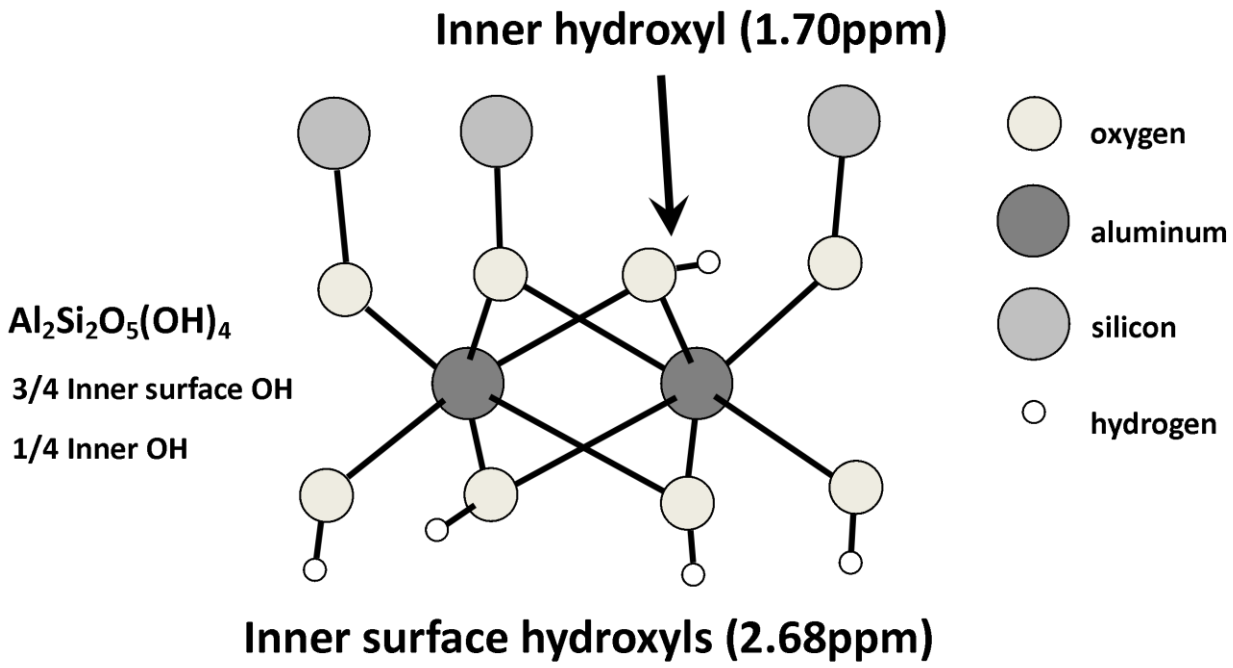

Figure 14: Schematic outlining the ^{1}H NMR signals observed for the different hydroxyl groups in kaolinite.

2.1.3.2 kDMSO

The ^{1}H NMR spectrum of kDMSO, shown in Figure 15, has two distinct peaks at 2.87ppm and 1.54ppm which are attributed to the DMSO methyl groups and the inner hydroxyl groups in the clay mineral. The peak from the inner surface hydroxyls was not clearly resolved in the spectrum.

Curve fitting of the experimental spectrum was done using a model composed of four ^{1}H sites with ratios in accordance with the chemical equation determined from TGA and %CHNS elemental analysis: $Al_2Si_2O_5(OH)_4[DMSO]_{0.64}[H_2O]_{0.03}$ (see chapter 5). The four peaks had area ratios relative to the inner hydroxyls of 3.86, 3.00, and 0.06 for DMSO, the inner surface hydroxyls and surface water respectively. The chemical shift values determined for kGa-1b were used for fitting the hydroxyl peaks and the surface water's peak. The results of this fit are shown in Figure 16 and Table 4, and the model is shown schematically in Figure 17.

This four site model gives a reasonable fit to the experimental spectrum (Figure 15), but it poorly simulates the signal in the 3-8ppm region. To account for this discrepancy, the model was refined using five sites where the signal from DMSO's methyl groups is split into two peaks that are equal in area. A best fit was found when the chemical shift of the keyed-in DMSO methyl was 4.23 ppm. This de-shielding effect is also observed in the solid state ^{13}C NMR spectrum of kaolinite DMSO intercalates (Thompson, 1985) and is attributed to the methyl group's close proximity to the kaolinite siloxane groups. The accuracy of this five site model supports the numerous ^{13}C and ^{29}Si NMR studies indicating that intercalated DMSO has one of its methyl groups key into the siloxane ring in the silicon sheet of the clay mineral (Thompson, 1985; Duer *et al.*, 1992; Hayashi and Akiba, 1994), and demonstrates this technique could be used to identify intercalation in kaolinite.

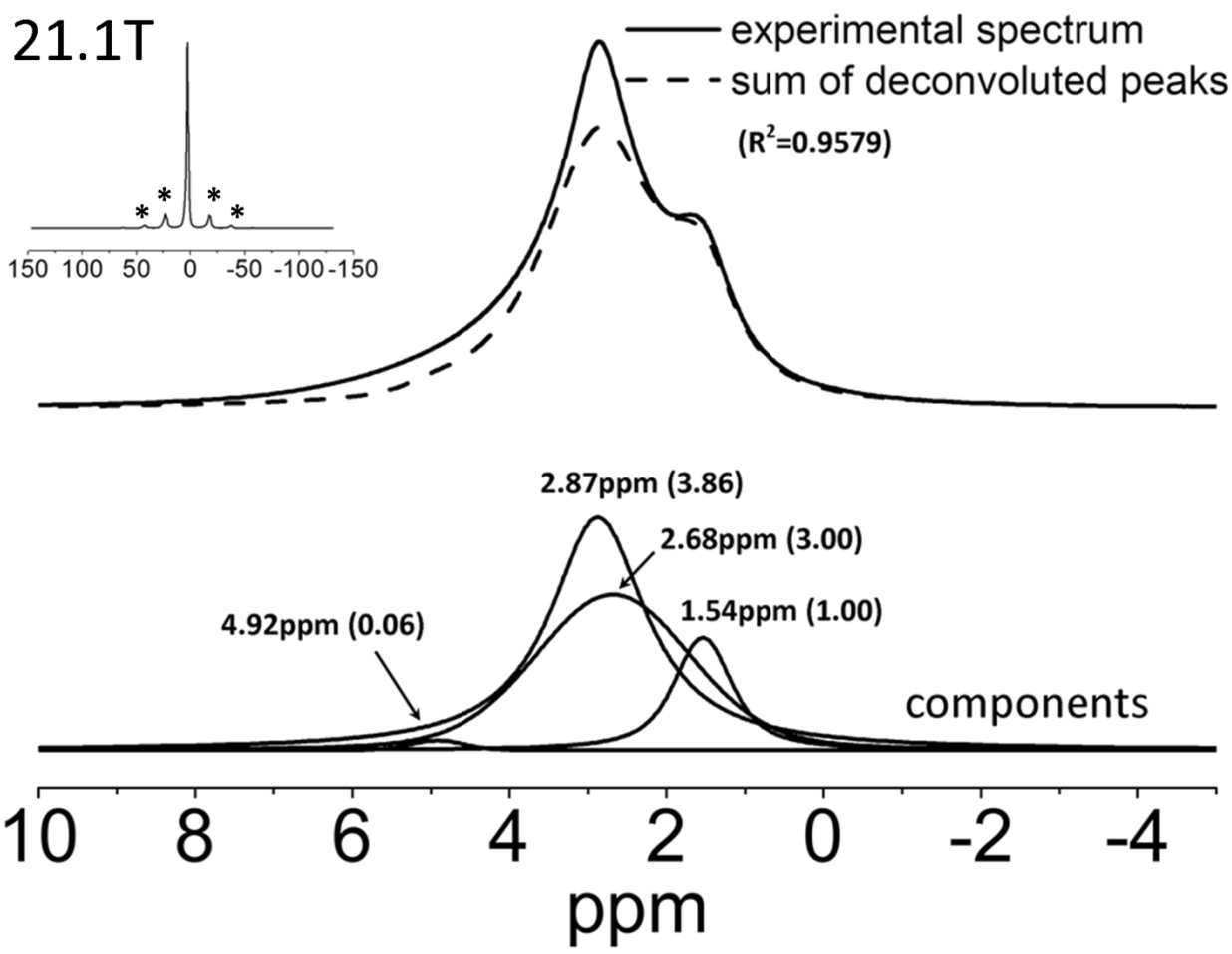

Figure 15: ^{1}H MAS NMR of KDMSO and curve fitting results using a four site model. An expanded scale spectrum is shown as an inset. Rotational artifacts resulting from MAS are denoted with an asterisk.

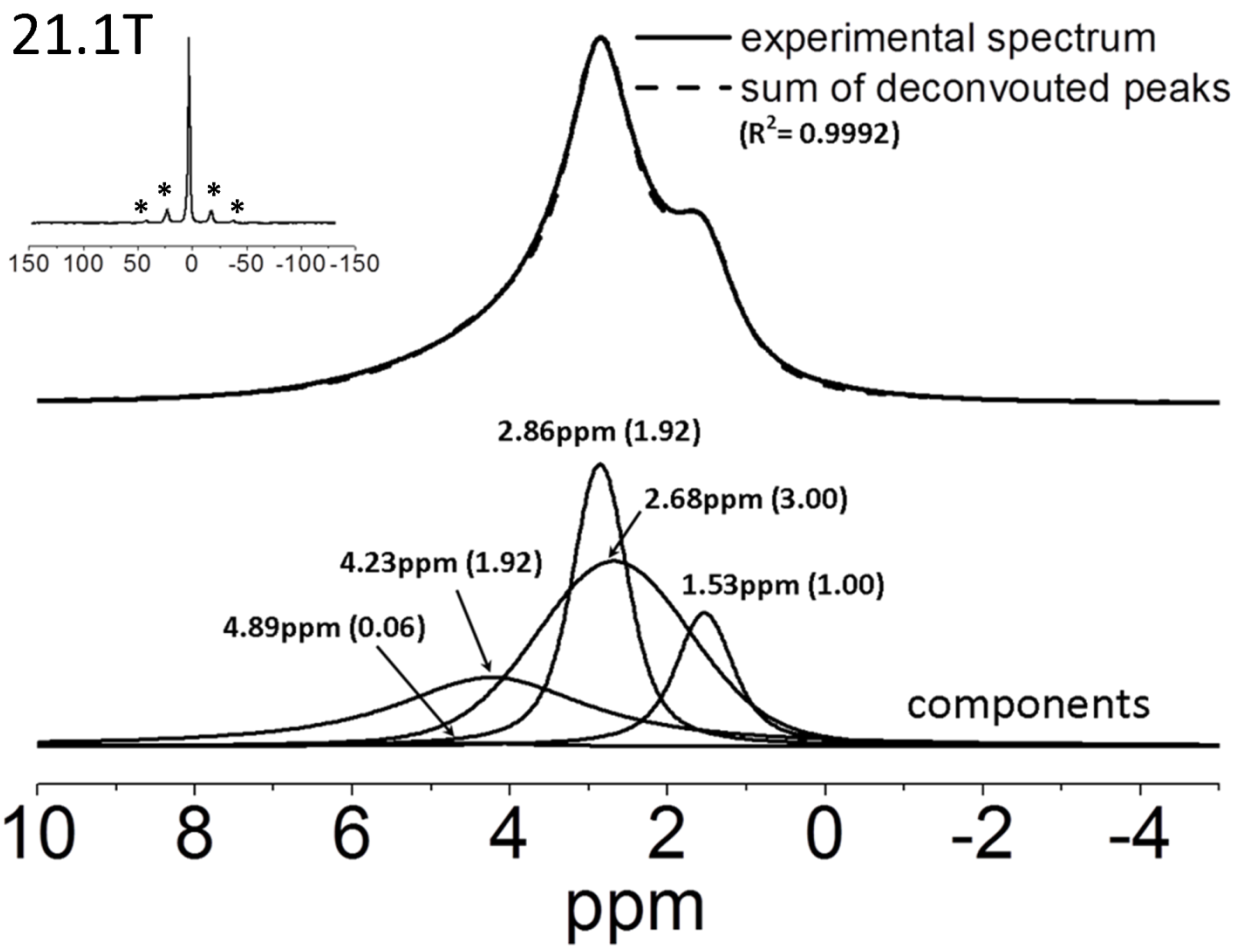

Figure 16: ^{1}H MAS NMR of KDMSO and curve fitting results using a five site model where there are two sites for the DMSO CH_3 groups. An expanded scale spectrum is shown as an inset. Rotational artifacts resulting from MAS are denoted with an asterisk.

Table 4: Summary of ^{1}H NMR peaks identified for kDMSO using a five site model.

Chemical shift (ppm)	Rel. abundance	Attribution
1.53	1.00	inner AlOH; kDMSO+kGa-1b
2.68	3.00	inner surface AlOH; kDMSO+kGa-1b
2.86	1.92	CH_3; kDMSO
4.23	1.92	CH_3, keyed-in; kDMSO
4.89	0.06	HOH; water

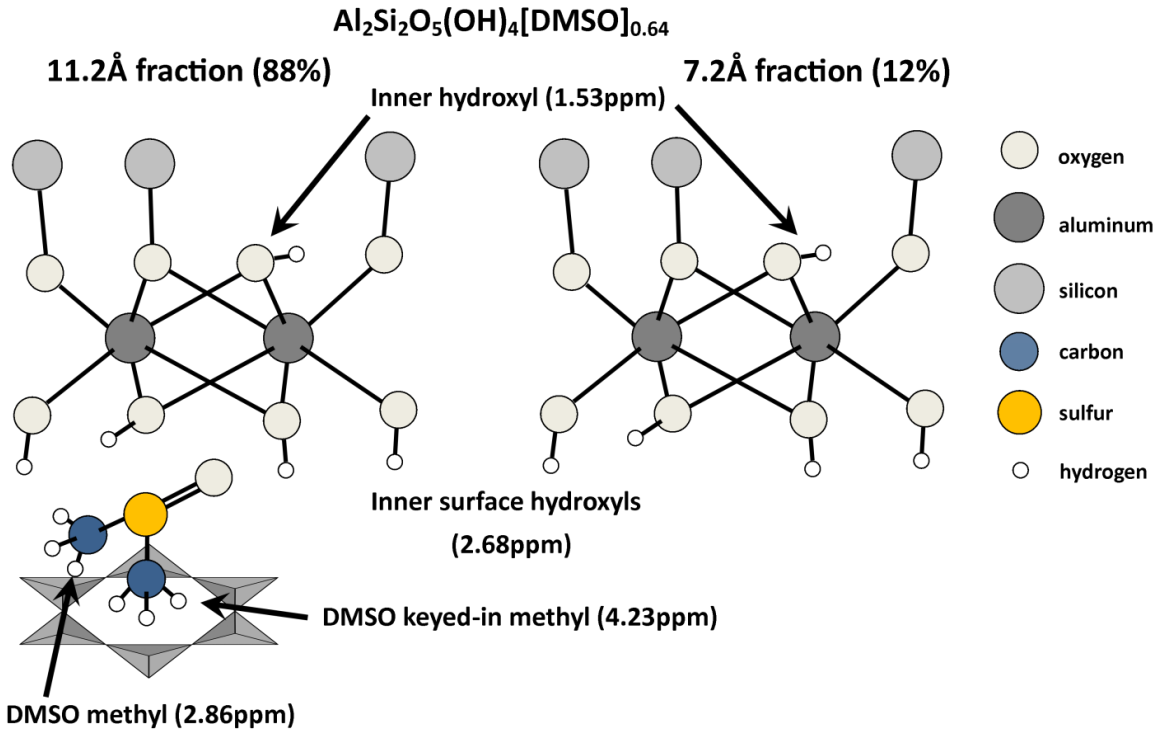

Figure 17: Schematic outlining the ^{1}H NMR signals observed in kDMSO. This summary uses the results in Figure 16 for the five site model used for fitting the experimental spectrum where there are two distinct DMSO methyl species. The surface water present in the material is not shown in this schematic.

2.1.3.3 kmethoxy

The ^{1}H NMR experimental spectrum of kmethoxy shown in Figure 18 and Figure 19 has two distinct peaks at 1.70ppm and 3.48ppm, which are attributed respectively to the clay mineral's inner hydroxyls and OCH_3 groups from methoxy groups grafted to the clay mineral and intercalated methanol. Similarly to kDMSO, the peak corresponding to the inner surface hydroxyls could not be definitely identified from the experimental spectra.

Fitting the experimental spectrum was done using a seven site model based on the stoichiometry: $Al_2Si_2O_5(OH)_{3.44}(OCH_3)_{0.56}$ $[NMF]_{0.09}$ $[H_2O]_{0.35}$ determined through a combination of TGA and %CHNS elemental analysis (see chapter 5). The model also took into account the residual 7.2Å kGa-1b fraction that makes up 12% of the total material in kmethoxy. Peak areas relative to the inner hydroxyls were calculated to be 2.51, and 1.48 respectively for the clay mineral's inner surface OH groups and the OCH_3 grafted groups. Based on %CHNS elemental analysis, NMF peaks areas relative the inner hydroxyl were calculated to be 0.09 for the carbonyl and NH groups, and 0.28 for the CH_3 group. Fitting was done using values of 8.30, 6.84 and 2.56ppm attributed to the HC=O, NH, and CH_3 groups in NMF respectively. Surface and interlayer water was modeled as a single peak with a peak area relative the inner hydroxyls of 0.70. A best fit was found when the chemical shift of the water peak was 1.38ppm. A summary of this fit is shown in Figure 18 .

The seven site model was able to roughly model the lineshape of the experimental spectrum, but does not account well for the signal in the 3-6ppm region. This is especially so for the methoxy group's peak at 4.00ppm, which has a chemical shift value that is quite a bit higher than expected. This sort of de-shielded signal might have been expected if the methoxy group partially keys into the siloxane ring of the silicon sheet, however, the solid state ^{13}C CPMAS NMR spectrum of this material (see chapter 5) was the same as free methanol, suggesting this isn't this case. In addition to this, the chemical shift value of the water peak at 1.38ppm is much lower compared to the water peaks in kGa-1b and kDMSO. Water in solid materials that is isolated and not under the influence of hydrogen bonding interactions could result in chemical shift values in this range from 0.8-1.5ppm (Grünberg *et al.*, 2004). However this is not expected in a material that has high quantities of water in it, such as kmethoxy.

The seven site model was refined by splitting up the signal from the inner surface hydroxyls into two distinct peaks, giving eight peaks total. Their relative areas were set according to the abundance of the 8.6Å and 7.2Å fractions calculated from XRD results (see chapter 5). This gives integrals relative to the inner hydroxyls of 2.15 and 0.36 for the 8.6Å and 7.2Å fraction's inner surface hydroxyls respectively. The same peak parameters used for fitting the inner and inner surface hydroxyl peaks of kGa-1b are also used here for these peaks. A best fit was obtained when the inner surface hydroxyls in the 8.6Å fraction has a chemical shift value of 2.13ppm and when the water has a chemical shift value of 4.82ppm. A summary of this fit is shown in Figure 19 and Table 5, and the model is shown schematically Figure 20.

One important advantage of the eight site model is it places the peak for the grafted methoxy groups at 3.48ppm, which is much closer to the chemical shift value expected for this functional group compared to the seven site model. The chemical shift value for the water was also very close to that found for the surface water in kGa-1b and kDMSO, indicating that the interlayer water is hydrogen bonded itself or to the clay surfaces. The accuracy of the fit using the stoichiometric ratio of the inner surface hydroxyls' established from other methods also offers clear evidence of a grafted kaolinite.

In the eight site model, the chemical shift value of the inner surface hydroxyls attributed to the 8.6Å fraction is quite low compared to those in kGa-1b. This is attributed to a decrease in interlayer cohesion between the aluminum and silicon layer caused by the grafted methoxy groups. This decrease in interlayer cohesion will cause these inner surface hydroxyls to have a smaller chemical shift value that approaches the ones found for the isolated inner hydroxyls. This is quite different from kDMSO, where fitting found no such shift in the inner surface hydroxyls' chemical shift. This is probably because DMSO's sulfoxide groups will compensate for this loss of interlayer cohesion by forming strong hydrogen bonding interactions with the kaolinite's inner surface hydroxyls. Interlayer water in kmethoxy might be expected to interact similarly, but its effect is not expected to be as great, leading to the decrease in chemical shift values for the kaolinite's inner hydroxyls observed. This observation is significant since it suggests this can be used to distinguish between intercalated and grafted species in kaolinite.

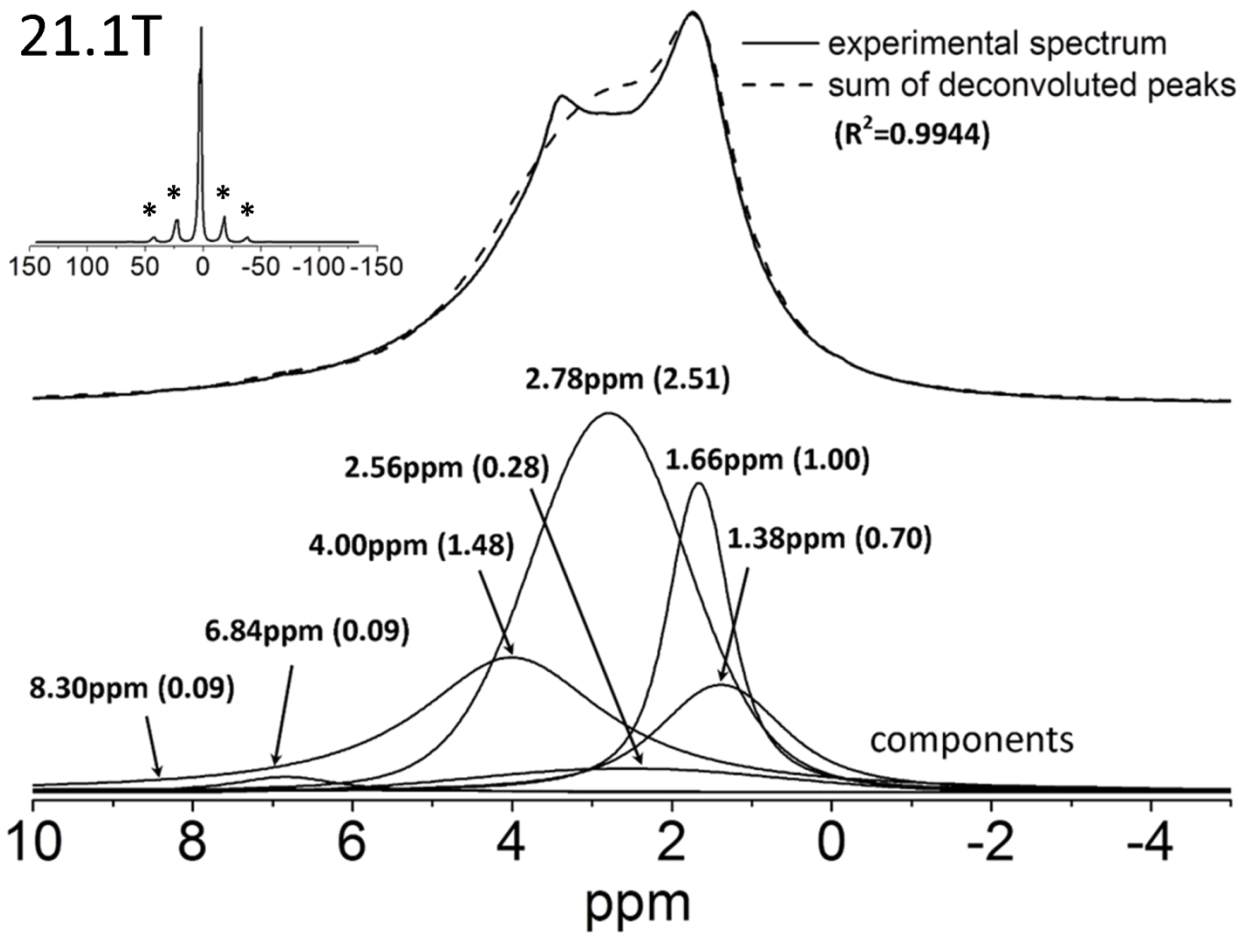

Figure 18: ^{1}H MAS NMR of kmethoxy and curve fitting results using a seven site model. The interlayer water present in this material was included as a single peak with a chemical shift value of 1.38ppm. An expanded scale spectrum is shown as an inset. Fitting was done using the same parameters used for analysis of kGa-1b for the 2.68ppm and 1.70ppm peaks. Rotational artifacts resulting from MAS are denoted with an asterisk.

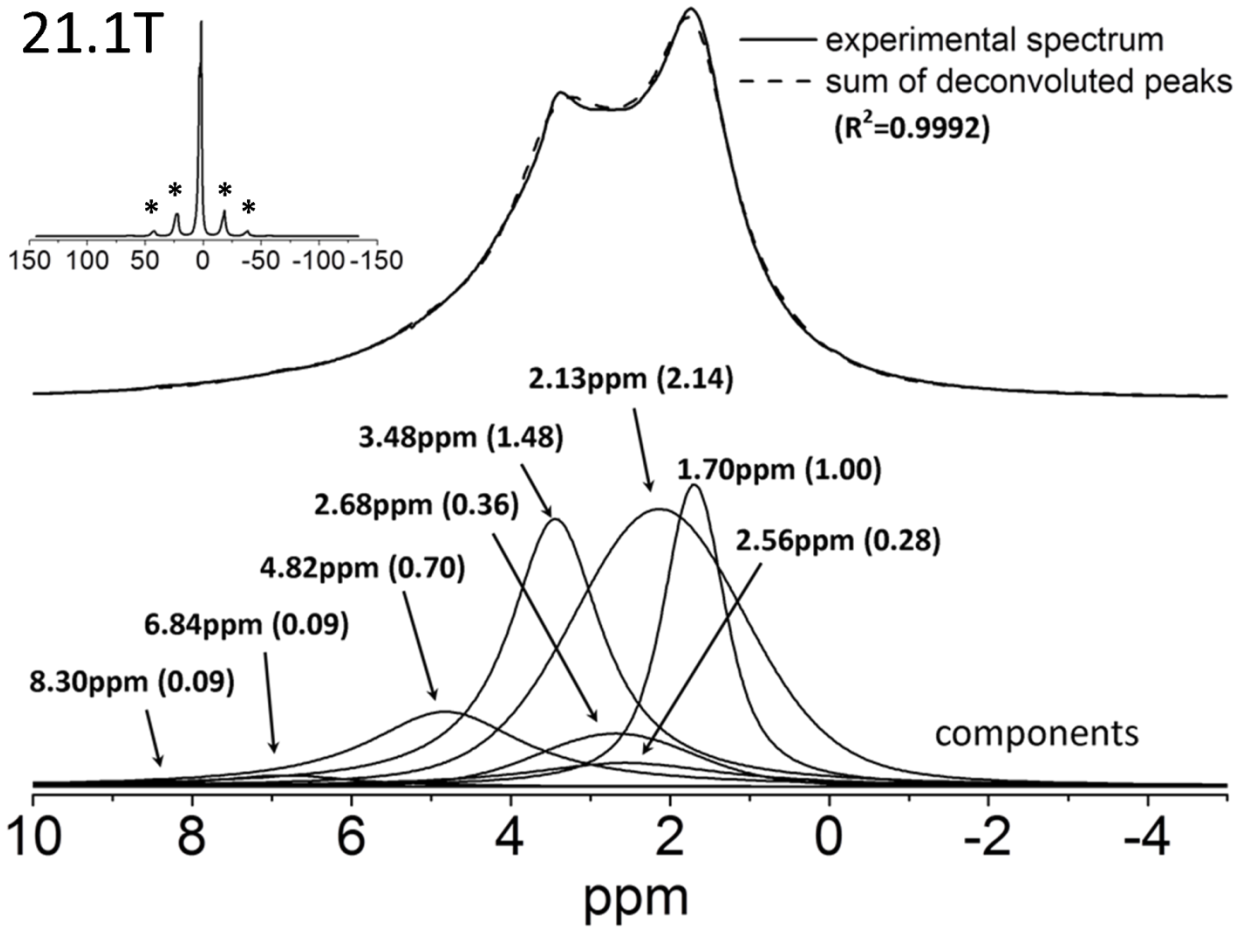

Figure 19: ^{1}H MAS NMR of kmethoxy and curve fitting results using an eight site model. The interlayer water present in this material was included as one single peak with a chemical shift value of 4.82ppm and the inner surface hydroxyls as two peaks with chemical shift values of 2.68 and 2.13ppm. These latter values are attributed to clay mineral's inner surface hydroxyls in the 7.2Å and 8.4Å XRD fractions respectively. An expanded scale spectrum is shown as an inset. Fitting was done using the same parameters used for analysis of kGa-1b for the 2.68ppm and 1.70ppm peaks. Rotational artifacts resulting from MAS are denoted with an asterisk.

Table 5: Summary of ^{1}H NMR peaks identified for kmethoxy.

Chemical shift (ppm)	Rel. abundance	Attribution
1.70	1.00	inner AlOH; kmethoxy+kGa-1b
2.13	2.14	inner surface AlOH; kmethoxy
2.56	0.28	CH_3; NMF
2.68	0.36	inner surface AlOH; kGa-1b
3.48	1.48	OCH_3; kmethoxy
4.82	0.70	HOH; water
6.84	0.09	NH; NMF
8.30	0.09	HC=O; NMF

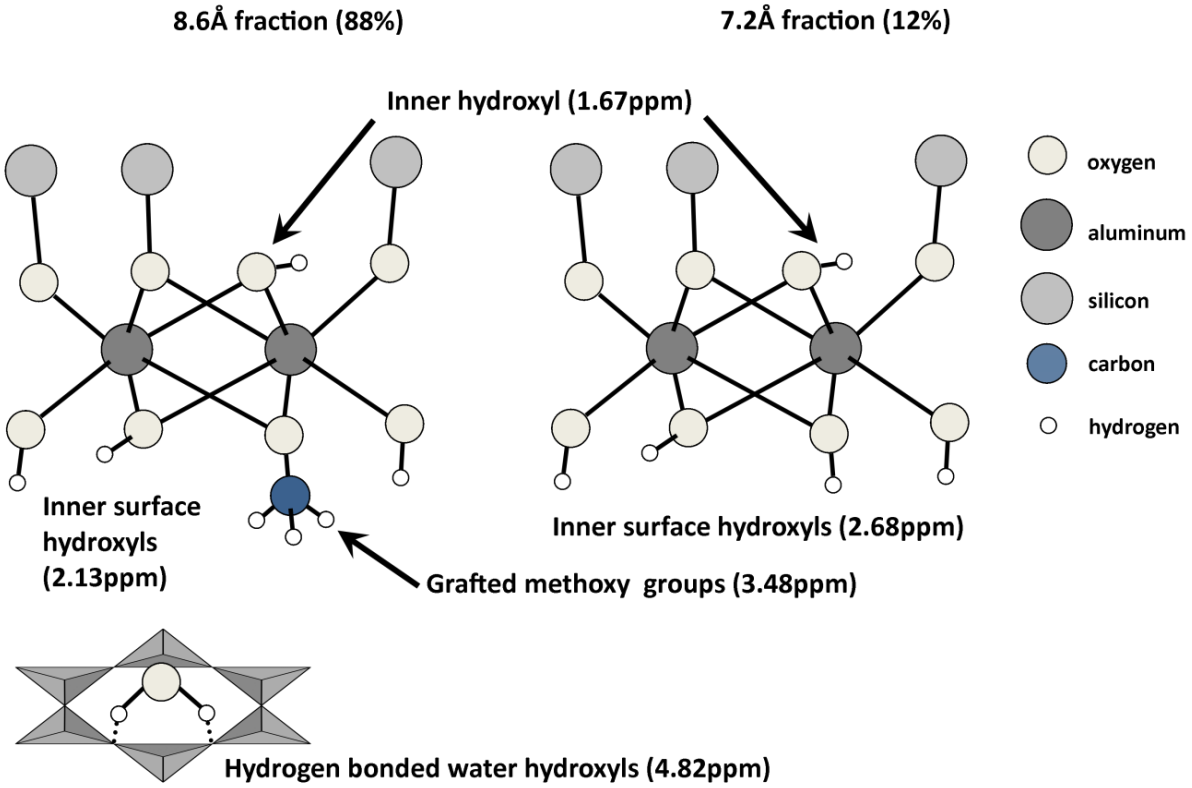

Figure 20: Schematic outlining the ^{1}H NMR signals observed in kmethoxy. This schematic uses the results for the eight site model used for fitting to the experimental spectrum where the clay mineral's inner surface hydroxyls in the 8.4Å and 7.2Å fractions have different chemical shift values

2.1.3.4 Kmethoxy(ht)

The ^{1}H NMR spectrum of kmethoxy(ht) shown in Figure 21 is very similar to kmethoxy, where two distinct peaks can be observed at 1.64 and 3.45ppm, attributed to kaolinite inner hydroxyl and grafted methoxy groups respectively. The main difference between the two is a small shoulder that can be seen around 2.4ppm.

Fitting the experimental spectrum was done using the eight site model used to fit kmethoxy. Because this material was prepared using a kDMSO precursor, the three NMF peaks in the model were replaced with a single DMSO peak at 2.86ppm, giving six sites in total. Based on the stoichiometry: $Al_2Si_2O_5(OH)_{3.13}(OCH_3)_{0.87}[H_2O]_{0.25}[DMSO]_{0.004}$ determined through a combination of XRD, TGA and %CHNS elemental analysis (see chapter 5), relative peak areas for the clay mineral's inner and inner surface OH groups, and OCH_3 grafted groups were calculated as 1.00, 2.23, and 2.30 respectively relative to the inner hydroxyls. The relative areas of the inner surface hydroxyls were divided up further according to the abundance of the 7.2Å kGa-1b fraction identified in XRD, giving values of 1.87 for the 8.4Å fraction and 0.36 for the 7.2Å fraction. Residual DMSO from the kDMSO precursor would give a peak area of 0.03 and water in this material would give a peak area of 0.50. The results of this fit are summarized in Figure 21 and Table 6 and are shown schematically in Figure 22.

This model found a best fit for the 8.4Å fraction's inner surface hydroxyls at 1.89ppm. This is similar to the 2.13ppm value found for kmethoxy. Fitting also found similar chemical shift values for the methoxy groups and water, which all suggests the hypothetical model used for fitting these two spectra is valid.

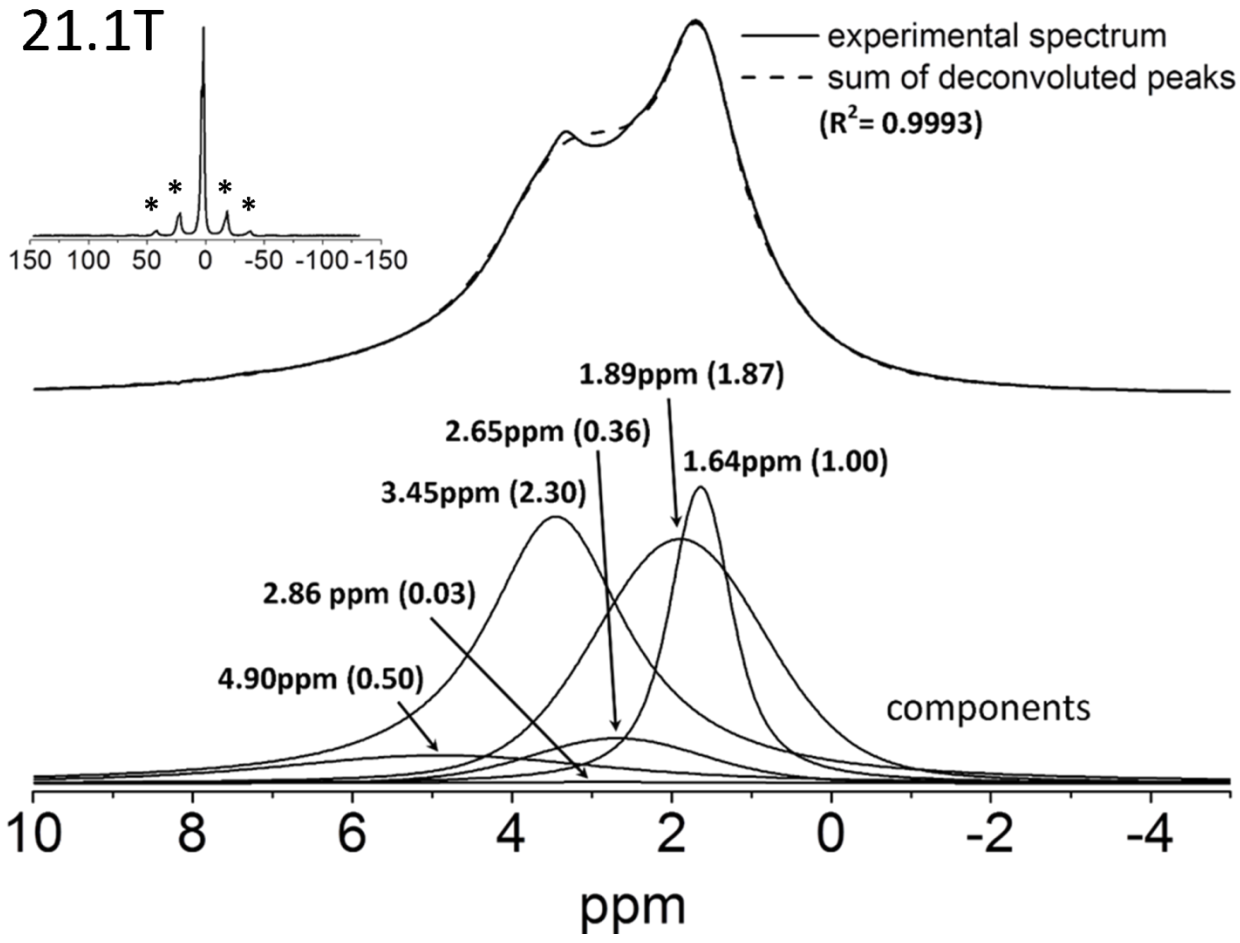

Figure 21: ^{1}H MAS NMR of kmethoxy(ht) and curve fitting results using a six site model where the clay mineral's inner surface hydroxyls in the 8.4Å and 7.2Å fractions have different chemical shift values. An expanded scale spectrum is shown as an inset. Fitting was done using the same

parameters used for analysis of kGa-1b for the 2.68ppm and 1.64ppm peaks. Rotational artifacts resulting from MAS are denoted with an asterisk.

Table 6: ^{1}H MAS NMR peaks identified in kmethoxy(ht).

Chemical shift (ppm)	Rel. abundance	Attribution
1.64	1.00	inner AlOH; kmethoxy+kga1b
1.89	1.87	inner surface AlOH; kmethoxy
2.65	0.36	inner surface AlOH; kga1b
2.86	0.03	CH_3; residual DMSO
3.45	2.30	OCH_3; kmethoxy
4.90	0.50	HOH; water

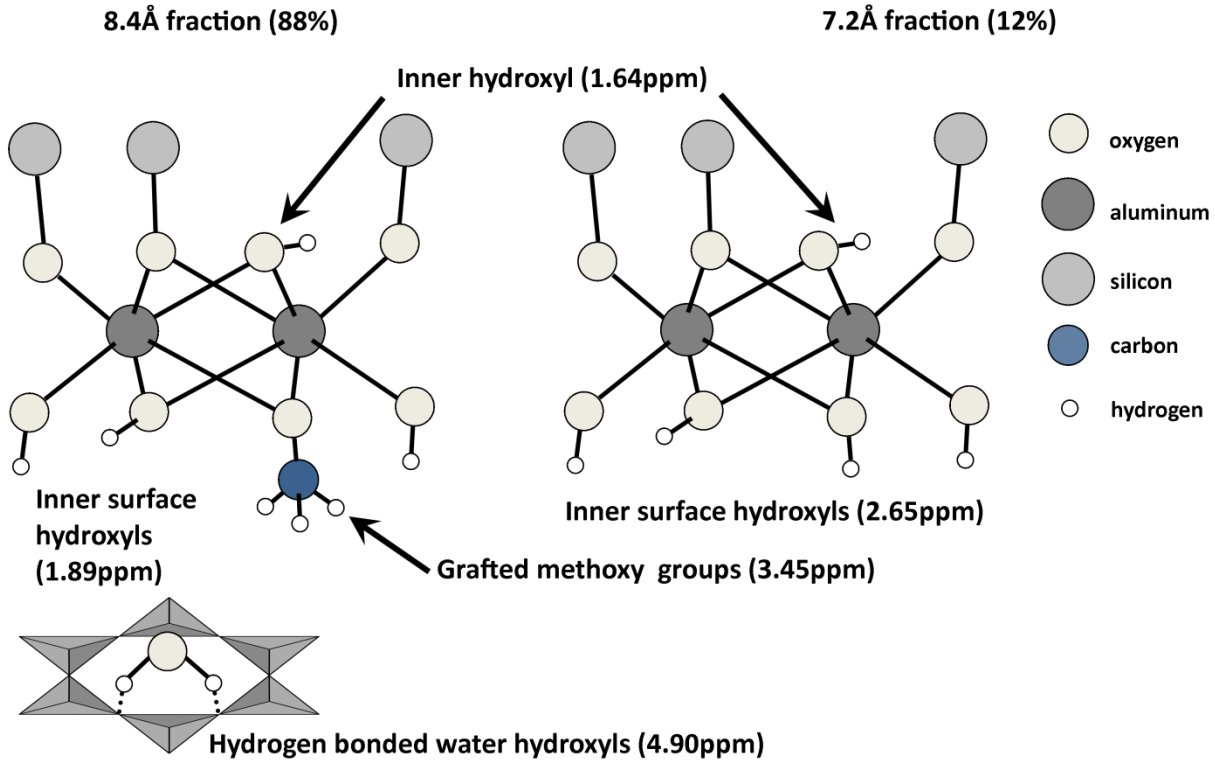

Figure 22: Schematic outlining the ^{1}H NMR signals observed in kmethoxy(ht). This schematic uses the results for the six site model used for fitting the experimental spectrum.

2.1.4 Summary of the experiments and conclusions

Solid state ^{1}H NMR spectra were measured for one natural kaolinite: KGa-1b, and three modified kaolinites: kDMSO, kmethoxy, and kmethoxy(ht).

KGa-1b showed two peaks at 2.68 and 1.70 ppm attributed to the clay mineral's inner surface and inner hydroxyl protons respectively. This spectrum was fitted with high accuracy with a model based on the known stoichiometry of the clay mineral, where the population of the inner surface and inner hydroxyls are in a 3:1 ratio.

The spectrum of kDMSO gave a best fit using a model where the interlayer DMSO gives rise to two methyl peaks at 2.86 and 4.23ppm and the clay mineral's inner surface and inner surface hydroxyl peaks were at 2.68 and 1.70 ppm respectively. This result is in agreement with the known structure of this material where DMSO's methyl groups become inequivalent when intercalated in the kaolinite interlayer space.

In kmethoxy, the kaolinite inner hydroxyl's peaks were identified at 1.70ppm, and the grafted methoxy groups and intercalated methanol at 3.48ppm. Fitting the experimental gave a best fit when the signal from the inner surface hydroxyls was divided up into two peaks at 2.13ppm and 2.68ppm, attributed to the 8.4Å and 7.2Å fractions identified in XRD. This difference in

chemical shift is attributed to a decrease in interlayer cohesion between the aluminum and silicon layer caused by the grafted methoxy groups. Similar results were obtained from fitting this model to another methanol grafted kaolinite, kmethoxy(ht), which suggests it is valid.

2.2 Solid state ^{1}H NMR study of deuterium exchanged natural and modified kaolinites

2.2.1 Introduction

Deuteration is a commonly used strategy for reducing the dipolar interactions in ^{1}H NMR of solid samples by diluting the proton signal through their substitution with deuterium. This unfortunately is quite difficult to accomplish in natural kaolinites, since its hydroxyl groups are highly resistant to exchange with deuterium and will fully exchange only under very high temperature and pressure (Romo, 1956). In kaolinites with an interlayer space expanded by intercalation, however, its hydroxyl groups are much more accessible and can be exchanged under mild conditions (Ledoux and White, 1964a; Ledoux and White, 1964b). Ledoux and White (1964b) also reported that the hydroxyl groups undergo selective deuteration, where at room temperature about 60% of the inner surface hydroxyls in a kaolinite intercalated with hydrazine exchanged compared with 22% of its inner hydroxyls. Thus in addition to lowering proton dipolar interactions, this selectiveness for deuterium exchange could be used to identify the different hydroxyl groups in kaolinite's ^{1}H NMR spectrum.

The goal of this study is to examine the ^{1}H NMR spectra of deuterium exchanged kaolinites in order to accurately distinguish between the different hydroxyl groups identified in Part I-a and attempt to improve the resolution of the spectra.

2.2.2 Description of samples

According to Ledoux and White (1964b), the hydroxyl groups of an expanded kaolinite can be partially exchanged with deuterium at room temperature. Deuterium exchanged kaolinites: kGa-1b-d, kDMSO, kmethoxy-d were prepared in this manner by dispersing samples of kGa-1b, kDMSO, and kmethoxy respectively in D_2O at room temperature.

Details of the experimental procedures used to prepare the samples the material characterisation results are can be found in section 5.2**.**

2.2.3 IR Results & discussion

2.2.3.1 kGa-1b-d

The IR spectra shown in Figure 23 and Figure 24 are nearly identical to kGa-1b before the deuterium exchange experiments. There are no peaks observed in the 2800-2500cm^{-1} region characteristic of O-D stretching vibrations, indicating that the clay mineral's hydroxyls were not exchanged with deuterium. This is not surprising since previous reports indicated that the

hydroxyl groups in kaolinite are quite resistant to exchange with deuterium, requiring high temperatures and pressures in D_2O for exchange to occur (Romo, 1956).

2.2.3.2 kDMSO-d

It is expected that when kDMSO is exposed to D_2O, it will replace DMSO in the interlayer space, and consequently its inner and inner surface hydroxyl groups will be deuterated. This will yield an unexpanded deuterated kaolinite.

The IR spectrum of kDMSO-d in Figure 23 indicates this is indeed the case, and that the clay mineral's hydroxyl groups were partially exchanged with deuterium. This can be seen through the appearance of four new bands at 2725.4, 2709.5, 2696.4, and 2676.3 cm^{-1}which are very similar to those reported by Ledoux and White (1964b). The authors attributed the first three to deuterated inner surface hydroxyls and the band at 2676.3 cm^{-1} to deuterated inner hydroxyls. When comparing the relative intensities of these four bands compared to their non-deuterated counterparts in the 3750-3500cm^{-1} region (Figure 24), it appears the inner hydroxyls are more resistant to exchange than the inner surface hydroxyls. This is in agreement with Ledoux and White's (1964b) report that the inner hydroxyl groups are less accessible for exchange than the inner surface hydroxyls.

Despite intense O-D stretching bands observed in the 2800-2500cm^{-1} region suggesting important amounts of the kaolinite's hydroxyls were exchanged, the OH stretching bands remained very intense (Figure 24). This is plausibly partially due to the 12% fraction of unmodified kaolinite in the material. Based on the deuterium exchange experiment with kGa-1b, these hydroxyls in an unexpanded kaolinite will not exchange with deuterium and will make an important contribution to the overall signal of the OH stretching bands.

The OH stretching bands in the 3750-3500cm^{-1} region (Figure 24) appear to be the same as those in kGa-1b, with none of those characteristic of DMSO in the kaolinite interlayer space visible. This confirms that DMSO was removed from the kaolinite's interlayer space as a result of the exchange procedure.

2.2.3.3 Kmethoxy-d

The appearance of O-D stretching bands in 2800-2500cm^{-1} region of kmethoxy-d (Figure 23) indicates that partial exchange of the kaolinite's OH groups with deuterium was achieved. Unlike in kDMSO-d, where the O-D stretching bands are fairly well resolved, in kmethoxy-d their resolution is poor and gives rise to a complex line shape. The first three peaks are very similar in value to the 2725.4, 2709.5, and 2696.4 cm^{-1} bands reported in kDMSO-d, which suggests they are resulting from the clay mineral's inner surface hydroxyls that have been exchanged with deuterium. The 2726.7cm^{-1} band, however, is noticeably less intense compared to the same band in kDMSO-d. Knowing the OH stretching counterpart of this band is a result of the in phase stretching of all three inner surface hydroxyls, it might be expected to be especially sensitive to changes occurring to the inner surfaces hydroxyls, for example as a result of replacing these hydroxyls with grafted methoxy groups. The inner hydroxyl band is harder to accurately identify since D_2O's O-D stretching bands appear within the same region from 2700-2300 cm^{-1}.The 2680.5 cm^{-1} band is close in value to the one identified for the inner hydroxyl in kDMSO-d and is attributed as such in kmethoxy-d as well. Other O-D stretching bands at 2633.8 and 2593.9cm^{-1} were attributed to D_2O. These bands are much more intense than in kDMSO-d as result of the high water content in kmethoxy, which was replaced with D_2O during the exchange experiments.

Similarly to kDMSO-d, kmethoxy-d's O-H stretching region from 3750-3500cm^{-1} is mostly the same as kGa-1b (Figure 24). Characteristic kmethoxy bands such as the one at 3646cm^{-1}, appear to have been completely removed during the experiment, suggesting that hydrolysis of the grafted methoxy groups occurred during the exchange experiments.

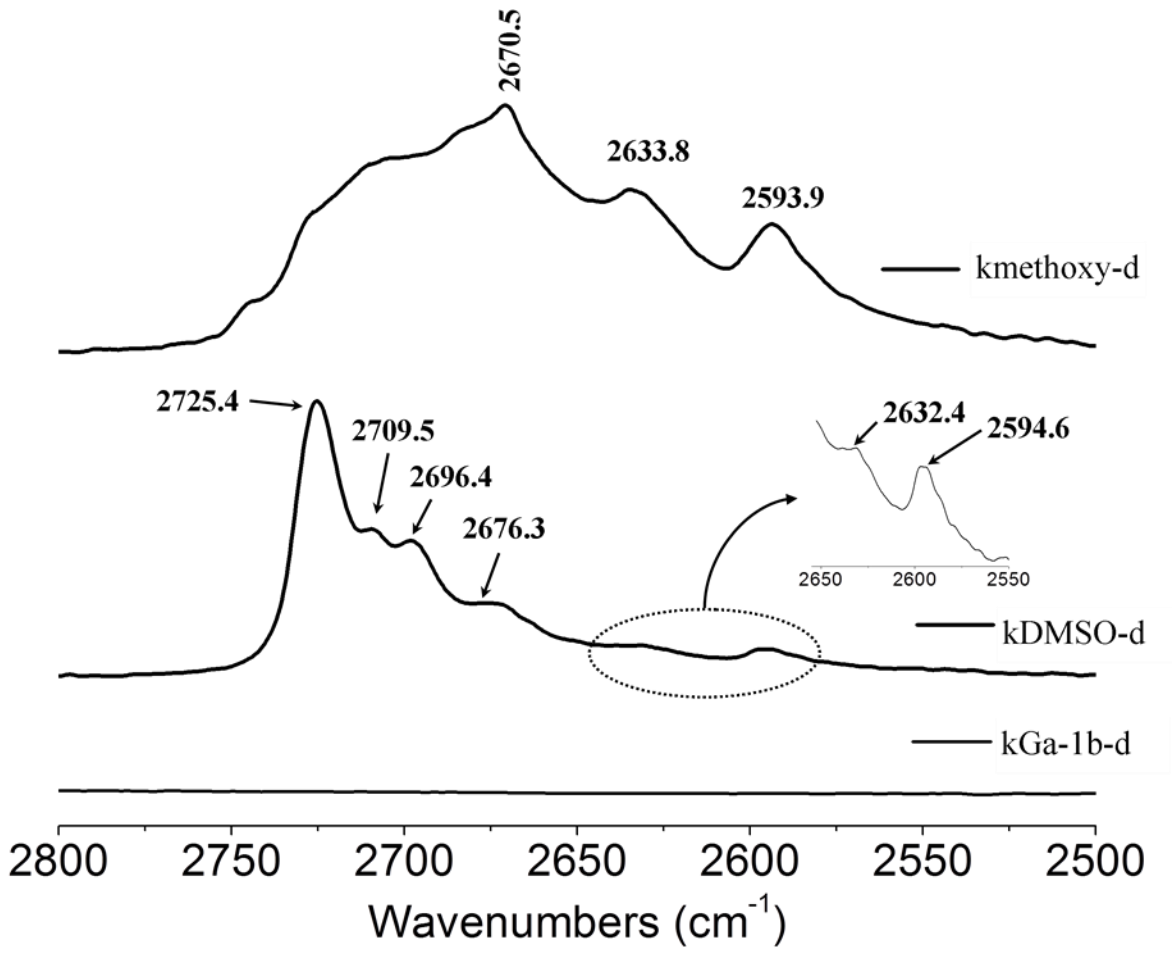

Figure 23: ATR-FTIR spectrum of deuterated kaolinites. A close-up of the 2800-2500cm^{-1} region is shown.

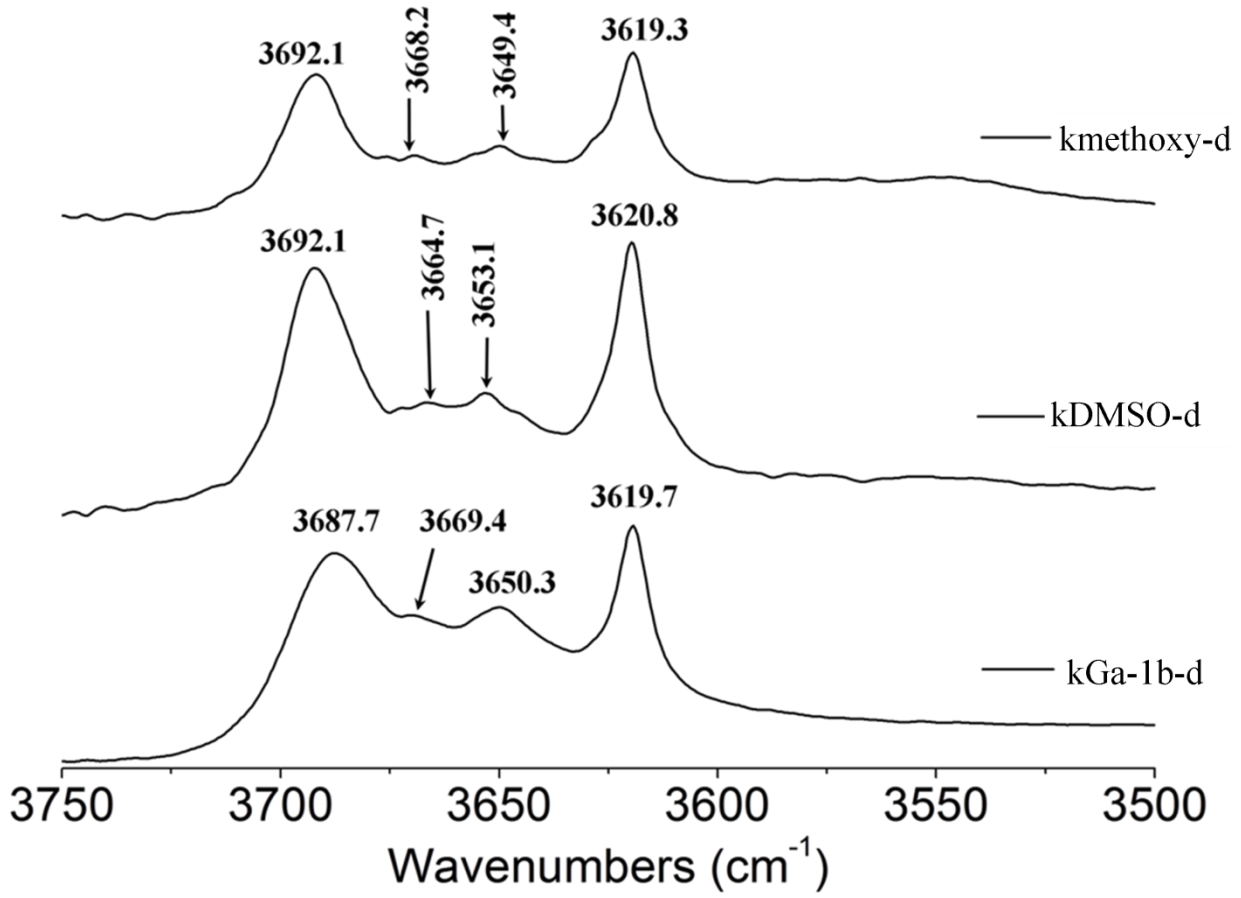

Figure 24: ATR-FTIR spectrum of deuterated kaolinites. A close-up of the 3750-3500cm^{-1} region is shown.

2.2.4 TGA and %CHNS elemental analysis results & discussion

2.2.4.1 kGa-1b-d

The TGA weight loss curve for kGa-1b-d in Figure 25 shows a total weight loss of 13.9%, which is almost identical to kGa-1b (13.8%) (see chapter 5). This indicates none of the kaolinite's hydroxyl groups were exchanged with deuterium. This is in agreement with the IR results which showed no O-D bands in this material

2.2.4.2 kDMSO-d

The TGA weight loss curve for kDMSO-d shown in Figure 25 shows a total weight loss of 16%, compared to 27.4% for kDMSO (see chapter 5). This difference in weight loss is a result of less material being lost from room temperature to 300°C where only 1.7% was lost in kDMSO-d compared to 16.2% in kDMSO (see chapter 5). This is attributed to loss of DMSO from the interlayer space of kDMSO-d as a result of the exchange experiment. Assuming this 1.7% weight loss is entirely due to DMSO, the molar amount of DMSO remaining in kDMSO-d is calculated to be 0.022 moles DMSO/100g. This agrees very well with the carbon content determined by %CHNS (Table 7), which gives a value of 0.025 moles DMSO/100g.This gives the following stoichiometry for the material:

$Al_2Si_2O_5(OH)_{4-x}(OD)_x$ $[DMSO]_{0.0661}$

2.2.4.3 kmethoxy-d

The TGA weight loss curve for kmethoxy-d (Figure 25) shows a total weight loss of 17.6%, compared to 16.3% for kmethoxy (see chapter 5). This difference is attributed to the heavier weight of deuterium from D_2O and Al-OD groups in kmethoxy-d compared to hydrogen from H_2O and Al-OH groups in kmethoxy. This weight loss increase from room temperature to 300°C in kmethoxy-d (3.2%) compared to kmethoxy (2.6%) is attributed primarily to exchange of H_2O with D_2O. No nitrogen was found in %CHNS analysis of kmethoxy-d (Table 7), which indicates full removal of NMF from kmethoxy-d during the exchange experiment. This absence of NMF in kmethoxy-d indicates the weight lost from room temperature to 300°C in TGA must be entirely from D_2O. Since the ratio of weight loss in this region between these two materials (1.2) is greater than the molar mass ratio between D_2O and H_2O (1.1), additional D_2O must have been loaded in kmethoxy-d during the exchange experiment. The increase in weight loss from 300 to 650°C in kmethoxy-d (14.4%) compared to kmethoxy (13.7%) is attributed to exchange of Al-OH with Al-OD groups.

%CHNS results (Table 7) show a decrease in carbon content from 1.5% in kmethoxy to 0.70% kmethoxy-d. This indicates partial hydrolysis of the grafted methoxy groups in kmethoxy-d. TGA

results for kmethoxy-d support this result, where the kaolinite's dehydroxylation temperature (509.3°C) was significantly greater than in kmethoxy (480.7°C), indicating the loss of covalently grafted material. Previous studies have shown that extensive washing in water can partially hydrolyze functional groups that are grafted on kaolinite (Tunney, 1995). Because the exchange experiment involved dispersing kmethoxy in D_2O for 72h, it isn't surprising some of the methoxy groups in kmethoxy-d were hydrolyzed.

Based on these results, the following stoichiometry was calculated for kmethoxy-d:

$Al_2Si_2O_5(OH)_{3.44-x}(OD)_{x+0.30}(OCH_3)_{0.26}[D_2O]_y$

This model assumes the methoxy groups hydrolyzed during the exchange experiments will be replaced by OD groups rather than OH groups.

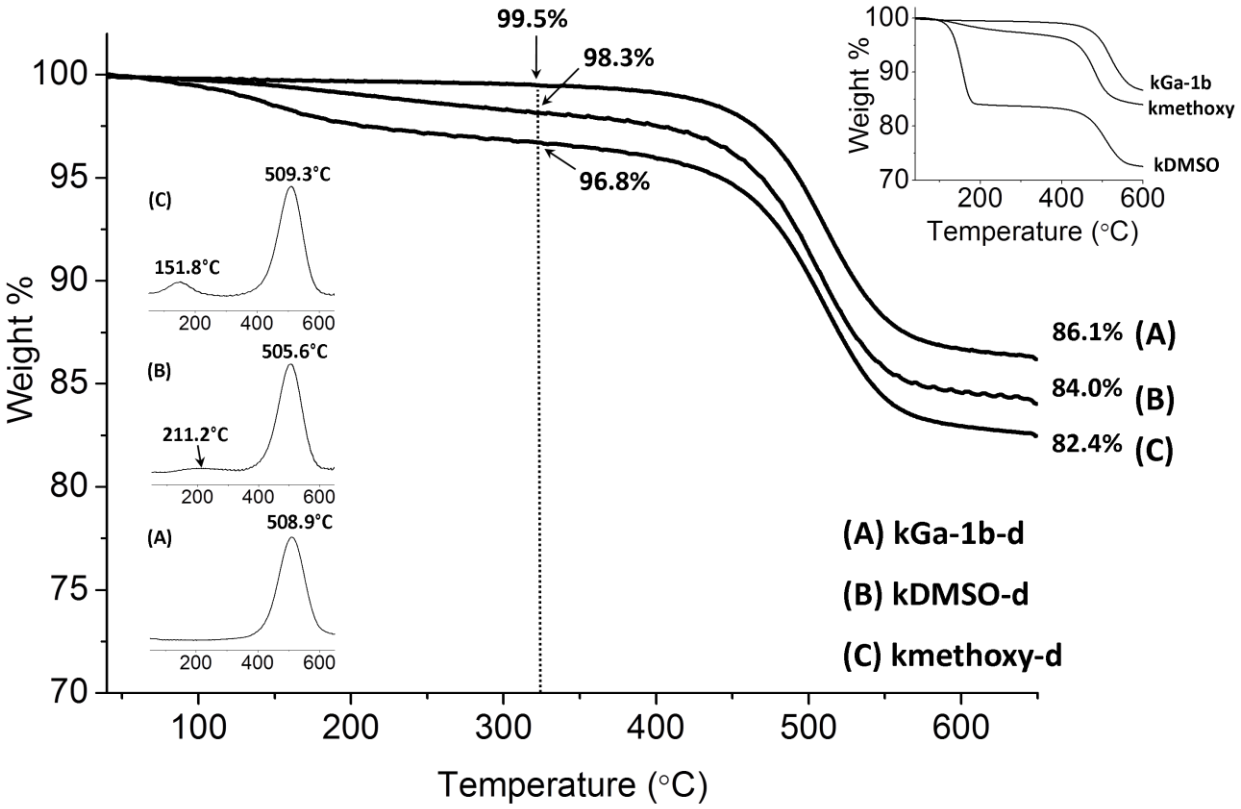

Figure 25: TGA weight loss curves of deuterated kaolinites. The 1st derivative plots and the weight loss curves for the undeuterated materials are included as insets. The weight loss values at 300°C and 650°C are marked on their respective curves.

Table 7: %CHNS elemental analysis of natural and modified kaolinites

	%N (±0.1%)	%C (±0.1%)	%H (±0.1%)	%S (±0.1%)
kDMSO	0.0	5.0	2.6	6.2
kDMSO-d[a]	0.0	0.6	1.7	0.2
kmethoxy	0.1	1.5	2.0	0.0
kmethoxy-d[a]	0.0	0.7	1.9	0.0

[a] Deuterium exchanged samples.

2.2.5 ^{1}H MAS NMR analysis & discussion

2.2.5.1 kDMSO-d

The ^{1}H NMR spectrum of kDMSO-d shown in Figure 26 shows two distinct peaks centered at 1.74ppm and 2.58ppm attributed to kaolinite's inner and inner surface hydroxyls respectively. Compared to kGa-1b, kDMSO, and kmethoxy, the 1.74ppm peak is significantly better resolved and much more intense than the peak at 2.58 ppm, which is attributed to the different affinity these groups have towards exchange with deuterium. Kaolinite's inner hydroxyls are known to be more resistant to exchange with deuterium than the inner surface hydroxyls (Ledoux and White, 1964b), so this result offers strong evidence that the 1.74ppm peak is from kaolinite inner hydroxyls.

A 3 site model was constructed using the stoichiometry, $Al_2Si_2O_5(OH)_{4-x}(OD)_x$ $[DMSO]_{0.066}$, calculated from TGA, and %CHNS results, and this was used to fit the experimental spectrum. This model uses the values reported by Ledoux and White (1964b), where 22% and 60% of kaolinite's inner and inner surface hydroxyls respectively exchange with deuterium at room temperature. The 12% fraction of unmodified kaolinite determined from XRD in kDMSO (see chapter 5) was also taken into account, where it was assumed none of its hydroxyls were exchanged with deuterium. From this, peak areas relative to kaolinite's inner hydroxyls were calculated to be 0.49 and 1.76 for residual DMSO and the kaolinite's inner surface hydroxyls

respectively. A summary of this fit is shown in Figure 26 and Table 8.

In contrast to the curve fitting results for kDMSO, this model gave a very good fit to the experimental spectrum of kDMSO-d using only a single site for DMSO. This is attributed to the exchange experiments removing significant amounts of DMSO from the interlayer space, resulting in the remaining intercalated DMSO adopting a different configuration where its methyl groups no longer key into kaolinite's siloxane rings on the silicon sheets.

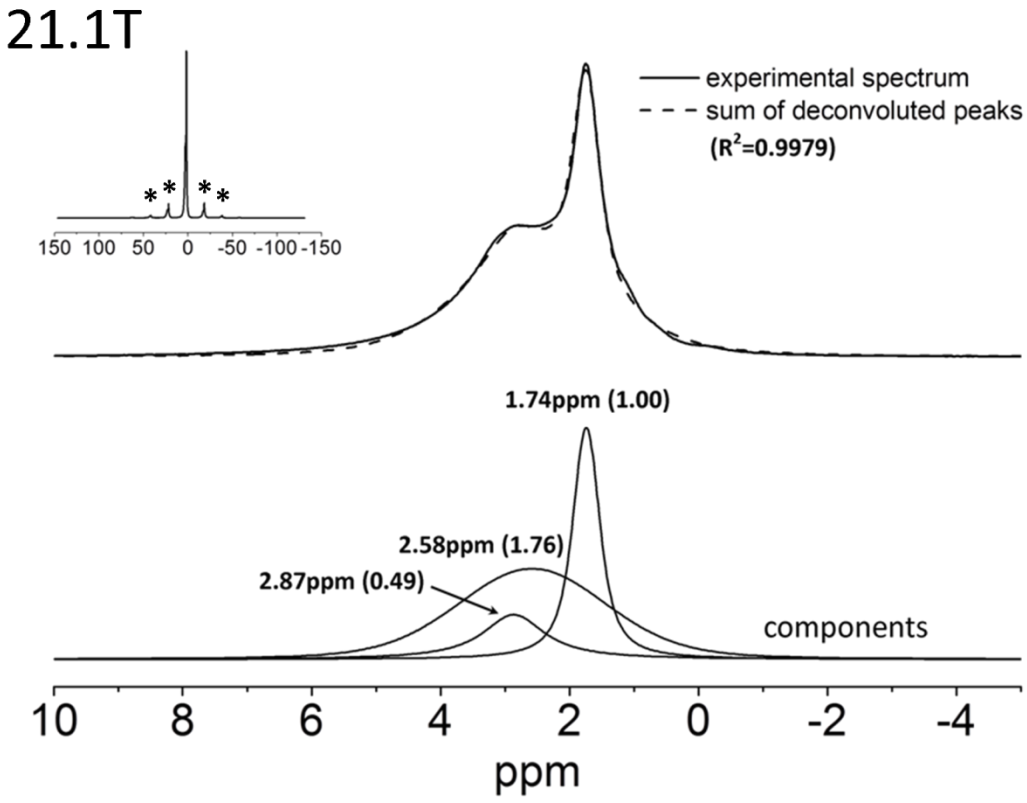

Figure 26: ^{1}H MAS NMR of spectra kDMSO-d and curve fitting results using a three site model. An expanded scale spectrum is shown as an inset showing the entire spinning sideband manifold. Rotational artifacts resulting from MAS are denoted with an asterisk.

Table 8: ^{1}H MAS NMR of kDMSO-d curve fitting results shown in Figure 26.

Chemical shift (ppm)	Rel. abundance	Attribution
1.74	1.00	inner AlOH
2.58	1.76	inner surface AlOH
2.87	0.49	CH_3; DMSO

2.2.5.2 kmethoxy-d

Similarly to kDMSO-d, the ^{1}H NMR spectrum of kmethoxy-d shown in Figure 27 shows an increase in the resolution of the kaolinite inner hydroxyl peak at 1.70ppm. The intensity of this peak was not significantly reduced compared to the same one in kmethoxy, which is expected due to the inaccessibility of these inner hydroxyls for exchange with deuterium. The 3.21ppm peak attributed to grafted methoxy groups was also not significantly affected, indicating that an important amount of grafted materials remains after washing in D_2O. NMF CH_3 groups, HC=O and NH peaks were absent, which is in line with %CHNS results that showed they were removed during the exchange experiments. Their absence also contributed to the decrease in spectral line broadening from 2-4ppm and 10-5ppm compared to kmethoxy.

A four site model was constructed using the stoichiometry:

$Al_2Si_2O_5(OH)_{3.44-x}(OD)_{x+0.30}(OCH_3)_{0.26}[D_2O]_y$ determined from TGA and %CHNS results (see chapter 5), and this was used to fit the experimental spectrum. The 12% fraction of unmodified kaolinite determined from XRD results for kmethoxy (see chapter 5) was taken into account, where it was assumed none of its hydroxyls were exchanged with deuterium. Peak areas relative to the inner hydroxyls were calculated to be 0.97 for the OCH_3 grafted groups, and 0.86 and 0.45 for the kaolinite inner surface OH groups in the 8.6Å and 7.2Å XRD fractions respectively. A summary of this fit is shown in Figure 27.

The model gave a best fit using chemical shift values for the inner surface hydroxyls (2.12ppm) that were very similar to the one identified in kmethoxy (2.13ppm). The fit was also very accurate in the 1-3ppm region using the calculated peak ratio of the inner hydroxyls and inner surface hydroxyls. This suggests the model proposed for kmethoxy where decreased interlayer cohesion between the aluminum and silicon layer caused by the grafted methoxy groups causes the kaolinite's inner surface hydroxyls to have a lower chemical shift values is valid. The model was also shown to be very accurate using the fractions of deuterium substitution reported by Ledoux and White(1964b), which suggests methanol grafted kaolinites will give similar yields of deuterated hydroxyls.

The fit was noticeably less accurate when fitting the 3-10ppm region of the experimental spectrum, indicating the model needs to account for additional peaks in this region. One possible explanation is that this additional signal is from H_2O generated from exchange

between the D_2O in kmethoxy-d and water from moisture in the atmosphere. This was used to refine the aforementioned four site model, where water in the material was accounted for as a single peak, giving five peaks total in the model. This significantly improved the accuracy of the fit, suggesting the model is valid. A best fit was found using a peak area that correspond almost exactly to the water content in kmethoxy, indicating the interlayer and surface D_2O in kmethoxy-d was fully exchanged with H_2O. This result shows that the interlayer D_2O in kmethoxy-d is readily exchangeable and requires being kept under airtight conditions at all times to prevent exchange with water from moisture in the air. A summary of this fit is shown in Figure 28 and Table 9.

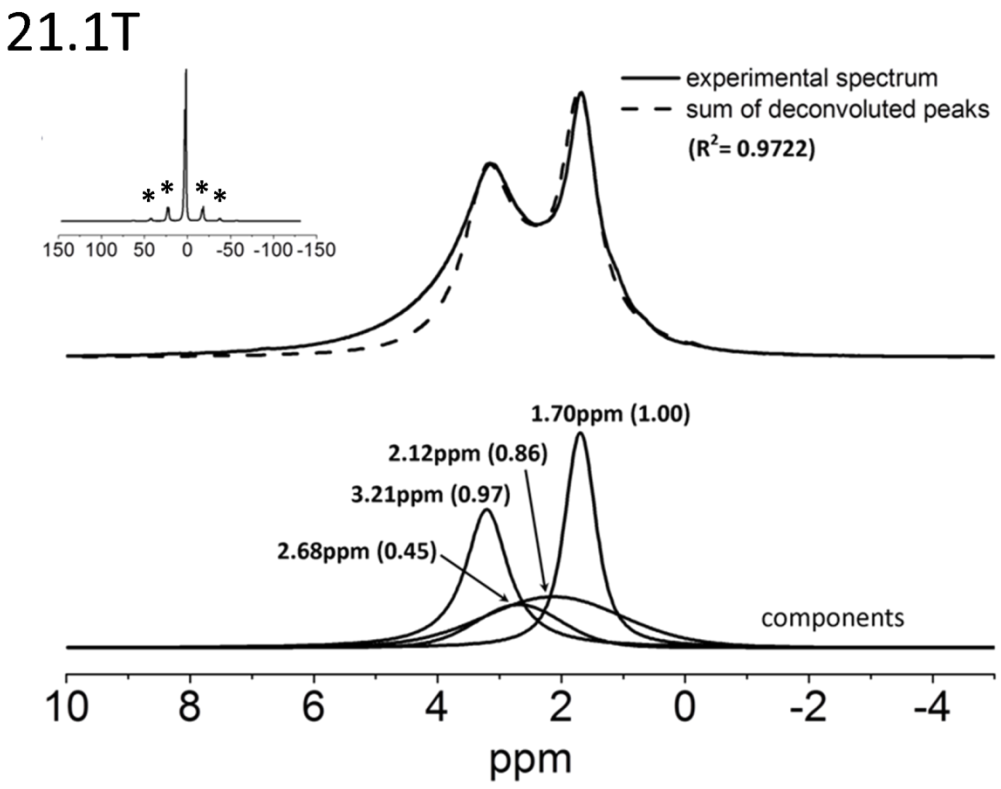

Figure 27: ^{1}H MAS NMR of spectra kmethoxy-d and curve fitting results using a 4 site model. An expanded scale spectrum is shown as an inset showing the entire spinning sideband manifold. Rotational artifacts resulting from MAS are denoted with an asterisk.

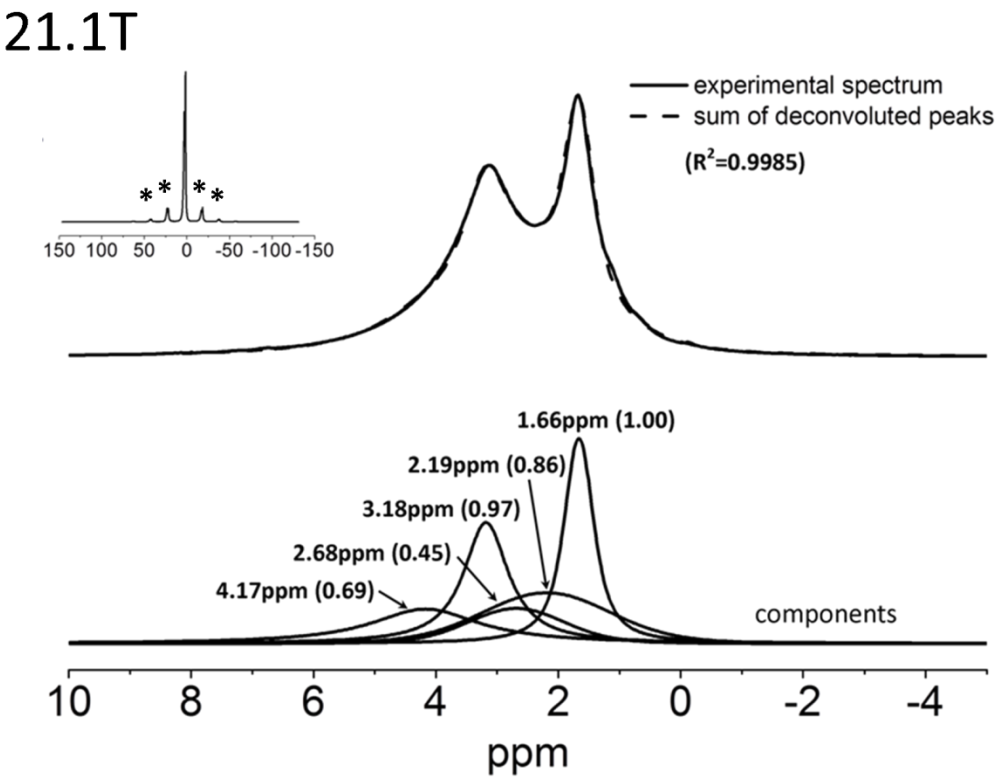

Figure 28: ^{1}H MAS NMR of spectra kmethoxy-d and curve fitting results using a five site model. An expanded scale spectrum is shown as an inset showing the entire spinning sideband manifold. Rotational artifacts resulting from MAS are denoted with an asterisk.

Table 9: Summary of ^{1}H NMR peaks identified for kmethoxy-d

Chemical shift (ppm)	Rel. abundance	Attribution
1.66	1.00	inner AlOH; kmethoxy+kGa-1b
2.19	0.86	inner surface AlOH; kmethoxy
2.68	0.45	inner surface AlOH; kGa-1b
3.18	0.97	OCH_3; kmethoxy
4.17	0.69	OH; water

2.2.6 Summary and conclusions

Partial exchange of the clay mineral's hydroxyl groups with deuterium was achieved for kDMSO-d and kmethoxy-d at room temperature. KGa-1b's hydroxyls were found to be un-exchangeable under these conditions. IR results confirmed exchange with deuterium occurred based on the appearance of O-D stretching bands in the 2800-2500cm^{-1} regions. TGA and %CHNS elemental analysis showed evidence that interlayer organic matter was removed in kDMSO-d and kmethoxy-d during the deuterium exchange experiments, and these results were used to calculate stoichiometries used for curve fitting experimental ^{1}H spectra of these materials.

^{1}H NMR experiments showed different affinities of the kaolinites' hydroxyl groups towards exchange with deuterium, where the peaks attributed to inner surface hydroxyls were significantly more affected than those attributed to inner hydroxyls. Kaolinite's inner hydroxyls are known to be more resistant to exchange with deuterium than the inner surface hydroxyls, so these results validate the attribution of these two peaks.

A three site model for kDMSO-d was constructed using XRD, TGA, %CHNS results, and the deuterium exchange yields reported by Ledoux and White (1964b) and was accurately fitted to the experimental spectrum. The model was accurate using a single peak for DMSO's CH_3

groups, suggesting the remaining intercalated DMSO adopts a different configuration where its methyl groups no longer key into kaolinite's siloxane rings on the silicon sheets.

A five site model for kmethoxy-d using XRD, TGA and %CHNS results, and taking into account the deuterium exchange yields reported by Ledoux and White (1964b) was accurately fitted to the experimental spectrum. A good fit was achieved using deuterium exchange ratios for the clay mineral's hydroxyl groups that were similar to kDMSO-d, suggesting that methanol grafted kaolinites will give similar yields of deuterated hydroxyls. Fitting this model found that the chemical shift value for the inner surface hydroxyls in the 8.6Å fraction was very similar to those in kmethoxy, suggesting the hypothesis that kaolinite's inner surface hydroxyls have a lower chemical shift values in methanol grafted kaolinite, is valid. The model gave a best fit to the experimental spectrum using a peak area for water that correspond almost exactly to the water content in kmethoxy, indicating the interlayer and surface D_2O in kmethoxy-d was fully exchanged with H_2O.

Further studies could investigate the ^1H NMR spectra of intercalated and grafted complexes using compounds where all their hydrogens have been exchanged with deuterium (e.g. D6-DMSO, D4 methanol, D6 ethylene glycol). This would allow the changes occurring to the kaolinite hydroxyl protons as a result of intercalation or grafting to be examined without interference.

2.3 ^{27}Al solid state NMR study of natural and modified kaolinites

2.3.1 Introduction

^{27}Al is a 100% abundant isotope of aluminum with a high gyromagnetic ratio, making it, in theory, a very sensitive nucleus to study by NMR. It is also a major constituent of phyllosilicates and other geological materials, making it a useful nucleus for studying the structure of many solid materials. In practice though, most routine study of ^{27}Al nuclei in solid materials is limited to identifying species with very large differences in chemical shift values, such as those in different coordination environments. This is because ^{27}Al is a quadrupolar nucleus which gives rise to its own set of interactions which can have a significant effect on the line shape and resolution of its NMR spectrum.

These quadrupolar effects result from the non-uniform nuclear charge distribution in a spin >½ nucleus (Figure 29). This generates a nuclear quadrupole moment, which can then couple to the components of electric field gradients (EFG) around the nucleus in a particular direction. This interaction can be represented as a symmetric, second rank tensor in the laboratory frame of reference (V) and in its own principal axis system (V_{PAS}) as follows:

$$V = \begin{bmatrix} V_{XX} & V_{XY} & V_{XZ} \\ V_{YX} & V_{YY} & V_{YZ} \\ V_{ZX} & V_{ZY} & V_{ZZ} \end{bmatrix} \qquad V_{PAS} = \begin{bmatrix} V_{XX} & 0 & 0 \\ 0 & V_{YY} & 0 \\ 0 & 0 & V_{ZZ} \end{bmatrix} \tag{2.16}$$

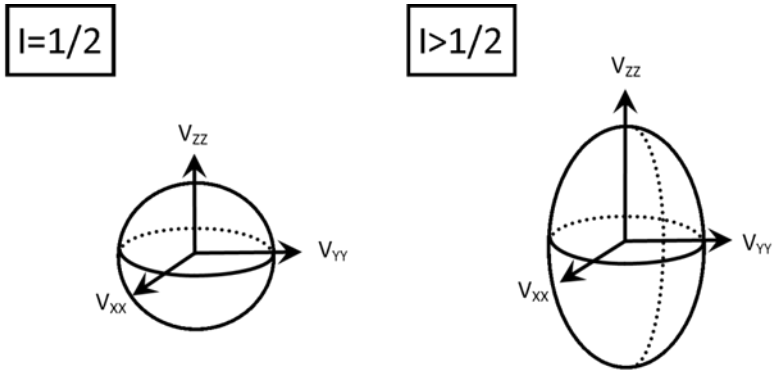

Figure 29: Nuclear charge distribution in a spin ½ nucleus compared to a spin >½ nucleus. The non-spherical charge distribution in a spin >½nucleus generates a nuclear quadrupole moment.

The individual components of V^{PAS} are commonly labelled such that:

$$V_{ZZ} \geq V_{YY} \geq V_{XX} \tag{2.17}$$

Because the sum of each component must be zero, only two parameters are required to characterise the magnitude of the principal component. Usually, the vector V_{ZZ} and a dimensionless quantity known as the quadrupolar asymmetry parameter, η_Q, are used. η_Q is described in the following equation:

$$\eta_Q = \frac{(V_{XX} - V_{YY})}{V_{ZZ}} \; ; \; 1 \geq \eta_Q \geq 0 \tag{2.18}$$

The product of V_{ZZ} and the nuclear quadrupole moment gives a value C_Q known as the quadrupole coupling constant. This is represented in the following equation:

$$C_Q = \frac{eQV_{ZZ}}{h} \qquad (2.19)$$

Where e is the magnitude of the charge on an electron, *h* is the Planck constant, and Q is the nuclear quadrupole moment. Similar to this is the quadrupolar frequency (ν_Q), which is described by the following equation:

$$\nu_Q = \frac{\omega_Q}{2\pi} = \frac{3C_Q}{2I(2I+1)} \qquad (2.20)$$

where ω_Q and ν_Q are the quadrupolar frequency in units of rad•s^{-1} and Hz respectively and I is the spin quantum number of the nucleus.

In the presence of a magnetic field, this quadrupolar frequency combines with the Zeeman interaction to give inequivalent energies for each possible m↔m±1 transition. This gives rise to complex line shapes for even single component systems (see Figure 30).

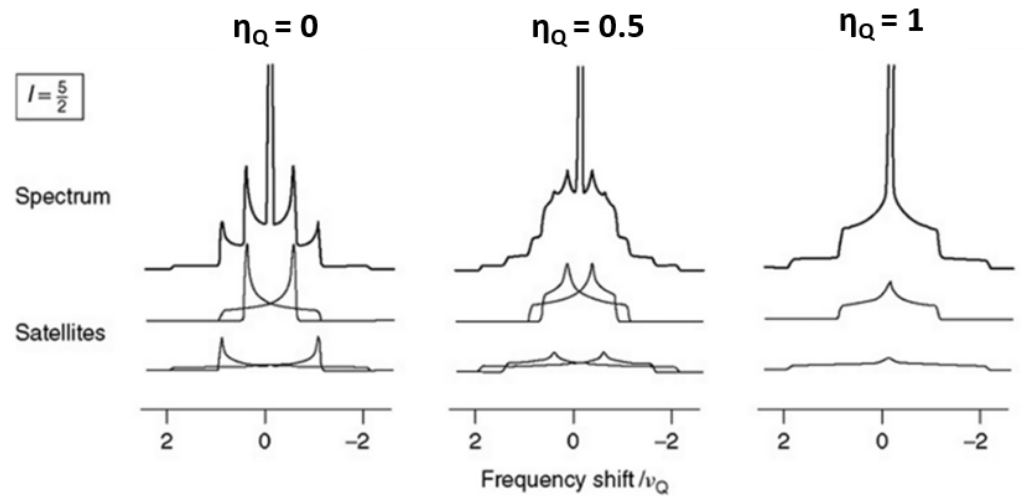

Figure 30: First order quadrupolar spectra of powder samples simulated for a spin quantum number I=5/2 nucleus with different values of η_Q. Adapted from: (Vega, 2012).

A number of strategies can be employed to minimize these quadrupolar effects. Working with stronger magnets can minimize them by increasing the magnitude of the Larmor frequency (ν_0) relative to it. The widely used magic angle spinning (MAS) technique can also average these interactions for the central m=-1/2 ↔ m=+1/2 transition, but only partially. This is because the quadrupolar interaction is dependent on a 4^{th} order Legendre polynomial term that cannot be averaged out by spinning at the magic angle. Spinning at a second angle where the terms of the higher order interaction are averaged out can completely eliminate the effects of this quadrupolar interaction. Double rotation (DOR) (Samoson *et al.*, 1988) and dynamic angle spinning (DAS) (Llor and Virlet, 1988) experiments are examples using this approach. These two techniques, however, require specialized probes and setups that are impractical for routine NMR analysis. Examining multiple quantum (MQ) transitions by means of a 2D experiment can

also eliminate this interaction without the need for special probes (Frydman and Harwood, 1995; Medek *et al.*, 1995). These experiments, however, are not very sensitive and require careful experimental design to maximize the multiple quantum transitions.

Even with careful experimental design however, accurate determination of NMR parameters such as C_Q, η_Q, and δ_{iso} can be challenging, especially in complex samples containing multiple sites with similar parameters. Most modern studies of quadrupolar nuclei determine these values through simulation and fitting the line shapes of experimental spectra with the help of specialized computational software. A number of software suites exist for this purpose such as SIMPSON (Bak *et al.*, 2011), Wsolids1 (Eichele, 2015), Dmfit (Massiot *et al.*, 2002), and QUEST (Perras *et al.*, 2012).

Compared to the ^{1}H nucleus, solid state ^{27}Al NMR of kaolinite has been studied much more extensively. Much of this has been focused on finding the existence of two aluminum sites predicted by X-ray studies (Bish and Von Dreele, 1989). To this day, however, there still exists some controversy regarding evidence of multiple aluminum species based on ^{27}Al NMR experiments. Some authors report multiple sites (Rocha *et al.*, 1994; Paris, 2014) whereas others not (Ashbrook *et al.*, 2000; Zhou *et al.*, 2009). This is believed to be due to the very small differences between the parameters for each aluminum species making it difficult to distinguish between them.

The ^{27}Al NMR literature on intercalated and grafted kaolinite complexes is much more limited, however, the studies that have been done show a high likelihood of observing multiple species of Al, especially in grafted complexes. Tunney (1995) for example reported major changes occurring to the ^{27}Al NMR spectra of kaolinite grafted with ethylene glycol, which they attributed as the evidence that ethylene glycol was covalently grafted to the aluminum sheets in the clay mineral. Hirsemann *et al.* (2011) expanded upon this work by performing multiple quantum magic angle spinning (MQMAS) experiments on ethylene glycol grafted kaolinite, and found two Al species with different chemical shifts and quadrupolar parameters. They also performed a REAPDOR (rotational echo adiabatic passage double resonance) experiment and conclusively showed that ethylene glycol was grafted to kaolinite's internal aluminol surfaces. Matusik *et al.* (2012) also examined the ^{27}Al NMR spectra of methanol grafted kaolinite, but only showed the lineshape and center of gravity of the central transition. No in-depth analyses of the ^{27}Al NMR spectra of methanol grafted kaolinites in the literature are known at this time.

The goal of this project is to investigate the ^{27}Al spectra of a natural kaolinite, KGa-1b, an intercalated complex kDMSO and two grafted kaolinite methanol complexes, kmethoxy and kmethoxy(ht) and to attempt to identify multiple aluminum species in the ^{27}Al NMR spectra and to demonstrate this technique can be used to distinguish the aluminum sites in intercalated and grafted complexes from those in the unmodified clay mineral. The experimental spectra will be

simulated and fitted in order to extract δ_{iso} values and the quadrupolar parameters C_Q, η_Q to definitely show evidence of different sites.

2.3.2 Description of samples

This study examined the same natural (kGa-1b) and modified kaolinite samples (kDMSO, kmethoxy, kmethoxy(ht)) described in section 2.1.2. Samples of a deuterium exchanged kaolinite, kDMSO-d (see section 2.2.2), were also examined in comparison with kDMSO.

Samples of a less crystalline kaolinite kGa-2 were examined for comparison with kGa-1b to see if differences in the crystallinity of natural kaolinite samples results in observable differences in their ^{27}Al NMR spectra. kGa-2 is a highly pure kaolin obtained from the Clay Mineral Society's Source Clay Repository (The Clay Minerals Society, 3635 Concorde Pkwy Suite 500, Chantilly VA 20151-1110, USA). Sample preparation for kGa-2 was done in the same manner as described for kGa-1b (see section 5.2).

2.3.3 ^{27}Al MAS NMR results & discussion

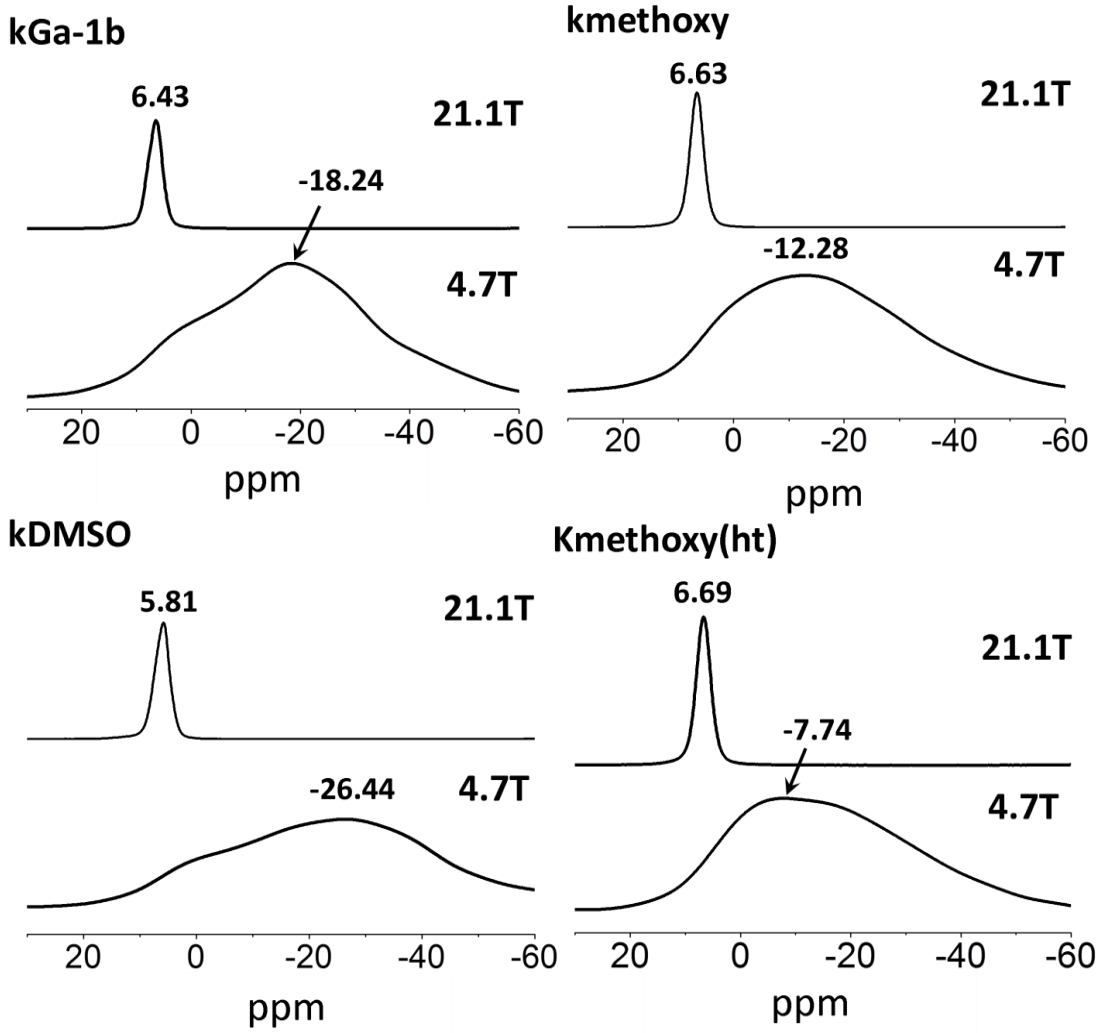

Figure 31: ^{27}Al MAS NMR spectra of kGa-1b, kDMSO, kmethoxy, and kmethoxy(ht) measured at 4.7T and 21.1T.

2.3.3.1 kGa-1b

The ^{27}Al MAS NMR spectrum of kGa-1b (Figure 31) indicates that the sample contains predominantly octahedral Al-O species. The central peak centered at 6.43ppm when measured at 21.1T is consistent with a six-coordinated species of Al-O, which is expected to give a signal between -10 and 15ppm (Mackenzie and Smith, 2002). At 4.7T, the position of the central peak is significantly shifted towards lower chemical shifts, where it is centered at -18.24ppm. There are also a number of shoulder features visible on both sides of the peaks which are a result of the amplified quadrupolar effects when working at lower magnetic field strength and MAS rates.

Because ^{27}Al is an I=5/2 nucleus, a single species of aluminum will give rise to 3 observable M=±1 transitions: a central (CT) transition for m=-1/2↔m=+1/2, and two satellite (ST) transitions for the m=±1/2↔m=±3/2 (i.e. ST1) and m=±3/2↔m=±5/2 (i.e. ST2) pairs. The quadrupolar interaction distorts the energy levels of these states. This will result in a distinct signal for each (Figure 30). Figure 31 shows only one single peak which is a combination of the CT and ST transitions. In the 1st pair of spinning side bands, the signal of the CT transition drops dramatically, while the ST transitions' intensities drop to a much lesser degree to the point that they become clearly resolved (Figure 32). This phenomenon is well known in the literature (Samoson, 1985) and studying ST transitions in this manner is sometimes employed as a strategy for analyzing spectra containing poorly resolved sites (Paris, 2014).

Trace amounts of tetrahedral Al-O aluminum were also observed in the spectrum measured at 21.1T (Figure 32). This peak was centered at 71.02ppm, which is consistent with a four coordinated Al-O species, which is expected to give a signal between 50-80ppm (Mackenzie and Smith, 2002). This is a result of small amounts of aluminum substitution in the tetrahedral silicon sheet, which is known to be present in kGa-1b (see chapter 5).

The spectrum of kGa-1b was also compared to a high defect kaolinite KGa-2 to attempt to identify any differences in their spectra to identify possible ^{V}Al peaks resulting from structural defects. The two spectra were almost identical (Figure 33), and showed no obvious sign of ^{V}Al peaks in the 20-60ppm region. This is in contrast to the spectra of metakaolinites which show a strong signal in this region (Yang *et al.*, 2010), clearly demonstrating their absence in the material.

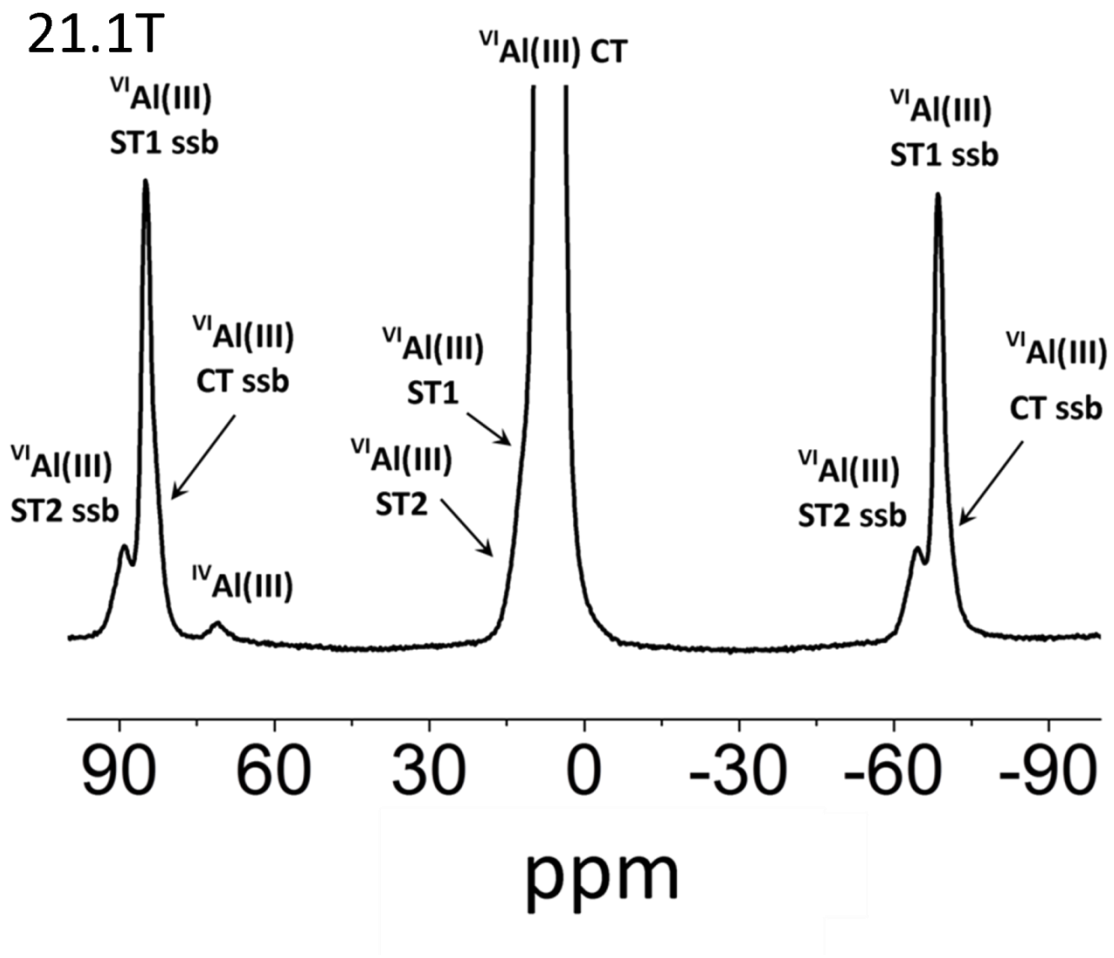

Figure 32: Close-up of ^{27}Al MAS NMR spectra of the kGa-1b measured at 21.1T shown in Figure 31. The spectrum is zoomed in to show the line shape of the 1st spinning sideband pair and the tetrahedral aluminum species present.

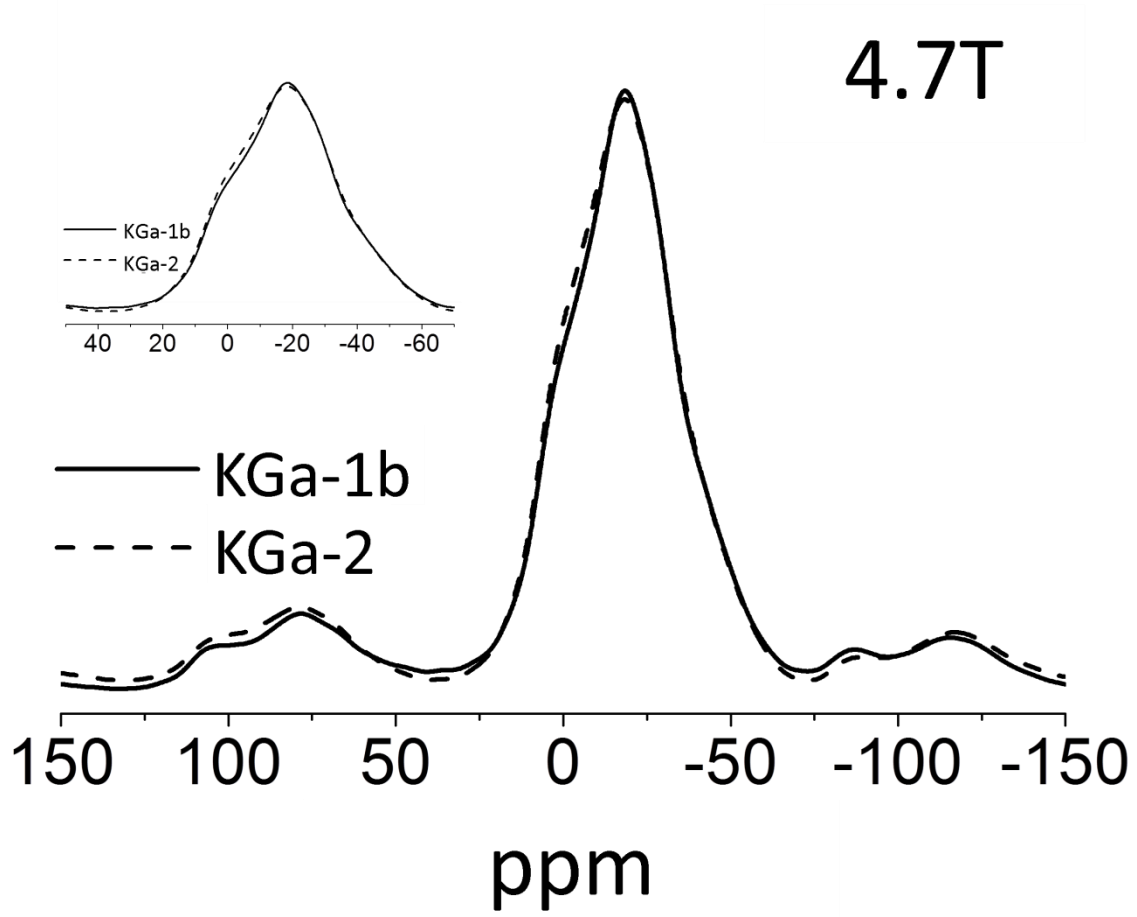

Figure 33: ^{27}Al MAS NMR spectra of kGa-2 compared to kGa-1b, measured at 4.7T. A close up of the central peak is shown as an insets.

2.3.3.2 kDMSO

The ^{27}Al MAS NMR spectrum of kDMSO measured at 4.7T (Figure 31) shows some observable differences when compared to kGa-1b. The central transition in kDMSO shifts from -18.24 to -26.44ppm, and superimposing this spectrum with kGa-1b (Figure 34) clearly shows that the peak's shape broadens at lower chemical shift values. At 21.1T, on the other hand, kDMSO's central peak appears almost identical to kGa-1b's and is only slightly shifted to 5.81ppm. These results suggest that the differences between these two spectra are a result of quadrupolar parameters rather than δ_{iso}. The shift towards lower chemical shift values suggests the magnitude (C_Q) of the quadrupolar interaction in its aluminum sites is greater than in kGa-1b.

The spectrum of kDMSO-d at 21.1T is almost identical to that of kGa-1b (Figure 35), which is attributed to the removal of DMSO from the kaolinite interlayer space. %CHNS results (see chapter 5) showed that 88% of the interlayer DMSO was removed in kDMSO-d, indicating that the central peak's shift is dependent on interlayer DMSO.

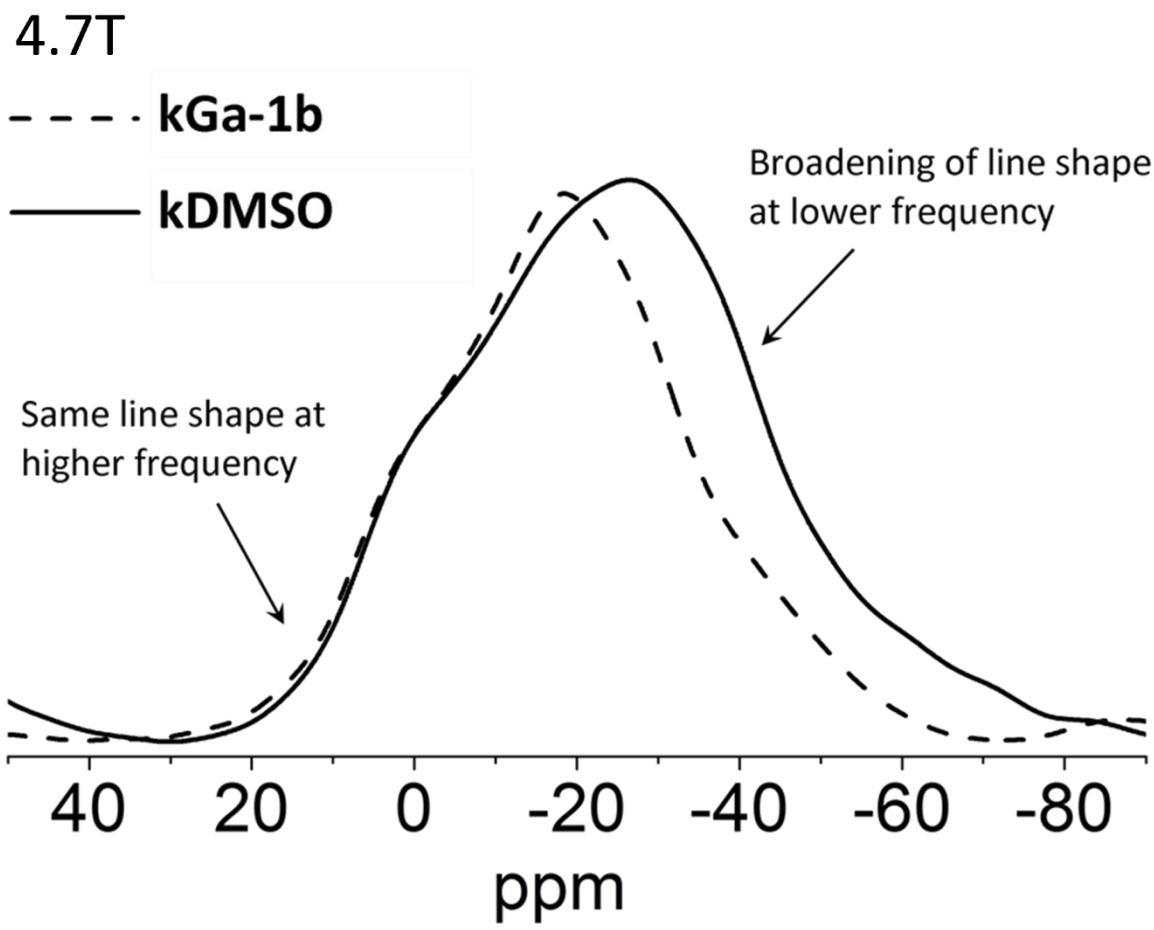

Figure 34: Superposition of the ^{27}Al NMR spectra of kGa-1b and kDMSO. The broadening towards lower chemical shift values in kDMSO is attributed to higher values of C_Q.

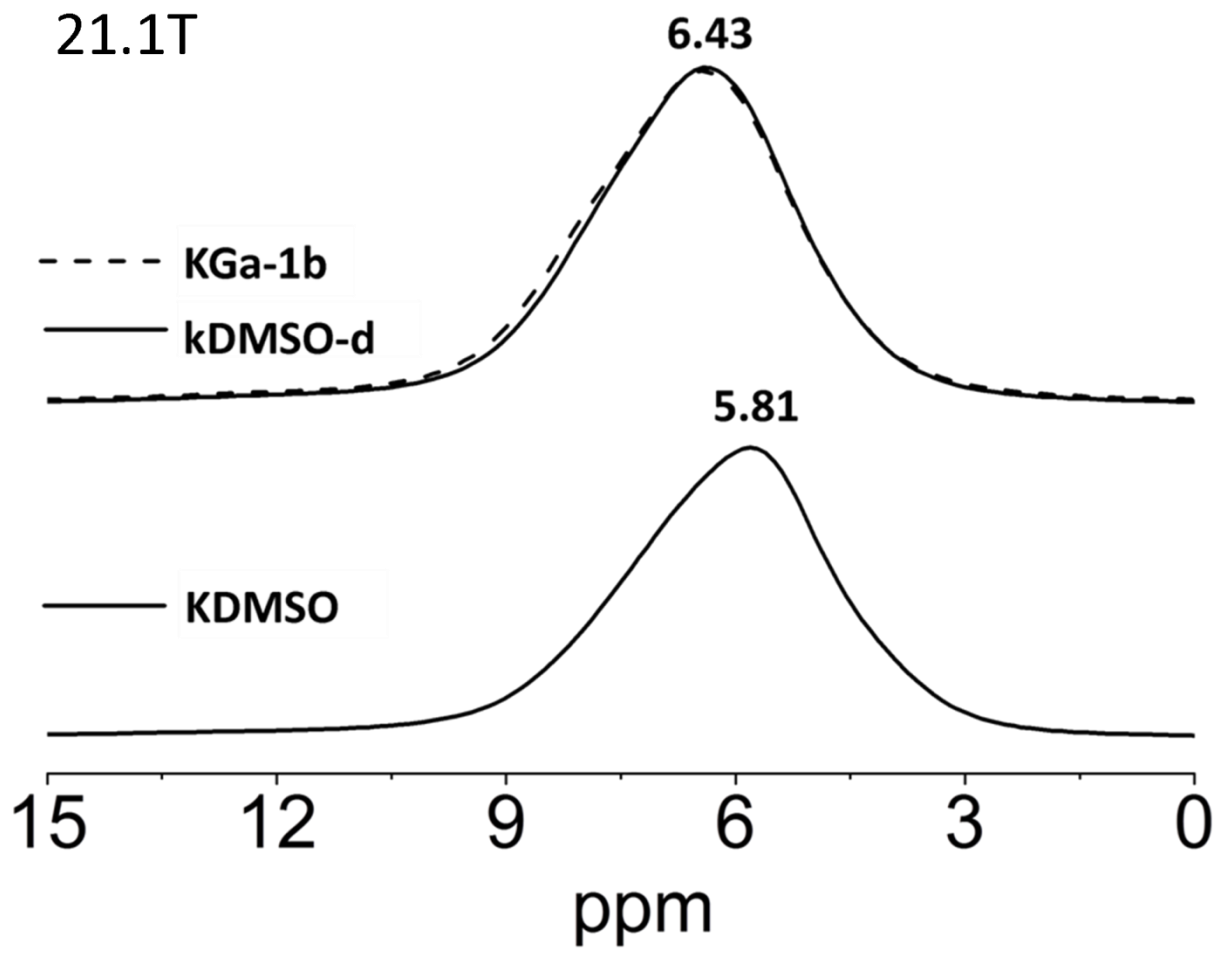

Figure 35: ^{27}Al MAS NMR spectra of kDMSO-d compared to kDMSO and kGa-1b.

2.3.3.3 Kmethoxy and Kmethoxy(ht)

The ^{27}Al NMR spectra of kmethoxy and kmethoxy(ht) (Figure 31) show some observable changes when compared to kGa-1b that are quite different from kDMSO. At 21.1T, the spectra appear mostly unchanged, where there is a slight shift of their central peak from 6.43ppm in kGa-1b, to 6.63-6.69 ppm. This is in contrast to kDMSO where the shift was towards lower chemical shift values instead. At 4.7T, this shift is much more dramatic, where the central peak is shifted to values between -7.74 and -12.28ppm. The shape of the peaks is smooth and mostly featureless. These results suggest there are different aluminum sites present in these two kaolinites which have different quadrupolar parameters from kGa-1b. The shift towards higher chemical shift values suggests the magnitude (C_Q) of this quadrupolar interaction is lower than in kGa-1b.

The comparison of the spectra of kmethoxy and kmethoxy(ht) at 4.7T shows that the central peak in kmethoxy(ht) is shifted slightly more towards higher chemical shift values with a center of gravity at -7.74ppm. Its central peak also has a shoulder around -12ppm, which is similar to the center of gravity of kmethoxy's central peak (Figure 36). Based on XRD fractions of the two materials (see chapter 5), the proportion of modified kaolinite to unmodified kaolinite is about the same in both materials, but the quantity of grafted material is greater in kmethoxy(ht) compared to kmethoxy. This suggests that the shifts observed in the ^{27}Al NMR of these two materials is dependent on the quantity of grafted methoxy groups.

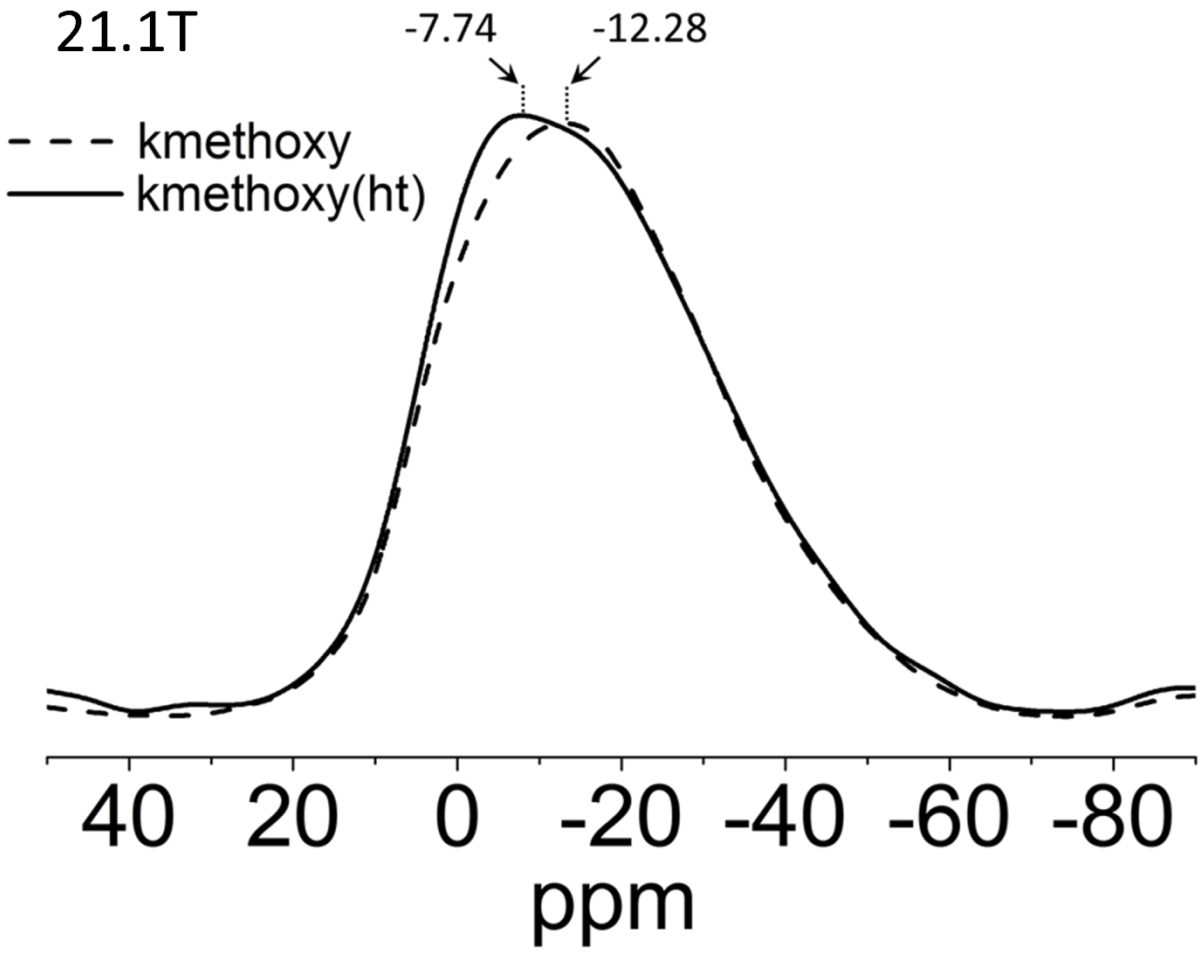

Figure 36: ^{27}Al MAS NMR spectra of kmethoxy(ht) compared to kmethoxy. These spectra were obtained on a 4.7T magnet. There is a notable shift of the weight of the central transition in kmethoxy(ht) towards higher frequencies.

2.3.4 Simulation and fitting of ^{27}Al NMR experimental spectra

2.3.4.1 kGa-1b, one site model

This model assumes that a single Al(III) species is present in kGa-1b. A best fit was found using values of δ_{iso} = 8.2ppm, C_Q= 3.21MHz and η_Q= 0.75 when fitted to the 4.7T experimental spectrum. This gives a reasonably good fit to the experimental spectrum, but some details are missing. Neither the central peak's shoulder on the lower frequency side of the spectrum nor its gradual, rather than segmented, drop in intensity is well simulated using a single aluminum site. The results of this fit are summarized in Figure 37 and Table 10.

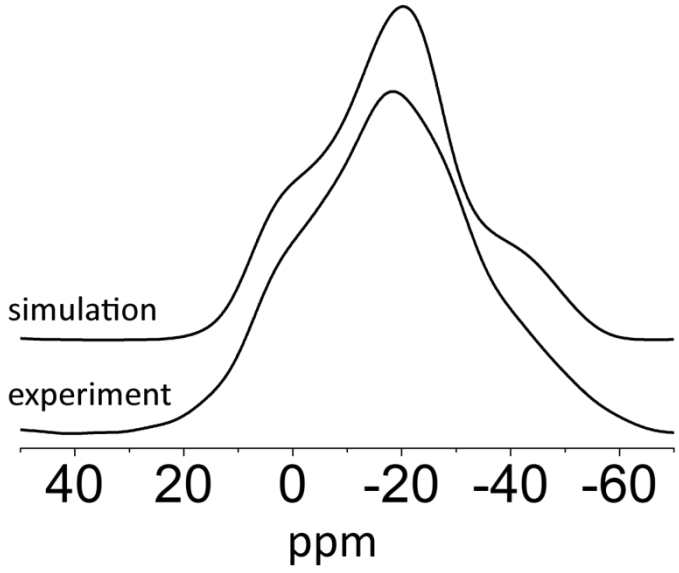

Figure 37: ^{27}Al MAS NMR spectra of kGa-1b at 4.7T fitted to a simulated spectrum using one unique Al(III) site. The chemical shift value and quadrupolar parameters of the site are summarized in Table 10.

Table 10: ^{27}Al MAS NMR parameters of kGa-1b identified from fitting the 4.7T experimental spectra in Figure 37.

	$\delta_{iso\ (ppm)}$	$C_{Q\ (MHz)}$	η_Q
site 1	8.2	3.2	0.75

2.3.4.2 kGa-1b, two site model

This model assumes kGa-1b has two unique Al(III) species of equal intensity. A best fit to the 4.7T spectrum was found when using two sites that differ in their value of C_Q by 0.50MHz and η_Q by 0.1. Fitting these parameters to the experimental spectrum 21.1T found a best fit when the δ_{iso} values of the two sites were 7.7ppm and 7.8ppm. This fit and the parameters extracted from it are shown in Figure 38, Figure 39 and Table 11, and are represented schematically in Figure 40. This model improves upon the one site model by correctly identifying the shoulder and tailing of the central peak at lower frequencies, and gives parameters that are very similar to those reported previously in the literature (Paris, 2014).

Assigning the δ_{iso} values to either sets of quadrupolar parameters gives a good fit, but the higher value of 7.8ppm was assigned to the site with a lower value of C_Q. There are a number of

reasons for this assignment. There are reports that the value of C_Q in aluminosilicates is dependent on Al-O bond length in the form of longitudinal strain for octahedral aluminum, and the O-Al-O bond angles in the form of shear strain in tetrahedral aluminum (Ghose and Tsang, 1973). In these cases, C_Q was found to increase with increasing strain. Other reports have also demonstrated a relationship between bond angle and δ_{iso} (Lippmaa *et al.*, 1986), and the mean distance between tetrahedral atoms and δ_{iso} (Kohn *et al.*, 1997) in aluminosilicates. From this, it could be construed that the different sites identified in kGa-1b are a result of subtle differences in aluminum octahedra in the crystal structure, with the more strained aluminum octahedron having greater values of C_Q, and a lower value of δ_{iso}. This might be explained in terms of the subtle differences resulting from layer distortion caused by lateral mismatch of the octahedral and tetrahedral sheets within a layer. This effect would mostly be seen in the tetrahedral sites due to the fact they are corner vs. edge sharing for the octahedral sites, making them much more flexible., but it could affect octahedral sites as well (Brigatti *et al.*, 2013).

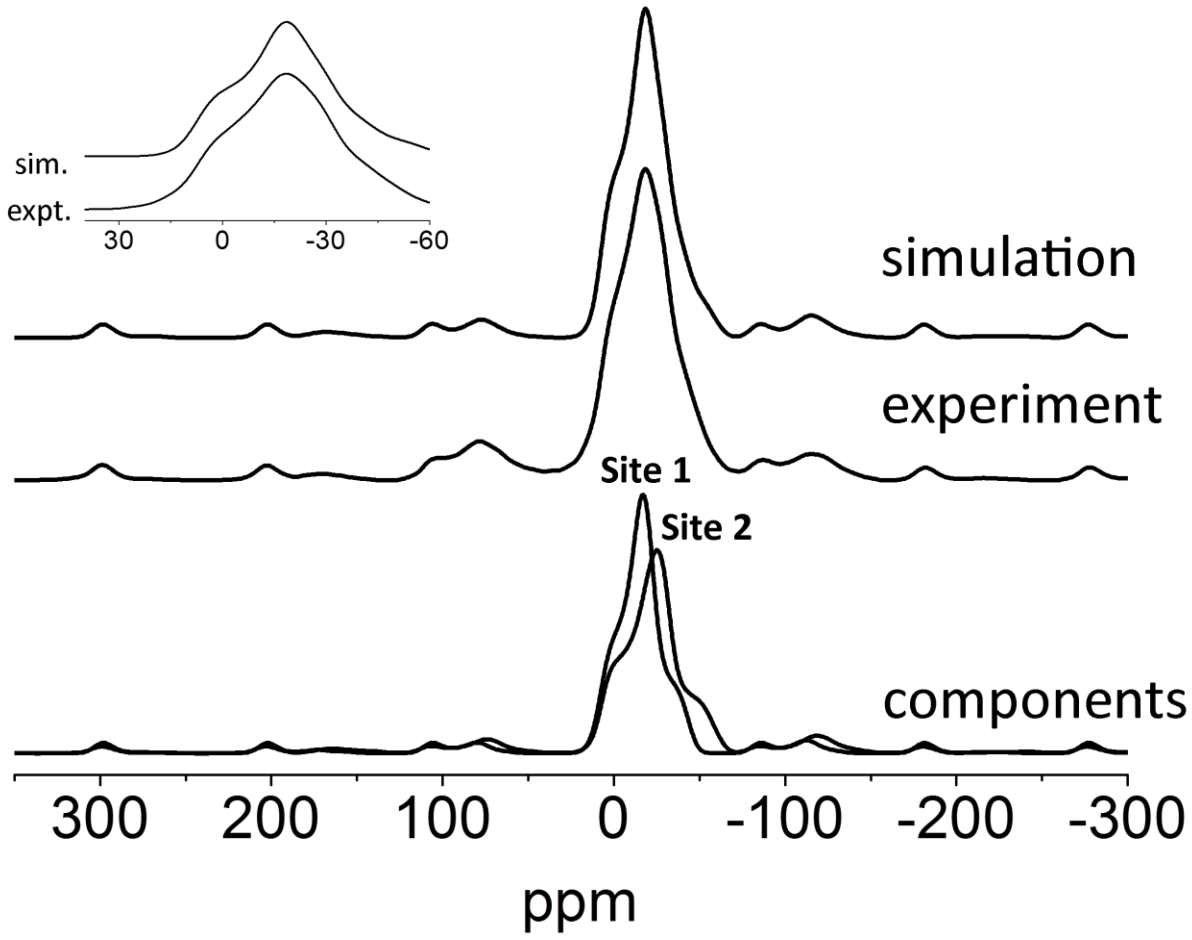

Figure 38: ^{27}Al MAS NMR spectra of kGa-1b at 4.7T fitted to a simulated spectrum using two unique Al(III) sites. A close up of the central peak is shown as an inset. The chemical shift value and quadrupolar parameters of the each site are summarized in Table 11.

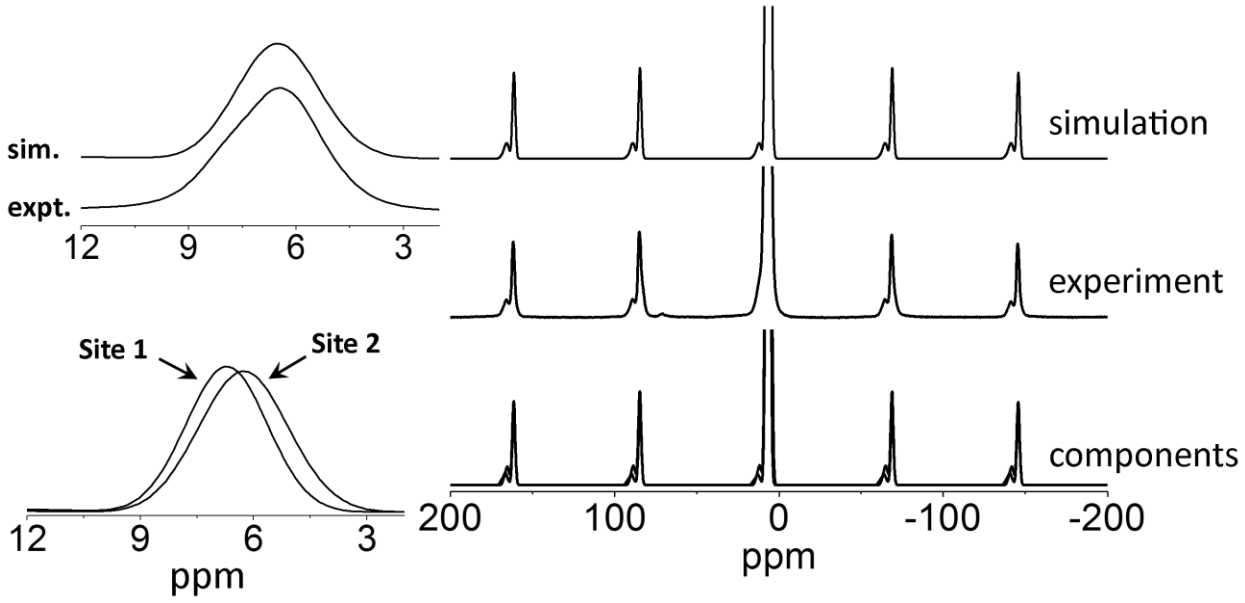

Figure 39: ^{27}Al MAS NMR spectra of kGa-1b at 21.1T fitted to a simulated spectrum using two unique Al(III) sites. A close up of the central peak and its simulated components are shown as insets. The chemical shift value and quadrupolar parameters of the each site are summarized in Table 11.

Table 11: ^{27}Al MAS NMR parameters of kGa-1b identified from fitting the 4.7T and 21.1T experimental spectra in Figure 38 and Figure 39.

	δ_{iso} (ppm)	C_Q (MHz)	η_Q	Rel. abundance
site 1	7.8 (8.0)[a]	2.9 (3.0)[a]	0.92 (0.9)[a]	0.50
site 2	7.7 (7.5)[a]	3.4 (3.4)[a]	0.78 (0.8)[a]	0.50

[a] (Paris, 2014)

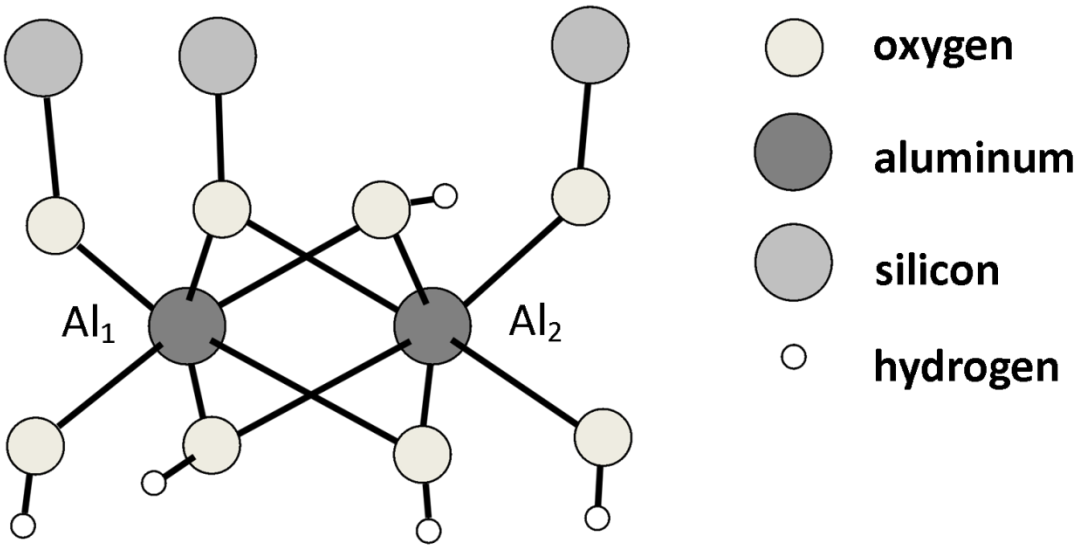

Al_1:	Al_2:
δ_{iso}=7.7ppm	δ_{iso}=7.8ppm
C_Q= 3.4MHz	C_Q= 2.9MHz
η_Q=0.78	η_Q=0.92

Figure 40: Summary of the two different ^{27}Al(III) octahedral sites identified for kGa-1b. This uses the parameters identified for the two site model.

2.3.4.3 kDMSO, three site model

This model assumes that the coverage of the interlayer surfaces with DMSO is complete in the 11.2Å XRD fraction, and that DMSO interacts equally with all the AlOH groups in the structure, resulting in one additional Al(III) site compared to kGa-1b. Taking into account the 88% abundance of the 11.2Å fraction, and the 12% abundant unmodified kaolinite fraction having two distinct aluminum species, this gives relative abundances of 0.88:0.06:0.06.

A best fit to the 4.7T spectrum was found using values of C_Q=3.72MHz and η_Q=0.72 for a δ_{iso} value of 7.8ppm. This gives a decent fit for central peak at higher chemical shift values, but it poorly simulates the peak's broad shoulder at lower chemical shift values. A summary of this fit is shown in Figure 41 and Table 12.

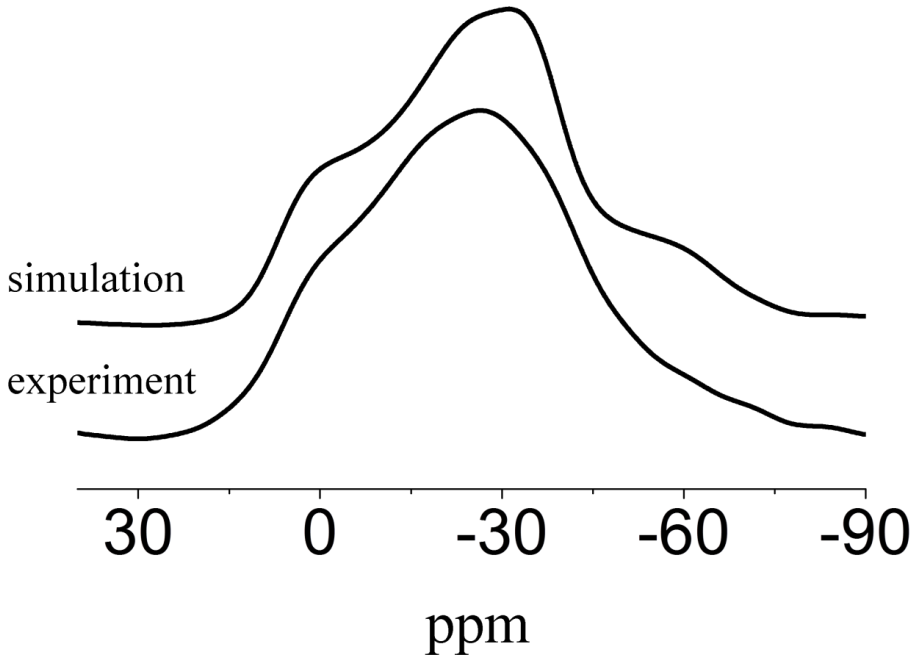

Figure 41: ^{27}Al MAS NMR spectra of kDMSO at 4.7T fitted to a simulated spectrum using one unique Al(III) site for the DMSO modified and two sites for the unmodified fraction in the material. The chemical shift value and quadrupolar parameters of the each site are summarized in Table 13.

Table 12: ^{27}Al MAS NMR parameters of kDMSO identified from fitting the 4.7T experimental spectra in Figure 41.

	δ_{iso} (ppm)	C_Q (MHz)	η_Q	Rel. abundance
11.2Å fraction	7.8	3.7	0.72	0.88
site 1, 7.2Å fraction	7.8	2.9	0.92	0.06
site 2, 7.2Å fraction	7.7	3.4	0.78	0.06

2.3.4.4 kDMSO, four site model

This is a refinement of the three site model, where the 11.2Å fraction modified by DMSO is expected to give two signals of equal intensity, giving four Al(III) sites total with relative abundances of 0.44:0.44:0.06:0.06. Fitting this model to the experimental spectrum at 4.7T gives a best fit when the two sites in the DMSO modified fraction have a value of C_Q that is 0.3-0.8MHz higher and an η_Q that is 0.06-0.20 lower than those in the unmodified clay mineral. Fitting these parameters to the experimental spectrum measured at 21.1T gave a best fit when the δ_{iso} values of the sites in the DMSO modified fraction were 7.5 and 7.4ppm, which were assigned to the sites with a higher and lower value of C_Q respectively. This fit and the parameters extracted from it are shown in Figure 42, Figure 43, and Table 13, and the results are represented schematically in Figure 44.

The key advantage of this model over the 3 site one is that it correctly simulates the shoulder and tailing of the central peak at lower frequencies. Like in kGa-1b, however, the summit of the central peak is still too sharp, but the position of the central peak's features and the sidebands is mostly correct.

The 0.3-0.8MHz increase in C_Q can be explained as a distortion of the aluminum octahedral in the clay mineral as a result of its interaction with intercalated DMSO. Since the value of C_Q in

^{27}Al NMR spectra of aluminosilicates is shown to be dependent on the Al-O bond length and the O-Al-O bond angles (Ghose and Tsang, 1973), DMSO sulfoxide groups interacting with kaolinite Al-OH groups in the octahedral sheet could, in theory, distort these Al-O octahedron resulting in a more important quadrupolar effect. The keyed in methyl structure adopted by DMSO in the silicon sheet could also be expected to distort the Si-O groups, which could result in additional distortions in the octahedral sheet through their shared oxygen.

There is some precedence for this claim of distorted Al-O octahedra in kDMSO. Raupach *et al.* (1987) for example reported slight differences in the horizontal ab plane for their refined structures of kaolinite DMSO intercalates which they attributed to distortions in individual kaolinite layers as a result of intercalated DMSO. Simulation studies have shown similar results as well (Michalková and Tunega, 2007). Infrared studies have also shown that hydrogen bonding interactions occur between aluminum hydroxyls in the clay mineral and interlayer DMSO, resulting in new OH stretching bands in kaolinite DMSO intercalates (Johnston *et al.*, 1984; Frost *et al.*, 1998). These results all support the model of a slightly distorted aluminum octahedron in kDMSO, resulting in a greater value of C_Q.

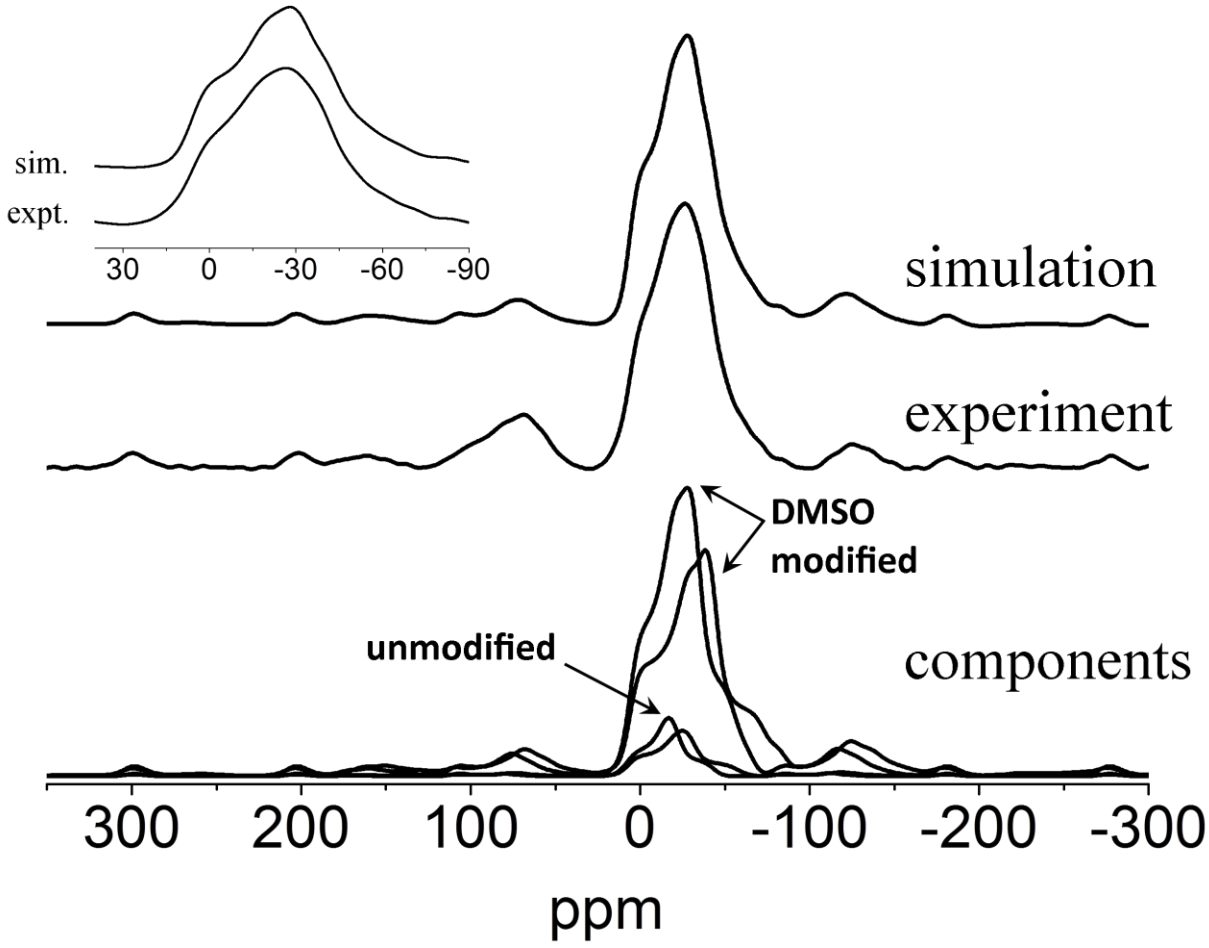

Figure 42: ^{27}Al MAS NMR spectra of kDMSO at 4.7T fitted to a simulated spectrum using two unique Al(III) sites each for the DMSO modified and unmodified fractions in the material. A close up of the central peak is shown as an inset. The chemical shift value and quadrupolar parameters of the each site are summarized in Table 13.

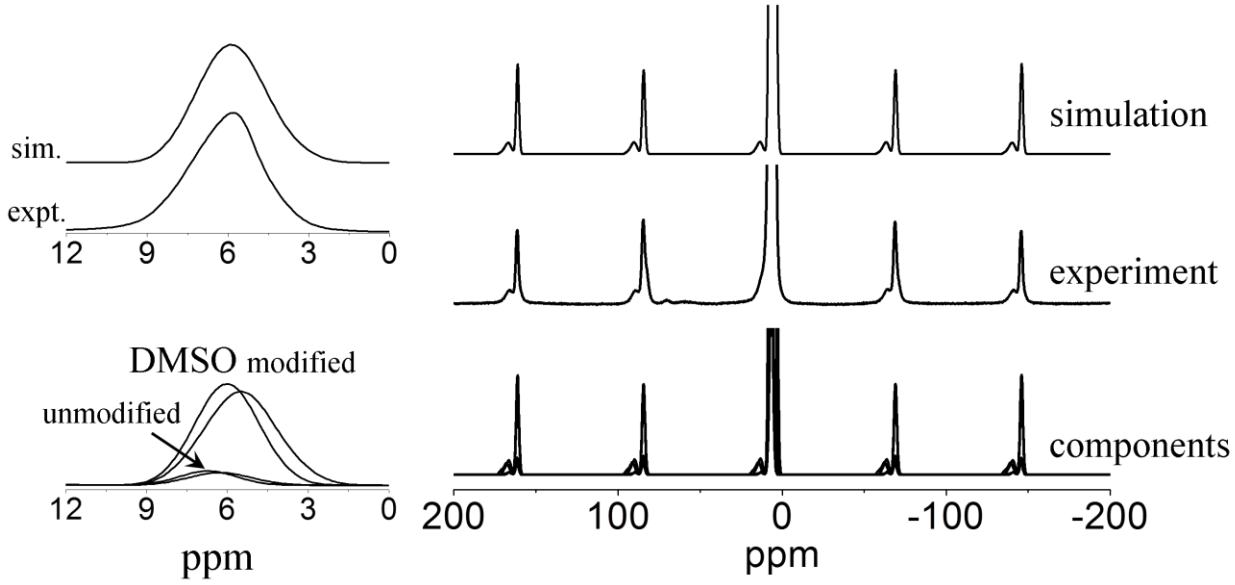

Figure 43: ^{27}Al MAS NMR spectra of kDMSO at 21.1T fitted to a simulated spectrum using two unique Al(III) sites each for the DMSO modified and unmodified fractions in the material. A close up of the central peak and its components are shown as insets. The chemical shift value and quadrupolar parameters of the each site are summarized in Table 13.

Table 13: ^{27}Al MAS NMR parameters of kDMSO identified from fitting the 4.7T and 21.1T experimental spectra in Figure 42 and Figure 43.

	$\delta_{iso\ (ppm)}$	$C_{Q\ (MHz)}$	η_Q	Rel. abundance
site 1, 11.2Å fraction	7.5	3.5	0.67	0.44
site 2, 11.2Å fraction	7.4	3.9	0.70	0.45
site 1, 7.2Å fraction	7.8	2.9	0.92	0.06
site 2, 7.2Å fraction	7.7	3.4	0.78	0.05

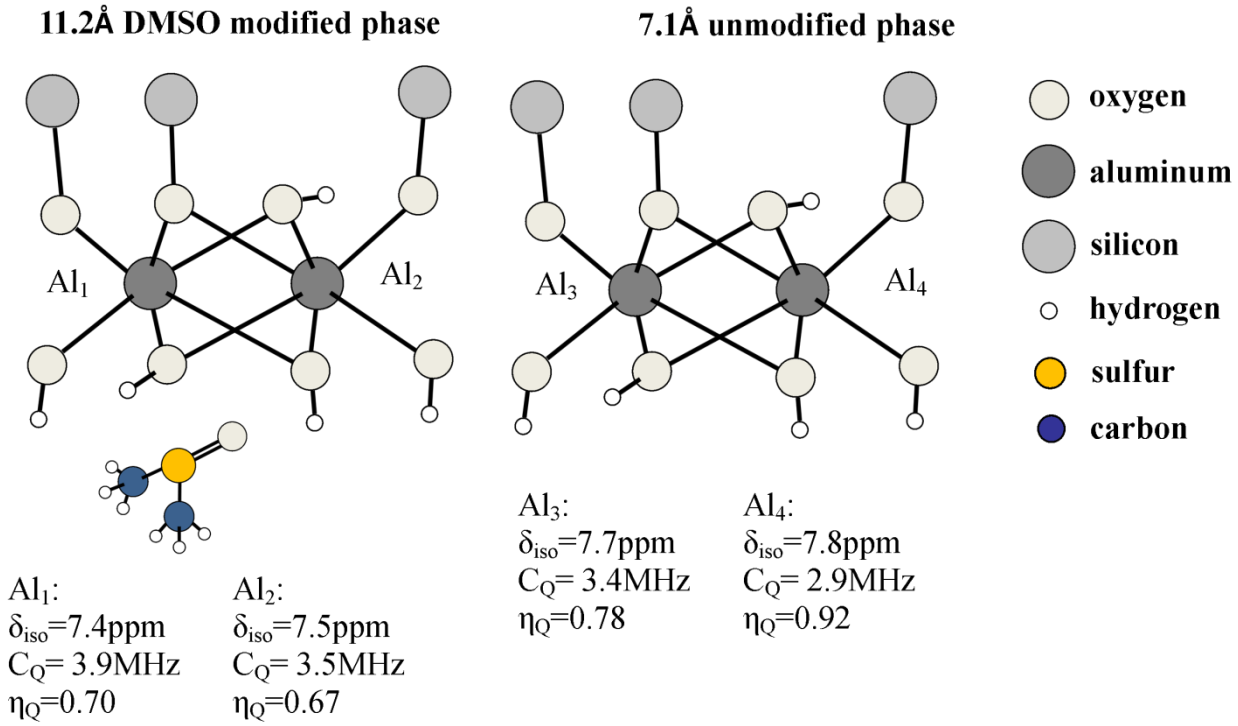

Figure 44: Summary of the different ^{27}Al NMR sites identified for kDMSO. This schematic uses the parameters identified for the four site model.

2.3.4.5 Kmethoxy, three site model

This model assumes that the 8.6Å fraction identified in XRD (see chapter 5) results in one additional Al(III) site compared to kGa-1b, giving three sites total. Taking into account the 12% fraction of unmodified clay mineral identified in XRD, this gives abundance ratios of 0.88:0.06:0.06. The best fit to the 4.7T spectrum was found using a C_Q value of 3.01MHz, a η_Q of 0.5, and a δ_{iso} value of 7.8ppm. A summary of this fit is shown in Figure 45 and Table 14.

This model however doesn't give a good fit to the experimental spectrum. Similarly to kDMSO, the model poorly accounts for the central peak's broadness at lower chemical shift values. Additionally, its broadness at higher chemical shift values is also not well accounted for.

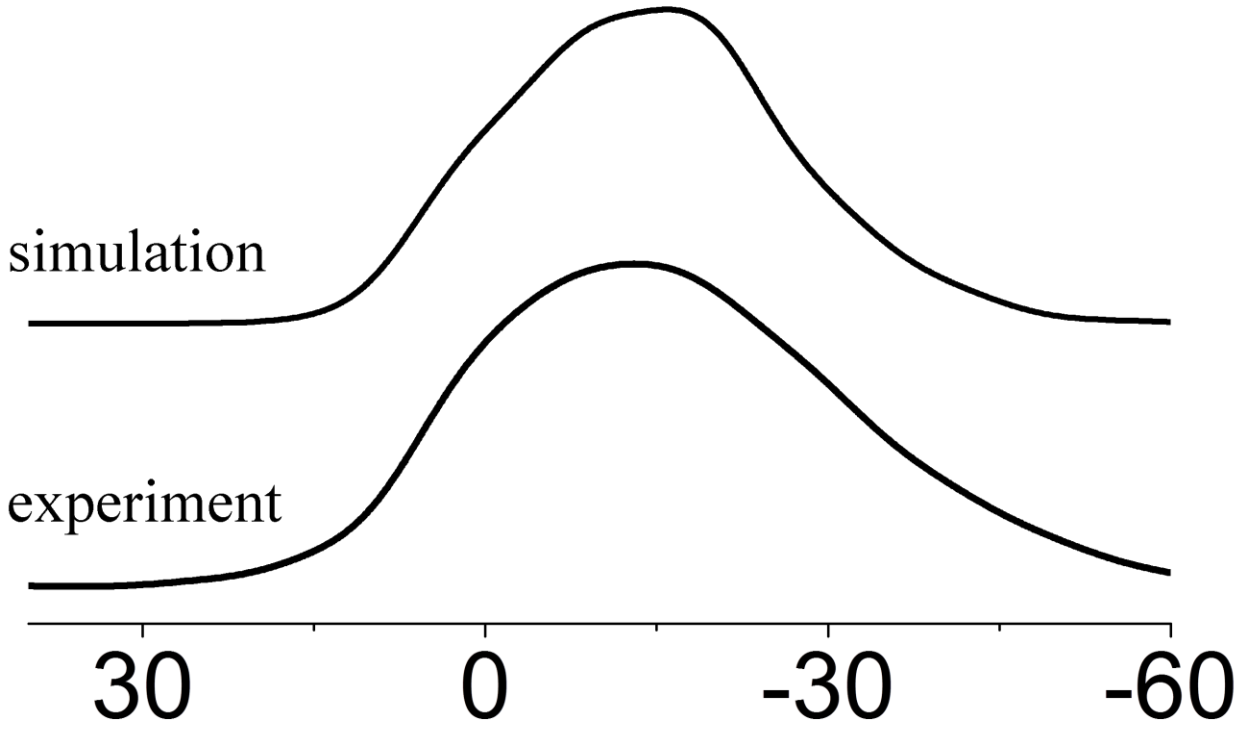

Figure 45: ^{27}Al MAS NMR spectra of kmethoxy at 4.7T fitted to a simulated spectrum using one unique Al(III) site for the methoxy modified fraction and two sites for the unmodified fraction in the material. The chemical shift value and quadrupolar parameters of the each site are summarized in Table 14.

Table 14: ^{27}Al MAS NMR parameters of kmethoxy identified from fitting the 4.7T experimental spectra in Figure 45.

	$\delta_{iso\ (ppm)}$	$C_{Q\ (MHz)}$	η_Q	Rel. abundance
8.6Å fraction	7.8	3.0	0.54	0.88
site 1, 7.2Å fraction	7.8	2.9	0.92	0.06
site 2, 7.2Å fraction	7.7	3.4	0.78	0.06

2.3.4.6 Kmethoxy, six site model

This is a refinement to the three site model, where the 8.6Å fraction will have four unique Al(III) sites where two of these sites are from aluminum sites affected by grafted methoxy groups, and two others are from those unaffected. This gives six sites total. From the structure $Al_2Si_2O_5(OH)_{3.44}(OCH_3)_{0.56}$ $[NMF]_{0.09}$ $[H_2O]_{0.35}$ calculated from a combination of XRD, TGA, and %CHNS (see chapter 5), there are 0.28 units of OCH_3 grafted on average per unit of aluminum. This gives an abundance of grafted to non-grafted aluminums of 0.28:0.72 in the 8.6Å fraction. Assuming grafted and non-grafted Al will give two different sites and accounting for the 12% fraction of unmodified clay mineral identified in XRD (see chapter 5), this gives six sites with an abundance ratio of 0.12:0.12:0.32:0.32:0.06:0.06. A best fit to the 4.7T spectrum was found using sites with values of C_Q that were 0.6MHz lower and 0.3MHz greater than those in the unmodified clay mineral, which are attributed to ungrafted and grafted aluminums sites in the 8.6Å fraction. Fitting this model to the experimental spectrum at 21.1T found no additional refinement of the δ_{iso} values was needed. A summary of this fit is shown in Figure 46, Figure 47 and

Table 15, and the results are represented schematically in Figure 48.

This refined model accounts for both the significant tailing of the central peak at lower chemical shift values and the broadened signal at higher chemical shifts. The tailing of the central peak at lower frequency still appears segmented, and the summit of this peak also appears a bit too wide, but otherwise this model offers a significant improvement to the basic three site model.

These results suggest that two sets of aluminum species are present in the 8.6Å fraction of kmethoxy, where one of these is aluminum that is modified by grafted methoxy groups and the other where it is not. The aluminum species with the lower C_Q values are attributed to the aluminums that are not modified by covalently grafted methoxy groups. Intercalated polar compounds such as water, ungrafted methanol and residual NMF could produce an effect on kaolinite's AlOH groups that is similar to what observed for DMSO, resulting in a distortion of Al-O octahedron and greater values of C_Q. The aluminum species with the lower C_Q values are attributed to the aluminums affected by covalently grafted methoxy groups. This effect of replacing an OH with an -OCH_3 group is expected to be quite different from the effect of intercalating polar molecules such as DMSO. Grafting an --OCH_3 group would significantly reduce its interaction with both Si-O groups in an adjacent silicon sheet and any matter in the interlayer space. In the absence of these interactions, the Al-O groups are hypothesized to adopt a conformation that is closer to an ideal octahedral geometry, resulting in a lower value of C_Q.

These ^{27}Al parameters are quite different to those identified by Hirsemann (Hirsemann, 2011) for ethylene glycol grafted kaolinite. They found one site with a δ_{iso} of 6.7ppm, a C_Q of 3.3MHz and a η_Q of 0.64, and a second site with a δ_{iso} of 3.7ppm, a C_Q of 4.4MHz, and η_Q of 0.76. These sites were attributed to aluminum species unaffected and affected by grafted ethylene glycol respectively. The fact that the authors found aluminums sites with different values of δ_{iso}, while this study did not, could possibly be the result of differences in the interlayer structure of grafted ethylene glycol and grafted methanol. This could possibly be because of the different molecular dimensions of these compounds, and future work should investigate this effect.

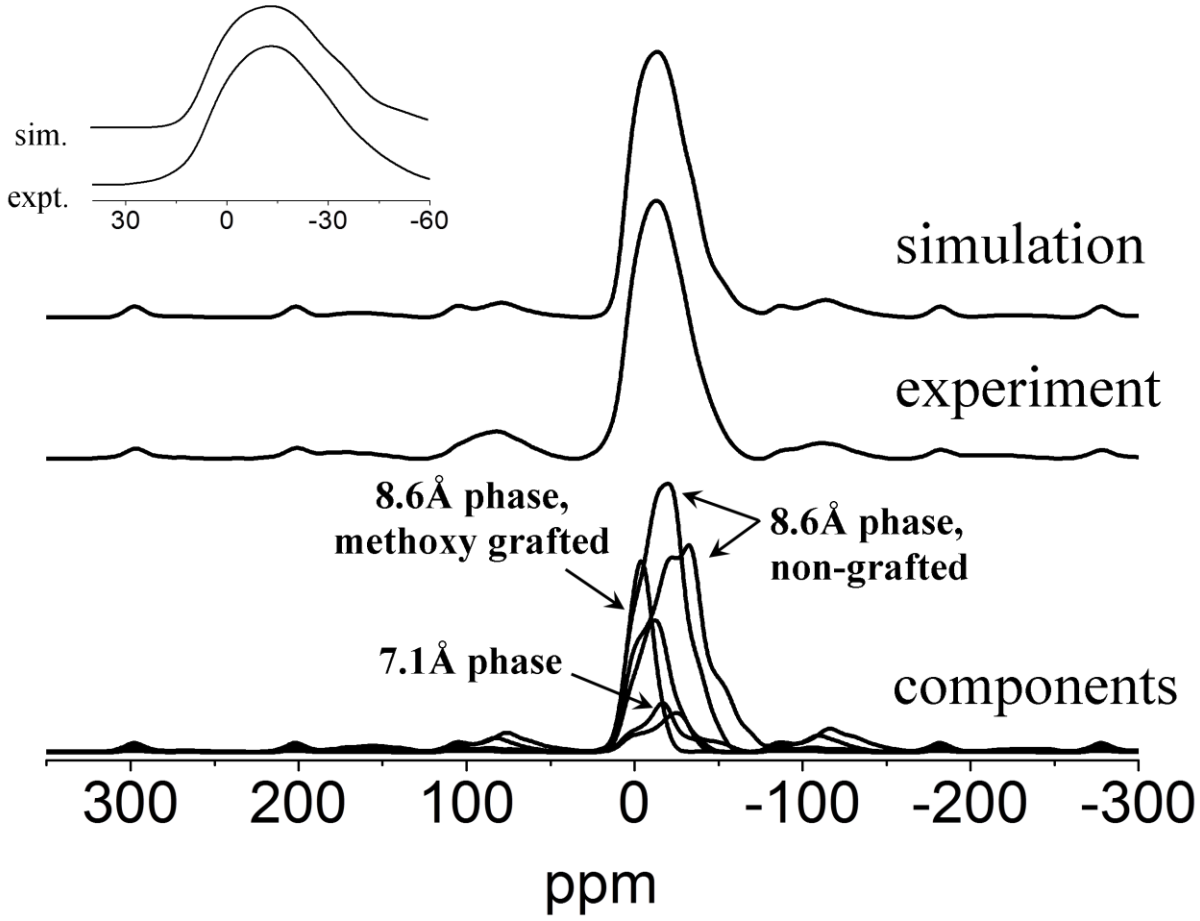

Figure 46: ^{27}Al MAS NMR spectra of kmethoxy at 4.7T fitted to a simulated spectrum using four unique Al(III) sites for the methoxy modified and two sites for the unmodified fraction in the material. A close up of the central peak is shown as an inset. The chemical shift value and quadrupolar parameters of the each site are summarized in

Table 15.

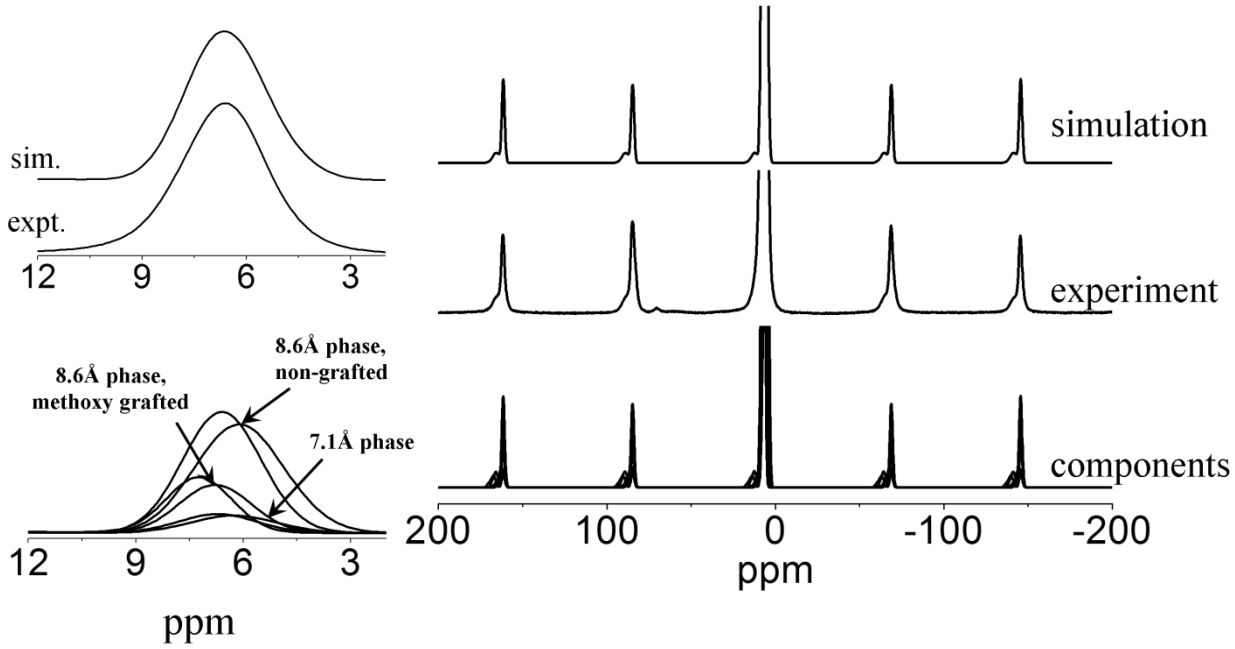

Figure 47: ^{27}Al MAS NMR spectra of kmethoxy at 21.1T fitted to a simulated spectrum using four unique Al(III) sites for the methoxy modified and two sites for the unmodified fraction in the material. A close up of the central peak and its components are shown as insets. The chemical shift value and quadrupolar parameters of the each site are summarized in Table 15.

Table 15: ^{27}Al MAS NMR parameters of kmethoxy identified from fitting the 4.7T experimental spectra in Figure 46.

	$\delta_{iso\ (ppm)}$	$C_{Q\ (MHz)}$	η_Q	Rel. abundance
site 1, 8.6Å phase	7.8	3.2	0.60	0.32
site 2, 8.6Å phase	7.7	3.7	0.60	0.33
site 1, 8.6Å grafted phase	7.8	2.2	0.64	0.13
site 2, 8.6Å grafted phase	7.7	2.8	0.64	0.12
site 1, 7.1Å phase	7.8	2.9	0.92	0.05
site 2, 7.1Å phase	7.7	3.4	0.78	0.05

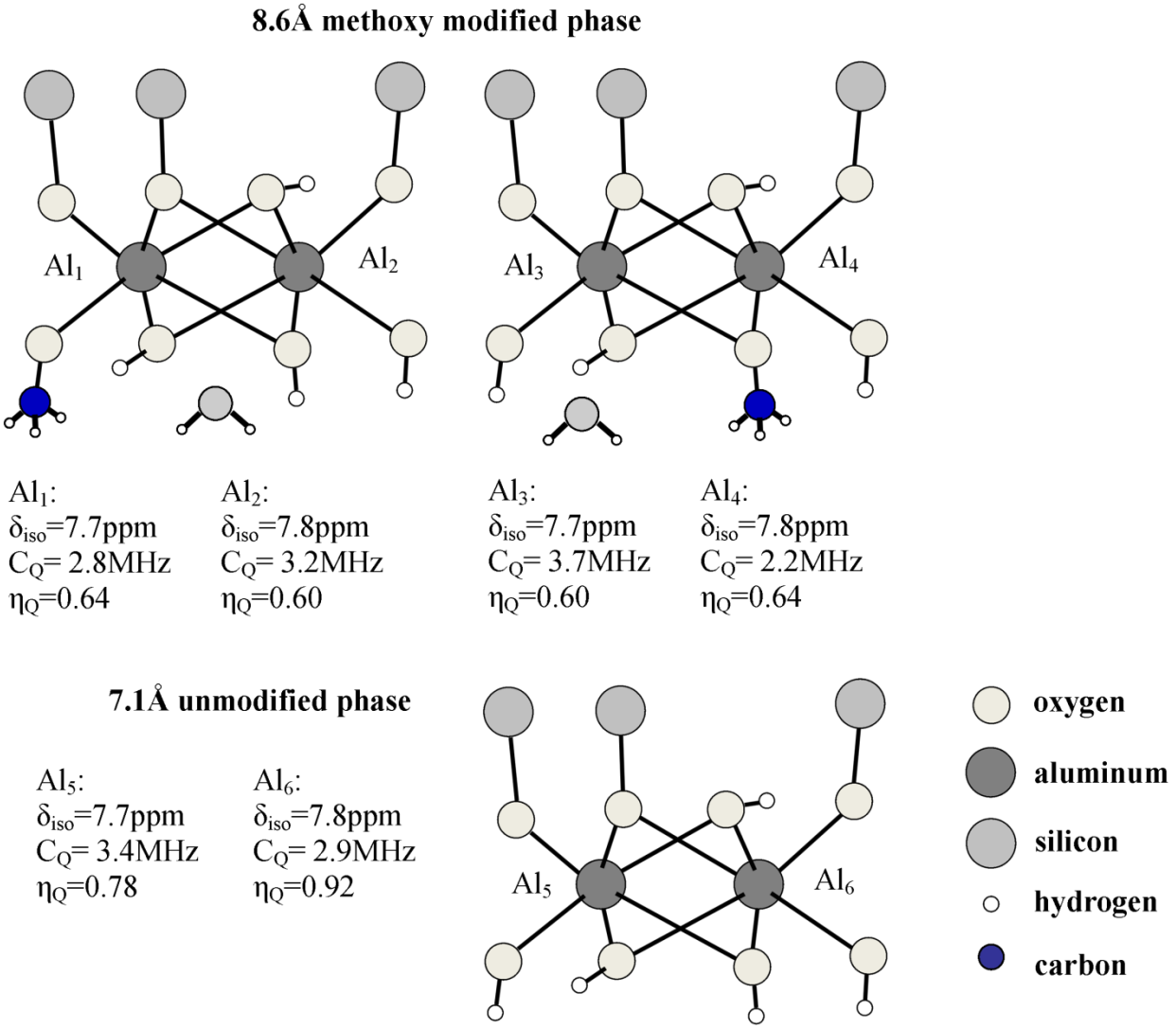

Figure 48: Summary of the different ^{27}Al sites identified for kmethoxy. This schematic uses the parameters identified for the six site model.

2.3.4.7 kmethoxy(ht), six site model

This model is the same as the six site model used to fit kmethoxy's experimental spectra. From the structure $Al_2Si_2O_5(OH)_{3.13}(OCH_3)_{0.87}$ $[H_2O]_{0.25}$ calculated from a combination of XRD, TGA, and %CHNS (see chapter 5), it was determined that there are 0.44 units of OCH_3 grafted on average per unit of aluminum. Assuming that the grafted methoxy groups result in a different species of Al(III) in ^{27}Al NMR, the abundance of grafted to un-grafted aluminum is 0.44:0.56 in the 8.4Å fraction. Assuming both grafted and non-grafted sites will have two different sites each, accounting for the 12% fraction of unmodified kaolinite identified in XRD, this gives 6 sites with an abundance ratio of 0.19:0.19:0.25:0.25:0.06:0.06. A best fit to the 4.7T spectrum was found using a set of sites with values of C_Q that were about 0.60MHz lower than their counterparts in the unmodified clay mineral and a set with values of C_Q that was 0.40MHz greater, attributed to ungrafted and grafted aluminum sites in the material. Fitting this model to the experimental spectrum measured at 21.1T found no refinement of δ_{iso} values was necessary. A summary of this fit is shown in Figure 49, Figure 50, and Table 16, and it is shown schematically in Figure 51.

This model has similar drawbacks to kmethoxy when fitted to the experimental spectrum such as the summits of the central peak being a bit too wide and the tailing of this same peak at lower frequencies appearing segmented. The shape of the two summits of this peak, however, is close to the experimental spectrum and the values of C_Q and η_Q identified were fairly close to those found from fitting the spectrum of kmethoxy, suggesting this six site model is an accurate

representation of both these materials. The accuracy of the fits for these two methanol grafted kaolinites that have different quantities of grafted material also suggests that the hypothesis that grafted aluminum species experience smaller quadrupolar effects is valid.

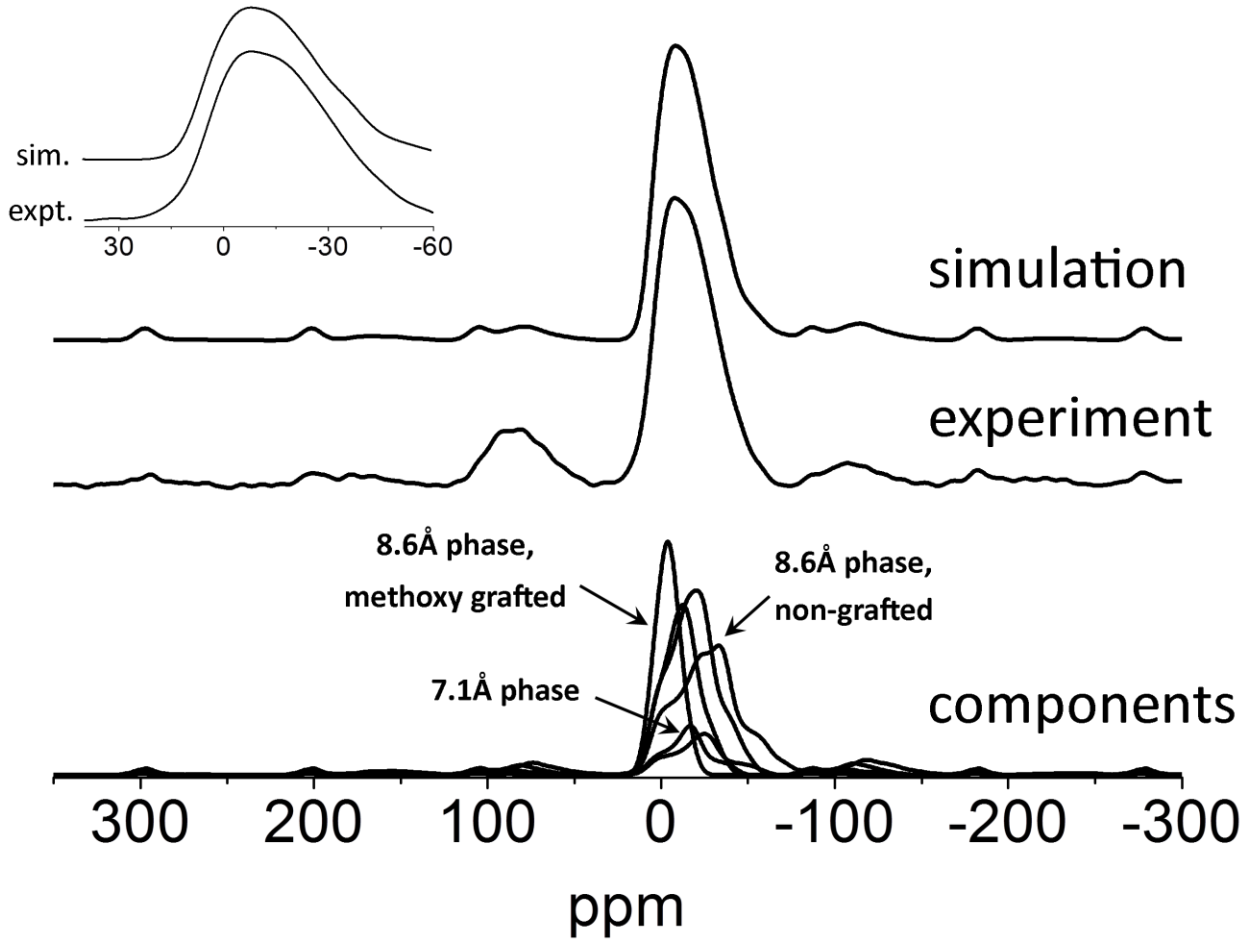

Figure 49: ^{27}Al MAS NMR spectra of kmethoxy(ht) at 4.7T fitted to a simulated spectrum using four unique aluminum sites each for the methoxy modified and two sites for the unmodified fraction in the material. A close up of the central peak is shown as an inset. The chemical shift value and quadrupolar parameters of the each site are summarized in Table 16.

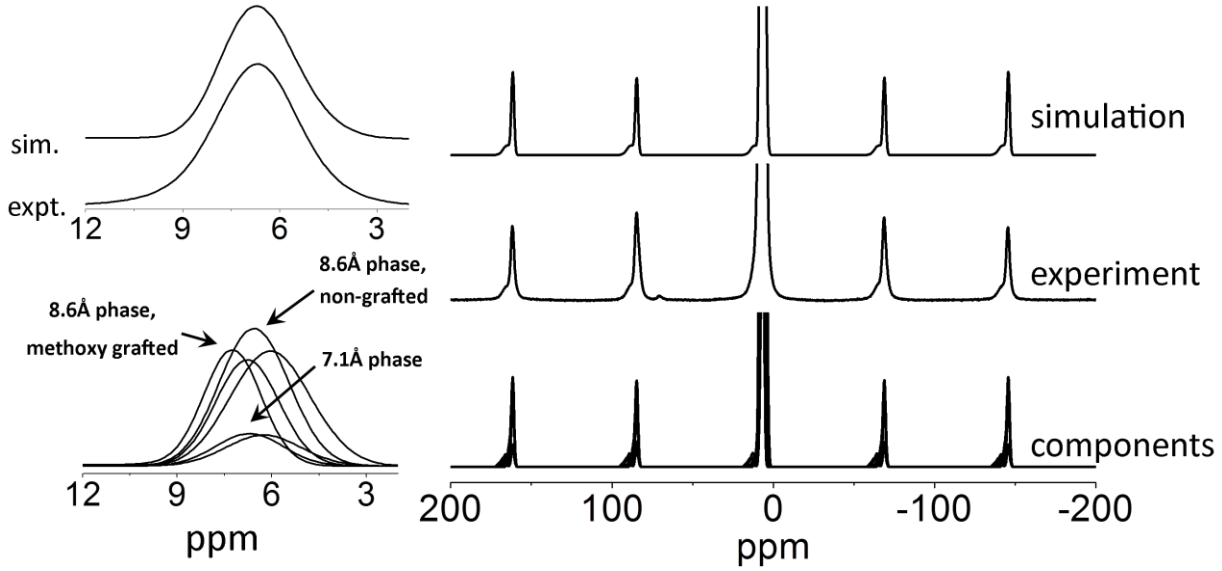

Figure 50: ^{27}Al MAS NMR spectra of kmethoxy(ht) at 21.1T fitted to a simulated spectrum using four unique Al(III) sites for the methoxy modified and two sites for the unmodified fraction in the material. A close up of the central peak and its components are shown as insets. The chemical shift value and quadrupolar parameters of the each site are summarized in Table 15.

Table 16: ^{27}Al MAS NMR parameters of kmethoxy(ht) identified from fitting the 4.7T experimental spectra in Figure 49.

	$\delta_{iso\ (ppm)}$	$C_{Q\ (MHz)}$	η_Q	Rel. abundance
site 1, 8.4Å phase	7.8	3.24	0.64	0.26
site 2, 8.4Å phase	7.7	3.74	0.64	0.25
site 1, 8.4Å grafted phase	7.8	2.16	0.67	0.18
site 2, 8.4Å grafted phase	7.7	2.79	0.67	0.18
site 1, 7.1Å phase	7.8	2.88	0.92	0.06
site 2, 7.1Å phase	7.7	3.39	0.78	0.06

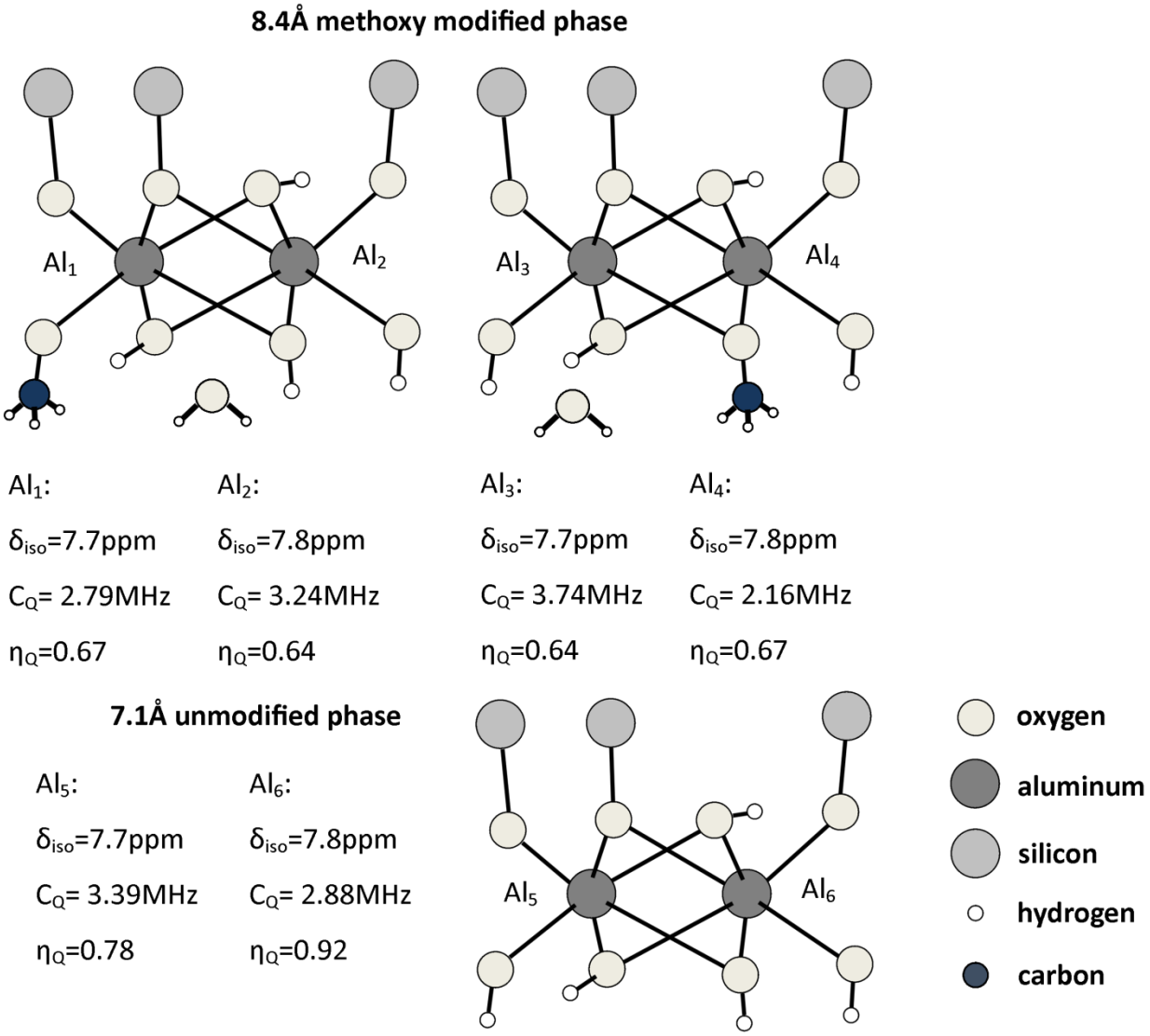

Figure 51: Summary of the different ^{27}Al sites identified for kmethoxy(ht). This schematic uses the parameters identified for the six site model.

2.3.5 ^{27}Al MQMAS NMR results & discussion

The MQMAS spectra of kGa-1b, kDMSO, kmethoxy, and kmethoxy(ht) shown in Figure 52 suggests that the differences in the ^{27}Al MAS NMR spectra for each was not a result of differences in their δ_{iso} values. At 21.1T, some shifts consistent with the materials' 1D spectra could be observed, but multiple sites could not be resolved in any of them. Similar observations were made for the spectra at 4.7T. The MQMAS experiment averages out the secondary quadrupolar interaction (Amoureux and Pruski, 2007), which can allow sites with values of δ_{iso} that are very similar but not identical that are being masked by this quadrupolar effect to be resolved. This was not the case, which supports the hypothesis that the differences between the aluminum sites in these kaolinite samples are a result of different quadrupolar parameters rather than different δ_{iso}.

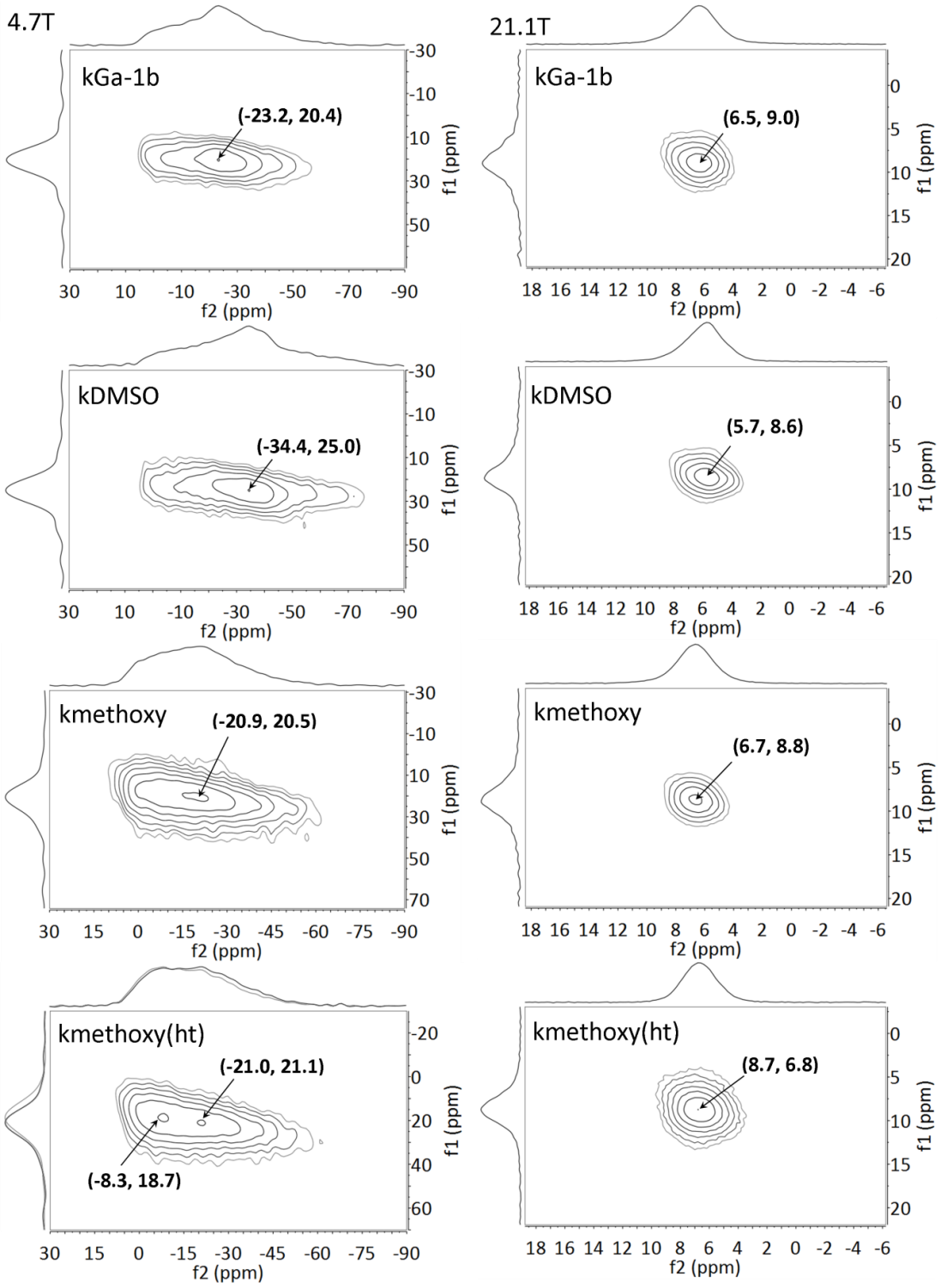

Figure 52: ^{27}Al 3QMAS NMR spectra of kGa-1b, kDMSO, kmethoxy, and kmethoxy(ht) obtained at 4.7T and 21.1T. 1D slices are shown using the coordinates highlighted.

2.3.6 Summary and conclusions

^{27}Al MAS NMR spectra of kGa-1b, kDMSO, kmethoxy and kmethoxy(ht) were measured at 21.1 T and 4.7 T. Predominantly octahedral aluminum sites were identified, with small amounts of tetrahedral aluminum due to aluminum substitution in the tetrahedral sheet of the clay mineral. No noticeable difference was observed when comparing spectra of low and high defect kaolinites kGa-1b and kGa-2.

Very little differences between the samples were observed at high field, but very noticeable changes were seen at low field which were attributed to different sites with very similar δ_{iso} values, but different quadrupolar parameters C_Q and η_Q. This hypothesis was supported by MQMAS experiments failing to resolve multiple aluminum sites in all the kaolinites studied.

The deuterium exchanged counterparts of kmethoxy and kDMSO gave spectra very similar to kGa-1b which suggests the differences observed between the modified and unmodified clay mineral are a result of interlayer material and that these effects are reversible upon removal of the interlayer material.

Simulation of the ^{27}Al MAS NMR spectra of kGa-1b identified two Al(III) sites with δ_{iso} values that differ by 0.1ppm and C_Q values that differ by 0.50MHz, attributed to distortions of the

octahedral sheet as a result of the layer distortion caused by lateral mismatch of the octahedral and tetrahedral sheets. In kDMSO, the aluminum species modified by interlayer DMSO resulted in an increase in their values of C_Q by about 0.6MHz and a decrease in their values of δ_{iso} values by about 0.3ppm. In kmethoxy, two sets of Al(III) sites were identified: one set with values of C_Q 0.6MHz lower than in the unmodified clay mineral and one where they are 0.3MHz higher attributed to non-grafted and grafted sites respectively. No change in the δ_{iso} values for these sites compared to those in kGa-1b was observed.

These shifts in C_Q for the modified kaolinites are believed to be a result of distortion of aluminum octahedra as a result of interaction with the interlayer material. For polar, H-bond acceptor intercalates such as DMSO that interact strongly with AlOH groups, it will result in higher values of C_Q. This effect that intercalates have on the C_Q of kaolinite's aluminum groups could be investigated for different intercalates such as NMF, urea and hydrazine to see if a trend can be observed. In covalently grafted kaolinites, the sites with grafted organic material experience less interaction with SiO groups on adjacent sheets in the clay mineral resulting in a lower C_Q value for the aluminums. The non-grafted aluminums, however, will experience a slight distortion to accommodate the grafted methoxy groups and an interaction with polar interlayer materials such as water and ungrafted methanol, resulting in a greater C_Q value. This effect was not observed in ^{27}Al NMR studies of ethylene glycol grafted kaolinites (Hirsemann *et al.*, 2011), which could possibly be due to the size differences between ethylene glycol and methanol. Additional work could be done to validate hypothesis, by investigating ^{27}Al spectra of

kaolinites grafted with with longer chained counterparts to ethylene glycol such as propanediols and butanediols. The effects that the quantity of grafted material have on the resulting spectrum could also be investigated.

These experiments also highlight the advantages of working at low magnetic field strength for identifying aluminum sites that have similar δ_{iso} values but different quadrupolar parameters. The sensitivity of the quadrupolar parameters to chemical environment of the kaolinite's interlayer combined with the isotopic abundance of the ^{27}Al aluminum nucleus and the relative low cost of low field NMR spectrometers make this a possible candidate for studying interlayer modification of kaolinites, especially in cases when X-ray diffraction methods give inconclusive results such as in delaminated or exfoliated structures.

3 New kaolinite polymer:clay nanocomposites formed by melt intercalation

3.1 Kaolinite functionalized with ethylene glycol based block-copolymers

3.1.1 Introduction

Poly(ethylene glycol) (PEG) is a versatile polyether with a wide range of applications. While the bulk of its use is in medicine as an excipient and drug delivery vessel for pharmaceutical products (Knop *et al.*, 2010) and as a laxative, it is also an important industrial polymer with applications as a surfactant, as a hydraulic fluid, as a lubricant, as a thickener, as a dispersant and as a moisturizer (Roff *et al.*, 1971; Stevens, 1999; Houssamy, 2002). It is also routinely used for the preservation and water proofing of wood materials (Håfors, 1990). PEG is also a very important compound in biomedical research. In addition to being very useful for separation and partitioning of biological material in aqueous media (Albertsson, 1970), it also greatly affects the biological properties of surfaces it is attached to. The latter is especially important since a PEGylated protein (i.e. a protein that has PEG covalently bonded to its surfaces) is rendered non-immunogenic and non-antigenic with minimal loss of activity of the protein, opening the way for intravenous treatments using proteins without provoking an immune response (Abuchowski *et al.*, 1977; Harris, 1992) .

Similar to simple glycols like ethylene glycol, propanediol and butanediol, PEG is highly compatible with kaolinite and was one of the first polymers to be intercalated inside its

interlayer space (Tunney and Detellier, 1996a). To this day, it remains one of the few known polymers that can be intercalated in kaolinite. These intercalated complexes of PEG and kaolinite were achieved using homopolymers of PEG, and examples using copolymers functionalities have yet to be demonstrated.

Copolymers are interesting because they allow much more control of the properties of the final material than in the case of a homopolymer by combining different functionalities with different properties. PEGs are common components of many copolymer functionalities. For example, poly(oxyethylene) glycol alkyl ethers, such as the non-ionic BRIJ surfactants, combine an ethylene glycol polymer and an n-alkyl polymer/oligomer in segmented blocks to obtain the desired surfactant properties. Similarly to the aforementioned BRIJ, poly(ethylene)-block-poly (ethylene glycol) polymers are cheap, abundant, and relatively stable polymers that melt at moderate temperatures (i.e. below 200°C). This makes them ideal candidates for melt intercalation reactions. Intercalated complexes of these compounds would be expected to have much more hydrophobic properties than the natural clay mineral due the incorporation of long alkyl chains in the clay mineral's interlayer. These properties could potentially be very useful for preparing adsorbent materials or delivery vessels for controlled release applications. The goal of this study is to attempt to functionalize the interlayer of kaolinite with block copolymers based on poly(ethylene glycol) and fully characterize the resulting materials.

3.1.2 Description of samples

Three commercially available poly(ethylene)-block-poly(ethylene glycol) (PEPEG) polymers (Sigma-Aldrich) were used in this study, each having a different molecular weight (M_n=575 Da, M_n=920 Da and M_n=2250 Da). The ethoxylate content of each is as follows: 16–24%(w/w) for the M_n=575 Da polymer, 45–55%(w/w) for the M_n=920 Da polymer, and 75–85%(w/w) for the M_n=2250 Da polymer. Samples of kaolinite intercalated with these PEPEG polymers were prepared in a manner similar to the one described by Tunney and Detellier (1996a), where melts of the polymer are dispersed together with a kaolinite pre-intercalated with DMSO (kDMSO). The resulting modified kaolinites are labelled according to the molecular weight of the polymer used: kPEPEG575, kPEPEG920, and kPEPEG2250. Samples of kPEPEG2250 were washed in water and calcined (kPEPEG2250(w)) in order to remove any residual DMSO prior to analysis.

Details of the experimental procedures used to prepare samples and the material characterisation results can be found in section 5.2.

3.1.3 XRD results & discussion

Powder X-ray diffraction of the prepared kPEPEG2250 in Figure 53 shows a new reflection appearing at 2θ angles of 8.03°. This would correspond to a *001* d-spacing value of 11.0Å for

the clay mineral, indicating a 0.2Å contraction compared to the *001* d-spacing of kDMSO. This contraction could be attributed to replacement of DMSO with the PEPEG polymer in the interlayer space. This would indicate that the polymer occupies a vertical space of 3.8Å in the interlayer space of the clay mineral. This is similar to the 4.0Å expansion of the interlayer space reported by Tunney and Detellier (1996a) for PEG intercalates, where the polymer adopted a flat, monolayer type arrangement. The similarity of these values suggests that the PEPEG polymer adopts a similar arrangement. Washing the material for 48hr in water and pyrolyzing it for 24h at 180°Cl(i.e.kPEPEG2250(w)), resulted in no change in the relative areas or intensity of the *001* reflections. Were the 11.0Å modified *001* d-spacing value controlled by interlayer DMSO rather than by the polymer, the interlayer space would have collapsed after washing in water. This result offers strong evidence that the polymer is present in the interlayer space of the clay mineral.

Nearly the same results were obtained using different polymer chain lengths, with kPEPEG575 and kPEPEG920 giving *001* d-spacing values of 11.1 Å and 11.0Å respectively. This is shown in Figure 54 and Table 17. This suggests that the *001* d-spacing value is independent of the polymer chain length and they all adopt a similar monolayer type arrangement in the clay mineral's interlayer space.

A schematic outlining these results is shown in Figure 55.

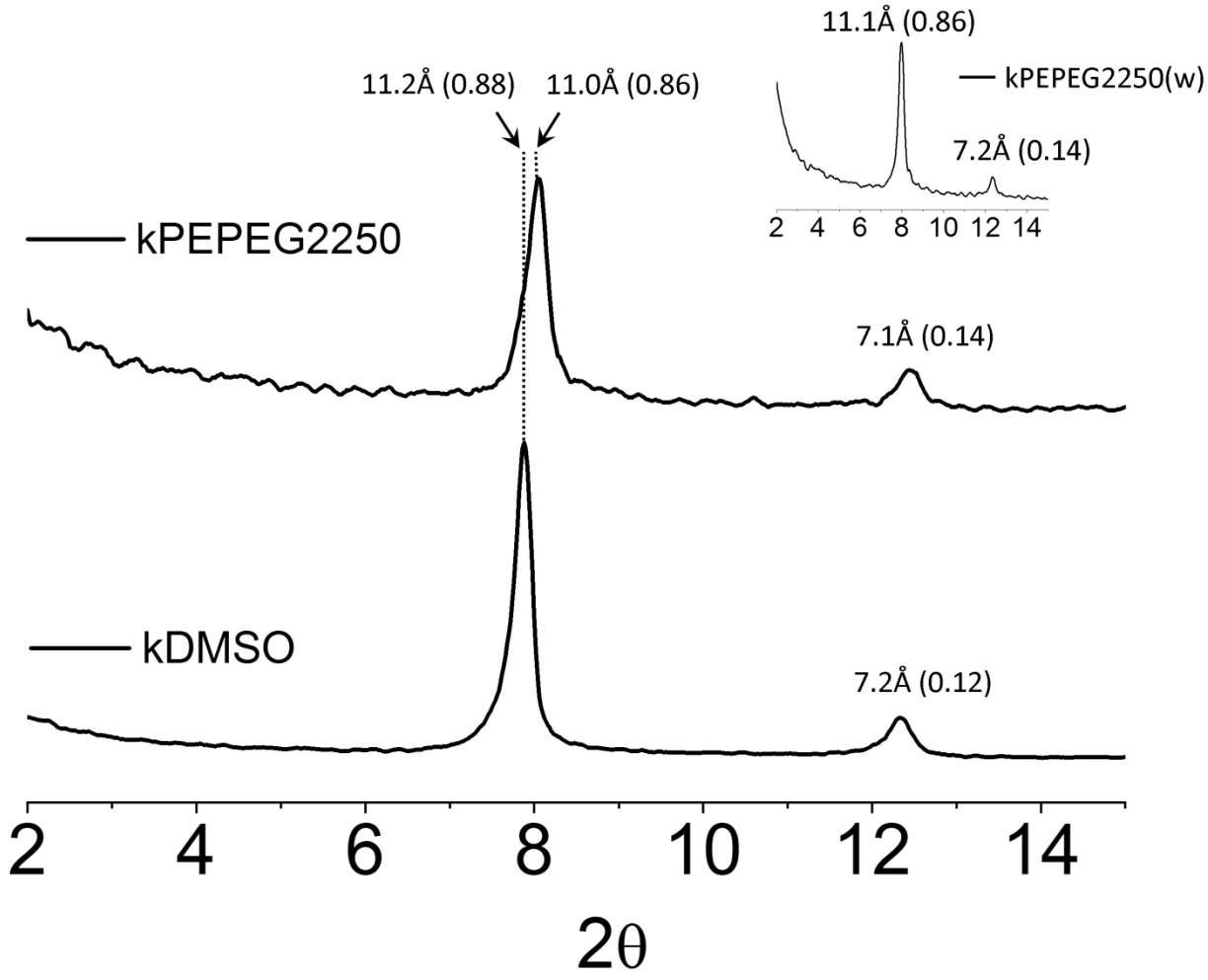

Figure 53: XRD trace and *001* d-spacing values for kPEPEG2250 compared to kDMSO. The water washed material kPEPEG2250 is shown as an inset. The abundance of each *001* reflection is shown in parentheses.

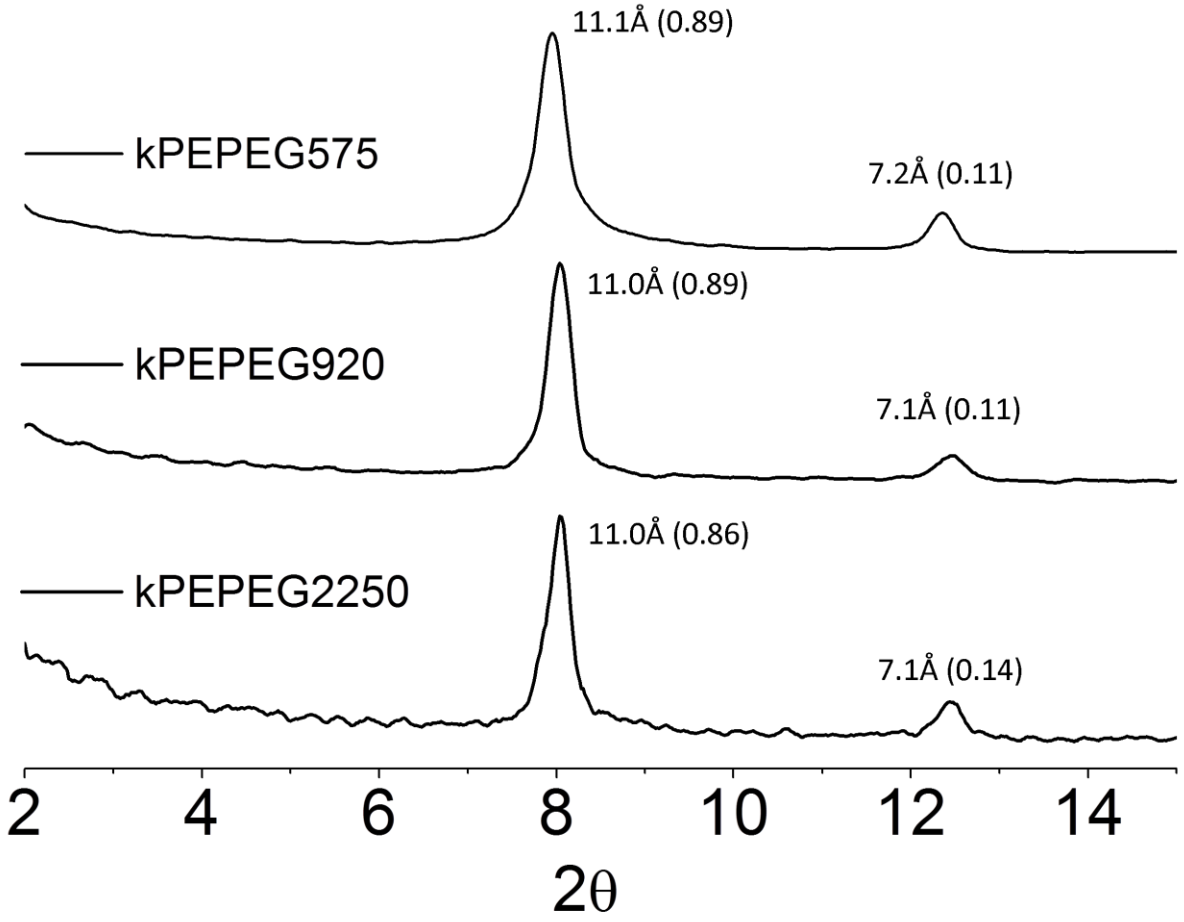

Figure 54: XRD trace and *001* d-spacing values for various kPEPEG materials. The relative abundance of each *001* reflection is shown in parentheses.

Table 17: Modified *001* d-spacing of kPEPEG materials prepared compared to kDMSO. These values are based on XRD data in Figure 54.

	modified 001 d-spacing	intercalation ratio
kDMSO	11.2	0.88
kPEPEG575	11.1	0.89
kPEPEG920	11.0	0.89
kPEPEG2250	11.0	0.86

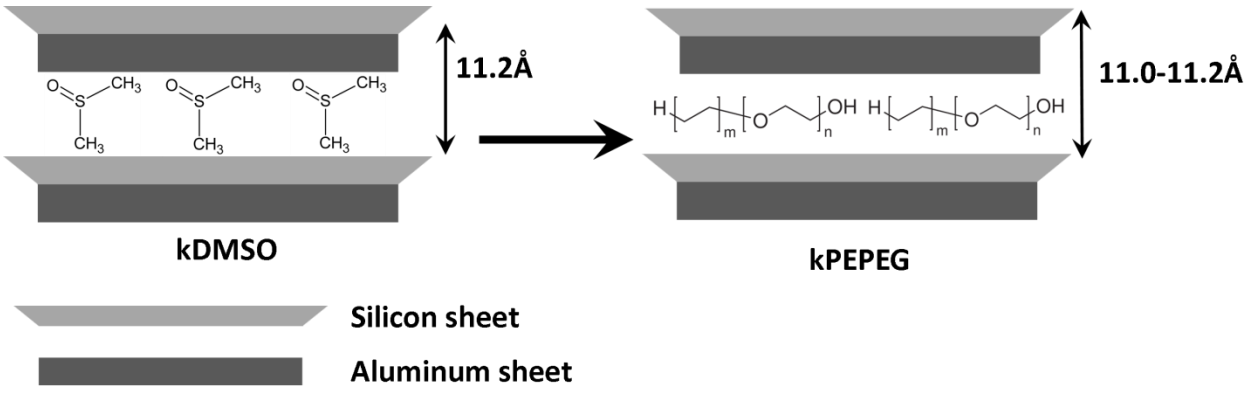

Figure 55: Side view schematic showing the interlayer space of kaolinite in the prepared kPEPEG materials.

3.1.4 TGA results & discussion

TGA analysis of kPEPEG2250 shown in Figure 56 indicates formation of a stable intercalated material. Up to 250°C, there is one major loss centered at 158.9°C corresponding to a 6.2% weight loss. This is attributed to decomposition of residual interlayer DMSO. This weight loss event is very similar to the 16.2% loss observed in kDMSO, indicating that some DMSO is still present in this material. In the water washed and pyrolyzed material kPEPEG2250(w) shown in Figure 57, this weight loss event disappears completely from the 1st derivative plot. This indicates that the washing procedure removed all but traces of DMSO from the material. Combined with the XRD results, this offers strong evidence that the PEPEG polymer is in the interlayer space of the clay mineral.

The total weight loss in the 250-600°C region amounts to 24.4%, with most of the loss attributed to decomposition of the polymeric material in the clay mineral. The complex 1st derivative curve makes it difficult to pinpoint the temperature this loss is centered at, but it is estimated to be somewhere between 357-431°C. The 1st derivative curve is mostly unchanged in this region for kPEPEG2250 and kPEPEG2250(w), which indicates the polymer remains intact in the material after the washing procedure.

The loss centered at 503.7°C is attributed to de-hydroxylation of the clay mineral. Its decomposition temperature is similar to kDMSO, with the 1st derivative maximum dropping by about 4°C. This is an indication that the Al-OH structure of the clay mineral is unchanged, and is evidence against a grafted complex being formed. If the polymer was covalently grafted to the clay mineral's surfaces, a significant drop in de-hydroxylation temperature of the clay mineral would be expected (Tunney and Detellier, 1994a; Letaief and Detellier, 2011) which isn't the case here.

A minor loss of 0.6% of the total weight was also observed in kPEPEG2250, centered at 49.1°C. This is attributed to surface adsorbed water.

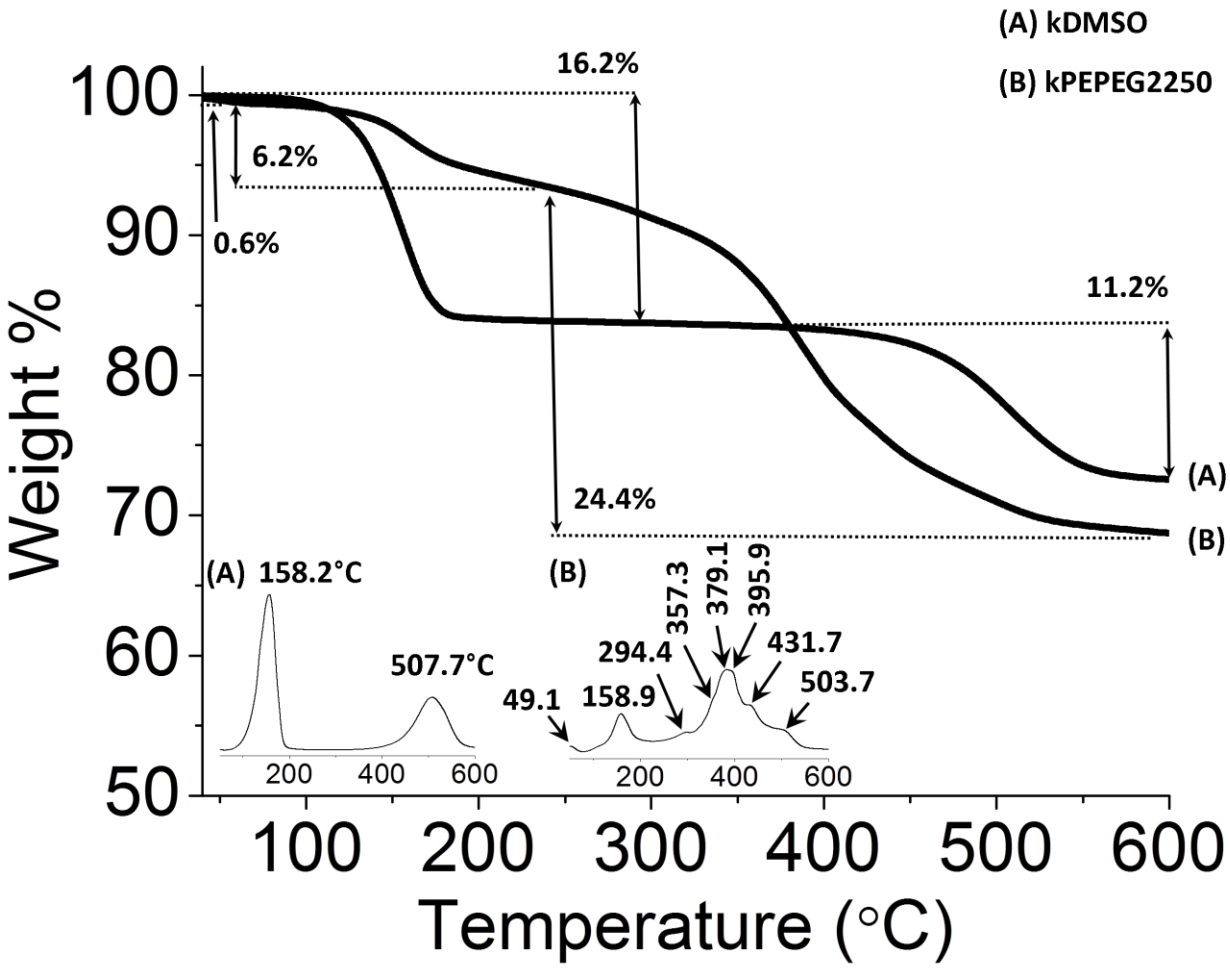

Figure 56: TGA weight loss of kPEPEG2250 compared to kDMSO. 1st derivative weight loss curves are shown as insets.

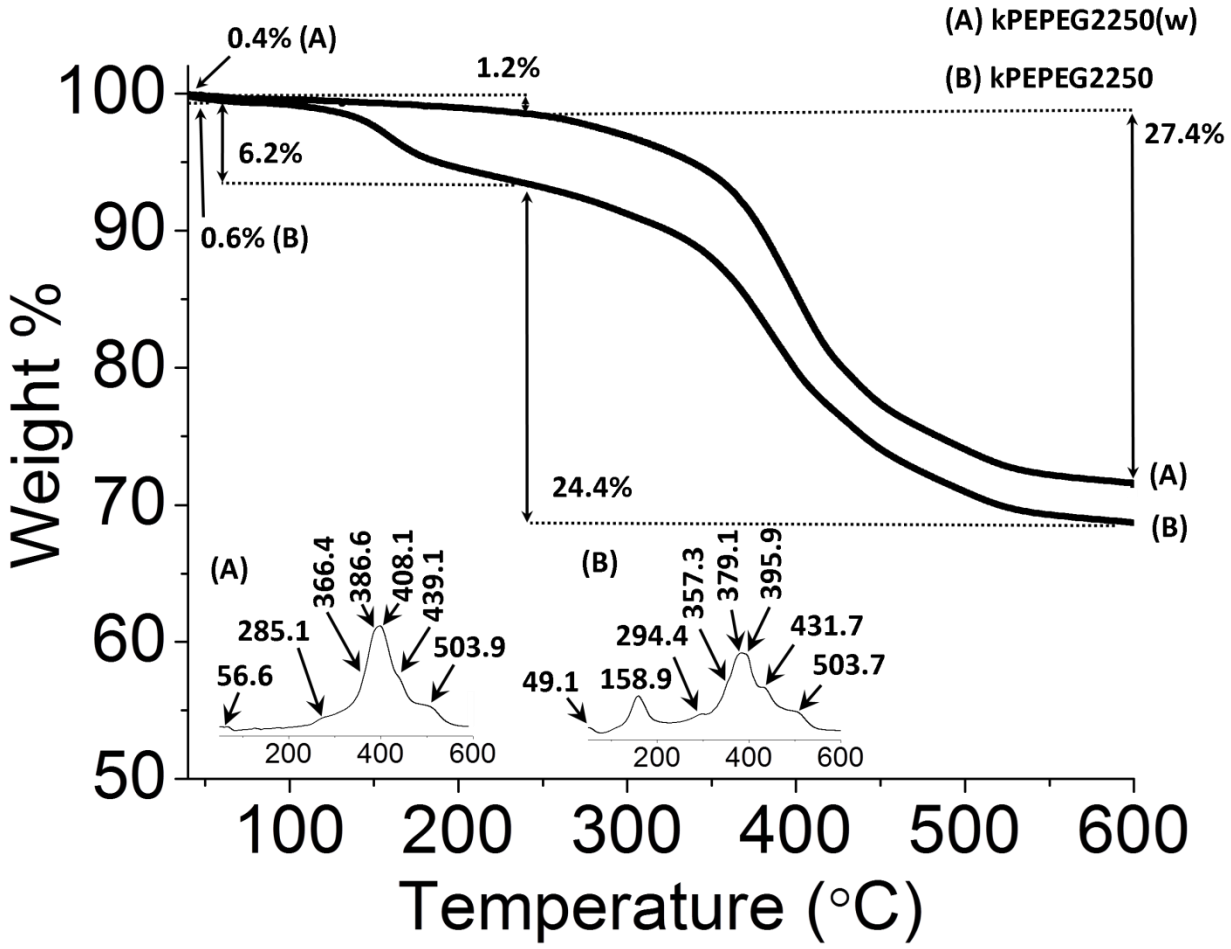

Figure 57: TGA weight loss of kPEPEG2250 the water washed material kPEPEG2250(w). 1st derivative weight loss curves are shown as insets.

3.1.5 IR results & discussion

The IR results for kPEPEG2250 shown in Figure 58, Figure 59 and Table 18 offer further evidence that the PEPEG polymer was intercalated in kaolinite. The OH stretching bands associated with DMSO interacting with the clay mineral's inner surface hydroxyl groups at 3660, 3536 and 3501cm^{-1} are no longer observed, and have been replaced with bands at 3649 and 3499cm^{-1}. These two bands are similar to those reported by Tunney and Detellier (1996a) for a PEG intercalated in kaolinite, which they attributed to the PEG's hydroxyl end groups interacting with the clay minerals inner surface hydroxyls. The presence of these bands strongly suggests the PEPEG polymer is present in the kaolinite interlayer space.

The clay mineral's OH deformation bands at 939 and 907cm^{-1} in kPEPEG2250 appear mostly unchanged compared to the unmodified clay mineral, kGa-1b. Normally a perturbation of these bands, especially the 939cm^{-1} band, would be indicative of a grafted complex. This was shown, for example, in the IR spectrum of methanol grafted kaolinite (Detellier and Tunney, 1996b). While there is likely interference in this region from PEPEG's CH deformation bands overlapping with the clay mineral's SiO stretching and OH deformation bands (Figure 60), the presence of these OH bands, the 939cm^{-1} band in particular, is evidence against a grafted complex being formed.

The weak band at 3026cm^{-1} is similar to the 3022cm^{-1} band observed in kDMSO, attributed to CH stretching modes of its methyl groups. This could also be attributed to methyl end groups in the PE block of the PEPEG polymer, however it disappears in kPEPEG(w) while the other polymer bands do not (Figure 60). This suggests it is a DMSO band, and would be in agreement with the TGA results which suggest DMSO is still present in kPEPEG2250.

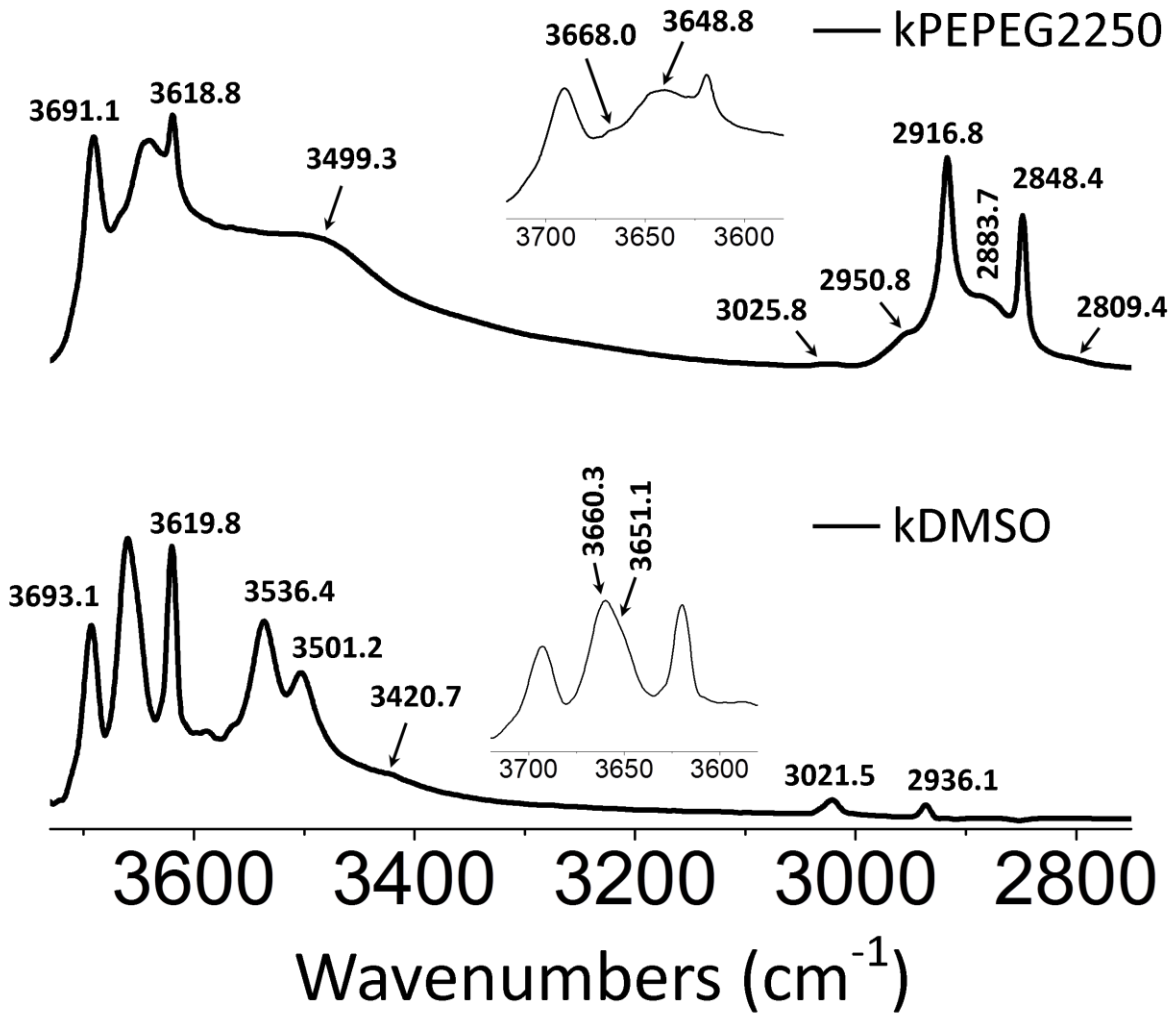

Figure 58: ATR-FTIR of the 3750-2750cm^{-1} region of kPEPEG2250 compared to kDMSO. Close ups of the 3720-3580cm^{-1} region are shown as insets.

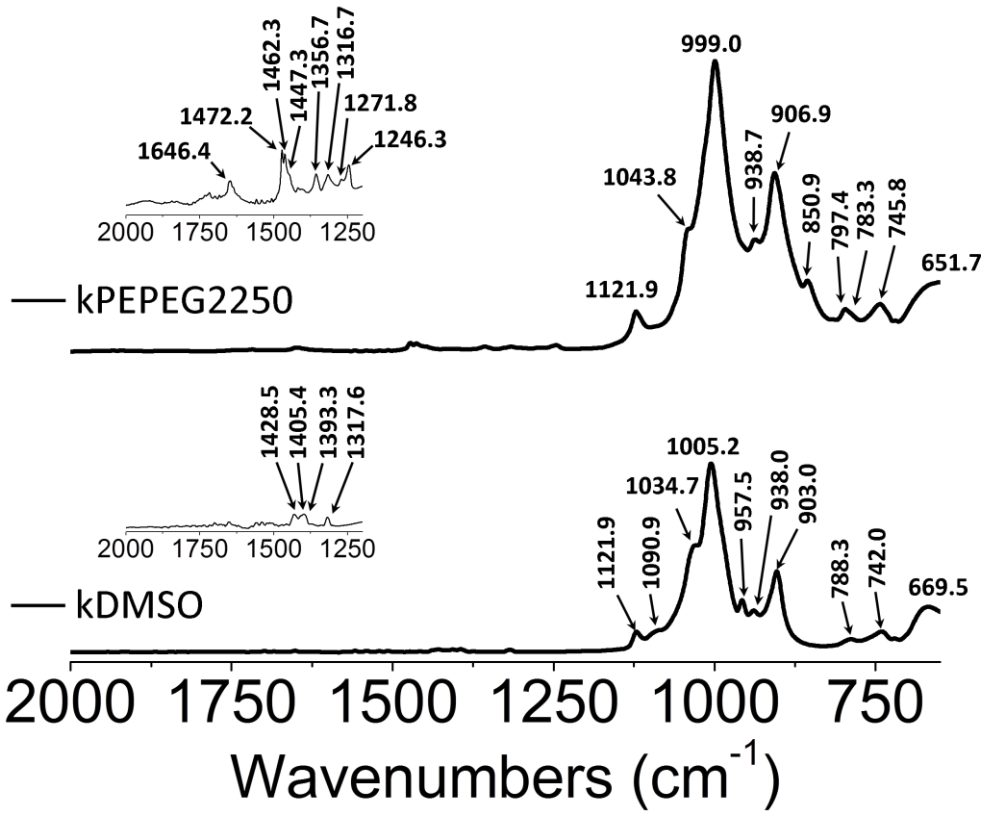

Figure 59: ATR-FTIR of the 2000-650cm^{-1} region of kPEPEG2250 region compared to kDMSO. Close ups of the 2000-1200cm^{-1} region are shown as insets.

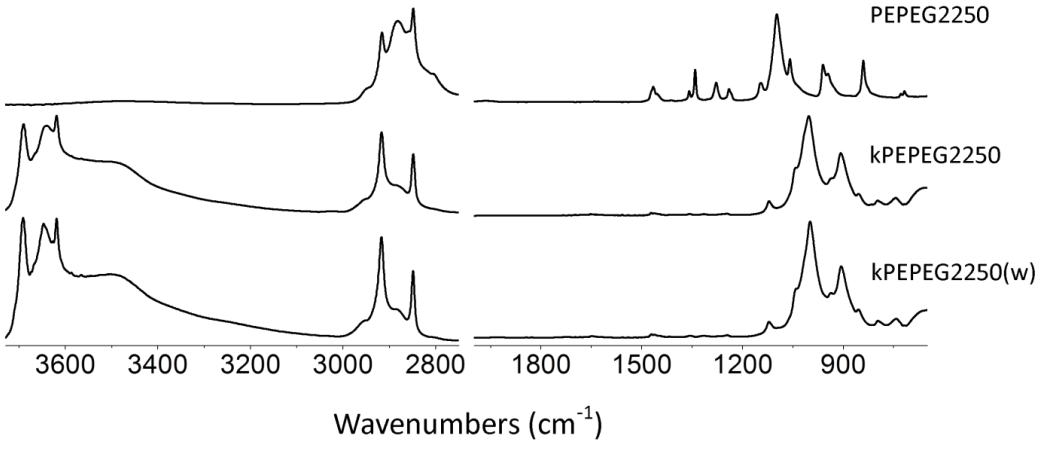

Figure 60: ATR-FTIR spectra of kPEPEG2250 comparing the neat polymer and the water washed product kPEPEG2250(w).

Table 18: Summary of IR bands identified in the spectrum of kPEPEG2250 shown in Figure 58 and Figure 59.

Frequency (cm^{-1})	Attribution
3691.1	OH stretch, Inner surface hydroxyl
3668.0	OH stretch, Inner surface hydroxyl
3648.8	OH stretch, Inner surface hydroxyl
3635.0	OH stretch, inner surface hydroxyl
3618.8	OH stretch, inner hydroxyl
3499.3	OH stretch, PEPEG and water
3025.8	CH stretch, DMSO
2950.8	CH stretch, DMSO and PEPEG
2916.8	CH stretch, PEPEG
2883.7	CH stretch, PEPEG
2848.4	CH stretch, PEPEG
2809.4	CH stretch, PEPEG
1646.4	HOH deformation, water
1472.2	HCH deformation, PEPEG
1462.3	HCH deformation, PEPEG
1447.3	HCH deformation, PEPEG
1356.7	HCH deformation, PEPEG
1316.7	HCH deformation, PEPEG
1271.8	HCH deformation, PEPEG
1246.3	HCH deformation, PEPEG
1121.9	SiO stretch and PEPEG CO ether stretch
1043.8	SiO stretch
999.0	SiO stretch
938.7	AlOH deformation
906.9	AlOH deformation
850.9	HCH deformation, PEPEG
797.4	HCH deformation, PEPEG
783.3	SiOAl deformation
745.8	SiO stretch
651.7	SiO stretch

3.1.6 ^{13}C CPMAS NMR results & discussion

The ^{13}C CPMAS NMR spectra of kPEPG2250 and kPEPEG2250(w) shown in Figure 61 are consistent with a kaolinite functionalized with the PEPEG2250 polymer. The two resonances at 44.2 and 43.1ppm characteristic of intercalated DMSO could no longer be observed, and these were replaced by a single peak at 41.0ppm. This chemical shift value agrees very well with the 40.96ppm value of solution state DMSO (SDBSweb). This could either be residual DMSO retained in the interlayer space where its methyl groups are not keyed into the siloxane ring of the clay mineral, or it could be DMSO that was displaced from the interlayer space and subsequently re-adsorbed on the surface of the material during the reaction. This peak completely disappears from the spectrum in the water washed and pyrolyzed material kPEPEG2250(w). Combined with the 11.1Å *001* d-spacing value found in XRD, this strongly suggests the PEPEG2250 polymer is present in the clay interlayer.

The PEPEG polymer peaks could also be observed and are mostly intact when compared to the neat polymer. The peak at 31.9ppm, attributed to PE CH_2 groups, remains mostly unchanged in kPEPEG2250. Other PE peaks are observed at 29.6, 23.5 and 13.8ppm, attributed to the -$CH_2CH_2CH_3$ group at the end of the PE chain. The two peaks at 71.5 and 70.1ppm in kPEPEG2250 are attributed to PEG CH_2 groups. In the neat polymer, these two are attributed to PEG CH_2O groups inside the polymer chain and at the end of the chain respectively. The ether carbon at the end of a PEG polymer chain (i.e. $OHCH_2CH_2O$-) is expected to have a slightly higher chemical shift value compared to those in the polymer backbone (Mahou and Wandrey,

2012). The small peak at 60.7ppm is attributed to the terminal hydroxyl carbon in the PEG chains. This peak was not observed in kPEPEG2250. The peaks at 71.0 and 31.9ppm were still observed in the washed and pyrolyzed material kPEPEG2250(w), however the other prominent PEG CH_2O peak at 71.5ppm could not definitely be identified. Judging by the broadness of the 70.0ppm peak it is probably still present, but in much lower intensity compared to kPEPEG2250.

A full summary of the ^{13}C peaks is shown in Table 19.

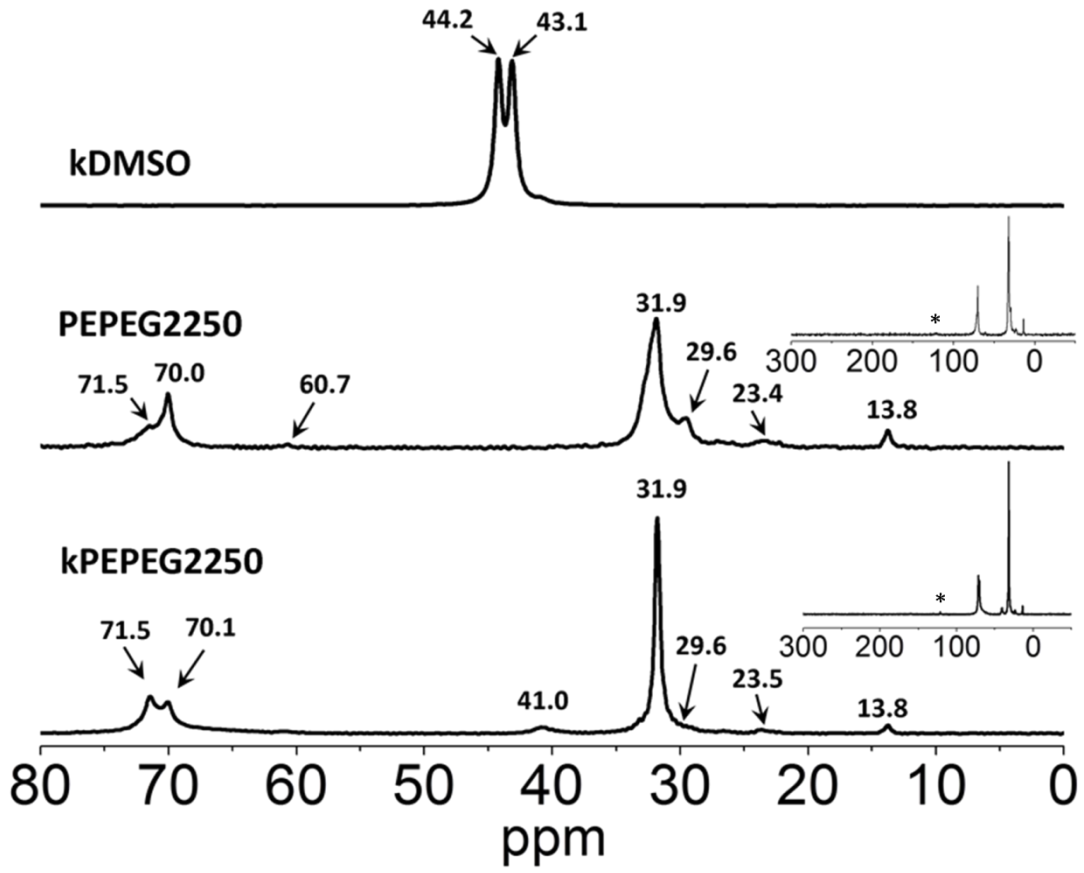

Figure 61: ^{13}C CPMAS NMR spectrum of kPEPEG2250 compared to the neat polymer PEPEG and kDMSO. Expanded scale spectra are shown as insets. Rotational artifacts resulting from MAS are denoted with an asterisk.

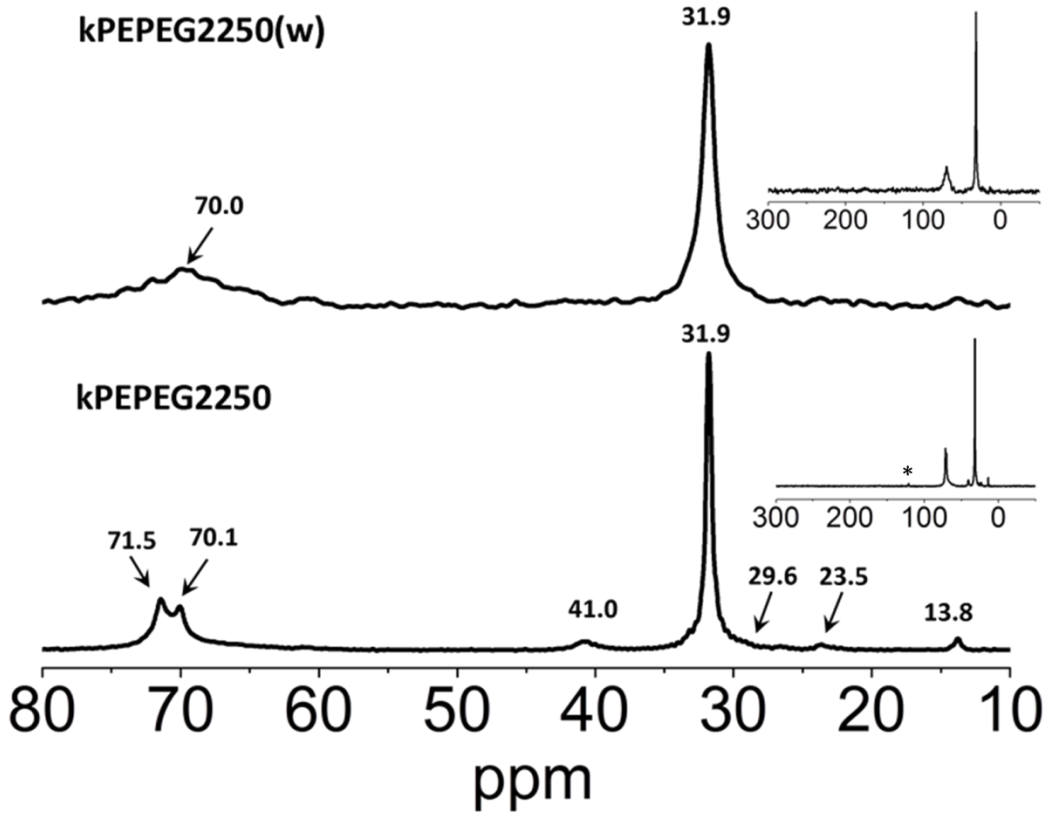

Figure 62: ^{13}C CPMAS NMR spectrum of kPEPEG2250 compared to kPEPEG2250(w). An expanded scale spectra of both materials are shown as insets. Rotational artifacts resulting from MAS are denoted with an asterisk.

Table 19: Summary of the ^{13}C CPMAS NMR peaks observed for kPEPEG2250.

Chemical shift (ppm)	Attribution
71.5	$HOCH_2$-CH_2O, PEG block end group
70.1	CH_2, PEG block
41.0	CH_3, DMSO
31.9	CH_2, PE block
29.6	CH_3CH_2-CH_2, PE block end group
23.5	CH_3-CH_2, PE block end group
13.8	CH_3, PE block end group

3.1.7 ^{13}C CPMAS NMR with dipolar dephasing results & discussion

This analysis was performed in order to determine if there was a visible change in the relaxation behaviour of the carbon signals in kPEPEG2250 compared to the neat polymer, to find evidence of intercalation. Tunney and Detellier (1996a) reported that PEG CH_2O carbons relax significantly faster in a ^{13}C CP MAS NMR experiment when they are intercalated in kaolinite because of their reduced mobility when inside the clay interlayer. They found that adding a 40μs (t_1) delay between the 90° pulse and the acquisition time in a CP experiment resulted in an almost complete decay of the CH_2O carbon signal, yielding a T_2 value of 14.7μs. In the un-intercalated polymer on the other hand, 25% of its signal was retained compared to a CP experiment with no delay added.

The CH_2 carbons on the PE block of kPEPEG2250 (Figure 63) lose almost all their original signal using a t_1 of 40μs. The CH_2O PEG carbons, on the other hand, were much less affected by this experiment. This same behaviour was also observed in the neat polymer (Figure 64). The difference between the relaxation behaviour of these two signals in the polymer can be explained in terms of the structure of the material. The PE block is composed of unbranched alkyl chains which can stack together very closely, making this block very rigid, and consequently its carbons relax quickly. In the PEG block, an oxygen atom is introduced into the repeating polymer chain which prevents adjacent chains from stacking as efficiently as in the PE block. This gives the PEG chain much more flexibility, resulting in its carbons relaxing more

slowly. The intensity of the DMSO and PE block's CH_3 end group's signal was also much less affected in this experiment, where they retained most of their original signal for a t_1 of 40µs. This is because the range of rotational mobility allowed by a methyl group results in a much slower relaxation compared to a CH_2 or CH carbon.

In kPEPEG2250(w) (Figure 65), the signal from the CH_2O carbons almost completely disappeared using a t_1 of 40µs. This suggests that kPEPEG2250 still has a significant fraction of un-intercalated polymer present which masks the signal drop experienced by the intercalated polymer. This hypothesis is supported by T_2 calculations shown in Figure 66 and Table 20, which shows a sharp drop in the T_2 values of the 70.1ppm CH_2O carbon signal from 75µs in PEPEG, to 46µs in kPEPEG2250, and finally to 21µs in kPEPEG2250(w). In kPEPEG2250(w), the T_2 values for the 71.5ppm, 70.1ppm and 31.9ppm were found to be 12-21µs, which agrees quite well with the T_2 value of 14.7µs reported by Tunney and Detellier (1996a). This indicates a reduction in the mobility of the polymer, and offers strong evidence it is intercalated in the clay mineral.

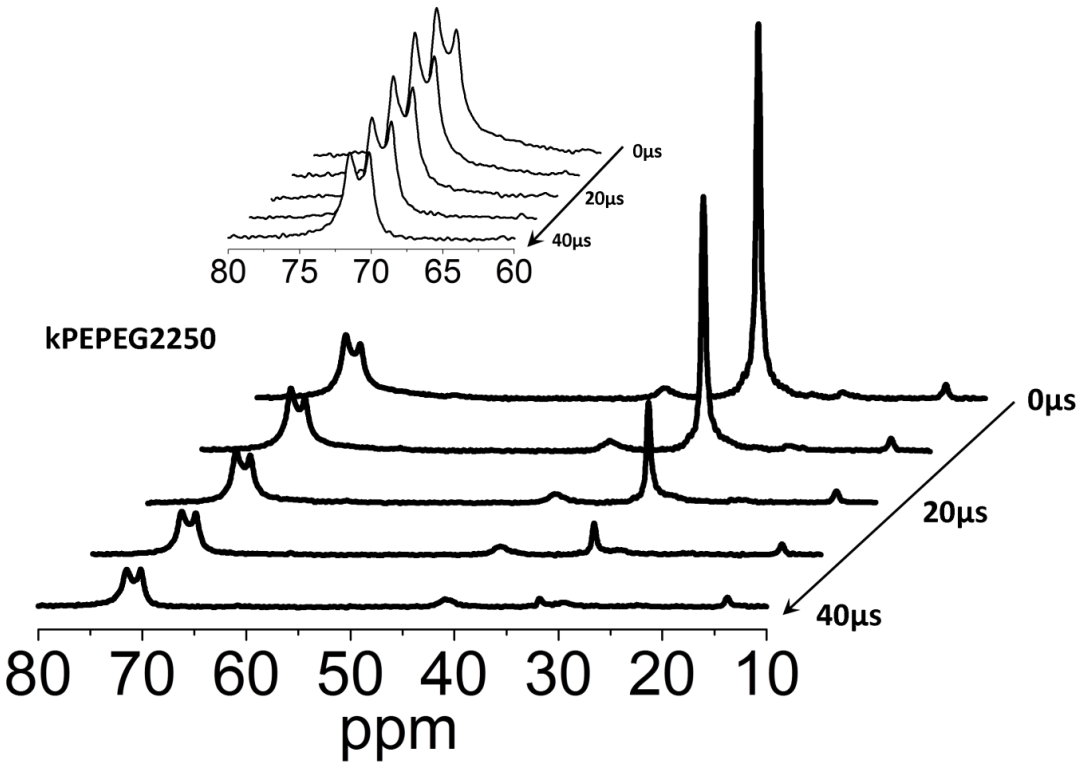

Figure 63: ^{13}C CPMAS NMR with dipolar dephasing spectra of kPEPEG2250. Shown are the spectra using t_1 times of 0, 10, 20, 30, and 40µs. A close up of the 80-60ppm region is shown as an inset.

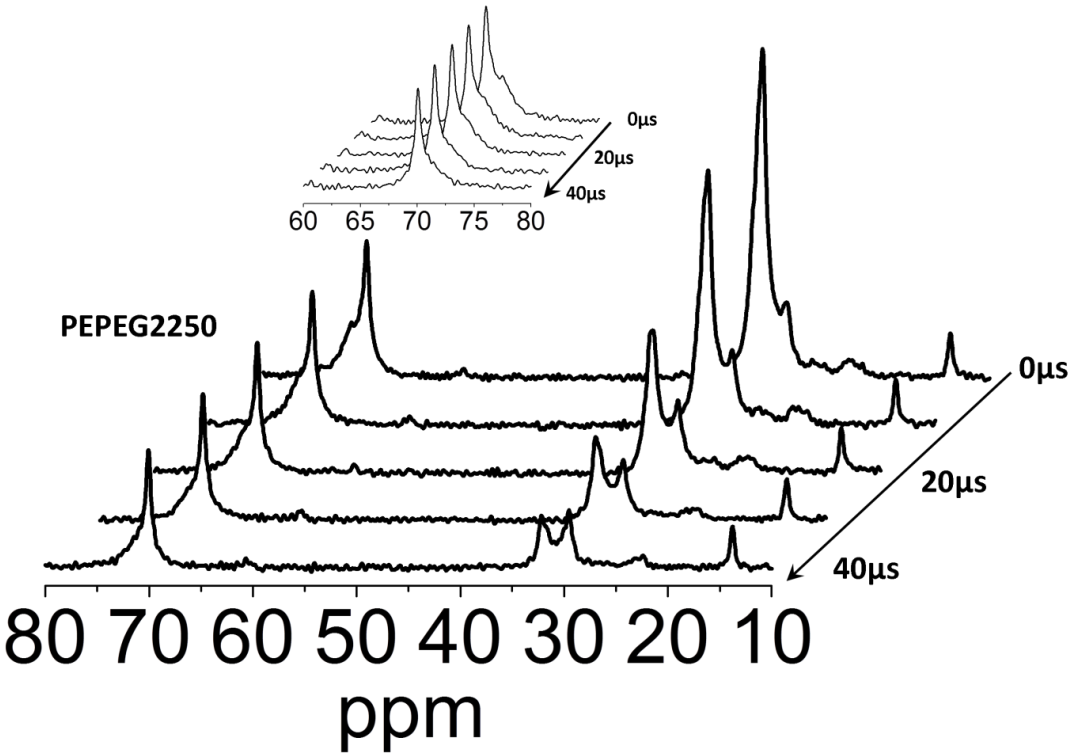

Figure 64: ^{13}C CPMAS NMR with dipolar dephasing spectra of PEPEG2250. Shown are the spectra using t_1 times of 0, 10, 20, 30, and 40µs. A close up of the 60-80ppm region is shown as an inset.

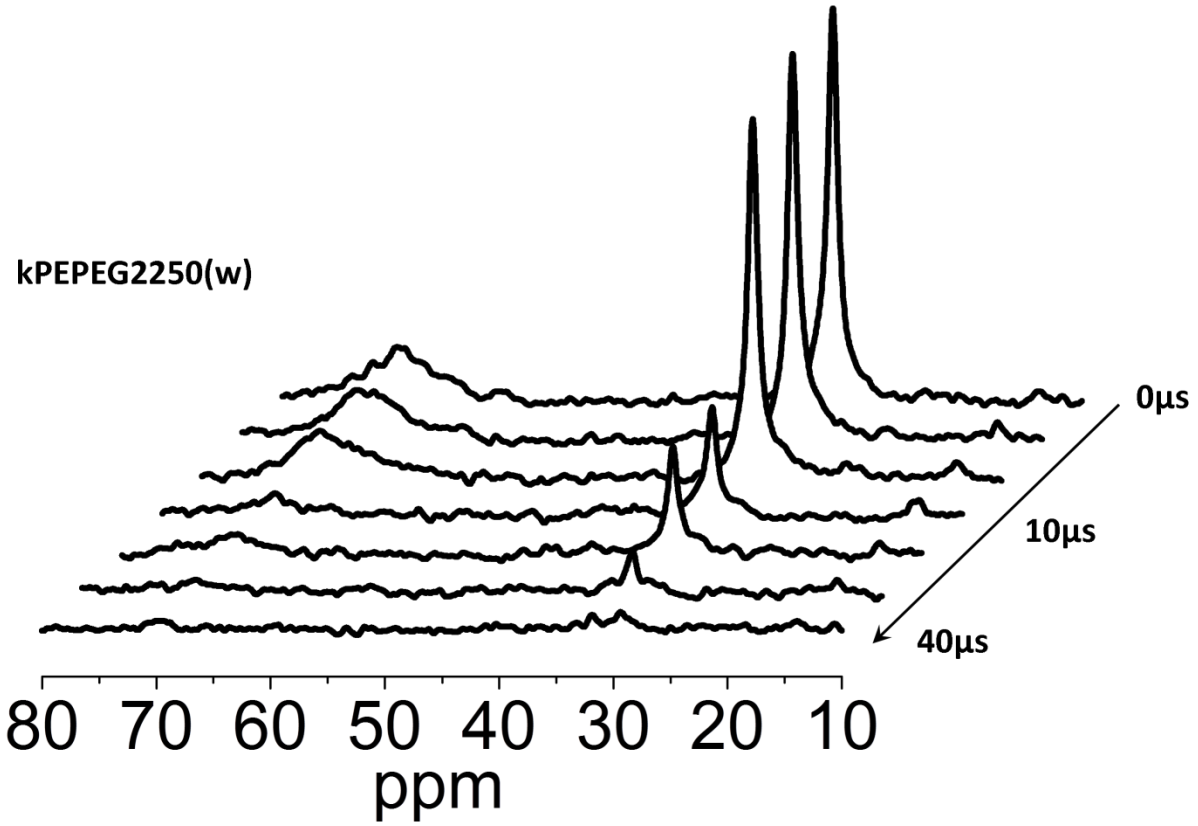

Figure 65: ^{13}C CPMAS NMR with dipolar dephasing spectra of kPEPEG2250(w). Shown are the spectra using t_1 times of 0, 2, 5, 10, 20, 30, and 40µs.

Table 20: Summary of T2 values calculated for kPEPEG compared to the washed and pyrolyzed product kPEPEG2250(w), and the neat polymer (PEPEG).

	T_2 (µs)		
Chemical shift (ppm)	PEPEG2250	kPEPEG2250	kPEPEG2250(w)
71.5	38	38	12
70.1	75	46	21
31.9	20	15	16

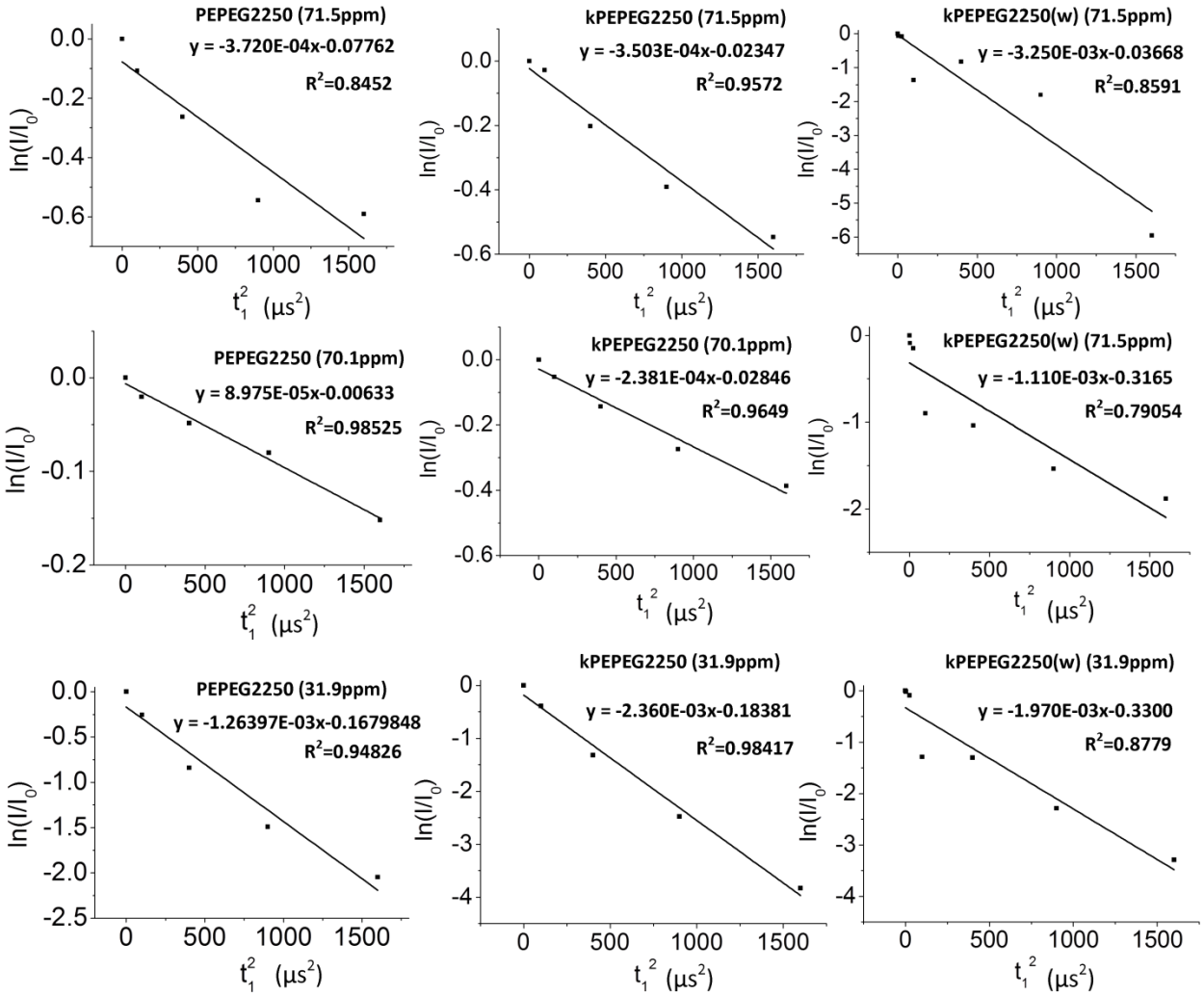

Figure 66: Plots of ^{13}C NMR signal decay as a function of t_1 times for kPEPEG compared to the washed and pyrolyzed product kPEPEG2250(w), and the neat polymer (PEPEG). The slope of these plots was used to calculate T_2 values.

3.1.8 Summary of results and conclusions

Using a kDMSO precursor, the interlayer of kaolinite was functionalized with a PEG copolymer, polyethylene-block-poly (ethylene glycol), by melt intercalation.

XRD results showed a slight contraction of the interlayer *001* d-spacing values compared to kDMSO, with values of 11.0-11.1Å. No change in the *001*-spacing or intercalation ratio was found in kPEPEG2250(w) which suggests the polymer is intercalated in the clay interlayer.

IR analysis showed loss of the characteristic DMSO bands in the OH stretching region of the clay mineral, which were replaced with stretching bands similar to those reported by Tunney and Detellier (1996a) for PEG intercalated in kaolinite. CH stretching bands attributed to the PEPEG polymer were observed, confirming its presence in the material.

TGA analysis showed a significant increase in the 300-600°C weight loss range, from 11.2% to 24.4%, attributed to the PEPEG polymer. No remarkable shift in the clay mineral's dehydroxylation temperature was observed, which suggests an intercalated rather than a grafted complex was formed. 6.2%(w/w) of DMSO remained in kPEPG2250, which was removed in the water washed and pyrolyzed material kPEPEG2250(w).

^{13}C CPMAS NMR analysis showed both PE and PEG block carbons of the PEPEG polymer in kPEPEG2250, which were mostly unchanged compared to the neat polymer. Dipolar dephasing experiments showed that the T_2 values of the PEG carbons drop significantly from PEPEG2250 to kPEPEG2250 and to kPEPEG2250(w) which suggests that intercalation of the polymer was achieved, and that an important fraction of un-intercalated polymer is present in kPEPEG2250.

These particular kaolinite intercalated complexes of polyethylene and polyethylene glycol are expected to significantly hydrophobize the clay mineral. This presents the possibility of using these materials as adsorbents for organic molecules in solution and as vessels for controlled release applications.

3.2 Kaolinite intercalated with poly(lactide)

3.2.1 Introduction

Poly(lactide) is a linear , saturated, biodegradable poly(ester). It is typically prepared by ring opening polymerization of lactide derived from the fermentation of plants rich in carbohydrates, such as corn, sugarcane, and tapioca (Auras *et al.*, 2011). While poly(lactide) was prepared as early as 1845 (Benninga, 1990), interest in the polymer has increased exponentially in the last two decades as a result of its biodegradability and its production from non-petroleum based feedstocks. This was motivated over increasing concerns about the future availability of oil and petroleum products used to make modern synthetic polymers, and over environmental concerns regarding the waste management of non-biodegradable polymer products.

Poly(lactide) is currently one of the most commonly studied and industrially manufactured synthetic biodegradable polymers. Since the polymer and its degradation products are highly biocompatible, it has many applications in medicine, for example as drug delivery systems, and as scaffolding in tissue engineering (Chasin, 1990; Shalaby and Johnson, 1994; Bose *et al.*, 2013). One of its key advantages compared to other poly(esters) used for biomedical applications such as poly(glycolide) is that it is insoluble in water. This also makes it useful for a number of disposable consumer products such as packaging material, drinking cups, and cutlery (Garlotta, 2001).

One of the chief concerns with poly(lactide) is its weak mechanical properties and susceptibility to thermal degradation (Matusik *et al.*, 2012; Södergård and Stolt, 2002). As such, it is often reinforced with additives and filler. Clay minerals are commonly used filler materials for this purpose, and there is interest in developing nanocomposites from PLA to improve their thermal and mechanical properties. Kaolinite has already been shown to be an effective reinforcing agent for films of poly(lactide) where Matusik *et al.* (2012) reported an increase in tensile and modulus of films of the polymer containing platelet and scroll shaped kaolinite particles. The authors, however, did not show its insertion into the kaolinite interlayer space, and to date no such intercalated composites have been prepared.

Other poly(esters) have been intercalated in the kaolinite interlayer space. Elbokl (2007) demonstrated the intercalation of poly(ethylene adipate), poly(butylene adipate), and poly(ethylene succinate) into a kaolinite-DMSO precursor. This was done via a melt of the polymers without any solvent. Evidence of the intercalated structures was shown by the clay minerals' OH stretching modes associated with intercalated DMSO disappearing from their IR spectra, and by the expansion of the *001* d-spacing of the clay minerals in XRD.

The goal of this work is to attempt to prepare poly(lactide) intercalates of kaoliniteas a first step towards developing them as potentialkaolinite based bionanocomposites.

3.2.2 Description of samples

A commercially available poly(L-lactide) (PLA) (Sigma-Aldrich; M_n=50,000 Da) was used in this study. Samples of kaolinite intercalated with this PLA polymer prepared in a manner similar to the one described by Elbokl (2007), where a pre-intercalated kaolinite is dispersed in a melt of the polymer. The resulting material is labelled kPLA. In contrast to the procedure described by Elbokl (2007), a kaolinite pre-intercalated with urea (kurea) was used. Urea has a very low toxicity, especially when compared to other compounds used to prepare kaolinite pre-intercalates such as formamides and DMSO making it an ideal candidate for preparing a potential bionanocomposite where such properties are desirable. Samples of the material prior to any washing or work-up being done were also isolated and analysed for comparison. This material is labelled kPLA(u).

Details of the experimental procedures used to prepare samples and the material characterisation results can be found in section 5.2.

3.2.3 XRD results & discussion

The XRD results shown in Figure 67 suggest formation of a PLA kaolinite intercalated complex. The 10.8Å *001* d-spacing of kurea expanded to a value of 12.1Å, which suggests intercalation of PLA in a monolayer type arrangement. Comparing kPLA to the unwashed product kPLA(u) (Figure 68) shows that the broad, amorphous reflections of the polymeric material from 2θ angles of 10-20° drop sharply after washing, but the reflection attributed to the 12.1Å *001* d-spacing does not. This suggests it is a kaolinite reflection rather than one from the neat polymer.

This *001* d-spacing value is slightly greater than for other intercalated linear poly(esters) such as poly(ethylene adipate) and poly(ethylene succinate) where *001* d-spacings of 11.5-11.7Å were reported (Elbokl, 2007). This can be explained as a result of a PLA polymer having greater vertical dimensions as a result of the branching methyl group in the polymer chain. Elbokl and Detellier (2009) also reported *001* d-spacing of 12.5-12.9Å for methyl branched methacrylamide and poly(methacrylamide) intercalates, which seems in line with these results.

A summary of these results is shown schematically in Figure 69.

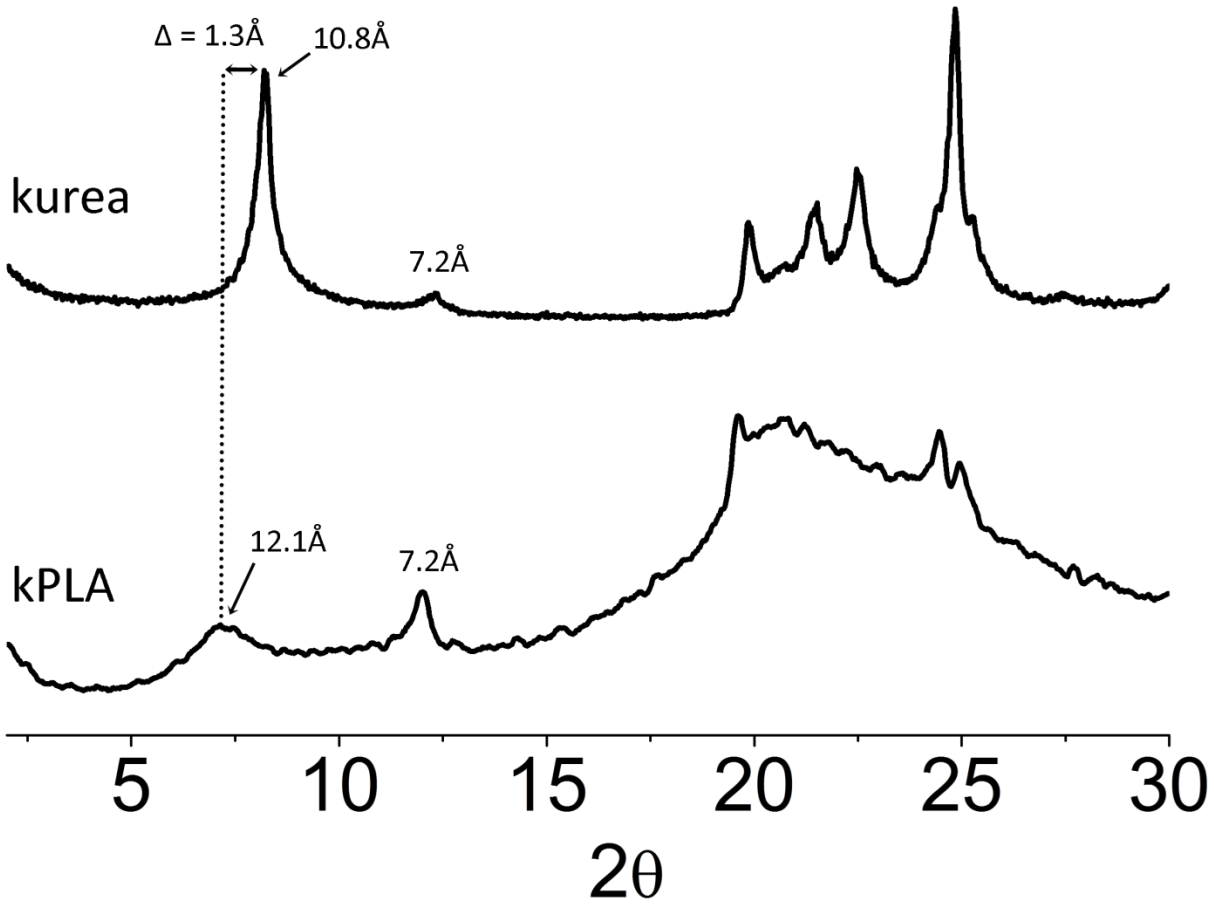

Figure 67: XRD trace of kPLA compared to its kurea precursor.

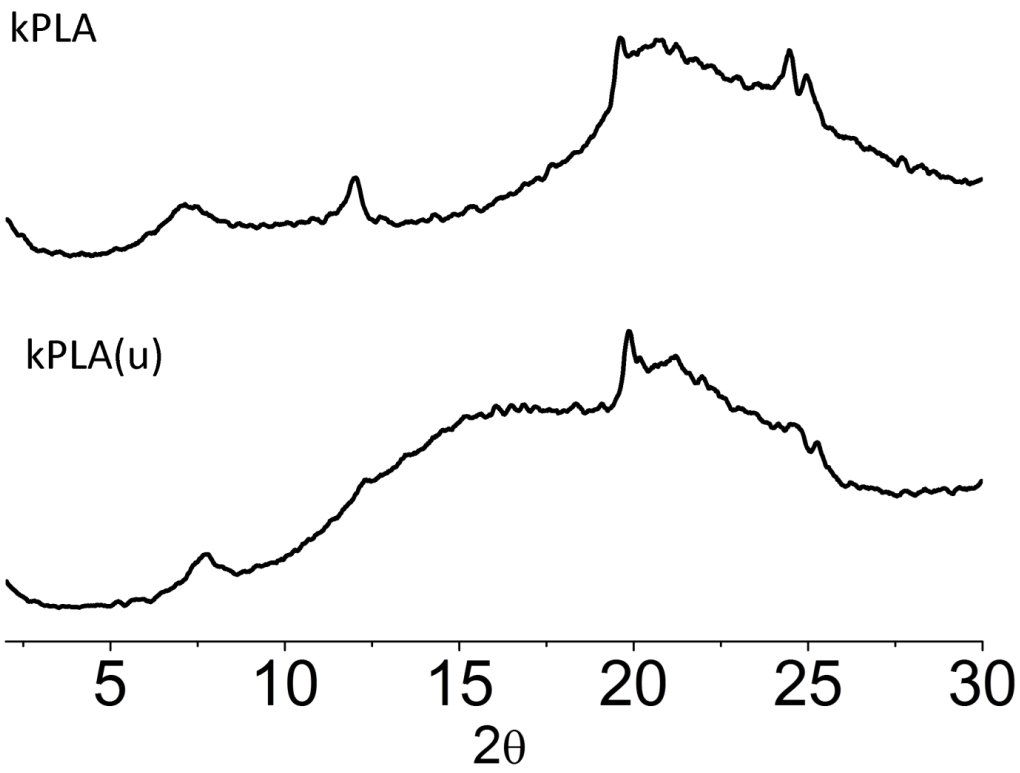

Figure 68: XRD trace of kPLA compared to the unwashed product kPLA(u). The washing procedure did not remove the reflection attributed to the kaolinite 12.1Å *001* d-spacing.

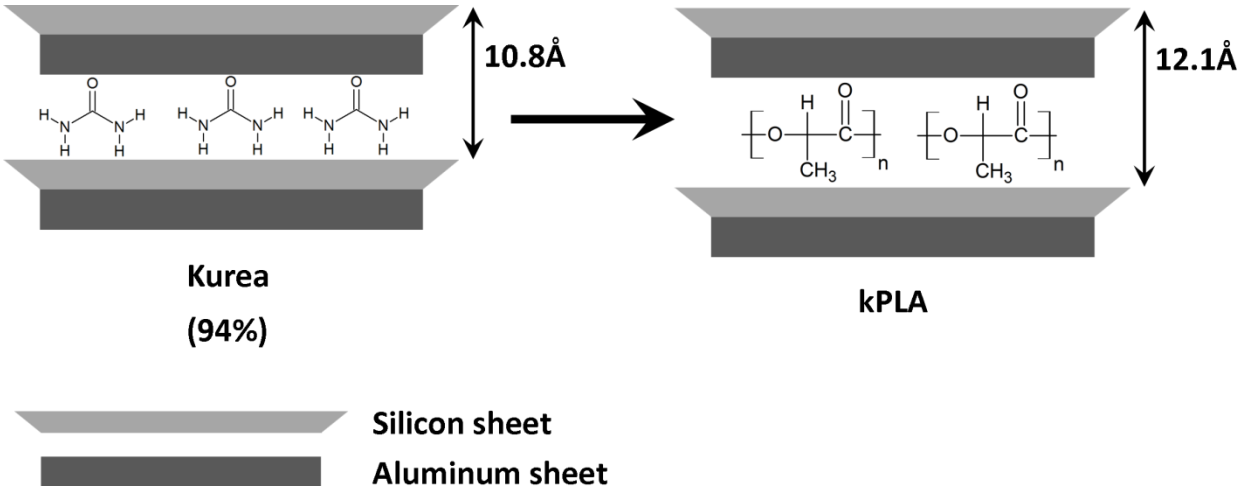

Figure 69: Schematic outlining the *001* spacing of an individual layer in kPLA compared to kurea.

3.2.4 IR results & discussion

Analysis of the IR spectrum of kPLA in Figure 70 and Figure 71 offers further evidence that urea was displaced from the interlayer space of the clay mineral and replaced with PLA. This can be seen from changes occurring in the 3500-3300cm^{-1} region where NH stretching bands characteristic of urea hydrogen bonding with kaolinite's inner surfaces are absent (Figure 70).

Additional changes can be seen in the 1700-1400cm^{-1} region. In kurea, 3 bands are observed at 1662.6cm^{-1}, 1620.8cm^{-1}, 1586.6cm^{-1}, and 1474.2cm^{-1}. These are attributed to its C=O stretching, NH stretching, and CN stretching modes respectively (Stewart, 1957). These bands were not observed in kPLA, and were replaced with bands at 1753.4 cm^{-1}, 1676.5 cm^{-1}, and 1615.3 cm^{-1}. These bands are all attributed to PLA C=O stretching modes. Kister *et al.* (1998) reported values of 1760cm^{-1} for the C=O stretching mode in PLA, which is similar to the band at 1753cm^{-1}, but they didn't observe bands at 1676 and 1615cm^{-1}. One possible explanation for these additional bands in kPLA is that they are acid groups generated from depolymerisation of PLA. This could be a result of the high temperatures used to form the PLA melt. These sorts of temperatures are reported to result in cleavage of PLA esters to form carboxylic acid end groups (Gupta and Deshmukh, 1982). This is also commonly observed in other poly(esters) (Södergård and Stolt, 2002). These bands, however, are redshifted much more than is expected for the C=O of an acid group. Another possible explanation is that these are C=O stretching modes of PLA hydrogen bonding with kaolinite's inner surfaces. This red shifting of carbonyl stretching frequencies has, for example, been demonstrated in macromolecules (Kolano *et al.*, 2006).

Elbokl (2007) also reported similar bands in other poly(esters) such as poly(ethylene adipate), poly(ethylene succinate), and poly(butylene adipate) intercalated in kaolinite which they attributed to ester carbonyls hydrogen bonding with kaolinite's inner surface hydroxyls. This result suggests that PLA is present in the interlayer space of the clay mineral.

A full summary of these results is shown in Table 18.

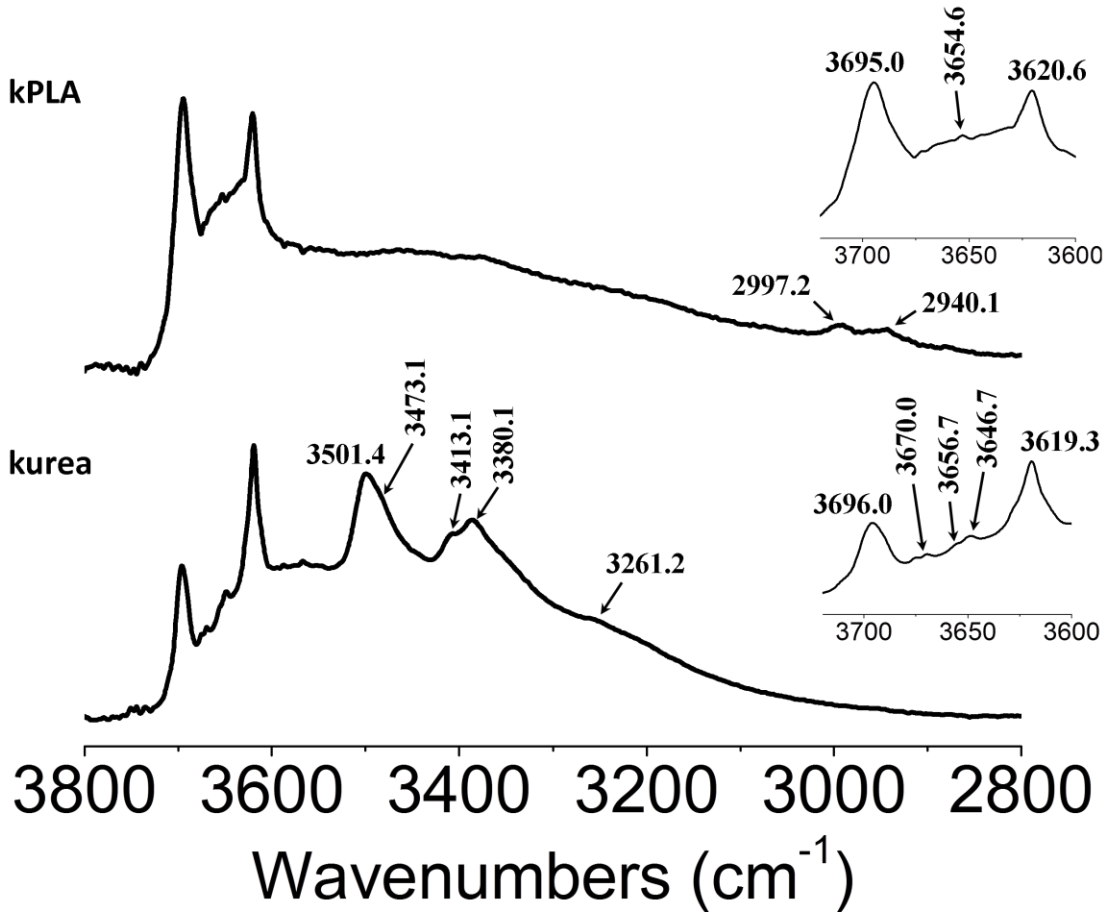

Figure 70: ATR-FTIR spectra of kPLA compared to its kurea precursor, showing the 3800-2800cm^{-1} region. Close ups of the 3720-3600cm^{-1} region are shown as insets.

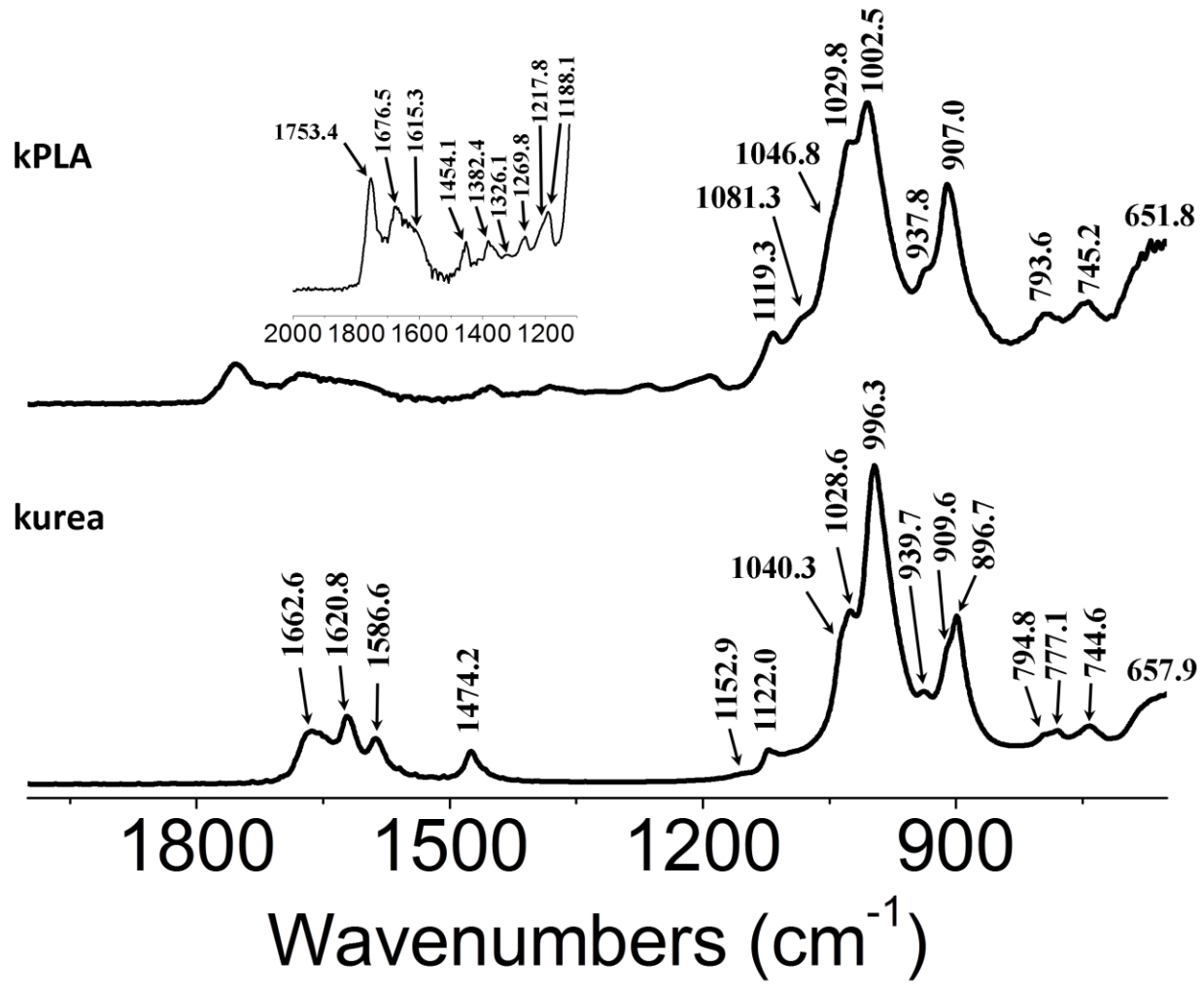

Figure 71: ATR-FTIR spectra of kPLA compared to its kurea precursor, showing the 2000-650cm^{-1} region. A close up of the 2000-1100cm^{-1} region for kPLA is shown as an inset.

Table 21: Summary of the IR bands identified in kPLA.

Frequency (cm^{-1})	Attribution
3695.0	OH stretch, kaolinite inner surface hydroxyl
3654.6	OH stretch, kaolinite inner surface hydroxyl
3620.6	OH stretch, kaolinite inner hydroxyl
2997.2 (2997[a])	CH stretch, PLA
2940.1 (2947[a])	CH stretch, PLA
1753.4 (1760[a])	C=O stretch, PLA
1676.5	C=O stretch, PLA H-bonded to kaolinite AlOH
1615.3	C=O stretch, PLA H-bonded to kaolinite AlOH
1454.1 (1452[a])	CH deformation, PLA
1382.4 (1348-1388[a])	CH deformation, PLA
1326.1 (1315-1300[a])	CH deformation, PLA
1269.8 (1270[a])	combination COC stretch+CH bend, PLA
1217.8 (1215-1185[a])	combination COC stretch+CH rocking, PLA
1188.1 (1215-1185[a])	COC stretch, PLA
1119.3	SiO stretch, kaolinite
1081.3 (1100-1090[a])	C-O stretch, PLA
1046.8	SiO stretch, kaolinite
1029.8	SiO stretch, kaolinite
1002.5	SiO stretch, kaolinite
937.8	AlOH deformation, kaolinite inner surface hydroxyl
907.0	AlOH deformation, kaolinite inner hydroxyl
793.6	Si-O-Al deformation, kaolinite
745.2	SiO stretch, kaolinite
651.8	SiO stretch, kaolinite

[a] Kister *et al.*, 1998

3.2.5 TGA results & discussion

Analysis of the TGA weight loss curve of kPLA (Figure 72) from 40-350°C suggests urea was displaced from the interlayer space of kaolinite. While the total weight loss occurring from 40-350°C is almost the same as in kurea, most of this weight in kurea is lost in a rapid decomposition event centered at 206°C. In kPLA, on the other hand, it occurs more gradually in an event centered at 294°C. One possible explanation for this higher temperature loss is that it is urea that is trapped inside the kaolinite interlayer by PLA molecules, resulting in a higher temperature weight loss compared to kurea. Another possible attribution is that it is PLA adsorbed on the external surfaces of the clay mineral. Based on the IR results which showed no urea bands, it seems more likely this is PLA on the surface of the clay mineral. This would indicate there is an important fraction of un-intercalated PLA in kPLA.

Additional weight losses centered at 372°C and 438°C suggest the presence of PLA in the interlayer space of the clay mineral. The 372°C weight loss is attributed to decomposition of intercalated PLA. The loss centered at 438°C is attributed to both the dehydroxylation of kaolinite and the decomposition of intercalated PLA. A drop in the dehydroxylation temperature is expected for kaolinites that have been amorphized by extensive mechanical processing (Horváth *et al.*, 2003) or had their internal surfaces modified by covalent grafting (Letaief and Detellier, 2011). However even under these circumstances, a dehydroxylation event centered 438°C is very low. Therefore, it is believed that this loss is a combination of both kaolinite dehydroxylation and PLA decomposition. These two losses occur at a temperatures

82-144°C higher than for surface adsorbed PLA, which is consistent for a polymer intercalated in the kaolinite interlayer space.

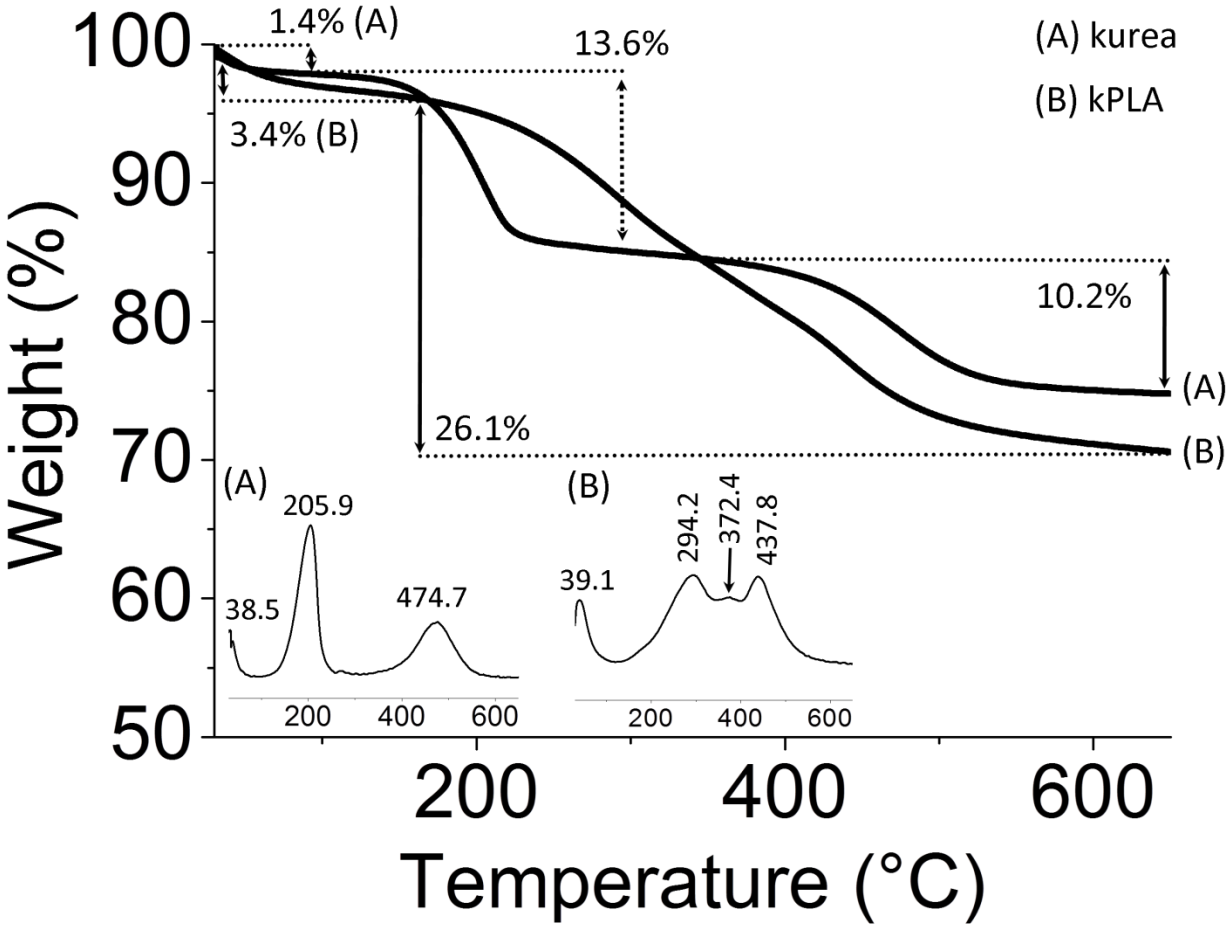

Figure 72: TGA weight loss curve of kPLA compared to kurea. The 1st derivative plots of the weight loss curves are shown as insets.

3.2.6 ^{13}C CPMAS NMR results & discussion

The ^{13}C CPMAS NMR spectrum of kPLA shown in Figure 73 suggests all urea was displaced from the interlayer space and replaced with PLA. The peak at 163.6ppm in kurea, attributed to the urea carbonyl group, could not be observed in kPLA, and in its place new carbonyl peaks at 170.0, 69.8 and 17.0ppm were observed. These peaks are attributed respectively to PLA carbonyl, –OCH-- and –CH3 carbons, and they agree well with the chemical shift values of neat PLA (Figure 74).

The key difference between the spectra of neat PLA and kPLA is the appearance of a new band at 178.4 ppm. One possible explanation is that it is from carboxylic acid carbons formed from depolymerisation of PLA. Espartero *et al.* (1996) reported ^{13}C chemical shift values of 171.5-172.1ppm for carboxylic acid carbons and 174.4-169.9ppm for ester carbons of lactic acid dimers and trimers in DMSO. The authors also reported values of 169.44, 68.95 and 16.70ppm for poly(lactide) in DMSO, and values of 176.3, 66.0 and 20.7ppm for monomeric lactic acid in DMSO. These results indicate there should be shift of 2.9ppm and 4.0ppm for the –OCH– and –CH_3 carbons respectively if a depolymerized product were obtained. While the –CH_3 peak has a slightly asymmetric shape suggesting the presence of additional peaks, this was not the case for the –OCH– peak.

Another explanation is that this shift is a result of strong interaction of the carbonyl functional group with the clay surfaces, resulting in a more de-shielded chemical shift value. Similar to the

red shifted carbonyl bands in the IR spectrum of kPLA, the ^{13}C peak shift could be a result of hydrogen bonding interactions with the clay mineral's surfaces. Elbokl (2007) reported similar values around 180ppm in the ^{13}C NMR spectra of various intercalated linear poly(esters) which he claimed were not depolymerized during the reaction. This explanation would indicate that there is a mixture of intercalated and surface adsorbed PLA in kPLA, attributed to the peaks at 178.4 and 170.1ppm respectively. This is in agreement with TGA results which showed weight loss events which were attributed to these two species.

A summary of these peaks is shown in Table 22.

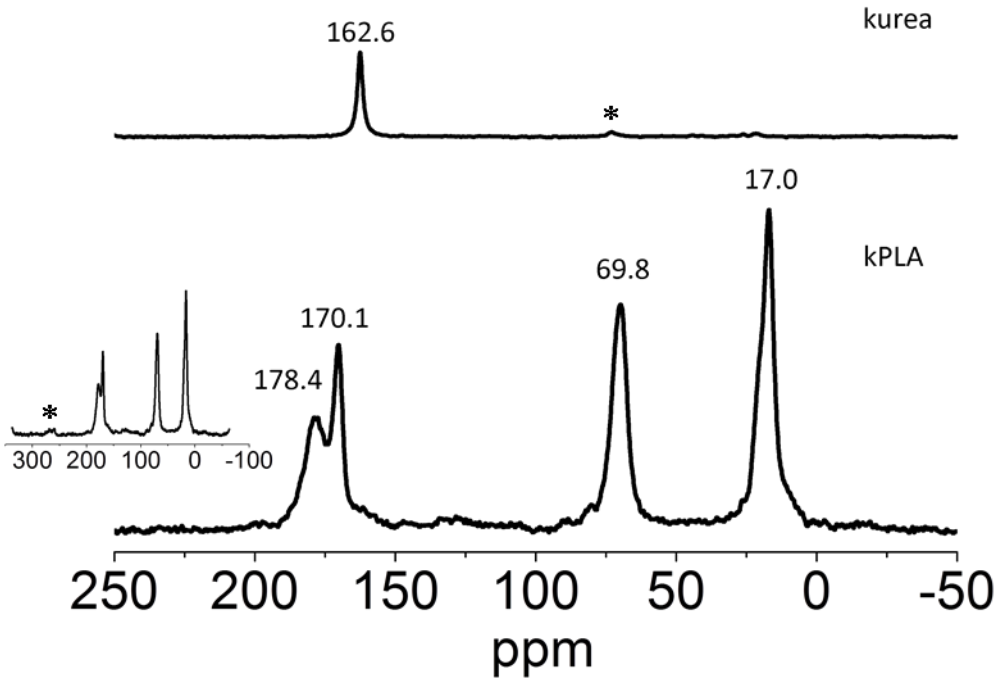

Figure 73: ^{13}C CPMAS spectrum of kPLA compared to kurea. An expanded scale spectrum of kPLA is shown as an inset. Rotational artifacts resulting from MAS are denoted with an asterisk.

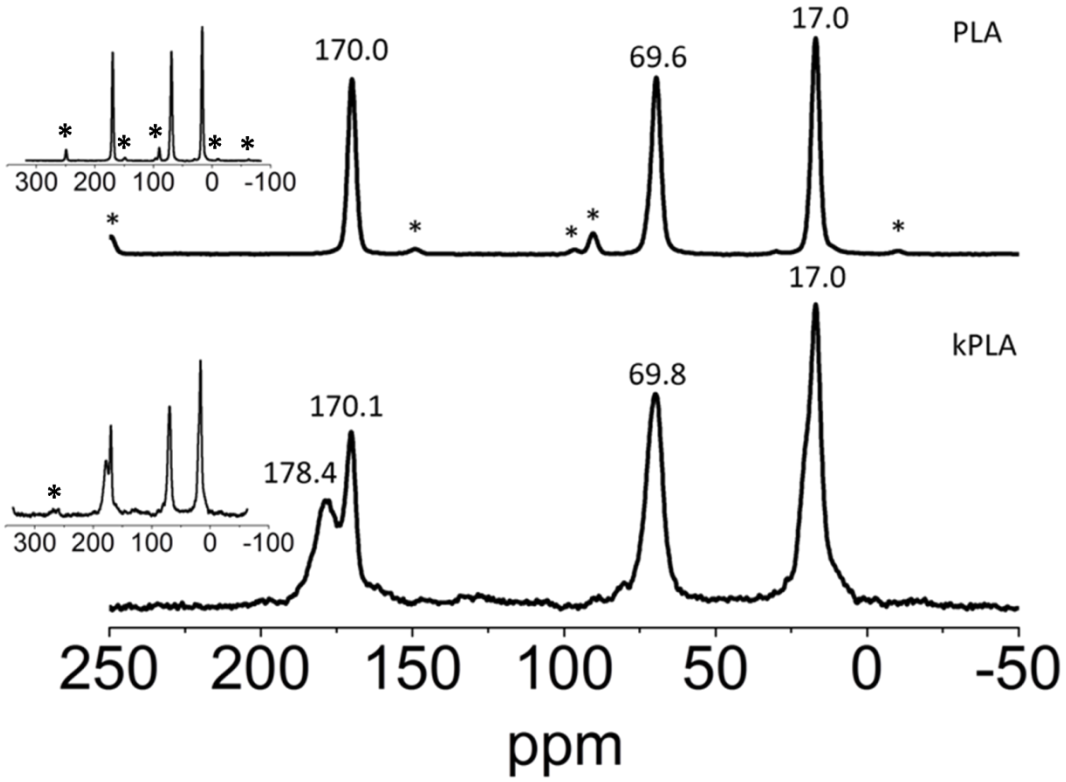

Figure 74: ^{13}C CPMAS spectrum of kPLA compared to the neat polymer. Rotational artifacts are denoted with asterisks. Expanded scale spectra for both materials are shown as insets. Rotational artifacts resulting from MAS are denoted with an asterisk.

Table 22: Summary of the ^{13}C CPMAS NMR peaks observed for kPLA.

Chemical shift (ppm)	Attribution
178.4	-C=O, PLA H-bonded to kaolinite's inner surfaces
170.1	-C=O, PLA
69.8	-CHO, PLA
17.0	-CH3, PLA

3.2.7 Summary of results and conclusions

PLA was intercalated in kaolinite by dispersing a kaolinite pre-intercalated with urea inside a melt of PLA. XRD results showed kurea's 10.8Å *001* d-spacing expanded to a value of 12.1Å, which suggests intercalation of the PLA inside the clay mineral in a monolayer type arrangement. IR results showed the disappearance of urea's N-H and C=O stretching bands which suggests it was completely displaced from the kaolinite interlayer space. A new set of C=O stretching bands were observed which were attributed to either the hydrolysis of PLA's ester groups to acids or PLA ester groups hydrogen bonding with kaolinite's inner surfaces. TGA results showed a sharp drop in weight lost from 40-200°C for kPLA compared to kurea which suggest displacement of urea from the interlayer space of the clay mineral. The several large weight loss events from 200-450°C were attributed to PLA present both as an intercalated and as a surface adsorbed species. ^{13}C CPMAS NMR results for kPLA compared to kurea showed the complete disappearance of urea's peaks and the appearance of PLA peaks, suggesting PLA completely displaced urea from the kaolinite interlayer space. A new peak was observed at 178.4ppm which was not present in neat PLA. This was attributed to PLA ester groups hydrogen bonding to kaolinite's inner surfaces.

This intercalated PLA material might be expected to have superior mechanical strength compared to the neat polymer, and future work could study its mechanical properties for use

as a biodegradable nanocomposite material. Optimization of the intercalation process to minimize depolymerisation could also be investigated. This could possibly be done through use of additives such as plasticizers to lower the melting temperature of the polymer or using a PLA that is a copolymerized with other functional groups such as poly(ethylene glycol).

4 Covalent grafting of glycols and glycol ethers containing polymerizable groups to kaolinite

4.1 Introduction

One key advantage of using kaolinite for preparing organo-mineral functionalized materials is that organic functional groups can be grafted to the clay mineral's internal surfaces. This is done by exploiting kaolinite's inner and outer surface hydroxyl groups to undergo condensation reactions to produce compounds which are covalently bonded to the clay mineral's surface. Glycols were the earliest such compounds used for these reactions, where ethylene glycol and isomers of propanediol were grafted using a kDMSO precursor (Tunney and Detellier, 1993). Gardolinski explored this topic in depth for his PhD dissertation (2005), where he demonstrated covalent grafting of a number of linear and branched diol molecules with up to ten carbons in their structure using a kDMSO precursor. He also explored the effectiveness of the reaction depending on the position of the hydroxyl groups in the diol molecules. He found that the position of the first hydroxyl group was important, with reactivity being the highest when it is present at the end of the diol molecule and dropping significantly when shifted by even a single carbon. He also found that the reactions were most effective when the second hydroxyl group's position is α to the first, where reactivity gradually drops off the further away they are from each other. The presence of branching methyl substituents between the two hydroxyl groups was also shown to have a deleterious effect on reactivity. Other studies also reported the replacement of methoxy groups in a methanol grafted kaolinite with propanediols and

butanediols through a transesterification mechanism (Itagaki and Kuroda, 2003; Murakami *et al.*, 2004). A full review of these studies is shown in Table 23.

Glycol mono-ethers are another important class of compounds that can be grafted to kaolinite. This was first explored by Tunney and Detellier (1993) as part of their work grafting ethylene glycol, where they grafted ethylene glycol methyl ether and di(ethylene glycol) butyl ether. Gardolinski and Lagaly (2005a) also demonstrated the high affinity of glycol mono-ethers towards grafting reactions in kaolinite where they grafted a variety of linear and branched glycol mono-ethers with long alkyl chains up to 16 carbons long, and with phenyl groups attached.

These studies suggest that 1,2 diols and glycol-ethers could be very suitable for grafting a variety of different functional groups on kaolinite. This could be used, for example, for the grafting of a polymerizable group to the clay mineral, which could then undergo in-situ polymerization to yield a polymer that is covalently grafted to the clay mineral. A bulky functional group grafted to kaolinite, such as a polymer, could theoretically prevent the kaolinite layers rolling up into scroll-like structures when exfoliated, yielding an ideal nanocomposite where the individual clay layers would be well dispersed in the polymer matrix. This could be a potential improvement over current methods where a scrolled up type structure is produced when kaolinite is exfoliated (Gardolinski and Lagaly, 2005b). The goal of this project is to graft compounds based on 1,2 diols and glycol-ethers containing polymerizable

groups to kaolinite's inner surfaces as a first step towards preparing kaolinite nanocomposites with polymers grafted to the clay mineral's surfaces.

Table 23: Literature review of diol compounds grafted in kaolinite.

Grafted compound	Structure	Kaolinite	Kaolinite precursor	001 d-spacing (Å)
ethylene glycol	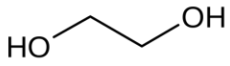	SPS (Cornwall, U.K.; H.I.=1.25[a])	kDMSO	9.3[a]
		KGa1 (Georgia, U.S.; H.I.=1.19[b])	kDMSO	9.5[c]
			kNMF	9.4[d]
1,2-propanediol	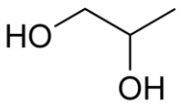	SPS (Cornwall, U.K.; H.I.=1.25[a])	kDMSO	10.9[a]
		KGa1 (Georgia, U.S.; H.I.=1.19[b])	kDMSO	10.9[c]
			kmethoxy	10.8[e]
1,3-propanediol		SPS (Cornwall, U.K.; H.I.=1.25[a])	kDMSO	9.6[a]
		KGa1 (Georgia, U.S.; H.I.=1.19[b])	kDMSO	9.8[d]
			kmethoxy	11.1[e]
1,3-dimethyl-1,3-propanediol	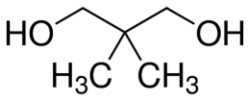	SPS (Cornwall, U.K.; H.I.=1.25[a])	kDMSO	10.1[a]
1,2-butanediol	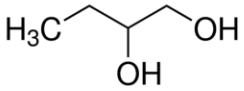	SPS (Cornwall, U.K.; H.I.=1.25[a])	kDMSO	11.4[a]
		KGa1b (Georgia, U.S.; H.I.=1.09[b])	kmethoxy	11.8[f]
1,3-butanediol	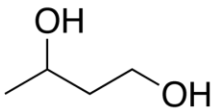	SPS (Cornwall, U.K.; H.I.=1.25[a])	kDMSO	11.3[a]
		KGa1b (Georgia, U.S.; H.I.=1.09[b])	kmethoxy	11.6[f]
1,4-butanediol	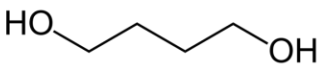	SPS (Cornwall, U.K.; H.I.=1.25[a])	kDMSO	11.3[a]
1,6-hexanediol	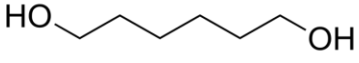	SPS (Cornwall, U.K.; H.I.=1.25[a])	kDMSO	11.1[a]

[a] Gardolinski and Lagaly, 2005b; [b] Pruett and Webb, 1993; [c] Tunney and Detellier, 1993; [d] Tunney, 1995; [e] Itagaki and Kuroda, 2003; [f] Murakami *et al.*, 2004.

4.2 Kaolinite functionalized with 3-allyloxy-1,2-propanediol

4.2.1 Description of samples

Samples of a kaolinite intercalated and grafted with diol molecules containing polymerizable groups was attempted using 3-allyloxy-1,2-propanediol (Figure 75). This compound was purchased from Sigma-Aldrich and used as is. Interlayer modification of kaolinite was done using a technique similar to the one described by Murakami *et al.* (2004) and Itagaki and Kuroda (2003). In this method, a kaolinite pre-intercalated and grafted with methanol (kmethoxy) is dispersed inside a solution containing the diol molecules, and the grafted methoxy groups are exchanged with the diol molecules through a transesterification mechanism. Isopropanol was chosen as a solvent for the solution containing the allyloxy diol molecules because of their solubility in it and because isopropanol is known to not intercalate inside the clay mineral and it can safely be used during the work-up steps in preparing functionalized kaolinites (Letaief, *et al.* 2008). Reactions were performed at room temperature and under refluxing conditions, and the resulting materials are labelled kallyloxy(low T) and kallyloxy respectively. These materials were washed in water to determine if covalent grafting was achieved and the resulting materials are labelled kallyloxy(low T)(w) and kallyloxy(w) respectively. The procedure used to prepared kallyloxy(low T) was also repeated using samples of an unmodified kaolinite, kGa-1b, for comparison. This material is labelled allyloxy(on kGa-1b).

Details of the experimental procedures used to prepare samples and the material characterisation results can be found in section 5.2.

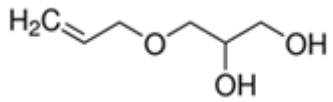

Figure 75: Structure of 3-allyloxy-1,2-propanediol

4.2.2 XRD results & discussion

An XRD trace of kallyloxy shown in Figure 76 suggests that the kaolinite interlayer was functionalized with the allyloxy compound. A new fraction corresponding to a *001* d-spacing value of 11.44Å was observed, which corresponds to an expansion of 2.82Å compared to the kmethoxy precursor. This d-spacing value suggests that the interlayer material adopts a monolayer type arrangement typically seen in interlayer functionalized kaolinites. Gardolinski and Lagaly (2005a) for example reported similar d-spacing values for kaolinite functionalized with butane and hexane diols. A schematic outline of this material is shown in Figure 77.

Washing kallyloxy in water did not regenerate the unmodified kaolinite or the kmethoxy precursor's structure, which strongly suggests the allyloxy compound was covalently grafted to kaolinite's inner surfaces. XRD results did, however, show slight contraction of the *001* d-

spacing to 10.8Å. This is attributed to the loss of ungrafted allyloxy from the interlayer space, leaving only the grafted species. This difference in d-spacing values between grafted and ungrafted species has been reported elsewhere. Tunney and Detellier (1994) for example reported a difference of 1.4Å in the *001* d-spacing values for grafted and non-grafted ethylene glycol.

When the reaction was done under non-refluxing conditions (Figure 78), a similar interlayer structure was obtained, yielding a d-spacing value of 11.4Å. However, a reflection corresponding to kmethoxy's *001* d-spacing value of 8.8Å was also observed, indicating that a fraction of the kmethoxy precursor material remains. Washing the material in water removed all but 13% of the 11.4Å fraction, and resulted in a partial regeneration of the 8.8Å faction characteristic of kmethoxy. This confirms that very little allyloxy groups were grafted under these conditions and suggests a significant amount of methoxy groups remained grafted in the 11.4Å fraction. This result clearly demonstrates the importance of working at high temperatures for these grafting reactions.

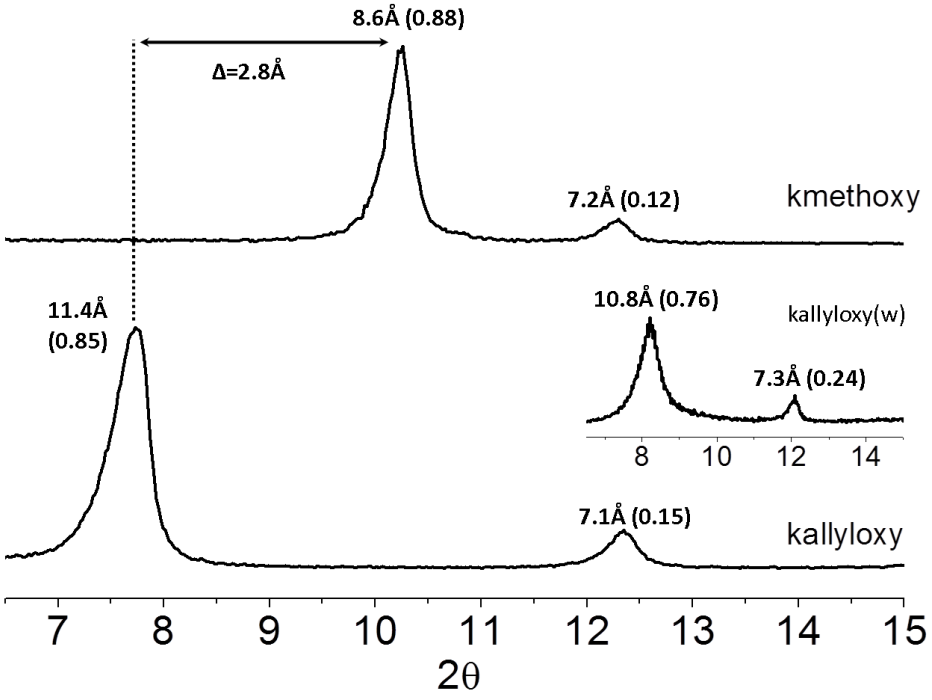

Figure 76: XRD trace of kallyloxy compared to kmethoxy. The water washed material, kallyloxy(w), is shown as an inset. Washing the material in water did not regenerate a kmethoxy fraction.

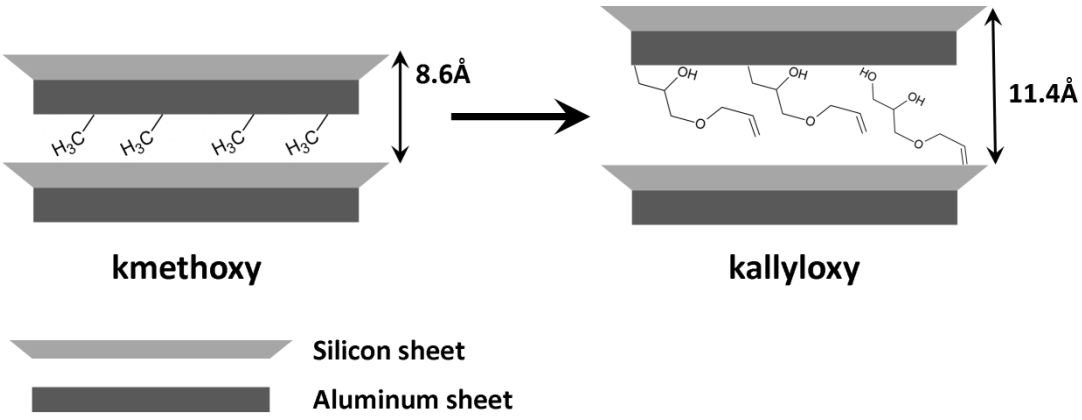

Figure 77: Side view schematic showing the interlayer space of kaolinite in the prepared kallyloxy material.

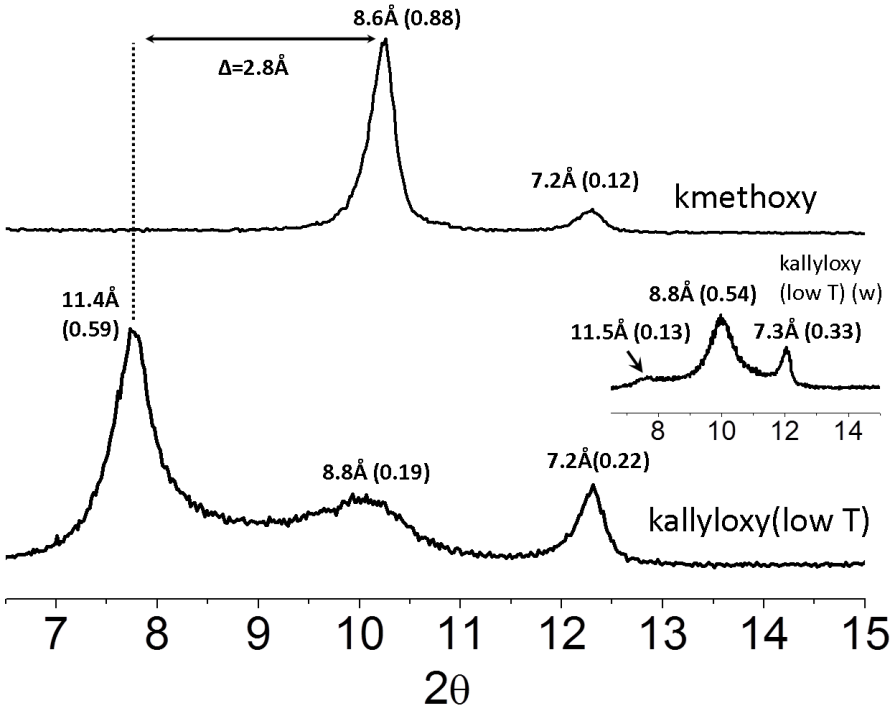

Figure 78: XRD trace of kallyloxy(low T), compared to kmethoxy. The water washed material, kallyloxy(low T)(w), is shown as an inset. Washing the material in water collapsed the 11.4Å fraction, partially regenerating the starting kmethoxy *001* d-spacing.

4.2.3 IR results & discussion

IR results for kallyloxy (Figure 79) show the appearance of new kaolinite OH stretching bands and the appearance of new C-H stretching bands which suggests the allyloxy compound is present in the kaolinite interlayer space. The new bands appearing at 3649 and 3632 cm^{-1} are attributed to interlayer allyloxy molecules perturbing nearby kaolinite inner surface hydroxyls. These bands are known to be very sensitive to changes occurring to the inner hydroxyls' environment (Tunney, 1995), and can be a key indicator of interlayer modification. A new band

was also observed at 3504 cm^{-1}, attributed to inner surface hydroxyls hydrogen bonding with the allyloxy compound. Bands in this range are often reported for other kaolinite intercalates, for example in DMSO- kaolinite (Johnston *et al.*, 1984), and offer further evidence of allyloxy in the kaolinite interlayer. New C-H stretching bands can also be observed in the 3000-2800 cm^{-1} region, which are attributed to allyloxy molecules.

The disappearance of characteristic kmethoxy bands at 3524.3 and 2843.8cm^{-1} in kallyloxy suggests there is no intercalated and grafted methanol remaining in this material. This suggests the complete replacement of these groups with the allyloxy compound.

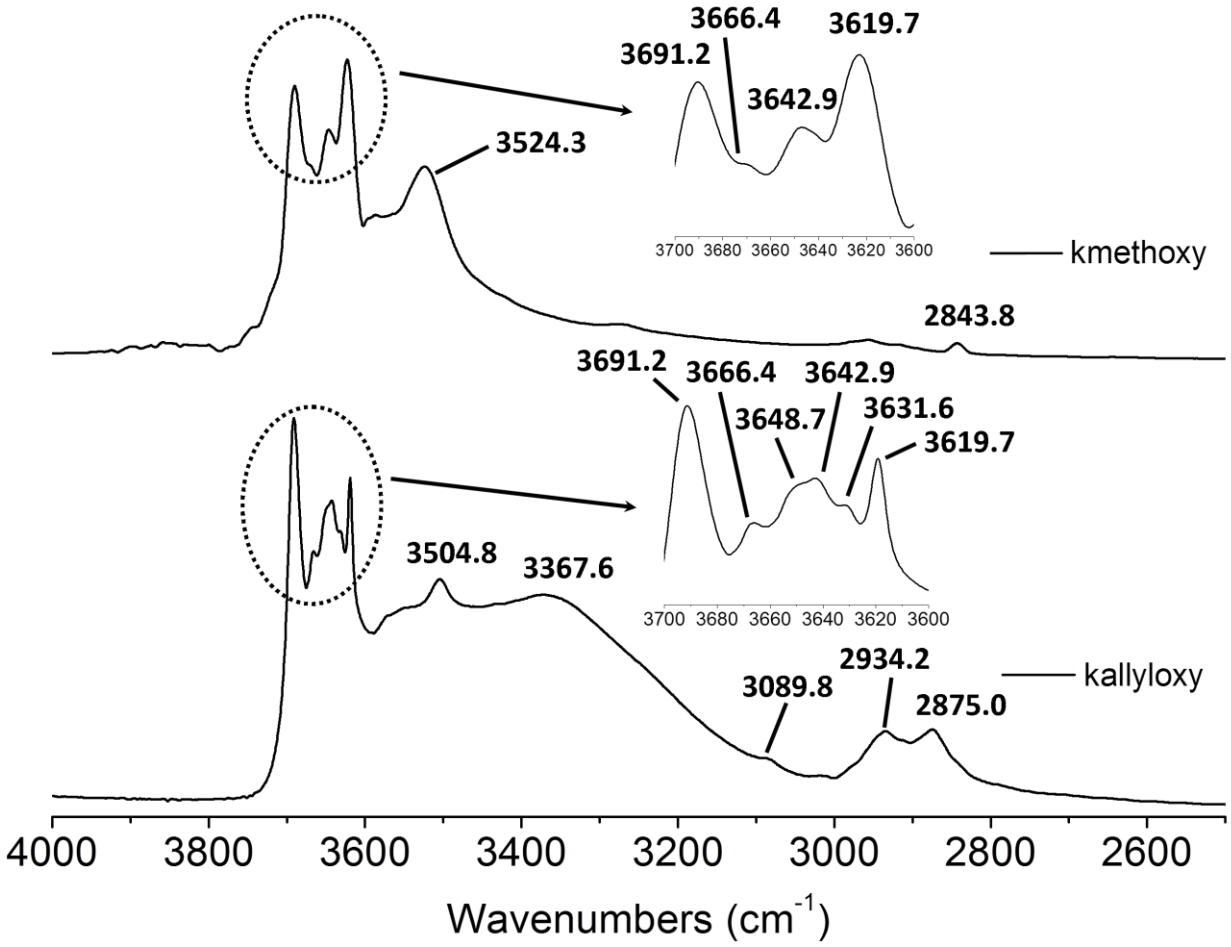

Figure 79: ATR-FTIR of kallyloxy compared to kmethoxy. The 4000-2500 cm^{-1} region is shown with close ups of the 3700-3600 cm^{-1} region shown as insets.

4.2.4 TGA results & discussion

The TGA results for kallyloxy (Figure 80) show an important weight loss event centered at 92°C, which is attributed to allyloxy adsorbed on kaolinite's outer surfaces. This is significantly lower than the boiling point of the neat allyloxy compound, but this sort of behaviour might be expected for molecules adsorbed on a solid support where they are in a pseudo liquid-like state. A similar behaviour was observed for indole adsorbed on kaolinite from solution, where the adsorbed indole's decomposition temperature, 87-146°C, was lower than its literature boiling point of 254°C (Fafard *et al.*, 2012). This result suggests there is an important fraction of surface adsorbed allyloxy compound in kallyloxy.

The weight loss events centered at 371°C are attributed to ungrafted allyloxy molecules in the kaolinite interlayer. The 371°C weight loss event is occurring over a range of temperatures much higher than the boiling point (233°C) of the allyloxy compound under standard conditions. However, the onset of this weight loss event, at 225°C, begins around this temperature, so the wide temperature range of this loss is most likely due to the slow diffusion of the decomposed molecules out of the clay layers. This result suggests this fraction of the allyloxyl molecules in kallyloxy are intercalated inside the kaolinite interlayer space.

The 458°C weight loss event falls inside the range usually expected for a grafted compound inside kaolinite (Tunney and Detellier, 1996). For example, this can clearly be seen for kmethoxy, where the grafted methanol species are lost in combination with the dehydroxylation of kaolinite's hydroxyls as a single weight loss event centered at 481°C (Figure 80). Based on the 1st derivative plot of kallyloxy (Figure 80), the dehydroxylation event in this material appears to occur separately from the 458C°C event, as a loss centered at 497°C. This suggests the weight loss event at 458°C is uniquely due to decomposition of grafted allyloxy molecules. These results all strongly point to allyloxy molecules being grafted to kaolinite's inner surfaces in kallyloxy.

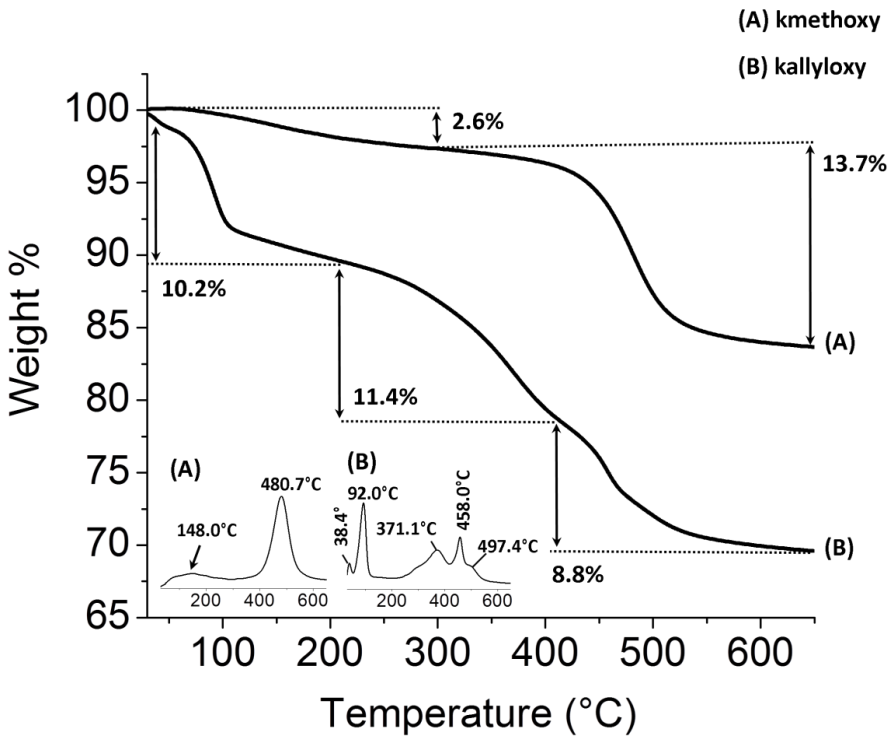

Figure 80: TGA weight loss curve for the pyrolysis of the kmethoxy starting material (A) compared to kallyloxy (B). The 1st derivative weight loss curves are shown as insets.

4.2.5 ^{13}C CPMAS NMR results & discussion

^{13}C CPMAS NMR results for kallyloxy (Figure 81) in the 200-80ppm region suggests two types of allyloxy species are present. The alkene carbon peaks at 134.4 and 117.3ppm appear as sharp, intense peaks and are similar to the chemical shift values of the neat allyloxy compound in the liquid state. These peaks are attributed to allyloxy molecules adsorbed on kaolinite's outer surfaces. The second set of alkene carbon peaks shows up as broad peaks at 134.2 and 126.7ppm with noticeably different chemical shift values from neat allyloxy. These are attributed to allyloxy in the kaolinite interlayer. This interpretation was tested by comparing this spectrum to that of the allyloxy compound adsorbed on the outer surfaces of kGa-1b (Figure 82). In the spectrum of allyloxy (on kga1b), the extra sets of peaks attributed to interlayer allyloxy were absent, which appears to validate this interpretation. The presence of these alkene carbon peaks also confirms that allyloxy's polymerizable group remained intact in kallyloxy.

The alkene carbon peaks with higher chemical shift values are attributed to the =CH-R alkene carbon. The interlayer species are slightly more shielded, with a chemical shift value 2.4ppm lower than the surface species. The peaks with lower chemical shift values are attributed to the terminal H_2C= alkene carbon. This carbon is significantly de-shielded when in the interlayer space compared to the surface species, where its chemical shift value is shifted 9.3ppm higher. These chemical shift changes are known to occur to nuclei confined in solid materials; for example ^{129}Xenon trapped inside clathrate materials (Ripmeester *et al.,* 1988). However, there

are no known reports of ^{13}C chemical shift value changes of this magnitude occurring in a kaolinite intercalate.

The peaks in the 80-60 ppm region (Figure 83) also suggest two types of allyloxy carbons are present. There are four discreet carbon peaks in the liquid state spectrum of the allyloxy compound, while in kallyloxy at least seven can be seen. Among these, the 64.2 and 66.0ppm peaks are attributed to the terminal hydroxyl carbons, with the 66.0ppm carbon is attributed to the grafted species. The other carbons are too poorly resolved to be accurately attributed.

The faint peak at 50.8ppm is attributed to trace methoxy groups remaining in the material. Its very low intensity suggests almost all the grafted methoxy groups were replaced during the reaction.

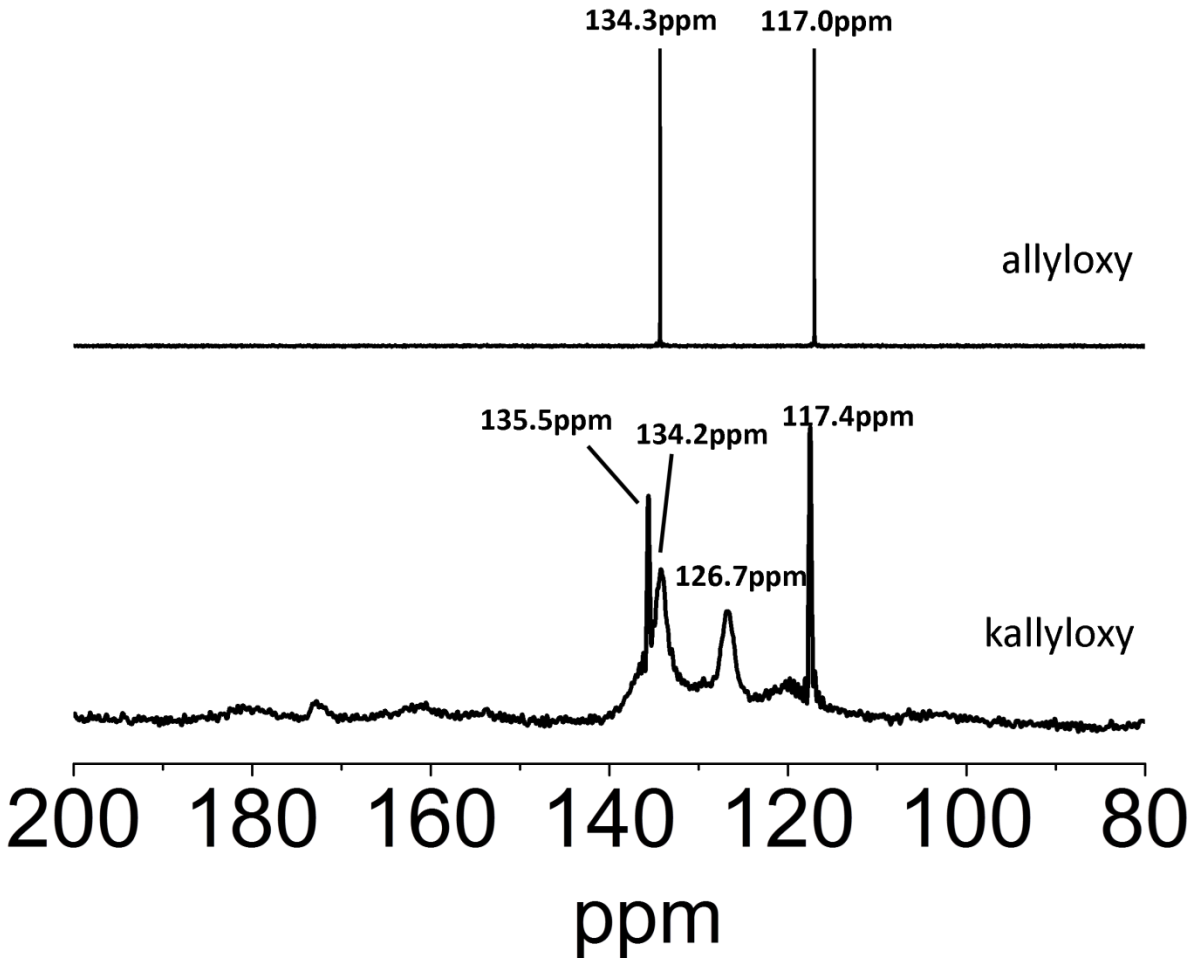

Figure 81: ^{13}C CPMAS NMR of kallyloxy compared to the high resolution liquid ^{13}C spectrum of neat allyloxy.

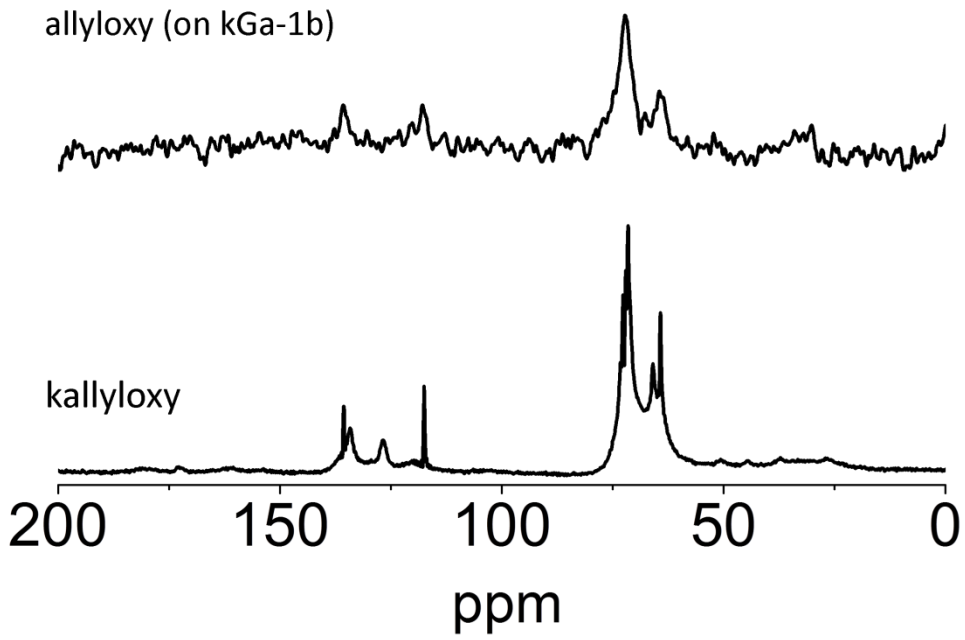

Figure 82: ^{13}C CPMAS NMR of kallyloxy compared to allyoxy adsorbed on the surface of kGa-1b, allyloxy (on kGa-1b). The peaks attributed to interlayer allyloxy were not observed in allyloxy (on kGa-1b).

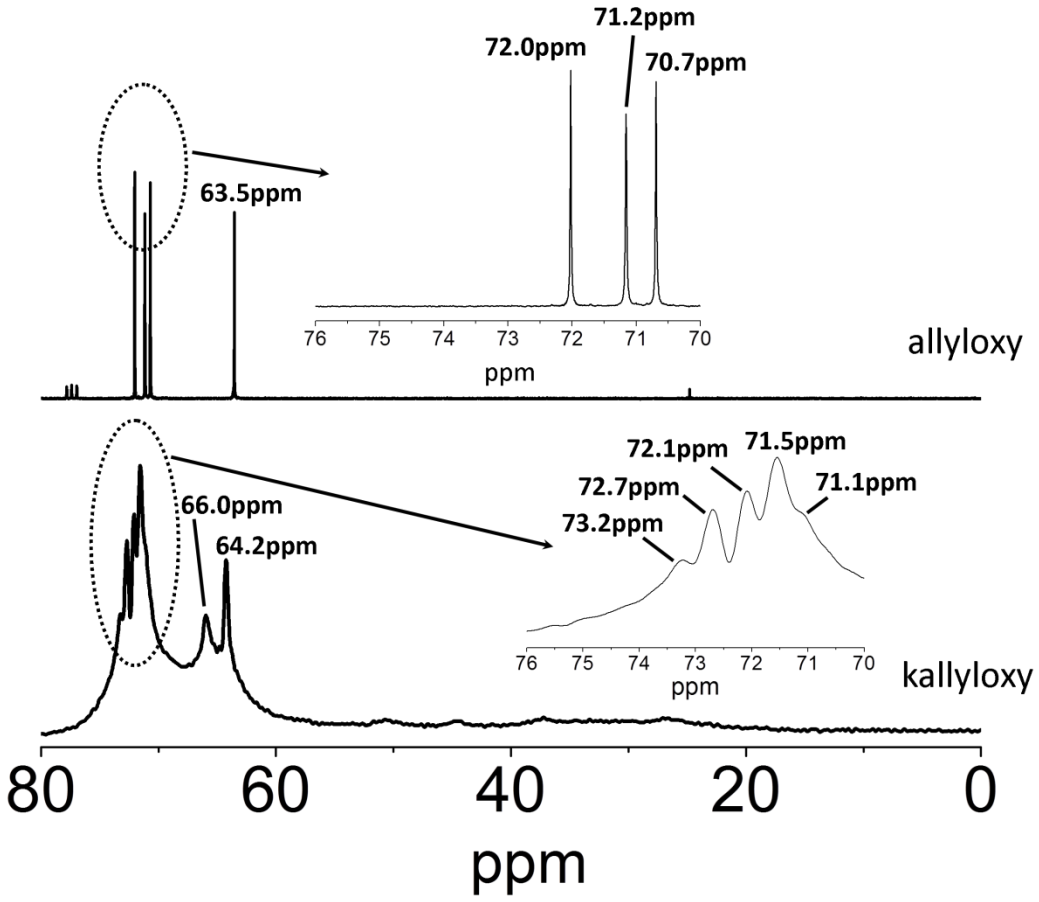

Figure 83: ^{13}C CPMAS NMR of kallyloxy compared to the high resolution liquid ^{13}C NMR spectrum of neat allyloxy. The 80-0ppm region is shown, with details in the 76-70ppm region as insets.

4.2.6 ^{13}C CPMAS with dipolar dephasing NMR results & discussion

The results shown in Figure 84 and Figure 85 show noticeably different relaxation behaviour between the carbon peaks, allowing accurate differentiation between interlayer and surface

adsorbed allyloxy groups. The carbon peaks at 134.2, 126.7, 73.2, 71.1, and 66.0ppm that disappear completely after a 40μs dephasing delay are attributed to interlayer allyloxy carbons while the 135.5, 117.3, 72.7, 72.0, 71.5, and 64.2ppm peaks that do not are attributed to surface adsorbed allyloxy. T_2 constants for each of these carbons were calculated from semi-quantitative analysis of the relaxation data (Figure 86) according to the method described by Alemany *et al.* (1983). Comparing the T_2 values of the two types of allyloxy species, the interlayer species all have T_2 constants below 20μs and the non-interlayer species have T_2 values in excess of this value. These results are summarized in Table 24. This difference in relaxation behaviour is attributed to the decreased mobility of the carbon nucleus when inside the kaolinite interlayer space. This behaviour has been previously shown for a number of intercalated kaolinites (Tunney and Detellier, 1996a; Elbokl and Detellier, 2008) and it offers strong evidence supporting intercalation of the allyloxy compound.

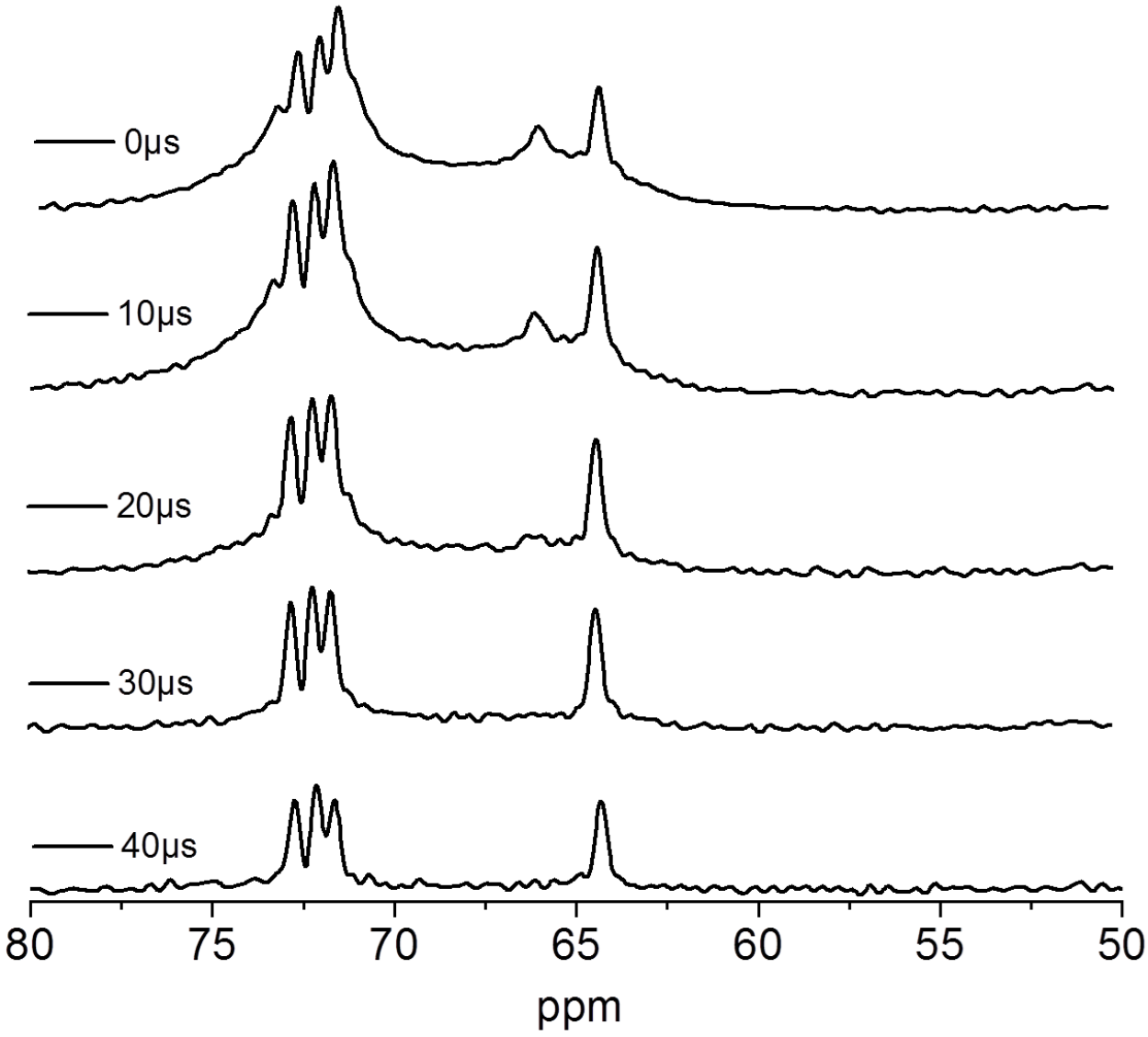

Figure 84: ^{13}C CPMAS NMR with dipolar dephasing of kallyloxy (80-40ppm region) using different dephasing times (μs). The constrained environment of the clay interlayer causes the carbons inside the clay interlayer to fully relax after 40μs, while those that are absorbed on the surface are much less affected.

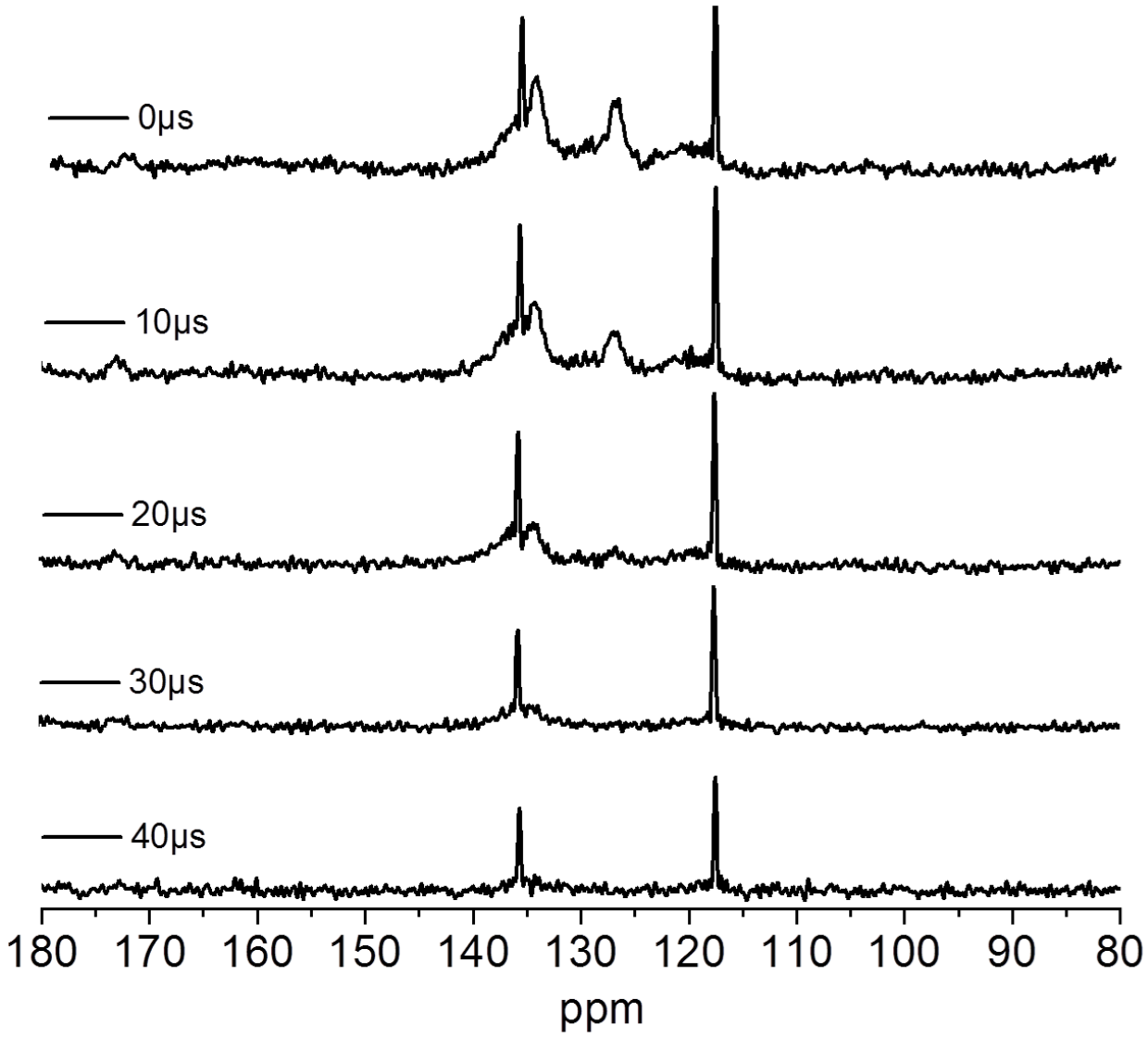

Figure 85: ^{13}C CPMAS NMR with dipolar dephasing of kallyloxy (180-80ppm region) using different dephasing times (μs). The constrained environment of the clay interlayer causes the carbons inside the clay interlayer to fully relax after 40μs, while those that are absorbed on the surface are much less affected.

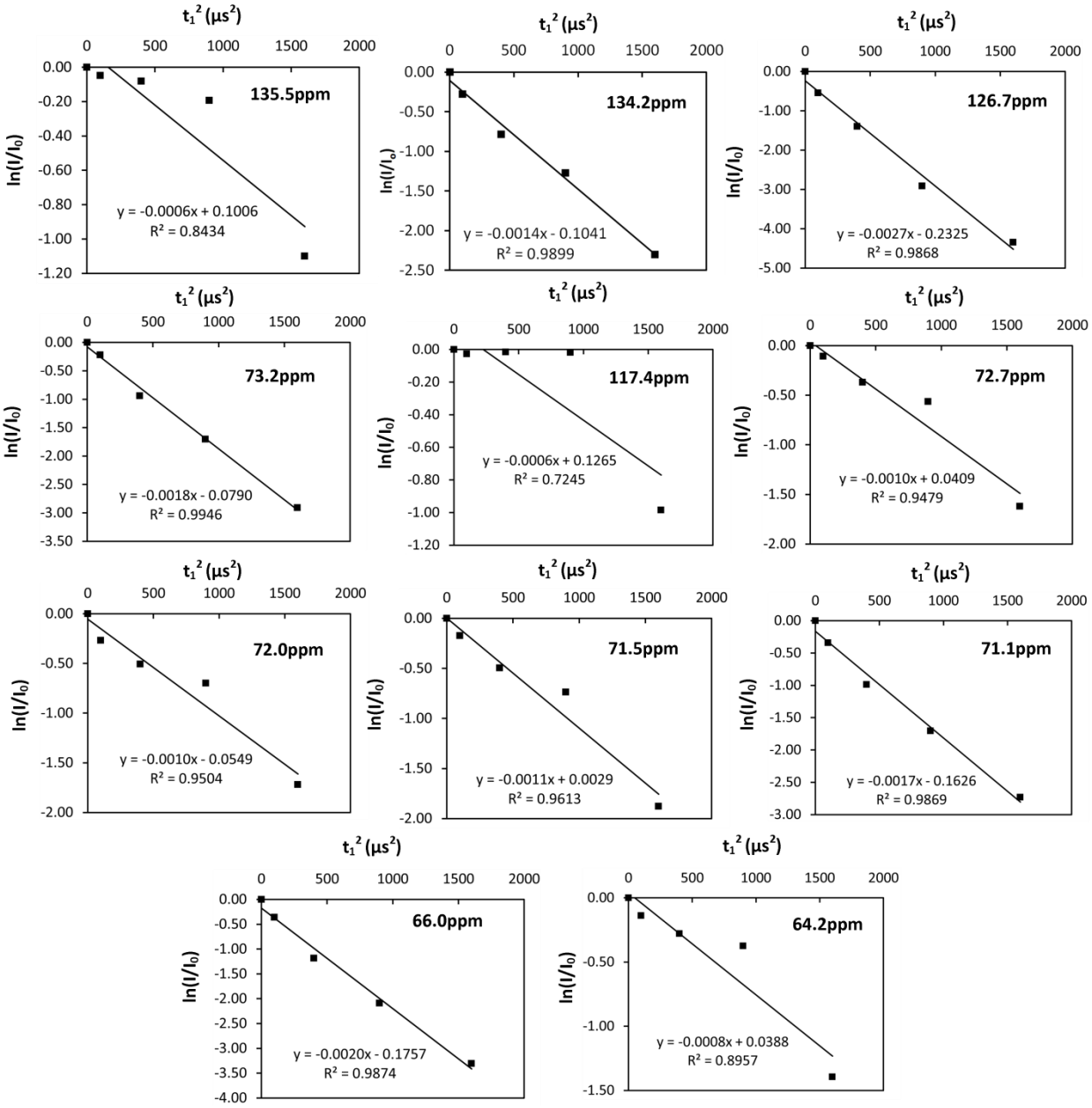

Figure 86: Plots of ^{13}C CPMAS NMR with dipolar dephasing signal as a function of dephasing time (t_1) for kallyloxy. These plots were used to extrapolate T_2 values for each carbon species in the sample.

Table 24: ^{13}C T_2 transverse relaxation times calculated for the carbons in kallyloxy using the plots in Figure 86. T_2 values below 20μs are attributed to carbons inside the clay interlayer space. The T_2 value for the 117.4ppm carbon was not calculated due to the data's poor fit to the linear regression plot.

chemical shift (ppm)	T_2 value (μs)	Location
135.5	28	surface
134.2	19	interlayer
126.7	14	interlayer
117.4	-	surface
73.2	17	interlayer
72.7	23	surface
72.0	23	surface
71.5	21	surface
71.1	17	interlayer
66.0	16	interlayer
64.2	25	surface

4.2.7 ^{29}Si CPMAS NMR results & discussion

^{29}Si NMR results of kallyloxy in Figure 87, shows perturbation of the Si nuclei similar to what is observed in DMSO-kaolinite intercalates. Examination of the ^{29}Si chemicals shifts in kallyloxy shows 3 distinct signals at -91.0, -91.6 and -92.2ppm. These chemical shifts are all characteristic of a tetrahedrally coordinated Q^3 silicate (Dupree *et al.*, 1984; Hayashi *et al.*, 1992a) which is consistent for kaolinite's structure where each silicon is bonded to 3 other O-Si groups and to one O-Al group.

The peaks at -91.0 and -91.6ppm are very similar to the two signals observed in unmodified kaolinite. Thompson (1984; 1985; 1987) and Thompson and Cuff (1985) examined the ^{29}Si NMR spectra for a number of natural and intercalated kaolinites, and concluded that the position of hydroxyl hydrogens was responsible for the different chemical shielding environments observed in ^{29}Si NMR. According to this, the 91.0 ppm peak should be attributed to Si-O groups H-bonded to Al-OH groups on an adjacent layer.

The -92.2ppm peak in kallyloxy is quite similar to the characteristic -92.7ppm peak in kDMSO. Thompson and Cuff (1985) rationalized that this peak arises from intercalated DMSO that orients itself such that one of its methyl groups partially keys into the siloxane rings in the silicon sheet of the clay mineral. This also perturbs DMSO's methyl groups, where two distinct peaks can be observed in its ^{13}C NMR spectrum (Thompson, 1985).It is hypothesized that a similar arrangement is adopted by intercalated allyloxy molecules, where the allyl double bond

is oriented in close proximity to the siloxane macro ring in the silicon sheet such that it is partially keyed-in (Figure 88). This close proximity to the silicon sheet would also be expected to affect the carbon's chemical shift values, which might be the cause behind the 9.3ppm shift observed for the terminal alkene carbon in the ^{13}C NMR spectrum of intercalated allyloxy. These results offer further evidence that allyloxy molecules are in the interlayer space of kallyloxy.

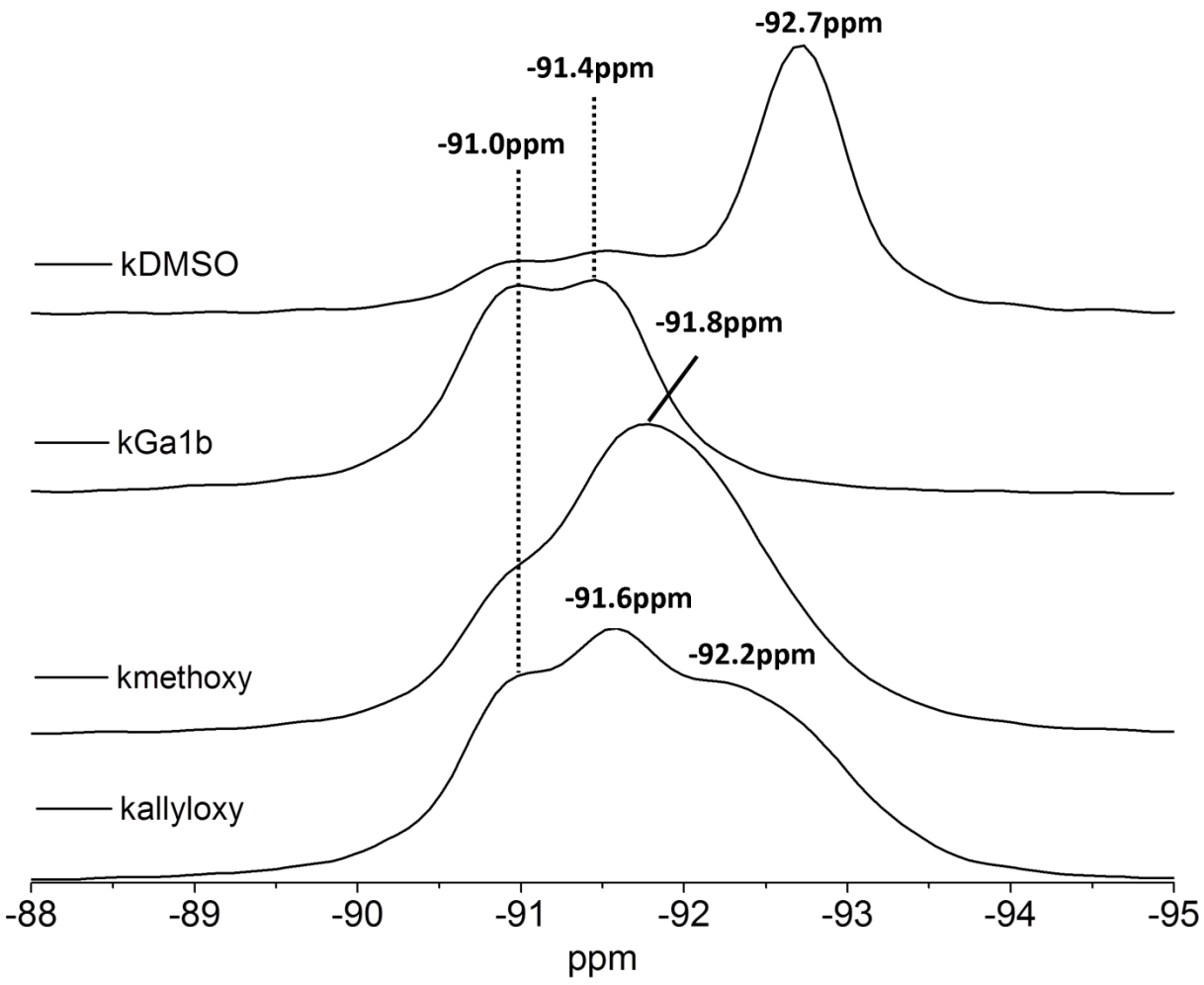

Figure 87: ^{29}Si CPMAS NMR of kallyloxy compared with other natural and modified kaolinites.

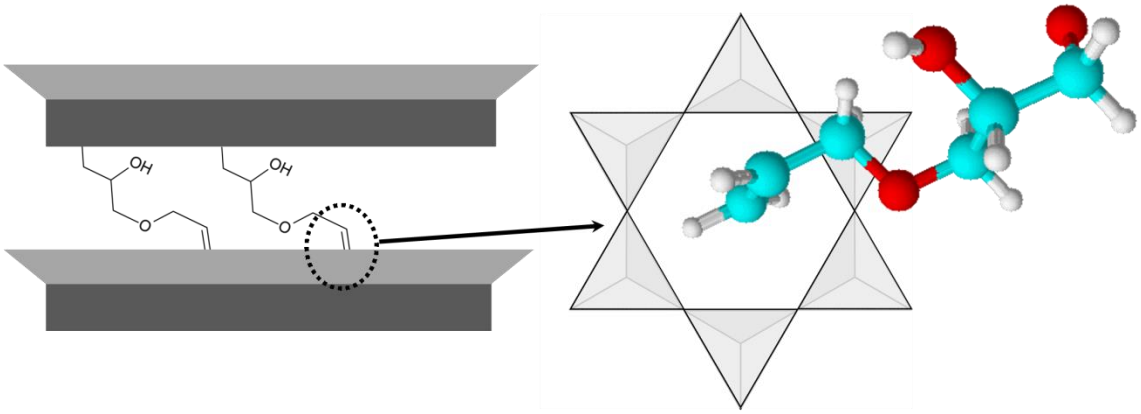

Figure 88: Proposed arrangement of the allyloxy compound in the kaolinite interlayer space.

^{29}Si and ^{13}C data suggest partial keying of the terminal allyl group carbon into the siloxane rings in the clay mineral.

4.2.8 Summary of experiments and conclusions

3-allyloxy-1,2-propanediol was successfully grafted on the inner surfaces of kaolinite using kmethoxy as a precursor while keeping the allyl functionalities fully intact. XRD results indicate a monolayer type arrangement was adopted by the allyloxy molecules, giving a *001* d-spacing of 11.4Å. When the reaction was performed at 90°C, *001* fractions corresponding to kmethoxy or the natural clay mineral were not regenerated when washed in water, indicating covalent grafting was achieved. IR results show the presence of allyloxy CH stretching bands, confirming its presence in the material. New kaolinite inner surface hydroxyl stretching bands were also observed in the place of the ones characteristic of kmethoxy, indicating replacement of the interlayer methoxy with the allyloxy compound. TGA results suggest a mixture of grafted and ungrafted allyloxy molecules in the interlayer, as well as allyloxy adsorbed on the outer surfaces of the clay mineral. ^{13}C CPMAS NMR results show new peaks not observed in the neat liquid spectrum of the allyloxy compound, which are attributed to interlayer allyloxy and surface adsorbed allyloxy. The terminal allyl group carbon is especially perturbed when in the interlayer space, showing a difference of 9.3 ppm compared to the surface adsorbed allyloxy molecule. ^{13}C CPMAS NMR experiments with dipolar dephasing showed a noticeable difference in the relaxation behaviour of the carbons allowing surface and interlayer allyloxy peaks to be accurately identified. ^{29}Si experiments show the appearance of a new peak similar to the one observed in kDMSO, which suggests the interlayer allyloxy partially keys into the siloxane macroring in the silicon sheet.

The success at preparing these materials opens up the possibility of performing in-situ polymerization reactions to yield a grafted polymer on the inner surfaces of the clay mineral. This could possibly be used to prepare an exfoliated nanocomposite material when the individual kaolinite layers are well dispersed in the polymer matrix and hampered from rolling up in a scroll like structure. This type of structure would be expected to impart great mechanical and thermal properties to the resulting material, making it highly desirable for a number of applications requiring these properties.

4.3 Kaolinite functionalized with ethylene glycol vinyl ether

4.3.1 Description of samples

Samples of a kaolinite intercalated and grafted with glycol ether molecules containing polymerizable groups was attempted using ethylene glycol vinyl ether (Figure 89). This compound was purchased from Sigma-Aldrich and used as is. Interlayer modification of kaolinite was done using a technique similar to the one described by Tunney and Detellier (1993), where a kaolinite pre-intercalated with DMSO (kDMSO) is dispersed in a solution containing the glycol ether molecules. Isopropanol was chosen as a solvent for the ethylene glycol vinyl ether solution for the reasons explained for in a previous section for kallyloxy (section 4.2.1). The resulting material is labelled kvinyloxy. This material was washed in water to determine if covalent grafting was achieved and the resulting material is labelled kvinyloxy(w).

The reaction was also attempted at room temperature using a kaolinite pre-intercalated and grafted with methanol (kmethoxy) in a manner similar to what was used to prepare kallyoxy(low T) (section 4.2). This was done to examine the effects of performing the reaction under mild, non-refluxing conditions. This material is labelled kvinyloxy(low T).

To examine the effects the clay mineral plays on catalyzing any side-reactions occurring under the conditions used to prepared kvinyloxy, solutions of vinyloxy and vinyloxy containing a

dispersion of unmodified kaolinite, kGa-1b, were refluxed and analysed. These samples are labelled vinyloxy(c) and vinyloxy(c-kGa-1b) respectively.

Details of the experimental procedures used to prepare samples and the material characterisation results can be found in section 5.2.

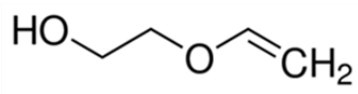

Figure 89: Structure of ethylene glycol vinyl ether

4.3.2 XRD results & discussion

Based on the XRD data shown in Figure 90, kaolinite's interlayer space was successfully functionalized with vinyloxy molecules. The 0.5Å increase of the *001* d-spacing compared to the kDMSO precursor suggests the vinyloxy molecules displaced DMSO from the interlayer space, adopting a monolayer type arrangement inside.

The XRD data of the water washed material shown in Figure 91, suggests a fraction of these interlayer vinyloxy molecules were successfully grafted to the inner surfaces of kaolinite. When the material was washed in water, the *001* d-spacing collapsed from 11.5Å to 10.4Å and 9.4Å. This type of behaviour has been observed before in grafted kaolinites, where the water washed

material experiences a contraction in its interlayer space. For example, Tunney and Detellier (1994), reported 10.8Å and 9.4Å *001* d-spacing values in kaolinites functionalized with ethylene glycol which they attributed to kaolinite intercalated with and grafted with ethylene glycol respectively. Water can also sometimes be intercalated in the interlayer space from these grafted kaolinites, giving values of 10.0Å and 8.4Å (Tunney and Detellier, 1994; Smirnov and Bougeard, 1999). From this, it is hypothesised that the 10.8Å fraction contains grafted vinyloxy groups and the 9.4Å fraction contains intercalated water.

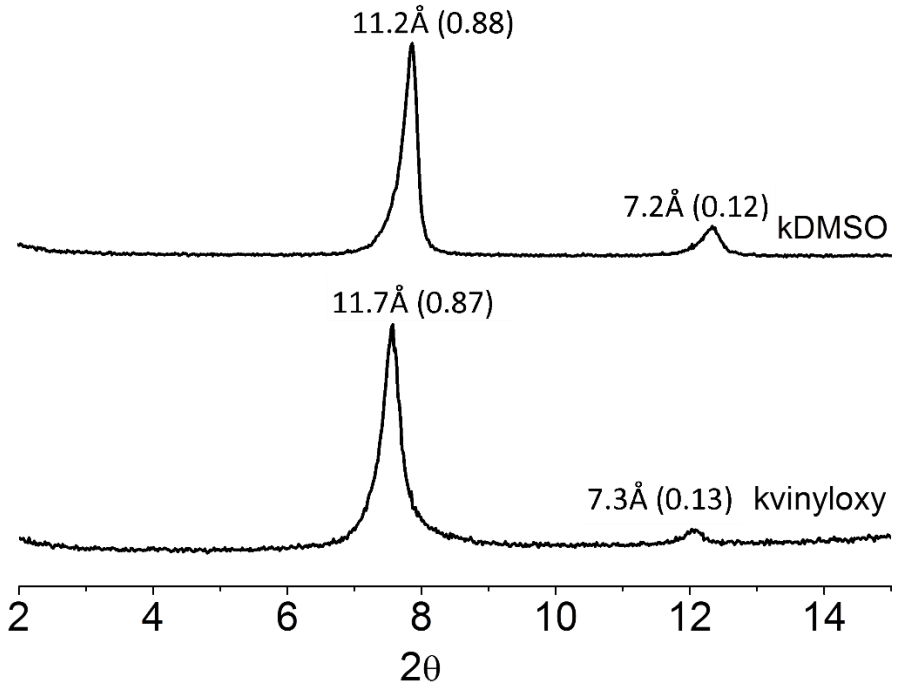

Figure 90: XRD results of kvinyloxy compared to starting kDMSO material.

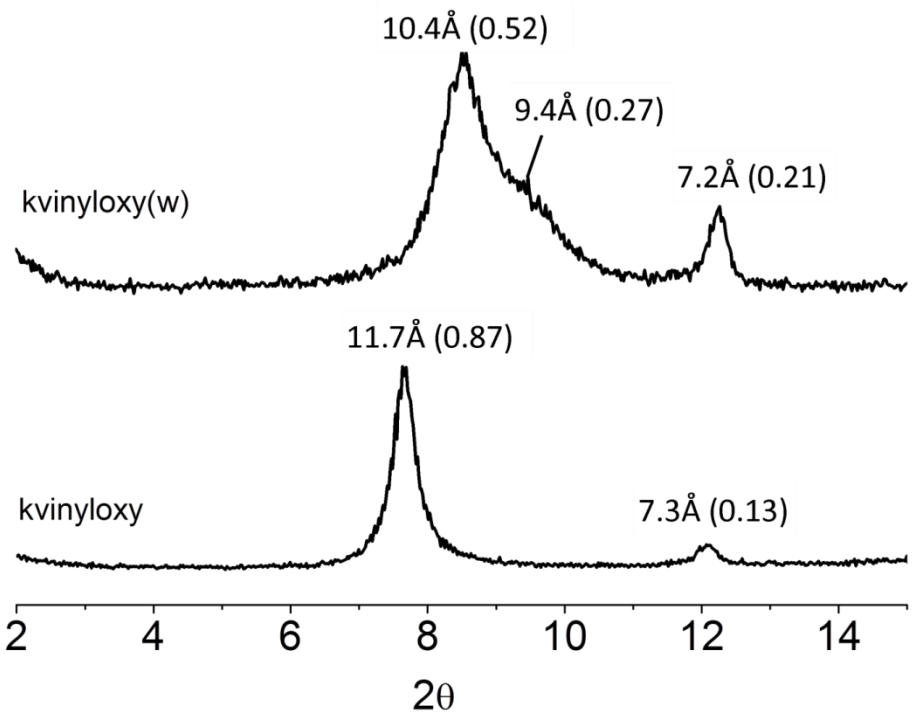

Figure 91: Oriented slide XRD of the washed material, kvinyloxy(w) compared to kvinyloxy.

4.3.3 IR results & discussion

Based on the IR spectrum of kvinyloxy shown in Figure 92, there is strong evidence that DMSO was removed from the kaolinite interlayer space and replaced with vinyloxy molecules. The absence of characteristic bands at 3660, 3536, and 3501 cm^{-1} attributed to kaolinite's inner surface hydroxyls interacting with interlayer DMSO, and DMSO C-H stretching bands 3021cm^{-1} all indicates that DMSO was removed from the interlayer space. The appearance of new bands at 2941 and 2872 cm^{-1}attributed to C-H stretching bands of the vinyloxy molecules, suggests they are present in the material. Additionally, the appearance of new OH stretching bands at 3648 and 3637 cm^{-1} indicates perturbation of the clay mineral's inner surface hydroxyl groups

and suggests that the vinyloxy molecules are present in the kaolinite interlayer space. This is similar, for example, to poly(ethylene glycol) intercalated in the interlayer space of kaolinite where a new inner surface OH stretching band at 3636 cm^{-1} was observed (Tunney and Detellier, 1996a).

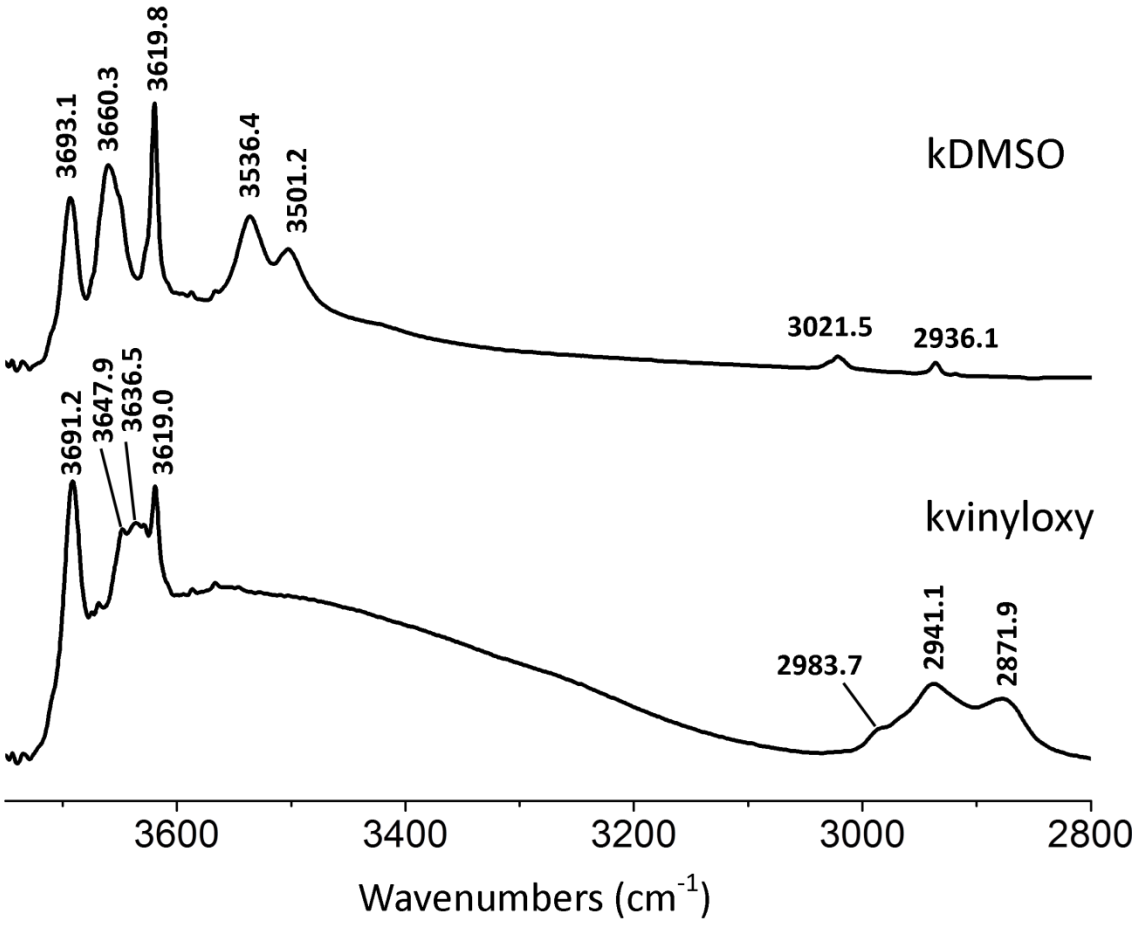

Figure 92: ATR-FTIR of kvinyloxy compared to starting kDMSO precursor.

4.3.4 TGA results & discussion

The TGA weight loss events between 200-400°C for kvinyloxy (Figure 93) suggests the vinyloxy compound is present in the kaolinite interlayer. The 1st derivative curve indicates there are two weight loss events centered at 304 and 352°C. These two events occur at much higher temperature than the boiling temperature of free vinyloxy (143°C), suggesting they are due to the vinyloxy molecules in the clay interlayer.

The shift in the kaolinite's dehydroxylation event to 490°C suggests that vinyloxy molecules are covalently grafted to the clay mineral's inner surfaces. In unmodified kaolinites, this event is normally centered at 512°C and intercalation doesn't have a significant effect on it (Letaief and Detellier, 2011). In kaolinites where compounds are grafted to the clay mineral's inner surfaces, however, dehydroxylation temperatures below 500°C are commonly observed (Janek *et al.*, 2007; Letaief and Detellier, 2011). A dehydroxylation temperature at 490°C in kvinyloxy suggests that vinyloxy molecules were grafted to the clay mineral's inner surfaces. Knowing that the grafted functional groups in kaolinite typically decompose at much higher temperatures than ungrafted ones (Tunney and Detellier, 1996b), it is hypothesized that the two weight loss events observed from the first derivative plot at 304 and 352°C are from the decomposition of ungrafted and grafted interlayer vinyloxy respectively.

There is also an important weight loss event centered at 114°C. This is attributed to a combination of residual DMSO and to vinyloxy adsorbed on the outer surfaces of the clay mineral.

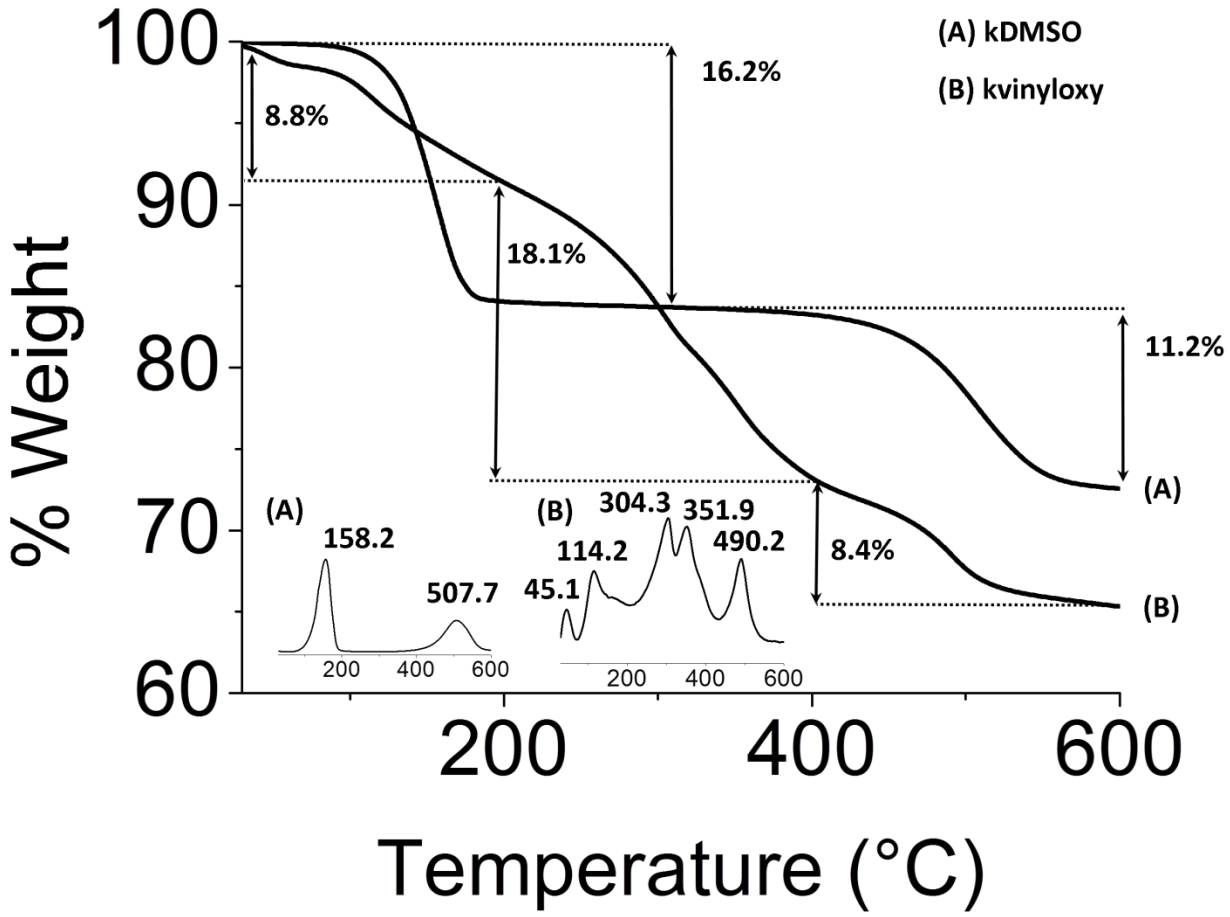

Figure 93: TGA weight loss curve for the pyrolysis of the kDMSO starting material (A) compared to kvinyloxy (B). The 1st derivative weight loss curves are shown as insets.

4.3.5 ^{13}C CPMAS NMR results & discussion

New ^{13}C NMR peaks are observed in kvinyloxy (Figure 94), suggesting that chemical modification of vinyloxy occurred during the synthesis of kvinyloxy This can be seen through the absence of the vinyl carbon peak expected around 150ppm and the appearance of an intense peak at 22.6ppm attributed to either a methyl or methylene carbon not neighbouring an oxygen atom. These peaks could be the result of in-situ polymerization/oligomerization of vinyloxy during the reaction. The complete absence of vinyl carbon peaks in the spectrum suggests all the vinyloxy molecules underwent this conversion. The broad peak from 29-47ppm is attributed to carbon groups on the repeating structure's backbone.

New peaks were also observed at 105.7 and 101.0 ppm, attributed to acetal carbons. The formation of acetals suggests that an intramolecular reaction occurred with the vinyloxy compound. This type of cyclic acetal product has been described previously, where acetals were reported to be produced from ethylene glycol vinyl ether intramolecularly in acidic conditions and with heating (Shostakovsky *et al.*, 1953; Arefalk *et al.*, 2005). This conversion was also observed at room temperature (Figure 95), so it isn't directly a result of the temperatures used for the grafting reaction. These acetal carbons along with the other carbons in the product's structure remained in the ^{13}C NMR spectrum after washing kvinyloxy in water, suggesting this cyclized product is grafted to the clay mineral's inner surfaces. A summary of these peaks and their attribution is shown in Figure 96, and a schematic outlining the interlayer structure of this compound in kaolinite is shown in Figure 97.

An intense carbon peak at 41.0ppm can also be observed, attributed to DMSO methyl carbons. The chemical shift value of this peak is more in line with free DMSO, which suggests that kDMSO's distinct keyed-in methyl structure is lost as a result of the intercalation and grafting of vinyloxy molecules. This peak was removed in the water washed material kvinyloxy(w), which is expected for molecules like DMSO that cannot form covalent bonds with the clay mineral's surfaces.

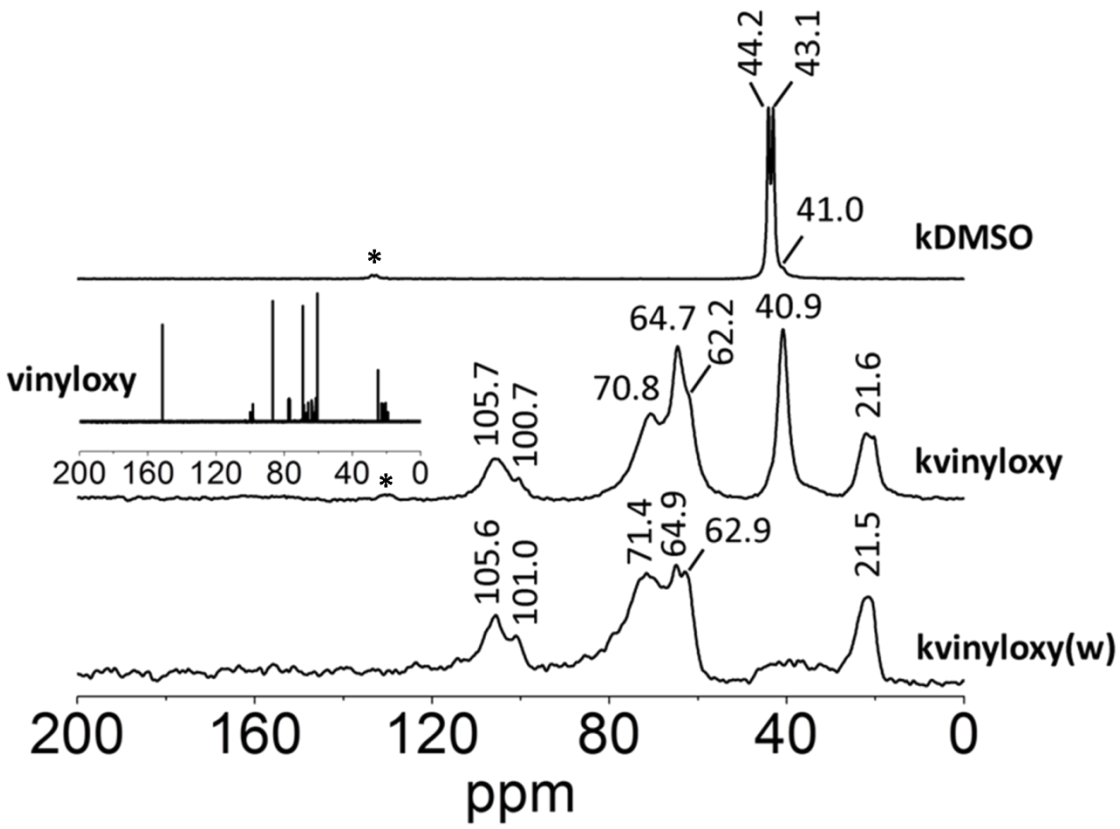

Figure 94: ^{13}C CPMAS NMR spectra of kvinyloxy compared to the water washed material kvinyloxy(w) and kDMSO. Rotational artifacts resulting from MAS are denoted with an asterisk.

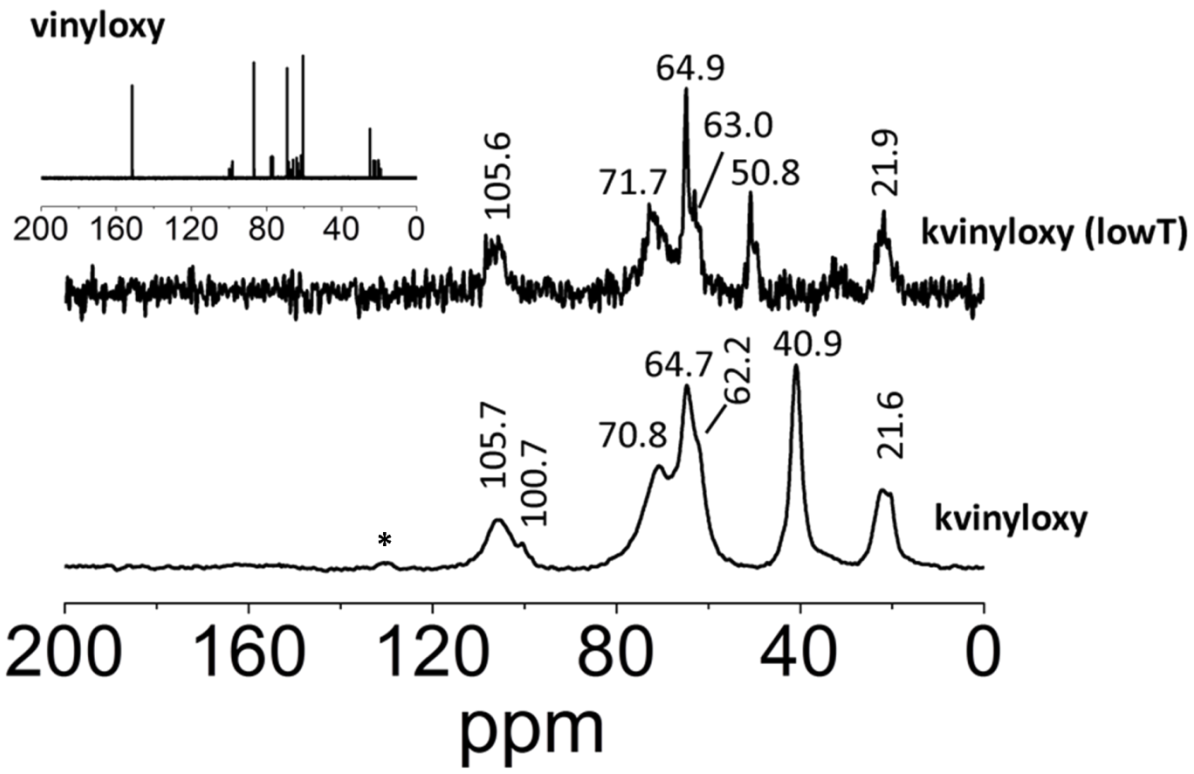

Figure 95: ^{13}C CPMAS NMR spectra of kvinyloxy compared to kvinyloxy prepared at room temperature using a kmethoxy precursor, kvinyloxy (lowT). A high resolution ^{13}C liquid NMR spectrum of the unmodified vinyloxy compound used to prepare kvinyloxy is shown as an inset. Rotational artifacts resulting from MAS are denoted with an asterisk.

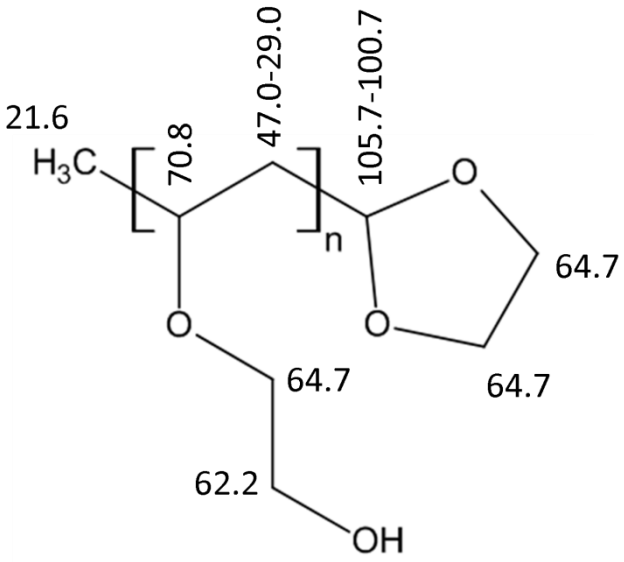

Figure 96: Attribution of the ^{13}C NMR chemical shifts observed in kvinyloxy.

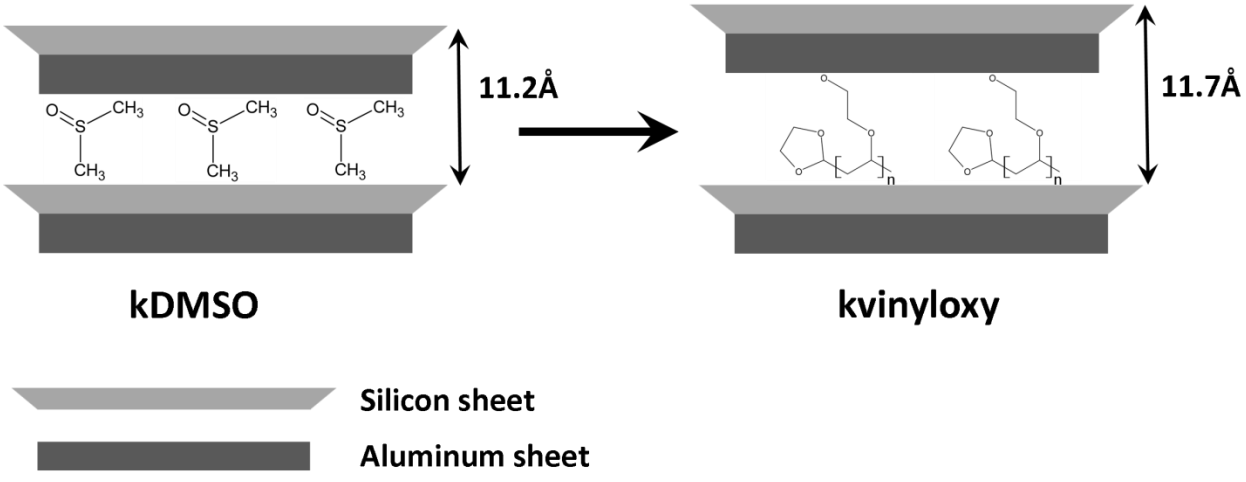

Figure 97: Side view schematic showing the interlayer space of kaolinite in the prepared kvinyloxy material.

4.3.6 Liquid ^{13}C NMR analysis of kaolinite catalyzed acetalization of ethylene glycol vinyl ether

High resolution liquid ^{13}C NMR results shown in Figure 98 indicate that kaolinite plays an important role in the acetalization of vinyloxy. When kGa-1b is absent from the reaction mixture, only a small fraction of the vinyloxy molecules were converted after 5 days under reflux conditions. However, when kGa-1b was added to the mixture, complete conversion of vinyloxy to the acetal product was achieved in 24 hours. This suggests that the clay surfaces play a role in catalyzing this conversion and that this isn't limited to when the vinyloxy molecules are confined in the clay interlayer spaces.

The ^{13}C DEPT NMR results shown in Figure 99 further supports the hypothesis of an intramolecular acetalization occurring. These results indicate the 100ppm resonances are CH carbons and the 22 ppm resonances are CH_3 carbons, which support the hypothesis that these peaks are from acetal and methyl carbons respectively. Based on these ^{13}C DEPT NMR results, a hypothetical mechanism for this intramolecular conversion can be constructed (Figure 100). This mechanism assumes the clay mineral acts as an acid catalyst to activate the vinyl group in vinyloxy, initiating the cationic polymerization/oligomerization. This sort of reactivity is favoured in olefins that contain electron donating groups, such as the $–OCH_2CH_2OH$ group in vinyloxy (Matyjaszewski, 1996). No CH_2 carbon peaks were observed around, so it is probable that the intramolecular reaction occurs much more rapidly than the intermolecular reaction with other vinyloxy molecules. This is in contrast to kvinyloxy, where there is some signal observed in this region. This is possibly due to the grafting of hydroxyl groups in vinyloxy on the

clay mineral surfaces, which will prevent them undergoing the cyclization reaction.

Kaolinite has long been known to exhibit acid/base properties (Brady *et al.*, 1996; Sposito, 2008). The bulk of these properties are believed to originate from defects and edge groups giving rise to protonated -Si-OH and -Al-OH_2OH groups in the clay mineral (Liu *et al.*, 2013). This results in the bulk clay mineral mildly acidic properties, giving a solution pH between 4.5 and 7.0 when in water (Solomon and Murray, 1972). Theoretical pKas have been calculated to be 6.9 and 5.7 for the -Si-OH and -Al-OH_2OH sites respectively (Liu *et al.*, 2013). In non-aqueous media and conditions under which water content is dramatically reduced like high temperature refluxing, these properties are greatly magnified. Under these conditions, kaolinite was reported to catalyze the polymerization of various styrene monomers (Solomon and Murray, 1972). This sort of clay catalyzed cationic polymerization/oligomerization has been reported in the literature (Yahiaoui *et al.*, 2003; Oral *et al.*, 2009), however these usually involve ring opening mechanisms and use smectite clay minerals that have been pre-functionalized with bulky alkyl ammonium salts. This sort of mechanism is not commonly reported for kaolinite.

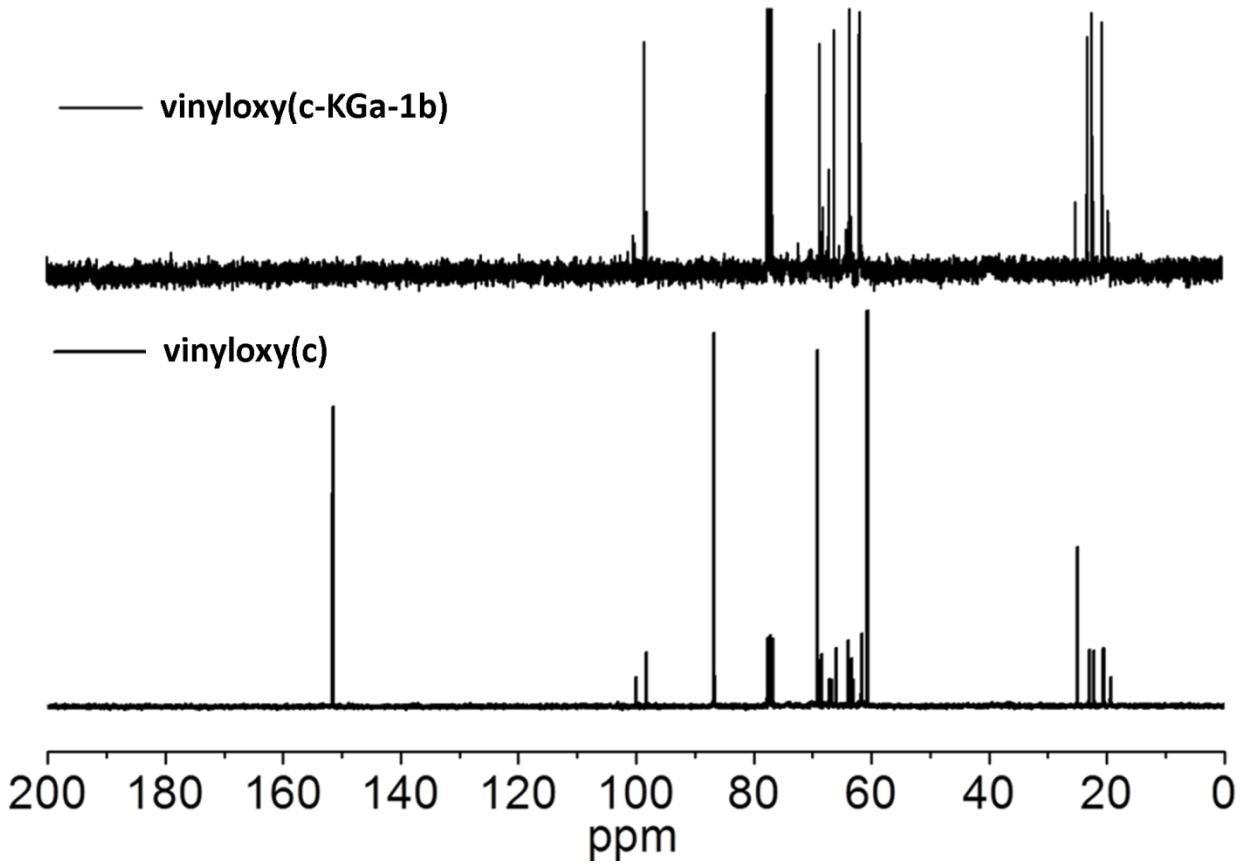

Figure 98: High resolution ^{13}C NMR refluxed solutions of neat vinyloxy (i.e. vinyloxy(c)), and kGa-1b dispersed in vinyloxy, (i.e. vinyloxy(c-kGa-1b)).

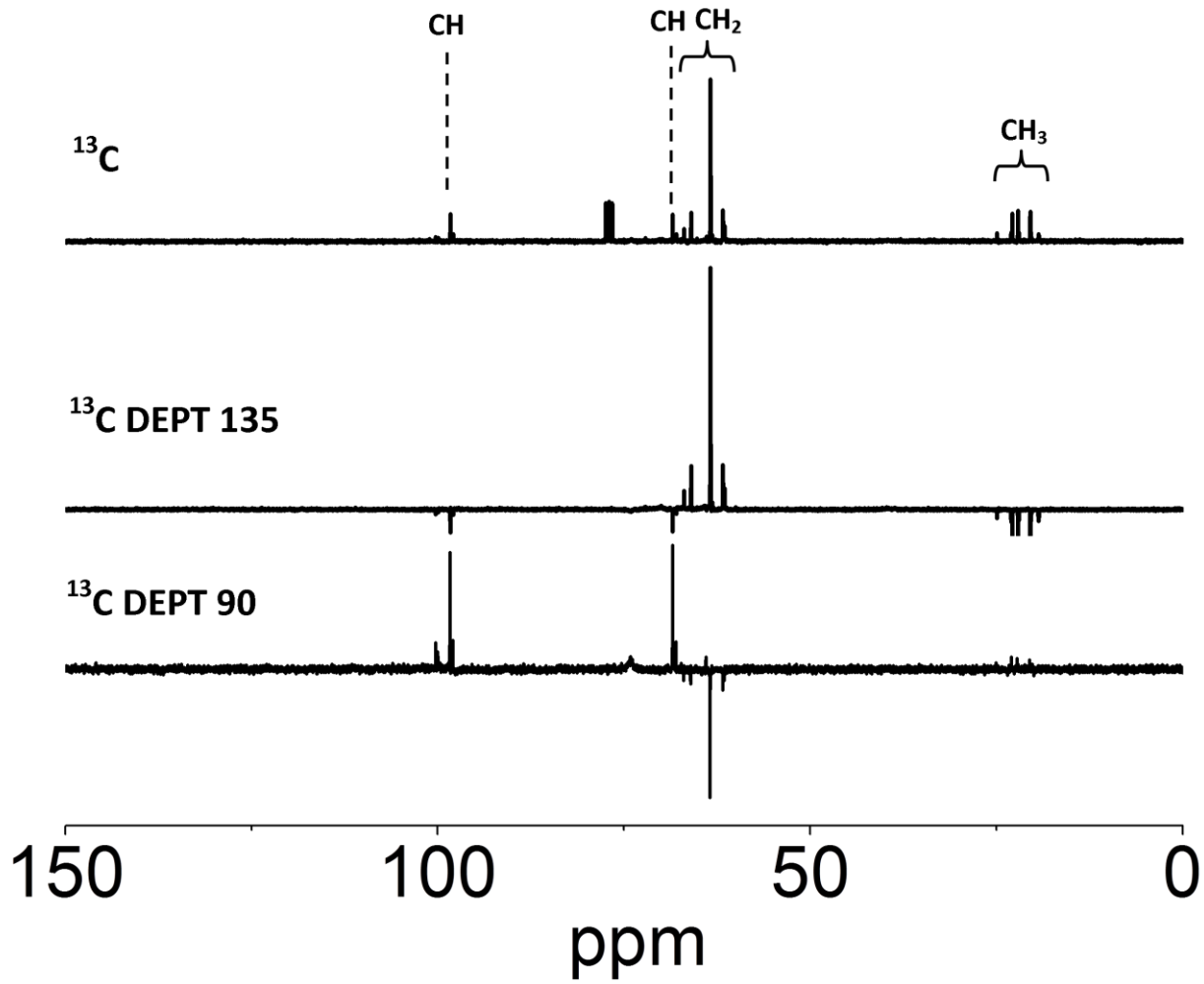

Figure 99: High resolution ^{13}C NMR DEPT experiments of vinyloxy (c-kGa-1b). In DEPT 90, only CH carbons give a positive signal, and in DEPT 135 only CH_2 carbons give a positive signal.

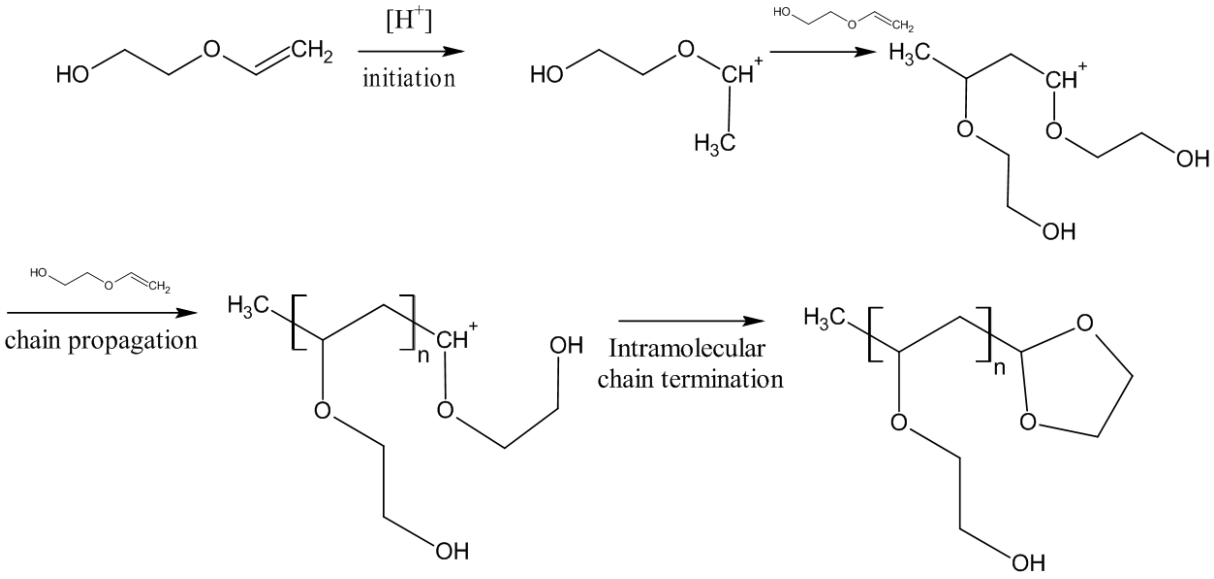

Figure 100: Proposed mechanism for the clay catalyzed acetalization of vinyloxy.

4.3.7 Summary of experiments and conclusions

The interlayer of kaolinite was successfully intercalated with 2-vinyloxy ethanol using a kDMSO precursor and the resulting product was grafted to the clay mineral's inner surfaces. XRD results show an expansion of the *001* d-spacing to 11.7Å, which indicates the vinyloxy molecules adopt a monolayer type arrangement in the interlayer space. Washing the material did not regenerate kaolinite 7.2Å *001* d-spacing value suggesting the vinyloxy are grafted to the clay mineral's inner surfaces. IR results show the appearance of new CH stretching bands and new kaolinite inner surface OH stretching bands attributed to vinyloxy molecules in the interlayer space of the clay mineral. TGA weight loss curves show the appearance of new weight loss events between 300-400°C attributed to decomposition of interlayer vinyloxy molecules, and a drop in the kaolinite dehydroxylation temperature suggesting grafting of vinyloxy groups to the clay mineral's inner surfaces. NMR results show retention of the vinyloxy material in the clay after washing it extensively in water, and the in –situ polymerization/oligomerization and acetalization of vinyloxy. This acetalization was also observed when the reaction was performed at room temperature.

Experiments where vinyloxy was refluxed with kGa-1b produced the same type of acetal product found in kvinyloxy. ^{13}C and ^{13}C DEPT NMR experiments on the liquid product gave results consistent with an acetal product. It is proposed that this product is made from the intramolecular acetalization of vinyloxy with the clay mineral's outer surfaces playing a catalytic role as an acid catalyst. Side reactions of this sort are sometimes observed when preparing

kaolinites with organic compounds grafted to their inner surfaces, however they are often just mentioned as a side note and are not well understood (Tunney, 1995). Kaolinite's catalytic role under these conditions in non-aqueous media presents a possible interesting avenue for future research.

5 Experimental details and supplementary results

5.1 Procedures for material characterisation

5.1.1 Solid state ^{1}H nuclear magnetic resonance

^{1}H MAS NMR experiments were performed by staff at the National Ultrahigh-Field NMR Facility for Solids (1200 Montreal Road (M-40), Ottawa ON K1A0R6). The experiments were done on a Bruker AVANCE II 900 MHz (21.1T) spectrometer equipped with a 4 mm H/X MAS Bruker probe. All experiments used a 90°-90° rotor-synched quadrupolar-echo pulse sequence (p1,p2=4µs; d6=55.6µs; d1=5s) to suppress the proton background signal from the probe and a MAS rate of 18000 Hz. The d1 was found to be sufficient for complete relaxation allowing quantitative analysis of peaks areas.

The chemical shift scale was referenced to the tetramethylsilane (TMS) peak at 0.0 ppm.

5.1.2 Solid state ^{29}Si cross polarization magic angle spinning nuclear magnetic resonance (^{29}Si CPMAS NMR)

Solid state ^{29}Si CPMAS NMR spectra were obtained on a Bruker AVANCE III 200MHz (4.7T) spectrometer equipped with a 7 mm triple resonance MAS probe. The cross polarization pulse sequence used the following parameters: p3=3.75µs; p15=10ms; d1=2.0s. The solid samples were packed into a 7mm zirconia rotor and spun at a frequency of 4000Hz. The chemical shift scale was referenced to the Tetrakis(trimethylsilyl)silane (TMSS) peak at -9.9ppm.

5.1.3 Solid state ^{13}C cross polarization magic angle spinning nuclear magnetic resonance (^{13}C CPMAS NMR)

All analyses were done using the following procedure unless specified otherwise:

Solid state ^{13}C CPMAS NMR spectra were obtained on a Bruker AVANCE III 200MHz (4.7T) spectrometer equipped with a 7 mm triple resonance MAS probe. The cross polarization pulse sequence used the following parameters: p3=3.3µs; p15=2ms; d1=2.0s. The solid samples were packed into a 7mm zirconia rotor and spun at a frequency of 4500Hz. The chemical shift scale was referenced to the glycine peak at 176.5ppm.

kvinyloxy(lowT) was analyzed using the following procedure:

^{13}C CPMAS NMR spectra were obtained on a Bruker AVANCE III 400MHz (9.4T) spectrometer equipped with a 4 mm triple resonance MAS probe. The cross polarization pulse sequence used the following parameters: p3=3.3µs; p15=2ms; d1=2.0s. Samples were packed into a 4mm zirconia rotor and spun at a frequency of 10 kHz. The chemical shift scale was referenced to the glycine peak at 176.5ppm.

5.1.4 ^{13}C CPMAS NMR with dipolar dephasing

5.1.4.1 Description of technique

^{13}C CPMAS with dipolar dephasing is a specialized ^{13}C cross polarization experiment where a dephasing delay (t_1) is inserted in the NMR pulse sequence between the 90° pulse and the acquisition time. The resulting spectral intensities will be highly dependent on the molecular dynamics of the carbon nuclei in the sample (Alemany *et al.* 1983). For example, carbons that are directly bonded to hydrogen (i.e. CH, CH_2) will experience strong dipolar coupling with their bonded hydrogens and will relax more rapidly than carbons without bonded hydrogens such as quaternary and carbonyl carbons. Highly mobile carbon species such as methyl carbons will also relax much more slowly than CH and CH_2 carbons due to the rotational motion allowed compared to a CH or CH_2 carbon. Thus, studying the signal decay as a function of the t_1 time can allow CH_3 and quaternary carbons to be distinguished from CH and CH_2 carbons in a spectrum.

This technique can also be used to study nuclei in a constrained environment, such as carbon species that are intercalated inside kaolinite. Given that an intercalated species' mobility is expected to be greatly diminished when compared to its un-intercalated counterpart, this technique can be employed to distinguish between surface adsorbed and intercalated species in kaolinite (Mercier *et al.*, 1994; Tunney and Detellier, 1996). This behaviour can be expressed numerically as the transverse relaxation time (T_2) for a given carbon nucleus, which is roughly calculated from a plot of the signal decay as a function of dephasing time.

5.1.4.2 Calculation of T_2 values

Alemany *et al.* (1983) reported that for carbons affected by strong ^{13}C-^{1}H dipolar coupling, the rate of ^{13}C signal decay will be described by the following equation:

$$I = I_0 e^{-t_1{}^2 / 2T_2{}^2} \qquad (5.1)$$

Where I is the signal intensity at a given t_1 time and I_0 is the signal intensity at t_1=0. Linearizing the above equation gives:

$$ln\left(\frac{I}{I_0}\right) = t_1{}^2 \times \left(\frac{1}{2T_2{}^2}\right) \qquad (5.2)$$

Plotting $\ln(I/I_0)$ as a function of t_1^2, the T_2 relaxation time can be calculated from the slope (A) of the plot:

$$A = -\frac{1}{2{T_2}^2} \tag{5.3}$$

$$T_2 = \sqrt{-\frac{1}{2A}} \tag{5.4}$$

5.1.4.3 Experimental procedure

Solid state ^{13}C CPMAS with dipolar dephasing NMR spectra were obtained on a Bruker AVANCE III 200MHz (4.7T) spectrometer equipped with a 7 mm triple resonance MAS probe. The cross polarization pulse sequence used the following parameters: p3=3.3µs; p15=2ms; d1=2.0s. Spectra were measured using a dephasing delay, t_1, ranging from 0–40µs.

The solid samples were packed into a 7mm zirconia rotor and spun at a frequency of 4500Hz. The chemical shift scale was referenced to the glycine peak at 176.5ppm.

5.1.5 Low field, Solid state ^{27}Al MAS NMR

Low field, solid state ^{27}Al MAS NMR spectra were obtained on a Bruker AVANCE III 200MHz (4.7T) spectrometer equipped with a 7 mm triple resonance MAS probe. A p1 of 1.4µs and a d1 of 2s were used. The d1 was found to be sufficient for complete relaxation. The solid samples were packed into a 7mm zirconia rotor and spun at a frequency of 5000Hz. The chemical shift scale was referenced to the $Al(NO_3)_3$ peak at 0.0ppm.

5.1.6 High field, Solid state ^{27}Al magic angle spinning nuclear magnetic resonance (^{27}Al MAS NMR)

High field ^{27}Al MAS NMR experiments were performed by staff at the National Ultrahigh-Field NMR Facility for Solids (1200 Montreal Road (M-40), Ottawa ON K1A0R6). The experiments were done on a Bruker AVANCE II 900 MHz (21.1T) spectrometer equipped 4 mm H/X MAS Bruker probe using a MAS rate of 18000 Hz. A p1 of 1µs and a d1 of 2s were used. The d1 was found to be sufficient for complete relaxation. The chemical shift scale was referenced to the $Al(NO_3)_3$ peak at 0.0ppm.

5.1.7 High field Solid state 27Al MQMAS NMR

High field ^{27}Al triple quantum (3Q) MAS NMR experiments were performed by staff at the National Ultrahigh-Field NMR Facility for Solids (1200 Montreal Road (M-40), Ottawa ON K1A0R6). The experiments were performed on a Bruker AVANCE II 900 MHz (21.1T) spectrometer equipped with a 4 mm H/X MAS Bruker probe. All experiments were rotor-synchronized in the F1 dimension (18 kHz spectral width, 55.56 µs evolution period increment) employing a three-pulse z-filter 3QMAS pulse sequence using an MAS rate of 18000 Hz. For each evolution period increment, 48 transients were accumulated using a 1s recycle delay. The total number of evolution period increments was 128. The spectral width in the direct F2 dimension was 100 kHz. The ^{27}Al selective 90° pulse width was 9 µs. The excitation and conversion pulse lengths optimized using 60 kHz of RF power for Al sites with small $C_Q(^{27}Al)$ were 5.75 µs and 1.75 µs respectively. The chemical shift scale was referenced to the $Al(NO_3)_3$ peak at 0.0ppm.

5.1.8 Low field Solid state ^{27}Al MQMAS NMR

Low field ^{27}Al triple quantum (3Q) MAS NMR experiments were performed by staff at the University of Ottawa NMR facility (10 Marie Curie Private, Ottawa ON, K1N 6N5). Experiments were done on a Bruker AVANCE III 200 MHz (4.7T) spectrometer equipped with a 2.5 mm H/X MAS Bruker probe. All experiments were rotor-synchronized in the F1 dimension (25 kHz spectral width, 40 µs evolution period increment) employing a three-pulse z-filter 3QMAS pulse

sequence. Spectra for kGa-1b and kDMSO used a 25kHz MAS rate, while spectra for kmethoxy and kmethoxy(ht) used at 24kHz MAS rate. For each evolution period increment, 1560 transients were accumulated using a 1s recycle delay. The total number of evolution period increments was 48. The spectral width in the direct F2 dimension was 100 kHz. The ^{27}Al selective 90° pulse width was 19 µs. The excitation and conversion pulse lengths optimized using 60 kHz of RF power for Al sites with small $C_Q(^{27}Al)$ were 3.6µs and 1.2 µs respectively. The chemical shift scale was referenced to the $Al(NO_3)_3$ peak at 0.0ppm.

5.1.9 ^{13}C NMR with proton decoupling and ^{13}C DEPT 135/DEPT 90 experiments

Solution ^{13}C NMR spectra with proton decoupling were recorded on a Bruker AVANCE 300 MHz spectrometer (7.0T) equipped with a liquids $^{1}H/^{13}C/^{31}P/^{19}F/^{2}H$ Quatro Nuclear Probe with Z gradient. Samples were dissolved in $CDCl_3$ containing 1%(v/v) TMS and loaded in 5mm glass tubes. The magnetic field was locked to the deuterium signal in $CDCl_3$ and shimmed prior to measurement. The chemical shift scale was referenced to the TMS peak at 0.0ppm.

^{13}C DEPT 135, DEPT 90 experiments were performed in the same manner. These experiments are used to determine the number of hydrogens attached to the carbons in a sample. A DEPT 90 experiment will give positive signals for CH carbons while a DEPT 135 experiment will give a positive signal for CH and CH_3 carbons and a negative signal for CH_2 carbons.

5.1.10 Attenuated total reflectance Fourier transfer infrared analysis (ATR-FTIR)

IR spectra were obtained on a Nicolet 6700 FTIR in attenuated total reflection mode with the SMART diamond ATR attachment. Sample analysis was done by evenly spreading 2-5mg of solid sample and firmly pressing it to the surface of the ATR crystal.

A background spectrum was obtained before each sample was measured. Measurements were taken from 4500 to 650cm^{-1} using an average of 128 scans with a resolution of 4cm^{-1}. Experimental spectra were measured using the same number of scans and spectral resolution as the background.

5.1.11 Powder X-ray diffraction (XRD)

XRD traces were obtained on a Philips PW 3710 diffractometer using a Cu $K\alpha$ radiation source (λ = 1.5406 Å) and a generator voltage and current of 45kV and 40mA respectively.

Sample analysis was done by pressing the solid material into a cylindrical disk with a diameter of ~0.5cm and thickness of ~2mm and mounting them on sample holders made from low diffracting materials.

5.1.11.1 Calculation of d-spacing values

D-spacing values are calculated from the Bragg diffraction equation (Bragg and Bragg, 1913):

$$n\lambda = 2d \sin\theta \qquad (5.5)$$

where n is a positive integer value describing a given lattice plane in a material, d is the lattice spacing, λ is the wavelength of the incident radiation (i.e. 1.5406 Å), and θ is the scattering angle.

5.1.12 Thermal gravimetric analysis

TGA weight loss curves were obtained on a Q500 Thermal Gravimetric Analyzer. 2-10mg of sample solid are loaded on a 50µL, tared high temperature platinum pan and analyzed using a steady temperature ramp program of 10°Cmin^{-1} under an N_2 atmosphere (flow rate 25mL min^{-1}). A 1 minute isothermal temperature hold is done at the beginning of the experiment to allow the sample pan's movements to stabilize after it is loaded inside the furnace.

5.1.13 %CHNS Elemental analysis

Elemental analysis was performed by staff at the G.G. Hatch Stable Isotope Laboratory (25 Templeton Street, Advanced Research Complex (ARC), Faculty of Science, University of Ottawa, Ottawa, ON, K1N 6N5). Samples were weighed into tin capsules which were loaded with standards into an Elementar, Isotope Cube elemental analyser. The loaded samples were then flash combusted with oxygen at about 1800°C and carried by helium through columns of reducing/oxidizing chemicals to get N_2, CO_2, and SO_2. These gases were separated by a trap and purge system of adsorption columns so that the thermal conductivity detector can detect each gas separately. The routine analytical precision for this method is ±0.1%.

5.1.14 Spectral deconvolution and curve fitting ^{1}H NMR spectra

Experimental NMR spectra were fitted with the help of the peak fitting software FityK (Wojdyr, 2010). Peak fitting was done using Voigt curves. Fourier transformation of the free induction decay plot in NMR will ideally give a purely Lorentzian line shape, however in the solid state the line broadening effects from dipolar interactions will produce a Gaussian convolution of this, giving a mixture of these two (Van Vleck, 1948; Kittel and Abrahams, 1953). The Voigt profile is a convolution of these two functions and is commonly used for curve fitting in spectroscopy and crystallography due to the wide variety of line shapes it can simulate (Armstrong, 1967; Langford, 1978).

The rotational sidebands were not included in this analysis, however this will still give an accurate fit since the vast majority of the signal intensity is in the central transition, and the relative signal intensities for each peak in the sidebands is the same as the central transition.

5.1.15 Curve fitting ^{27}Al NMR spectra

Because ^{27}Al is a quadrupolar nucleus, it will produce line shapes that cannot be described by classical curves and requires specialized software for simulating spectra for curve fitting. The experimental ^{27}Al NMR spectra in this work were fitted using Dmfit (Massiot *et al.*, 2002), an

NMR software package with several options for simulating NMR spectra of quadrupolar nuclei. Fitting was done using the built in QUAD function, which allows computation of spectra in static or finite MAS conditions and taking into account 2^{nd} order quadrupolar effects and chemical shift anisotropy. The central (CT) and satellite (ST1, ST2) transitions were simulated for a MAS rate of 5000Hz for the 4.7T spectra and 18000Hz for the 21.1T spectra using 10 and 2ppm of Gaussian line broadening respectively. The chemical shift anisotropy effects on the spectra were assumed to be negligible (Paris, 2014), and were not included in this analysis.

5.2 Procedures for sample preparation and material characterisation results

5.2.1 kGa-1b

KGa-1b is a highly crystalline, low defect kaolin (Hinckley Index = 1.09) obtained from the Clay Mineral Society's Source Clay Repository (The Clay Minerals Society, 3635 Concorde Pkwy Suite 500, Chantilly VA 20151-1110, USA). A full summary of the material and the sampling methods used to obtain it are described by Pruett and Webb (1993) and from the supplier.

Its chemical composition is characteristic of a highly pure, fine grained Georgia kaolin. Its particle size distribution indicates it contains 90% clay, where 57.8% of it is <2µm and 32.0% is <0.5µm. TiO_2 in the form of Anatase is the only significant impurity, however trace amounts of potassium, calcium, sodium, magnesium, iron and manganese are also present. A small amount of silicon in the tetrahedral sheet is substituted for aluminum, giving the material a very slight cation exchange capacity of 2.0 m_{eq}/100g. This is summarized in the following structure:

$(Mg_{0.02}Ca_{0.01}Na_{0.01}K_{0.01})[Al_{3.86}Fe(III)_{0.02}Mn_{(trace)}Ti_{0.11}][Si_{3.83}A_{0l.17}]O_{10}(OH)_8$

The <2µm clay fraction containing kaolinite was isolated by sedimentation using a method similar to previously published procedures (Jeffries and Jackson, 1949). 60g of kGa-1b was dispersed in 4L of distilled water by mechanical stirring in a beaker. The pH of the solution was

then adjusted to 9.0 by addition of 0.1N NaOH. This created a stable suspension of the clay particles in solution. Stirring was then stopped, and the solution was allowed to settle for 6 hours. The top 2/3 of the solution was siphoned off and set aside. The remaining solution was then re-dispersed in distilled water and the sedimentation procedure was repeated 3 more times. The four siphoned solutions were combined and the pH was adjusted to 6.0 by addition of 0.1N HCl. This rapidly flocculated the clay particles. The supernatant solution was decanted off as much as possible without loss of solids and discarded. The remaining solution containing the dispersed solids was evenly partitioned into four 700mL centrifugation vessels, their masses were equalized by addition of distilled water, and the vessels are were centrifuged at high speed until the solid material was completely deposited. The supernatant was discarded, the solids were re-dispersed in 300mL of distilled water, and the centrifugation procedure was repeated two more times. The final, isolated solids were combined and oven dried at 80°C for 24h.

Characterization results:

XRD (Å (intensity %)):d_{001}=7.16Å(89);d_{020}=4.47(22); $d_{1\text{-}10}$, d_{110}=4.37(29); $d_{11\text{-}1}$=4.19(26);$d_{1\text{-}1\text{-}1}$=4.15(21); $d_{02\text{-}1}$=3.86(17); d_{021}=3.75(11); d_{002}=3.58(100); TiO_2 (anatase) = 3.53(22); d_{111}=3.38(12); $d_{20\text{-}1}$=2.57(28); $d_{13\text{-}1}$=(20); d_{200}=2.50(32); d_{003}=2.39(25); $d_{20\text{-}2}$, $d_{1\text{-}32}$=2.34(47); d_{131}=2.30(33); $d_{20\text{-}3}$, $d_{1\text{-}32}$=1.99(20); $d_{20\text{-}3}$, $d_{1\text{-}32}$=1.94(12); $d_{13\text{-}3}$=1.90(13); $d_{1\text{-}3\text{-}3}$, d_{202}=1.84(11); d_{004}=1.79(14); $d_{24\text{-}1}$=1.69(13); $d_{20\text{-}4}$, $d_{1\text{-}33}$, $d_{1\text{-}5\text{-}1}$=1.67(28); $d_{1\text{-}51}$, d_{133}=1.62(17); $d_{2\text{-}2\text{-}4}$, $d_{1\text{-}3\text{-}4}$, $d_{31\text{-}3}$, d_{203}=1.54(12); d_{060}, $d_{33\text{-}1}$, $d_{3\text{-}3\text{-}1}$ = 1.49(35).

TGA (% weight lost (1st derivative peaks)): RT-300°C= 0.6%; 300-650°C=13.2% (516.4°C).

IR (ATR, cm^{-1}) : v(OH):3688.0 (m), 3668.2 (w), 3650.9(w), 3618.8(m); SiO vibrations: 1114.7(m), 1029.2(s), 1001.4(vs), 797.7(m), 786.0(m), 750.8(m), 676.4(m); δ(Al-OH): 937.7(m), 910.4(m).

Elemental analysis (%w/w): C=0.06; H=1.55; N=0.00; S=0.00.

^{29}Si CPMAS NMR (ppm):-90.9, -91.5.

5.2.2 kDMSO

The procedure used to prepare kDMSO is similar to the one described by Olejnik *et al.* (1968). 10g of kGa-1b was dispersed in a mixture of 60mL of dimethyl sulfoxide and 0.1mL of deionized water at 80°C for 3 weeks. The resulting solid product was isolated by centrifuging at high speed until all solid matter was deposited, and the supernatant solution was discarded. The solid was washed by dispersing it in 200mL of isopropanol, the solution was centrifuged at high speed until all solid matter was deposited, and the supernatant solution was discarded. This washing procedure was repeated three times. The final solid was oven dried at 80 C overnight.

Characterization results:

XRD (Å (I.R.)): d_{001}=11.22(0.88); d_{001}(residual kGa-1b)=7.18(0.12).

TGA (% weight lost (1st derivative peaks)): RT-300°C= 16.2% (158.2°C); 300-650°C=11.2% (507.7°C).

IR (ATR, cm^{-1}) : v(OH):3693.1 (m), 3660.3 (m), 3651.1(m), 3619.8(m), 3536.4 (m), 3501.2(m), 3420.7(vw, br); v(CH): 3021.5(w), 2936.1(w); δ(CH): 1428.5(vw), 1405.4(vw), 1393.3(vw), 1317.6(vw), 957.5(m); v(S=O): 1090.9(w); δ(AlOH): 938.0(m), 903.0(m); SiO vibrations: 1121.9(m), 1034.7(s), 1005.2(vs), 788.3(m), 742.0(m), 669.5(m).

Elemental analysis (%w/w): C=4.97; H=2.55; N=0.00; S=6.22.

^{13}C CPMAS NMR (ppm): 44.2, 43.1, 41.0(trace).

^{29}Si CPMAS NMR (ppm):-90.9, -91.5, -92.7.

5.2.3 kmethoxy

A kaolinite expanded by N-methyl formamide (kNMF) was used as a precursor to prepare kmethoxy. While more toxic than DMSO, NMF will intercalate very effectively inside kaolinite at even room temperature (Olejnik, 1970), and this precursor is commonly used to prepare a methanol grafted kaolinite at room temperature conditions (Komori *et al.*, 2000).

The method used for preparing kNMF is similar to the one described by Olejnik (1970). 10g of kGa-1b was dispersed in 750mL of N-methyl formamide at room temperature for 3 weeks. The

resulting solid material was then isolated by centrifugation high speed until all solid matter was deposited. The solid was washed by dispersing it in 100mL of isopropanol, centrifuging it as described above, and discarding the supernatant solution. The solid was then air dried at room temperature. NMF's intercalation was confirmed through a combination of XRD and ^{13}C CPMAS NMR. XRD results showed a 10.8Å expanded *001* d-spacing reflection, which was very similar to the 10.7Å one reported by Olejnik (1970). The intensity of the 10.8Å reflection compared to the 7.2Å one indicated an intercalation ratio of 0.88. ^{13}C CPMAS NMR showed two resonances at 164.3 and 26.9ppm which were attributed to the NMF carbonyl and methyl group respectively.

The kNMF precursor was then used to prepare kmethoxy in a method similar to the one described by Komori *et al.* (1998). 10g of kNMF was dispersed in 200mL of methanol at room temperature for 48h. This solid material was isolated by centrifugation at high speed until all solid matter was deposited, and the supernatant was discarded. The solid was re-dispersed in 200mL of methanol and this sequence was repeated 6 times. The final solid product was air dried at room temperature.

Characterization results:

XRD (Å (I.R.)): d_{001}=8.64(0.88); d_{001}(residual kGa-1b)=7.20(0.12).

TGA (% weight lost (1st derivative peaks)): RT-300°C= 2.6% (148.0°C); 300-650°C=13.7% (480.7°C).

IR (ATR, cm^{-1}) : v(OH): 3690.9(m), 3670.9(2), 3647.4(2), 3620.9(w), 3524.3(w, br), 3273.6 (vw); v(CH):2975.2(vw), 2956.4(vw), 2918.3(vw), 2842.6(vw); δ(HOH):1652.7(w); δ(AlOH): 940.0(m), 903.5(s); SiO vibrations: 1123.2(m), 1034.2(s), 998.2(vs), 858.8(m), 793.1(m), 747.0(m), 650.0(m, br).

Elemental analysis (%w/w): C=1.52; H=1.97; N=0.05; S=0.00.

^{13}C CPMAS NMR (ppm): 50.5.

^{29}Si CPMAS NMR (ppm):-90.9, -91.7.

5.2.4 kmethoxy(ht)

This material was prepared previously in the manner described by Tunney (1995). The general procedure used was as follows: 5g of a kaolinite: DMSO intercalated complex were mixed with 160mL of anhydrous methanol in a glass-lined autoclave vessel and sealed. The vessel was then heated in an oil bath at a temperature held between 190-270°C for 89 hours. The pressure inside the vessel while heating ranged from 200-630 psig. Afterwards, the vessel was allowed to cool to room temperature, unsealed and the resulting solid product inside was isolated by filtration and washed with 40mL of methanol. The solid product was then dried at 100°C for 1 hour.

Characterization results:

XRD (Å (I.R.)): d_{001}=8.46(0.88); d_{001}(residual kGa-1b)=7.19(0.12).

Elemental analysis (%w/w): C=2.35; H=2.01; N=0.00; S=0.05.

TGA (% weight lost (1st derivative peaks)): RT-300°C= 1.84% (37.0°C); 300-650°C=13.5% (478.4°C).

^{13}C CPMAS NMR (ppm): 49.4.

^{29}Si CPMAS NMR (ppm):-90.9, -92.1.

5.2.5 kGa-1b-d

100mg of kGa-1b was added to 5mL of D_2O in a glass vial. The vial was capped, and the resulting suspension is stirred magnetically at room temperature for 3 days.

The solid matter was isolated by centrifuging the suspension high speed until all solid matter was deposited, and supernatant solution was discarded. The deposited solid was then transferred to an evaporation dish by rinsing it with 2-3mL of acetone, and the solid was oven dried at 70°C for 1 h. The dried solid was then stored in a desiccator under nitrogen prior to analysis.

Characterization results:

TGA (% weight lost (1st derivative peaks)): RT-300°C=0.5%; 300-650°C =13.4% (508.9)

IR (ATR, cm^{-1}) : ν(OH): 3687.7(m), 3669.4(w), 3650.3(w), 3619.7(m); δ(HOH):1640.3(vw); δ (AlOH): 932.2(m), 908.8(s); SiO vibrations: 1114.2(m), 1024.5(s), 996.0(vs), 798.9(m), 747.6(m), 685.9(m, br).

5.2.6 kDMSO-d

100mg of kDMSO was added to 5ml of D_2O in a glass vial. The vial was capped, and the resulting suspension was stirred magnetically at room temperature for 3 days.

The solid matter was isolated by centrifuging the suspension at high speed until all solid matter was deposited, and supernatant solution was discarded. The deposited solid was then transferred to an evaporation dish by rinsing it with 2-3mL of acetone, and the solid was oven dried at 70°C for 1 h. The dried solid was then stored in a desiccator under nitrogen prior to analysis.

Characterization results:

TGA (% weight lost (1st derivative peaks)): RT-300°C= 1.7% (211.2°C); 300-650°C=14.3% (505.6°C).

IR (ATR, cm^{-1}) : ν(OH): 3692.1(m) , 3664.7(w), 3653.1(w), 3620.8(m); ν(OD): 2725.4(m), 2709.5(w), 2696.4(w), 2676.3(w), 2632.4(vw), 2594.6(vw); δ (AlOH): 938.7(m), 910.2(s); SiO vibrations: 1113.7(m), 1025.5(s), 998.8(vs), 791.2(m), 745.0(m), 716.0(m), 683.2(m, br).

Elemental analysis (%w/w): C=0.60; H=1.71; N=0.00; S=0.24.

5.2.7 kmethoxy-d

100mg of kmethoxy was added to 5ml of D_2O in a glass vial. The vial was capped, and the resulting suspension is stirred magnetically at room temperature for 3 days.

The solid matter was isolated by centrifuging the suspension at high speed until all solid matter was deposited, and supernatant solution was discarded. The deposited solid was then transferred to an evaporation dish by rinsing it with 2-3mL of acetone, and the solid was oven dried at 70°C for 1 h. The dried solid was then stored in a desiccator under nitrogen prior to analysis.

Characterization results:

TGA (% weight lost (1st derivative peaks)): RT-300°C= 3.2% (151.8°C); 300-650°C=14.4% (509.63°C).

IR (ATR, cm^{-1}) : v(OH): 3692.1(m) , 3668.2(w), 3649.4(w), 3619.3(m); v(OD): 2744.2(w, br), 2726.7(m, br), 2700.9(m, br), 2680.5(m, br), 2670.5(m), 2633.8(m, br), 2593.9(m); δ(HOH): 1652.0(vw); δ(DOD): 1456.5(vw); δ (AlOH): 938.7(m), 903.0(s); SiO vibrations: 1125.8(m), 1029.3(s), 999.6(vs), 796.8(m), 745.0(m, br), 716.0(m), 683.2(m, br).

Elemental analysis (%w/w): C=0.67; H=1.91; N=0.00; S=0.00.

5.2.8 kPEPEG2250

1g of poly(ethylene)-block-poly(ethylene glycol) (M_n=2250 Da) was heated to 150°C with stirring until a homogenous, viscous melt was obtained. 0.1g of kDMSO was added to this, and the resulting mixture was dispersed at 150°C under a gentle flow of nitrogen for 5 days. The solid product was dispersed in hot toluene, the resulting solution was centrifuged until all solid matter was deposited, and the supernatant was discarded. This was repeated until the supernatant solution was clear. The isolated solid was then washed in room temperature isopropanol using the aforementioned centrifugation procedure, and dried at 70°C overnight.

Characterization results:

XRD (Å (I.R.)): d_{001}=11.00(0.88); d_{001}(residual kGa-1b)=7.11(0.12).

TGA (% weight lost (1st derivative peaks)): RT-250°C= 6.8% (49.1, 158.9°C); 250-600°C=24.4% (294.4, 357.3, 379.1, 395.9, 431.7, 503.7°C).

IR (ATR, cm^{-1}): v(OH):3691.1 (m), 3668.0 (w), 3648.8(m), 3618.8(m), 3499.3 (w, br); v(CH): 3025.8(vw), 2950.8(w), 2916.8(m), 2883.7(w, br),2848.4(w), 2809.4(vw); δ (HOH): 1646.4(vw); δ(CH): 1472.2(vw), 1462.3(vw), 1447.3(vw), 1356.7(vw), 1316.7(vw), 1271.8(vw), 1246.3(vw); v(CO): 1043.8(s); δ(AlOH): 938.7(m), 906.9(s); SiO vibrations: 1121.9(m), 1043.8(s), 999.0(vs), 850.9(m), 797.4(m), 783.3(m), 745.8(m), 651.7(m, br).

^{13}C CPMAS NMR (ppm): 71.5, 70.1, 41.0(DMSO, trace), 31.9, 29.6(trace), 23.5(trace), 13.8(trace).

5.2.9 kPEPEG920

1g of poly(ethylene)-block-poly(ethylene glycol) (M_n=920 Da) was heated to 150°C with stirring until a homogenous, viscous melt was obtained. 0.1g of kDMSO was added to this, and the resulting mixture was dispersed at 150°C under a gentle flow of nitrogen for 5 days. The solid product was dispersed in hot toluene, the resulting solution was centrifuged until all solid matter was deposited, and the supernatant was discarded. This was repeated until the

supernatant solution was clear. The isolated solid was then washed in room temperature isopropanol using the aforementioned centrifugation procedure, and dried at 70°C overnight.

This gave a material that was nearly identical to kPEPEG2250.

5.2.10 kPEPEG575

1g of poly(ethylene)-block-poly(ethylene glycol) (M_n=575Da) was heated to 150°C with stirring until a homogenous, viscous melt was obtained. 0.1g of kDMSO was added to this, and the resulting mixture was dispersed at 150°C under a gentle flow of nitrogen for 5 days. The solid product was dispersed in hot toluene, the resulting solution was centrifuged until all solid matter was deposited, and the supernatant was discarded. This was repeated until the supernatant solution was clear. The isolated solid was then washed in room temperature isopropanol using the aforementioned centrifugation procedure, and dried at 70°C overnight.

This gave a material that was nearly identical to kPEPEG2250.

5.2.11 kPEPEG2250(w)

200mg of kPEPEG2250 was added to 200mL of water and the resulting mixture was dispersed at room temperature for 48h. The solid material was isolated by centrifuging the resulting solution until all solids were deposited, and the supernatant solution was discarded. The isolated solid was then washed once in 100mL of isopropanol and isolated by centrifugation as described above. The solid was then heated at 180°C for 24h under nitrogen.

Characterization results:

XRD (Å (I.R.)): d_{001}=11.08(0.86); d_{001}(residual kGa-1b)=7.17(0.14).

TGA (% weight lost (1st derivative peaks)): RT-250°C= 1.6% (56.6°C); 250-600°C=27.4% (285.1, 366.4, 386.6, 408.1, 439.1, 503.9°C).

IR (ATR, cm^{-1}) : ν(OH):3691.6 (m), 3668.5 (w), 3647.3(m), 3619.3(m), 3692.0 (w, br); ν(CH): 2953.0(w), 2917.8(m), 2887.4(w), 2848.9(w); δ(HOH): 1647.9(vw); δ(CH): 1472.9(vw), 1463.2(vw), 1445.4(vw), 1357.7(vw), 1317.6(vw), 1270.9(vw), 1246.8(vw); ν(CO): 1039.9(m); δ(AlOH): 938.2(m), 907.4(s); SiO vibrations: 1121.9(m), 1039.9(m), 999.4(vs), 855.8(m), 797.0(m), 743.4(m), 650.9(m, br).

^{13}C CPMAS NMR (ppm): 70.0(broad), 31.9.

5.2.12 kurea

Urea was one of the first compounds that was shown to intercalate inside kaolinite (Weiss, 1961) and to this day it remains one of the few that can intercalate inside an unexpanded kaolinite (Lagaly *et al.*, 2013). While solution based methods were classically used to prepare kaolinite-urea intercalates (Ledoux and White, 1966c), solid state mechanochemical intercalation methods are a very efficient alternative, where intercalation ratios close to 1.0 can be achieved in 1-2 hours (Makó *et al.*, 2009). This gives a much less crystalline final material, but not to the extent that the clay mineral is completely amorphized.

Kurea was prepared mechanochemically in a procedure similar to the one described by Letaief *et al.* (2006). 8g of solid urea was manually ground for 5min with a mortar and pestle. The resulting solid was then mechanically ground together in a ball mill using Al_2O_3 beads without any solvent for 30min. The solid was removed from the mill, ground manually for 1min with a mortar and pestle, and ball milled again for 30min. This sequence was repeated four times. The resulting solid material was washed by dispersing it in 200mL of isopropanol, centrifuging the resulting solution until all solids are deposited, and the supernatant solution was discarded. This washing procedure was repeated seven more times, which eliminated any crystalline urea peaks in XRD at 2θ angles of 22.2° and 29.3° in the material.

Characterization results:

XRD (Å (I.R.)): d_{001}=10.79(0.91); d_{001}(residual kGa-1b)=7.19(0.09); d_{060}=1.49.

TGA (% weight lost (1st derivative peaks)): RT-300°C=15.2% (38.5, 205.9°C); 300-650°C=10.2% (474.7°C).

IR (ATR, cm^{-1}) : v(OH): 3696.0(m), 3670.0(w), 3656.7(w), 3646.7(w), 3619.3(m), 3261.2(w, br); v(NH): 3501.4(m), 3413.1(m), 3380.1(m); v(C=O): 1662.6(m); δ(HNH): 1620.8(m), 1586.6(m); δ(HNC):1474.2(w); δ(AlOH): 939.7(m), 909.6(s), 896.7(s); SiO vibrations: 1152.9(w), 1122.0(w), 1040.3(s),.1028.6(s), 996.3(vs), 794.8(m), 777.1(m), 744.6(m), 657.9(m, br).

^{13}C CPMAS NMR (ppm): 162.6.

5.2.13 kPLA(u)

4.5g of poly(L-lactide) (M_n=50,000) was added to a 10mL round bottom flask submerged in an oil bath heated at 180°C. The solid was stirred magnetically for 1hour, generating a viscous melt of the polymer. To this, 500mg of kurea was added and the resulting dispersion was magnetically stirred for 24h at the lowest possible setting that still allows stirring to occur. An amount equivalent to around 3mg was removed, allowed to solidify, and manually ground into a fine powder.

Characterization results:

XRD (Å): d_{001}=11.41; d_{001}(residual kGa-1b)=7.17, d_{020}=4.47.

5.2.14 kPLA

The procedure was identical to the one described for kPLA(u), except the melt was heated for an additional 24h at 180°C. The reaction vessel was then cooled to room temperature, and the resulting solid was extracted by adding 10mL portions of CH_2Cl_2, dispersing the mixture for 1h, and decanting the solution extract. This extraction procedure was repeated until all solid material was removed from the reaction vessel. These extracts were combined together and the solid material was isolated by centrifuging the solution until all solid matter was deposited. The supernatant solution was discarded.

The resulting solid was then divided up into ten approximately equal portions and washed by dispersing each in 10mL of CH_2Cl_2. The solutions were centrifuged until all solid matter was deposited, and the supernatant solutions were discarded. This CH_2Cl_2 wash repeated was five times. This solids were combined into a 150mL solution of isopropanol, centrifuged until all solids were deposited, and the supernatant solution was discarded. This isopropanol wash was

repeated two times, and the final solid product was air dried in a fume hood at room temperature.

Characterization results:

XRD (Å): d_{001}=12.06; d_{001}(residual kGa-1b)= 7.18, d_{020}=4.52.

TGA (% weight lost (1st derivative peaks)): RT-120°C=3.4% (39.1); 120-650°C=26.1% (294.2, 372.4, 437.8°C).

IR (ATR, cm^{-1}) : v(OH): 3695.0(m), 3654.6(w), 3620.6(m);V(CH): 2997.2(w), 2940.1(w); v(C=O):1753.4(m), 1676.5(w), 1615.3(w, br); δ(CH): 1454.1(vw), 1382.4(vw), 1326.1(vw), 1269.8(vw), 1217.8(vw), 1181.1(w); v(COC): 1269.8(vw), 1217.8(vw), 1188.1(w), 1081.3(m); δ(AlOH): 937.8(m), 907.0(s); SiO vibrations: .1119.3(m); 1046.8(m), 1029.8(s), 1002.5(vs), 793.6(m), 745.2(m), 651.8(m, br).

^{13}C CPMAS NMR (ppm): 178.4, 170.1, 69.8, 17.0.

5.2.15 kallyloxy

12g of kmethoxy in methanol solution (1g/1mL) was added to a solution containing 60mL of 3-allyloxy-1,2-propanediol and 120mL of isopropanol. The mixture was refluxed at 90°C under a flow of N_2 for 7 days. The solid material was isolated by centrifuging the reaction mixture until

all solid matter was deposited, and the supernatant solution was discarded. The isolated solid was air dried in the fume hood at room temperature.

Characterization results:

XRD (Å, (I.R.)): d_{001}=11.43(0.85); d_{001}(residual kGa-1b)= 7.13(0.15).

TGA (% weight lost (1st derivative peaks)): RT-200°C=10.2% (38.4, 92.0°C); 200-400°C=11.4% (371.1°C); 400-650°C=8.8% (458.0, 497.4°C).

IR (ATR, cm^{-1}): ν(OH): 3691.2(m), 3666.4(w), 3648.7(m),3642.9(m), 3631.6(w), 3619.7(m), 3504.8(w), 3367.6(w, br); ν(CH): 3089.8 (vw), 2978.6(vw), 2934.2 (w), 2912.0(w), 2875.0(w); δ (C=C): 1674.9(vw), 1642.6(vw); δ(CH): 1456.5(vw), 1426.1(vw), 1406.8(vw), 1354.8(vw), 1320.5(vw), 1273.2(vw, br), 1254.5(vw), 1232.3(vw), 1214.5(vw, br); ν(CO): 1118.0(w); δ(AlOH): 934.8(m), 908.3(s); SiO vibrations: 1123.4(m), 1045.7(s), 1021.1(s), 1002.8(vs), 859.6(m), 797.0(m), 743.0(m), 649.9(m, br).

^{13}C CPMAS NMR (ppm): 135.5, 134.2, 126.7, 117.4, 73.2, 72.7, 72.1, 71.5, 71.1, 50.8(trace), 44.5(trace), 37.1(trace), 27.0(trace).

^{29}Si CPMAS NMR (ppm): -91.0, -91.6, -92.2.

5.2.16 kallyloxy(w)

A 500mg portion of kallyloxy was dispersed in 250mL of water for 12h. The resulting solution was then centrifuged until all solids were deposited, and the supernatant solution was discarded. The solid was redispersed in 30mL of isopropanol and the centrifugation procedure was repeated. The isolated solid was then air dried in the fume hood at room temperature.

Characterization results:

XRD (Å, (I.R.)): d_{001}=10.77(0.76); d_{001}(residual kGa-1b)= 7.29(0.24).

IR (ATR, cm^{-1}) : v(OH): 3691.2(m), 3675.6(w)**,** 3669.1(w), 3648.2(w), 3627.4(m), 3619.7(m), 3587.3(w), 3566.2(w), 3450.0(w, br); v(CH): 2950.5(w), 2919.3(w), 2877.2(w), 2869.0(w), 2837.8(w); δ(HOH):1635.3(vw); δ(CH): 1457.4(vw), 1375.9(vw), 1259.1(vw), 1210.2(vw); δ(AlOH):933.9(m), 907.8(s); SiO vibrations: 1118.0(m), 1026.0(s), 998.5(vs), 797.4(m), 787.3(m), 745.4(m), 650.4(m, br).

^{13}C CPMAS NMR (ppm): 134.2(trace), 127.3(trace), 73.5, 71.8, 66.2, 50.5, 44.8, 33.3, 26.6, 22.4.

5.2.17 kallyloxy(lowT)

3.5g of a kmethoxy in methanol solution (100mg/1mL) was added to a solution containing 15mL of 3-allyloxy-1, 2-propanediol and 30mL of isopropanol, and the resulting solution was dispersed at room temperature for 24h under a flow of N_2. The resulting solution was then centrifuged until all solids were deposited, and the supernatant solution was discarded. The solid was washed by dispersing it in 15mL of isopropanol, the solution was centrifuged until all solid matter was deposited, and the supernatant solution was discarded. This washing procedure was repeated again, and the resulting solid was air dried in the fume hood at room temperature.

Characterization results:

XRD (Å, (I.R.)): d_{001}=11.44(0.59); d_{001} (residual kmethoxy)=8.78 (0.19); d_{001}(residual kGa-1b)= 7.19(0.22).

5.2.18 kallyloxy(lowT)(w)

10mg of kallyloxy(lowT) was dispersed in 50mL of water for 12 hours. The resulting solution was then centrifuged until all solids were deposited, and the supernatant solution was discarded. The solid was washed by redispersed it in 15mL of isopropanol and the centrifugation procedure was repeated. This isopropanol wash is repeated one more time, and the isolated solid was then air dried in the fume hood at room temperature.

Characterization results:

XRD (Å, (I.R.)): d_{001}=11.53(0.13); d_{001} (kmethoxy)=8.78 (0.54); d_{001}(residual kGa-1b)= 7.29(0.33).

5.2.19 allyloxy (on kGa-1b)

500mg of raw kGa-1b was added to a solution containing 15mL of 3-allyloxy-1,2-propanediol and 30mL of isopropanol and the resulting solution is dispersed a room temperature for 24h under a flow of N_2. The resulting solution was then centrifuged until all solids were deposited, and the supernatant solution was discarded. The solid was air dried in the fume hood at room temperature.

Characterization results:

^{13}C CPMAS NMR (ppm): 135.6, 117.9, 72.2, 64.4, 30.3(trace).

5.2.20 kvinyloxy

500mg of kDMSO was dispersed in a mixture of 30mL of ethylene glycol vinyl ether and 60mL of isopropanol, and the solution was dispersed for 24h at 90°C. The resulting solution was then centrifuged until all solids were deposited and the supernatant solution was discarded. The solid material was washed by redispersing it in 100mL of isopropanol, the mixture was centrifuged until all solids were deposited, and the supernatant solution was discarded. The resulting solid was air dried in the fume hood at room temperature.

Characterization results:

XRD (Å, (I.R.)): d_{001}=11.69(0.87);d_{001}(residual kGa-1b)= 7.32 (0.13).

TGA (% weight lost (1st derivative peaks)): RT-200°C: 8.8%(45.1, 114.2°C); 200-400°C: 18.1%(304.3, 351.9°C); 400-600°C: 8.4%(490.2°C).

IR (ATR, cm^{-1}): ν(OH): 3691.2(m), 3647.9(m), 3636.5(m), 3619.0(m); ν(CH): 2983.7(w), 2941.1(w), 2871.9(w); δ(HOH): 1652.2(vw), 1636.8(vw); δ(CH): 1457.5(vw), 1388.0(vw), 1342.7(vw), 1323.4(vw); δ(AlOH): 797.0(m), 743.4(s); SiO vibrations: 1122.4(m), 1044.3(s), 1004.3(vs), 797.0(m), 745.8(m), 658.1(m).

^{13}C CPMAS NMR (ppm): 105.7, 100.7, 70.8, 64.7, 62.2, 40.9, 21.6.

5.2.21 kvinyloxy(w)

300mg of kvinyloxy was dispersed in 250mL of water for 12h. The resulting solution was then centrifuged until all solids were deposited and the supernatant solution was discarded. The solid material was redispersed in 100mL of isopropanol, centrifuged until all solids were deposited, and the supernatant solution was discarded. The resulting solid was oven dried at 80°C for 1h.

Characterization results:

XRD (Å, (I.R.)): d_{001}=10.39(0.52); d_{001}=9.35(0.27); d_{001}(residual kGa-1b)= 7.21 (0.21).

IR (ATR, cm^{-1}) : ν(OH): 3692.6(m), 3665.6(w), 3652.1(w), 3631.4(m), 3619.3(m), 3412.0(m,br); δ(CH): 2935.7(w), 2986.3(w), 2874.9(w); δ(HOH): 1639.7(vw), 1630.5(vw); δ(CH): 1461.8(vw), 1383.7(vw), 1344.2(vw); δ(AlOH): 797.0(m), 745.8(s); SiO vibrations: 1118.0(m), 1026.9(s), 1003.8(vs), 797.0(m), 747.8(m),649.9 (m, br).

^{13}C CPMAS NMR (ppm): 105.6, 101.0, 71.4, 64.9, 62.9, 21.5.

5.2.22 kvinyloxy(lowT)

3.5g of a solution of kmethoxy in methanol (100mg/mL) was added to a mixture of 15mL of ethylene glycol vinyl ether in 30mL of isopropanol, and the mixture was dispersed for 24h at room temperature. The resulting solution was then centrifuged until all solids were deposited and the supernatant solution was discarded. The solid material was air dried in the fume hood at room temperature.

Characterization results:

XRD (Å, (I.R.)): 11.20(89); 7.22(11).

^{13}C CPMAS NMR (ppm): 105.6, 71.7, 64.9, 63.0, 50.8, 21.9.

5.2.23 Thermally induced cyclization of ethylene glycol vinyl ether (i.e. vinyloxy(c))

8mL of ethylene glycol vinyl ether was dispersed in 15mL of isopropanol and the mixture was refluxed at 90°C for 5 days. A 1mL aliquot was removed and heated at 120°C for 15min to

evaporate the isopropanol solvent, yielding a viscous oil-like liquid. The resulting oil was dispersed in 2mL of $CDCl_3$ and transferred to an NMR tube for analysis.

Characterization results:

$^{13}C[^{1}H$ decoupling] (ppm): 151.7, 100.1, 98.5, 87.0, 69.3, 68.4, 67.3, 66.9, 66.1, 64.1, 63.6, 63.3, 61.8, 60.8, 25.2, 23.1, 22.3, 20.7, 19.3 ($CDCl_3$: 77.8, 77.4, 76.9; TMS: 0.0).

5.2.24 Kaolinite catalyzed cyclization of ethylene glycol vinyl ether (i.e. vinyloxy(c-KGa-1b)

8mL of ethylene glycol vinyl ether was dispersed in 15mL of isopropanol. To this 100mg of raw kGa-1b was added and the resulting mixture was refluxed at 90°C for 5 days. A 1mL aliquot was removed and heated at 120°C for 15min to evaporate the isopropanol solvent, yielding a viscous oil-like liquid. The resulting oil was dispersed with 2mL of $CDCl_3$ and transferred to an NMR tube for analysis.

$^{13}C[^{1}H$ decoupling] (ppm): 98.5, 68.6, 67.1, 66.2, 63.6, 61.9, 61.7, 25.2, 23.2, 23.1, 22.3, 22.2, 20.7, 20.6, 19.6 ($CDCl_3$:77.6, 77.2, 76.8; TMS: 0.0).

^{13}C DEPT 90 & DEPT 135 NMR (ppm): 98.5 (CH), 68.4 (CH), 67.0 (CH_2), 66.1 (CH_2), 63.5 (CH_2), 61.8 (CH_2), 25.1 (CH_3), 23.0 (CH_3), 22.3 (CH_3), 20.6 (CH_3), 19.5 (CH_3).

6 General conclusions and suggestion for future work

Solid state ^{1}H NMR of a natural kaolinite, kGa-1b, identified two main proton signals attributed to inner and inner surface hydroxyl protons. Deuterium exchanges studies were able to accurately attribute the two peaks. The ^{1}H NMR spectra of an intercalated kaolinite, kDMSO, and a grafted kaolinite, kmethoxy, were fitted with high accuracy using models consistent with the known structures of these materials. Comparison of the ^{27}Al NMR spectra of kGa-1b, kDMSO, kmethoxy measured at 4.7T and 21.1T suggested the presence of multiple aluminum sites with similar δ_{iso} values, but different quadrupolar parameters. These spectra were fitted with good accuracy using models consistent with known structures of these materials. Two different Al(III) sites in the octahedral sheet were found, with C_Q values varying by up to 0.6MHz. The ^{27}Al NMR spectra of two different kmethoxy materials were also compared. The results suggested the presence of sites whose low values of C_Q increased in intensity along with the quantity of grafted material. The results demonstrate that these techniques could be used to characterize both intercalated and grafted kaolinites, and could be applied to more complex systems where traditional characterisation methods are ambiguous.

The interlayer of kaolinite was directly functionalized with poly(ethylene)-block-poly(ethylene glycol) and with poly(lactide) using melts of the polymers. The polymers were found to completely displace their precursors from the interlayer space giving a monolayer type arrangement of the polymer. Success at preparing these materials opens up a whole new set up

possibilities for preparing intercalated complexes of PEG copolymers and PLA. The PEG copolymer modified kaolinites are expected to hydrophobize the clay mineral making them suitable as adsorbents for organic molecules in solution and as a vessel for controlled release applications. The PLA modified kaolinites would be expected to greatly enhance the mechanical strength of the polymer, and future work could look at its mechanical properties to evaluate its suitability as a nanocomposite material.

Kaolinite's inner surfaces were grafted with polymerizable functional groups through covalent grafting of ethylene glycol vinyl ether and 3-allyloxy-1,2-propanediol. Both were found to displace the precursor material from the interlayer space, adopting a monolayer type arrangement. The 3-allyloxy-1,2-propanediol molecules exhibited noticeable shifts in their ^{13}C signals, especially for the allyl groups, and a new ^{29}Si peak appeared in the spectra of the kallyloxy samples which suggest partial keying of the allyl group into the clay mineral siloxane rings. The allyl group in kallyloxy remained intact after the grafting reaction, demonstrating the possibility of preparing similar grafted compounds for in-situ chemical reactions and polymerization. These grafted products could prevent scrolling of kaolinite sheets when it is exfoliated, allowing dispersion of individual kaolinite platelet sheets in a polymer matrix to yield a nanocomposite material with very good physical properties. Ethylene glycol vinyl ether was found to undergo intramolecular cyclization to form an acetal product in kvinyloxy. This reaction was observed using kGa-1b, suggesting that the clay mineral's surfaces, both inner and outer, act as an acid catalyst. The acid catalyst properties of kaolinite observed in kvinyloxy are

not commonly reported and potential future work could investigate this for other reactions in-situ.

7 Bibliography

Abuchowski, A., Es, T. van, Palczuk, N. C., Davis, F. F. (1977). Alteration of immunological properties of bovine serum albumin by covalent attachment of polyethylene glycol. *Journal of Biological Chemistry*, *252*(11), 3578–3581.

Albertsson, P. Å. (1970). Partition of cell particles and macromolecules in polymer two-phase systems. *Advances in Protein Chemistry*, *24*, 309–341.

Alemany, L. B., Grant, D. M., Alger, T. D., Pugmire, R. J. (1983). Cross polarization and magic angle sample spinning NMR spectra of model organic compounds. 3. Effect of the ^{13}C-^{1}H dipolar interaction on cross polarization and carbon-proton dephasing. *J. Am. Chem. Soc. 105* (22), 6697-6704.

Amoureux, J.-P., Pruski, M. (2007). MQMASNMR: Experimental Strategies and Applications. In: *eMagRes*. John Wiley & Sons.

Andreas, L. B., Stanek, J., Le Marchand, T., Bertarello, A., Cala-De Paepe, D., Lalli, D., Wegner, S., Engelke, F., Felli, I.C., Pierattelli, R., Dixon, N.E., Emsley, L., Herrmann, T., Pintacuda, G. (2015). Protein residue linking in a single spectrum for magic-angle spinning NMR assignment. *Journal of biomolecular NMR*, *62*(3), 253-261.

Arefalk, A., Larhed, M., Hallberg, A. (2005) Masked 3-aminoindan-1-ones by a palladium-catalyzed three-component annulation reaction. *The Journal of organic chemistry*, *70* (3), 938-942.

Armstrong, B. H. (1967). Spectrum line profiles: the Voigt function. *Journal of Quantitative Spectroscopy and Radiative Transfer*, *7*(1), 61-88.

Ashbrook, S. E., McManus, J., MacKenzie, K. J., Wimperis, S. (2000). Multiple-quantum and cross-polarized 27Al MAS NMR of mechanically treated mixtures of kaolinite and gibbsite. *The Journal of Physical Chemistry B*, *104*(27), 6408-6416.

Auras, R. A., Lim, L.-T., Selke, S. E. M. Tsuji, H. *Poly(lactic acid): Synthesis, Structures, Properties, Processing, and Applications*. (John Wiley & Sons, 2011).

Bailey, S. W. (1980). Summary of recommendations of AIPEA nomenclature committee on clay minerals. *American Mineralogist*, *65*(1–2), 1–7.

Bailey, S. W. (1988a). Introduction. In: S. W. Bailey (Ed.), *Hydrous phyllosilicates (exclusive of micas)* (Vol. 19). Mineralogical Society of America.

Bailey, S. W. (1988b). Polytypism of 1:1 layer silicates. In: S. W. Bailey (Ed.), *Hydrous phyllosilicates (exclusive of micas)* (Vol. 19). Mineralogical Society of America.

Bak, M., Rasmussen, J. T., Nielsen, N. C. (2011). SIMPSON: a general simulation program for solid-state NMR spectroscopy. *Journal of Magnetic Resonance*, *213*(2), 366-400.

Bandy, M. C., Bandy, J. A. (1955). De Natura Fossilium (Textbook of Mineralogy) by Georgius Agricola. *Geological Society of America Special Paper*, *63*, 240.

Barron, P. F., Frost, R. L., Skjemstad, J. O., Koppi, A. J. (1983). Detection of two silicon environments in kaolins by solid-state ^{29}Si NMR. *Nature*, *302*(5903), 49–50.

Benninga, H. (1990). *A history of lactic acid making: a chapter in the history of biotechnology* (Vol. 11). Springer Science & Business Media.

Bergaya, F., Lagaly, G. (2013). Chapter 1 - General Introduction: Clays, Clay Minerals, and Clay Science. In: F. Bergaya, G. Lagaly (Eds.), *Handbook of Clay Science* (Vol. 5, pp. 1–19). Elsevier.

Bernal, J. D. (1949). The Physical Basis of Life. *Proceedings of the Physical Society. Section A*, *62*(9), 537.

Bish, D. L., Von Dreele, R. B. (1989). Rietveld refinement of non-hydrogen atomic positions in kaolinite. *Clays and Clay Minerals*, *37*(4), 289-296.

Blumstein, A. (1961). Etude des polymérisations en couche adsorbée I. *Bulletin de La Société Chimique de France*, (5), 899.

Bose, S., Vahabzadeh, S. Bandyopadhyay, A. Bone tissue engineering using 3D printing. *Materials Today* 16, 496–504 (2013).

Brack, A. (2013). Chapter 10.4 - Clay Minerals and the Origin of Life. In: F. Bergaya, G. Lagaly (Eds.), *Handbook of Clay Science* (Vol. 5, pp. 507–521). Elsevier.

Brady, P. V., Cygan, R. T., Nagy, K. L. (1996), Molecular controls on kaolinite surface charge. .*Journal of Colloid and Interface Science*, *183*(2), 356-364.

Bragg, W. H., Bragg, W. L. (1913). The Reflection of X-rays by Crystals. *Proceedings of the Royal Society of London. Series A, Containing Papers of a Mathematical and Physical Character*, *88*(605), 428–438.

Brandt, K. B., Elbokl, T. A., Detellier, C. (2003). Intercalation and interlamellar grafting of polyols in layered aluminosilicates. D-Sorbitol and adonitol derivatives of kaolinite. *Journal of Materials Chemistry*, *13*(10), 2566–2572.

Brigatti, M. F., Galán, E., Theng, B. K. G. (2013). Chapter 2 - Structure and Mineralogy of Clay Minerals. In F. Bergaya, G. Lagaly (Eds.), *Handbook of Clay Science* (Vol. 5, pp. 21–81). Elsevier.

Cairns-Smith, A. G. (1987). *Genetic Takeover: And the Mineral Origins of Life* (1st ed.). Cambridge University Press.

Camazano, M. S., Garcia, S. G. (1966). Interlayer complexes of kaolinite and halloysite with polar liquids. In: *Anales de Edafologia y Agrobiologia* (Vol. 25, p. 25).

Carroll, D. (1959). Ion exchange in clays and other minerals. *Geological Society of America Bulletin*, *70*(6), 749-779.

Chang, J.-H. (2014). Preparation and Characterization of Poly(trimethylene terephthalate) Nanocomposites. In J. K. Pandey, K. R. Reddy, A. K. Mohanty, M. Misra (Eds.), *Handbook of*

Polymer nanocomposites. Processing, Performance and Application (Vol. A: Layered Silicates, pp. 267–292). New York: Springer-Verlag Berlin Heidelberg.

Chasin, M. *Biodegradable Polymers as Drug Delivery Systems*. 45, (Marcel Dekker, 1990).

Cheng, H., Hou, X., Liu, Q., Li, X., Frost, R. L. (2015). New insights into the molecular structure of kaolinite–methanol intercalation complexes. *Applied Clay Science*, *109*, 55–63.

Chevelkov, V., Rehbein, K., Diehl, A., Reif, B. (2006). Ultrahigh Resolution in Proton Solid-State NMR Spectroscopy at High Levels of Deuteration. *Angewandte Chemie International Edition*, *45*(23), 3878-3881.

Cruz, M., Jacobs, H., Fripiat, J. J. (1972). The nature of interlayer bonding in kaolin minerals. In *Proceedings of the International Clay Conference, Madrid* (pp. 35–44).

Davis, C. H., Mathias, L. J., Gilman, J. W., Schiraldi, D. A., Shields, J. R., Trulove, P., Sutto, T.E., Delong, H. C. (2002). Effects of melt-processing conditions on the quality of poly(ethylene terephthalate) montmorillonite clay nanocomposites. *Journal of Polymer Science Part B: Polymer Physics*, *40*.

Dedzo, G. K., Detellier, C. (2016). Functional nanohybrid materials derived from kaolinite. *Applied Clay Science*, *130*, 33–39.

Dedzo, G. K., Letaief, S., Detellier, C. (2012). Kaolinite–ionic liquid nanohybrid materials as electrochemical sensors for size-selective detection of anions. *Journal of Materials Chemistry*, *22*(38), 20593–20601.

Dedzo, G. K., Ngnie, G., Detellier, C. (2016). PdNP Decoration of Halloysite Lumen via Selective Grafting of Ionic Liquid onto the Aluminol Surfaces and Catalytic Application. *ACS Applied Materials & Interfaces*, *8*(7), 4862–4869.

Duer, M. J., Rocha, J., Klinowski, J. (1992). Solid-state NMR studies of the molecular motion in the kaolinite: DMSO intercalate. *Journal of the American Chemical Society*, *114*(17), 6867-6874.

Dupree, R., Holland, D., McMillan, P. W., Pettifer, R. F. (1984). The structure of soda-silica glasses: a MAS NMR study. *Journal of Non-Crystalline Solids*, *68*(2), 399-410.

El Bokl, T. A. (2007). *Nanohybrid and nanocomposite materials from kaolinite* (Doctoral thesis). University of Ottawa (Canada).

Elbokl, T. A., Detellier, C. (2008). Intercalation of cyclic imides in kaolinite. *Journal of Colloid and Interface Science*, *323*(2), 338–348.

Elbokl, T. A., Detellier, C. (2009). Kaolinite–poly (methacrylamide) intercalated nanocomposite via in situ polymerization. *Canadian Journal of Chemistry*, *87*(1), 272-279.

Elias, H.-G. (2000). Plastics, General Survey. In: *Ullmann's Encyclopedia of Industrial Chemistry*. Wiley-VCH Verlag GmbH & Co. KGaA.

Espartero, J. L., Rashkov, I., Li, S. M., Manolova, N., Vert, M. (1996). NMR analysis of low molecular weight poly (lactic acid) s. *Macromolecules*, *29*(10), 3535-3539.

Fafard, J., Lyubimova, O., Stoyanov, S. R., Dedzo, G. K., Gusarov, S., Kovalenko, A., Detellier, C. (2013). Adsorption of indole on kaolinite in nonaqueous media: Organoclay preparation and characterization, and 3D-RISM-KH molecular theory of solvation investigation. *The Journal of Physical Chemistry C*, *117*(36), 18556–18566.

Frost, R. L., Fredericks, P. M., Bartlett, J. R. (1993). Fourier transform Raman spectroscopy of kandite clays. *Spectrochimica Acta Part A: Molecular Spectroscopy*, 49, 667–674.

Frost, R. L., Kristof, J., Horvath, E., Kloprogge, J. T. (2000). Kaolinite hydroxyls in dimethylsulphoxide-intercalated kaolinites at 77 K—a Raman spectroscopic study. *Clay Minerals*, *35*(2), 443–454.

Frost, R. L., Kristof, J., Paroz, G. N., Kloprogge, J. T. (1998). Molecular structure of dimethyl sulfoxide intercalated kaolinites. *The Journal of Physical Chemistry B*, *102*(43), 8519-8532.

Frydman, L., Harwood, J. S. (1995). Isotropic spectra of half-integer quadrupolar spins from bidimensional magic-angle spinning NMR. *Journal of the American Chemical Society*, *117*(19), 5367–5368.

Gardolinski, J. E. F. da C. (2006). *Interlayer grafting and delamination of kaolinite* (Doctoral thesis). Christian-Albrechts Universität Kiel, Germany.

Gardolinski, J., Lagaly, G. (2005a). Grafted organic derivatives of kaolinite: I. Synthesis, chemical and rheological characterization. *Clay Minerals*, *40*(4), 537–546.

Gardolinski, J., Lagaly, G. (2005b). Grafted organic derivatives of kaolinite: II. Intercalation of primary n-alkylamines and delamination. *Clay Minerals*, *40*(4), 547–556.

Garlotta, D. A literature review of poly (lactic acid). *Journal of Polymers and the Environment* 9, 63–84 (2001).

Ghose, S., Tsang, T. (1973). Structural Dependence of Quadrupole Coupling Constant e^2qQ/h for ^{27}Al and Crystal Field Parameter D for Fe^{3+} in Aluminosilicates. *American Mineralogist*, *58*, 748-755.

Giese, R. F. (1988). Kaolin minerals: structures and stabilities. In: S. W. Bailey (Ed.), *Hydrous phyllosilicates (exclusive of micas)* (Vol. 19). Mineralogical Society of America.

Green, C. H., Hellier, D. G. (1972). Chemistry of the S O bond. Part I. Nuclear magnetic resonance and infrared studies on trimethylene sulphite. *Journal of the Chemical Society, Perkin Transactions 2*, (4), 458-463.

Grünberg, B., Emmler, T., Gedat, E., Shenderovich, I., Findenegg, G. H., Limbach, H. H., Buntkowsky, G. (2004). Hydrogen Bonding of Water Confined in Mesoporous Silica MCM-41 and SBA-15 Studied by 1H Solid-State NMR. *Chemistry–A European Journal*, *10*(22), 5689-5696.

Guggenheim, S., Martin, R. T. (1995). Definition of clay and clay mineral: joint report of the AIPEA nomenclature and CMS nomenclature committees. *Clays and Clay Minerals*, *43*(2), 255–256.

Gupta, M.C. Deshmukh, V.G. (1982). Thermal oxidative degradation of poly-lactic acid. Part II: Molecular weight and electronic spectra during isothermal heating. *Colloid and Polymer Science*, 260, 514-517.

Håfors, B. (1990). The role of the Wasa in the development of the polyethylene glycol preservation method. In R. M. Rowell, J. R. Barbour (Eds.), *Archaelogical Wood: Properties, Chemistry, and Preservation* (Vol. 225). ACS Publications.

Harris, J. M. (1992). *Introduction to Biotechnical and Biomedical Applications of Poly (Ethylene Glycol, Poly (ethylene glycol) Chemistry*. Plenum, New York.

Hayashi, S., Akiba, E. (1994). Interatomic distances in layered silicates and their intercalation compounds as studied by cross polarization NMR. *Chemical Physics Letters*, *226*(5-6), 495-500.

Hayashi, S., Ueda, T., Hayamizu, K., Akiba, E. (1992a). NMR study of kaolinite. 1. Silicon-29, aluminum-27, and proton spectra. *The Journal of Physical Chemistry*, *96*(26), 10922-10928.

Hayashi, S., Ueda, T., Hayamizu, K., Akiba, E. (1992b) NMR study of kaolinite. 2. ^{1}H, ^{27}Al, and ^{29}Si spin-lattice relaxations. *Journal of Physical Chemistry, 96*(26), 10928-10933.

Hirsemann, D., Köster, T. K. J., Wack, J., van Wüllen, L., Breu, J., Senker, J. (2011). Covalent grafting to μ-hydroxy-capped surfaces? A kaolinite case study. *Chemistry of Materials*, *23*(13), 3152-3158.

Horváth, E., Frost, R. L., Makó, É., Kristóf, J., Cseh, T. (2003). Thermal treatment of mechanochemically activated kaolinite. *Thermochimica Acta*, *404*(1), 227-234.

Houssamy, S. F. (2002). Polyethylene glycol compounds for functional hydraulic fluids. Materials Research Innovations, 6(4), 141–152.

Hussain, F., Hojjati, M., Okamoto, M., Gorga, R. E. (2006). Review article: Polymer-matrix Nanocomposites, Processing, Manufacturing, and Application: An Overview. *Journal of Composite Materials*, *40*(17), 1511–1575.

Itagaki, T., Kuroda, K. (2003). Organic modification of the interlayer surface of kaolinite with propanediols by transesterification. *Journal of Materials Chemistry*,*13*(5), 1064-1068.

Janek, M., Emmerich, K., Heissler, S., Nüesch, R. (2007), Thermally induced grafting reactions of ethylene glycol and glycerol intercalates of kaolinite. *Chemistry of Materials*, *19*(4), 684-693.

Jeffries, C. D., Jackson, M. L. (1949). Mineralogical Analysis of Soils. *Soil Science*, *68*(1), 57-74.

Johnston, C. T., Sposito, G., Bocian, D. F., Birge, R. R. (1984). Vibrational spectroscopic study of the interlamellar kaolinite-dimethyl sulfoxide complex. *The Journal of Physical Chemistry*, *88*(24), 5959-5964.

Kister, G., Cassanas, G., Vert, M. (1998). Effects of morphology, conformation and configuration on the IR and Raman spectra of various poly(lactic acid)s. *Polymer*, *39*(2), 267-273.

Kittel, C., Abrahams, E. (1953). Dipolar broadening of magnetic resonance lines in magnetically diluted crystals. *Physical Review*, *90*(2), 238.

Knop, K., Hoogenboom, R., Fischer, D., Schubert, U. S. (2010) Poly(ethylene glycol) in Drug Delivery: Pros and Cons as Well as Potential Alternatives. *Angewandte Chemie International Edition* 49, 6288–6308.

Kohn, S. C., Michael, C., Henderson, B., Dupree, R. (1997). Si-Al ordering in leucite group minerals and ion-exchanged analogues: A MAS NMR study. *American Mineralogist*, *82*(11-12), 1133-1140.

Kolano, C., Helbing, J., Kozinski, M., Sander, W., Hamm, P. (2006). Watching hydrogen-bond dynamics in a β-turn by transient two-dimensional infrared spectroscopy. *Nature*, *444*(7118), 469-472.

Komori, Y., Enoto, H., Takenawa, R., Hayashi, S., Sugahara, Y., Kuroda, K. (2000). Modification of the interlayer surface of kaolinite with methoxy groups. *Langmuir*, *16*(12), 5506-5508.

Komori, Y., Sugahara, Y., Kuroda, K. (1998). A kaolinite-NMF-methanol intercalation compound as a versatile intermediate for further intercalation reaction of kaolinite. *Journal of Materials Research*, *13*(04), 930-934.

Lagaly, G. (1984). Clay minerals: their structure, behaviour and use - Clay-organic interactions. *Phil. Trans. R. Soc. London A*, *311*(1517), 315–332.

Lagaly, G., Ogawa, M., Dékány, I. (2013). Chapter 10.3 - Clay Mineral–Organic Interactions. In F. Bergaya, G. Lagaly (Eds.), *Handbook of Clay Science* (Vol. 5, pp. 435–505). Elsevier.

Langford, J. I. (1978). A rapid method for analysing the breadths of diffraction and spectral lines using the Voigt function. *Journal of Applied Crystallography*, *11*(1), 10-14.

LeBaron, P. C., Wang, Z., Pinnavaia, T. J. (1999). Polymer-layered silicate nanocomposites: an overview. *Applied Clay Science*, *15*(1), 11–29.

Ledoux, R. L., White, J. L. (1964a). Infrared study of the OH groups in expanded kaolinite. *Science*, *143*(3603), 244-246.

Ledoux, R. L., White, J. L. (1964b). Infrared study of selective deuteration of kaolinite and halloysite at room temperature. *Science*, *145*(3627), 47-49.

Ledoux, R. L., White, J. L. (1966). Infrared studies of hydrogen bonding interaction between kaolinite surfaces and intercalated potassium acetate, hydrazine, formamide, and urea. *Journal of Colloid and Interface Science*, *21*(2), 127-152.

Letaief, S., Detellier, C. (2011). Application of thermal analysis for the characterisation of intercalated and grafted organo-kaolinite nanohybrid materials. *Journal of Thermal Analysis and Calorimetry*, *104*(3), 831–839.

Letaief, S., Elbokl, T. A., Detellier, C. (2006). Reactivity of ionic liquids with kaolinite: melt intersalation of ethyl pyridinium chloride in an urea-kaolinite pre-intercalate. *Journal of Colloid and Interface Science*, *302*(1), 254–258.

Letaief, S., Pell, W., Detellier, C. (2011). Deposition of gold nanoparticles on organo-kaolinite—Application in electrocatalysis for carbon monoxide oxidation. *Canadian Journal of Chemistry*, *89*(7), 845–853.

Letaief, S., Tonle, I. K., Diaco, T., Detellier, C. (2008). Nanohybrid materials from interlayer functionalization of kaolinite. Application to the electrochemical preconcentration of cyanide. *Applied Clay Science*, *42*(1-2), 95-101.

Lippmaa, E., Samoson, A., Mägi, M. (1986). High-resolution ^{27}Al NMR of aluminosilicates. *Journal of the American Chemical Society*, *108*(8), 1730-1735.

Lipsicas, M., Raythatha, R., Giese, R. F., Costanzo, P. M. (1986). Molecular motions, surface interactions, and stacking disorder in kaolinite intercalates. *Clays and Clay Minerals*, *34*(6), 635–644.

Lipsicas, M., Straley, C., Costanzo, P. M., Giese, R. F. (1985). Static and dynamic structure of water in hydrated kaolinites. II. The dynamic structure. *Journal of colloid and interface science*, *107*(1), 221-230.

Liu, X., Lu, X., Sprik, M., Cheng, J., Meijer, E. J., Wang, R. (2013), Acidity of edge surface sites of montmorillonite and kaolinite. *Geochimica and Cosmochimica Acta*, *117*, 180-190.

Llor, A., Virlet, J. (1988). Towards high-resolution NMR of more nuclei in solids: Sample spinning with time-dependent spinner axis angle. *Chemical Physics Letters*, *152*(2-3), 248-253.

MacKenzie, K. J., Smith, M. E. (2002). *Multinuclear solid-state nuclear magnetic resonance of inorganic materials* (Vol. 6). Elsevier.

Mahou, R., Wandrey, C. (2012). Versatile route to synthesize heterobifunctional poly (ethylene glycol) of variable functionality for subsequent pegylation. *Polymers*, *4*(1), 561-589.

Makó, É., Kristóf, J., Horváth, E., Vágvölgyi, V. (2009). Kaolinite–urea complexes obtained by mechanochemical and aqueous suspension techniques—a comparative study. *Journal of Colloid and Interface Science*, *330*(2), 367-373.

Manning, D. A. C. (1995). Introduction. In D. A. C. Manning (Ed.), *Introduction to Industrial Minerals* (pp. 1–16). Dordrecht: Springer, Netherlands.

Massiot, D., Fayon, F., Capron, M., King, I., Le Calvé, S., Alonso, B., Hoatson, G., Durand, J., Bujoli, B., Gan, Z., Hoatson, G. (2002). Modelling one-and two-dimensional solid-state NMR spectra. *Magnetic Resonance in Chemistry*, *40*(1), 70-76.

Matusik, J., Scholtzová, E., Tunega, D. (2012). Influence of synthesis conditions on the formation of a kaolinite-methanol complex and simulation of its vibrational spectra. *Clays and Clay Minerals*, *60*(3), 227-239.

Matusik, J., Stodolak, E. Bahranowski, K. (2011) Synthesis of polylactide/clay composites using structurally different kaolinites and kaolinite nanotubes. *Applied Clay Science* 51, 102–109.

Matyjaszewski, K. (Ed.). (1996). *Cationic Polymerizations: Mechanisms, Synthesis & Applications*. New York: Marcel Dekker.

Mccabe, R. W., Adams, J. M. (2013). Chapter 4.3 - Clay Minerals as Catalysts. In: F. Bergaya, G. Lagaly (Eds.), *Handbook of Clay Science* (Vol. 5, pp. 491–538). Elsevier.

Medek, A., Harwood, J. S., Frydman, L. (1995). Multiple-quantum magic-angle spinning NMR: A new method for the study of quadrupolar nuclei in solids. *Journal of the American Chemical Society*, *117*(51), 12779–12787.

Mercier, L. A., Facey, G., Detellier, C. (1994). Organo-layered silicates. Interlamellar intercalation and grafting of ethylene glycol in magadiite. *Journal of the Chemical Society, Chemical Communications*, (18), 2111–2112.

Michalková, A., Tunega, D. (2007). Kaolinite: Dimethylsulfoxide Intercalate. A Theoretical Study. *The Journal of Physical Chemistry C*, *111*(30), 11259-11266.

Molina, C. B., Pizarro, A. H., Casas, J. A., Rodriguez, J. J. (2014). Aqueous-phase hydrodechlorination of chlorophenols with pillared clays-supported Pt, Pd and Rh catalysts. *Applied Catalysis B: Environmental*, *148*, 330–338.

Mousty, C. (2004). Sensors and biosensors based on clay-modified electrodes—new trends. *Applied Clay Science*, *27*(3), 159–177.

Murakami, J., Itagaki, T., Kuroda, K. (2004). Synthesis of kaolinite-organic nanohybrids with butanediols. *Solid State Ionics*, *172*(1), 279-282.

Murray, H. H. (1988). Kaolin minerals; their genesis and occurrences. In S. W. Bailey (Ed.), *Hydrous phyllosilicates (exclusive of micas)* (Vol. 19). Mineralogical Society of America.

Murray, H. H., Lyons, S. C. (1956). Correlation of paper-coating quality with degree of crystal perfection of kaolinite. *Clays Clay Miner*, *4*, 31–40.

Németh, J., Rodríguez-Gattorno, G., Díaz, D., Vázquez-Olmos, A. R., Dékány, I. (2004). Synthesis of ZnO nanoparticles on a clay mineral surface in dimethyl sulfoxide medium. *Langmuir*, *20*(7), 2855–2860.

Ngassa, G. B., Tonlé, I. K., Ngameni, E. (2016). Square wave voltammetric detection by direct electroreduction of paranitrophenol (PNP) using an organosmectite film-modified glassy carbon electrode. *Talanta*, *147*, 547–555.

Okada, A., Fukushima, Y., Kawasumi, M., Inagaki, S., Usuki, A., Sugiyama, S., Kurauchi, T, Kamigaito, O., Kenkyusho, K. K. T. C. (1986, September 19). Composite material and process for manufacturing same.

Okada, A., Kawasumi, M., Kohzaki, M., Fujimoto, M., Kojima, Y., Kurauchi, Kamigaito, O. Kenkyusho, K. K. T. C. (1988, March 14). Composite material and process for producing the same.

Okada, A., Usuki, A. (1995). The chemistry of polymer-clay hybrids. *Materials Science and Engineering: C*, *3*(2), 109–115.

Olejnik, S. (1970). The Intercalation of Polar Organic Compounds into Kaolinite. *Clay Minerals*, *8*(4), 421–434.

Olejnik, S., Aylmore, L. A. G., Posner, A. M., Quirk, J. P. (1968). Infrared spectra of kaolin mineral-dimethyl sulfoxide complexes. *The Journal of Physical Chemistry*, *72*(1), 241–249.

Oral, A., Tasdelen, M. A., Demirel, A. L., Yagci, Y. (2009) Poly (cyclohexene oxide)/clay nanocomposites by photoinitiated cationic polymerization via activated monomer mechanism. *Journal of Polymer Science Part A: Polymer Chemistry*,*47*(20), 5328-5335.

Paris, M. (2014). The two aluminum sites in the ^{27}Al MAS NMR spectrum of kaolinite: Accurate determination of isotropic chemical shifts and quadrupolar interaction parameters. *American Mineralogist*, *99*(2-3), 393-400.

Patakfalvi, R., Oszko, A., DeKany, I. (2003). Synthesis and characterization of silver nanoparticle/kaolinite composites. *Colloids and Surfaces A: Physicochemical and Engineering Aspects*, *220*(1), 45–54.

Perras, F. A., Widdifield, C. M., Bryce, D. L. (2012). QUEST—QUadrupolar Exact SofTware: A fast graphical program for the exact simulation of NMR and NQR spectra for quadrupolar nuclei. *Solid state nuclear magnetic resonance*, *45*, 36-44.

Plançon, A., Giese, R. F., Snyder, R. (1988). Hinckley Index For Kaolinites. *Clays and Clay Minerals*, 23(3), 249-260.

Plançon, A., Giese, R. F., Snyder, R., Drits, V. A., Bookin, A. S. (1989). Stacking faults in the kaolin-group minerals: Defect structures of kaolinite. *Clays and Clay Minerals*, *37*(3), 203–210.

Polymer Nanocomposites Market by Application & Type - 2020 | MarketsandMarkets. (2015). Retrieved from: http://www.marketsandmarkets.com/Market-Reports/polymer-nanocomposites-market-228956069.html

Pruett, R. J., Webb, H. L. (1993). Sampling and analysis of KGa-1b well-crystallized kaolin source clay. *Clays and Clay Minerals*, *41*(4), 514-19.

Raupach, M., Barron, P. F., Thompson, J. G. (1987). Nuclear magnetic resonance, infrared, and X-ray powder diffraction study of dimethylsulfoxide and dimethylselenoxide intercalates with kaolinite. *Clays and Clay Minerals*, *35*(3), 208-219.

Raythatha, R., Lipsicas, M. (1985). Mechanism of synthesis of 10-A hydrated kaolinite. *Clays and Clay Minerals*, *33*(4), 333-339.

Ripmeester, J. A., Ratcliffe, C. I., Tse, J. S. (1988). The nuclear magnetic resonance of ^{129}Xe trapped in clathrates and some other solids. *Journal of the Chemical Society, Faraday Transactions 1: Physical Chemistry in Condensed Phases*, *84*(11), 3731-3745.

Rocha, J., Pedrosa, J. D., Jesus, D. (1994). Spectroscopy of Kaolinite. *Clay Minerals*, *29*, 287-291.

Roff, W. J., Scott, J. R. Pacitti, J. (1971) *Handbook of common polymers*. (CRC Press).

Romo, L. A. (1956). The exchange of hydrogen by deuterium in hydroxyls of kaolinite. *The Journal of Physical Chemistry*, *60*(7), 987-989.

Ryan, L. M., Taylor, R. E., Paff, A. J., Gerstein, B. C. (1980). An experimental study of resolution of proton chemical shifts in solids: Combined multiple pulse NMR and magic-angle spinning. *The Journal of Chemical Physics*, *72*(1), 508-515.

Sakellariou, D., Lesage, A., Hodgkinson, P., Emsley, L. (2000). Homonuclear dipolar decoupling in solid-state NMR using continuous phase modulation. *Chemical Physics Letters*, *319*(3), 253-260.

Samoson, A. (1985). Satellite transition high-resolution NMR of quadrupolar nuclei in powders. *Chemical Physics Letters*, *119*(1), 29–32.

Samoson, A., Lippmaa, E., Pines, A., (1988) High resolution solid-state NMR., *Molecular Physics*, 65(4), 1013-1018.

Sanchez-Martin, M. J., Rodriguez-Cruz, M. S., Andrades, M. S., Sanchez-Camazano, M. (2006). Efficiency of different clay minerals modified with a cationic surfactant in the adsorption of pesticides: influence of clay type and pesticide hydrophobicity. *Applied Clay Science*, *31*(3), 216–228.

SDBSWeb : http://sdbs.db.aist.go.jp (National Institute of Advanced Industrial Science and Technology), accessed 2017/03/15.

Shalaby, S. W. Johnson, R. A. *Biomedical Polymers: Designed-to-degrade Systems*. (Hanser Publishers, 1994).

Shostakovsky, M. F., Gershtein N. A., Volkova Z. S. (1953), Reactions of vinyl ethers Communication VIII. Reactions of acetals derived from ethylene glycol. *Bulletin of the Academy of Sciences of the USSR, Division of chemical science* 2(1), 89-95.

Smirnov, K. S., Bougeard, D. (1999). A molecular dynamics study of structure and short-time dynamics of water in kaolinite. *The Journal of Physical Chemistry B*, *103*(25), 5266-5273.

Södergård, A., Stolt, M. (2002). Properties of lactic acid based polymers and their correlation with composition. *Progress in polymer science*, *27*(6), 1123-1163

Solomon, D. H., Murray, H. H. (1972). Acid-base interactions and the properties of kaolinite in non-aqueous media. *Clays Clay Miner*, *20*, 135–141.

Sposito, G., (1984). *The surface chemistry of soils.* Oxford University Press.

Stevens, M. P. (1999) *Polymer chemistry: an introduction*. (Oxford university press, New York).

Stewart, J. E. Infrared absorption spectra of urea, thiourea, and some thiourea-alkali halide complexes. *The Journal of Chemical Physics* 26, 248–254 (1957).

Sugahara, Y., Satokawa, S., Kuroda, K., Kato, C. (1988). Evidence for the formation of interlayer polyacrylonitrile in kaolinite. *Clays and Clay Minerals*, *36*(4), 343–348.

Svishchev, I. M., Kusalik, P. G. (1993). Proton chemical shift of water in the liquid state: computer simulation results. *Journal of the American Chemical Society*, *115*(18), 8270–8274.

Theng, B. K. G. (Ed.). (1979). Chapter 1 The Clay Minerals. In: *Formation and Properties of Clay-Polymer Complexes* (Vol. 9, pp. 3–36).

Thompson, J. G. (1984). Two possible interpretations of ^{29}Si nuclear magnetic resonance spectra of kaolin-group minerals. *Clays and Clay Minerals*, *32*(3), 233-234.

Thompson, J. G. (1985). Interpretation of solid state ^{13}C and ^{29}Si nuclear magnetic resonance spectra of kaolinite intercalates. *Clays and Clay Minerals*, *33*(3), 173-180.

Thompson, J. G. (1987). Further consideration of the ^{29}Si nuclear magnetic resonance spectrum of kaolinite. *Clays and Clay Minerals*, *35*, 38-42.

Thompson, J. G., Cuff, C. (1985). Crystal structure of kaolinite: dimethylsulfoxide intercalate. *Clays and Clay Minerals*, *33*(5), 490-500.

Tonlé, I. K., Diaco, T., Ngameni, E., Detellier, C. (2007). Nanohybrid kaolinite-based materials obtained from the interlayer grafting of 3-aminopropyltriethoxysilane and their potential use as electrochemical sensors. *Chemistry of Materials*, *19*(26), 6629–6636.

Tonlé, I. K., Letaief, S., Ngameni, E., Walcarius, A., Detellier, C. (2011). Square Wave Voltammetric Determination of Lead (II) Ions Using a Carbon Paste Electrode Modified by a Thiol-Functionalized Kaolinite. *Electroanalysis*, *23*(1), 245–252.

Tunney, J. J. (1995). *New nanocomposite materials from kaolinite as a mineral precursor.* (Doctoral thesis). University of Ottawa (Canada).

Tunney, J. J., Detellier, C. (1993). Interlamellar covalent grafting of organic units on kaolinite. *Chemistry of Materials*, *5*(6), 747-748.

Tunney, J. J., Detellier, C. (1994a) Preparation and characterization of two distinct ethylene glycol derivatives of kaolinite. *Clays and Clay Minerals*, *42*(5), 552-560.

Tunney, J., Detellier, C. (1994b). Preparation and characterization of an 8.4 Å hydrate of kaolinite. *Clays and Clay Minerals*, *42*(4), 473–476.

Tunney, J. J., Detellier, C. (1996a). Aluminosilicate Nanocomposite Materials. Poly (ethylene glycol)- Kaolinite Intercalates. *Chemistry of Materials*, *8*(4), 927–935.

Tunney, J. J., Detellier, C. (1996b). Chemically modified kaolinite. Grafting of methoxy groups on the interlamellar aluminol surface of kaolinite. *Journal of Materials Chemistry*, *6*(10), 1679–1685.

Tunney, J. J., Detellier, C. (1997). Interlamellar amino functionalization of kaolinite. *Canadian Journal of Chemistry*, *75*(11), 1766–1772.

U.S. Department of Agriculture, Natural Resources Conservation Service. National soil survey handbook, title 430-VI. http://www.nrcs.usda.gov/wps/portal/nrcs/detail/soils/ref/?cid=nrcs142p2_054242 accessed: (06/24/2016).

U.S. Geological Survey, (2017), Mineral commodity summaries 2017: U.S. Geological Survey, 202 p., https://doi.org/10.3133/70180197.

Van Damme, H., Pellenq, R. J.-M., Ulm, F.-J. (2013). Chapter 14.3 - Cement Hydrates. In: F. Bergaya & G. Lagaly (Eds.), *Handbook of Clay Science* (Vol. 5, pp. 801–817). Elsevier.

Van Vleck, J. H. (1948). The dipolar broadening of magnetic resonance lines in crystals. *Physical Review*, *74*(9), 1168.

Vega, A.J. (2012). Chapter 2: Quadrupolar Nuclei in Solids. In: Wasylishen, R. E., Ashbrook, S. E., Wimperis, S. (Eds.) *NMR of quadrupolar nuclei in solid materials* (pp. 17–44). John Wiley & Sons.

Vinogradov, E., Madhu, P. K., Vega, S. (1999). High-resolution proton solid-state NMR spectroscopy by phase-modulated Lee–Goldburg experiment. *Chemical physics letters*, *314*(5), 443-450.

Wada, K. (1961). Lattice expansion of kaolin minerals by treatment with potassium acetate. *American Mineralogist*, *46*, 78-91.

Wada, K. (1967). A Study of Hydroxyl Groups in Kaolin Minerals Utilizing Selective Deuteration and Infrared Spectroscopy. *Clay Minerals*, *7*(1), 51–61.

Wang, L., Wu, D., Yuan, P., Chen, Z., Chen, Z. (2002). ^{1}H MAS NMR spectra of kaolinite/formamide intercalation compound. *Chinese Science Bulletin*, *47*(6), 504-508.

Weiss, A. (1961). Eine Schichteinschlußverbindung von Kaolinit mit Harnstoff. *Angewandte Chemie*, *73*(22), 736–736.

Weiss, A. (1981). Replication and evolution in inorganic systems. *Angewandte Chemie International Edition*, *20*(10), 850–860.

Weiss, A., Becker, H. O., Orth, H., Mai, G., Lechner, H., Range, K. J. (1969). Particle size effects and reaction mechanism of the intercalation into kaolinite. In: *Proc. Int. Clay Conf. Tokyo* (Vol. 2, pp. 180–184).

Weiss, A., Choy, J. H., Meyer, H., Becker, H. O. (1981). Hydrogen reorientation, a primary step of intercalation reactions into kaolinite. In: *Proceedings of the International Clay Conference, Bologna, Pavia, Abstracts* (p. 331).

Weiss, A., Thielepape, W., Göring, G., Ritter, W., Schäfer, H. (1963a). Kaolinit-einlagerungs-verbindungen. In: *Proceedings of the International Clay Conference* (Vol. 1, pp. 287–305).

Weiss, A., Thielepape, W., Orth, H. (1966). Neue Kaolinit-Einlagerungsverbindungen. In: *Proceedings of the International Clay Conference, Jerusalem* (Vol. 1, pp. 277–293). Israel Program for Scientific Translation, Jerusalem.

Weiss, A., Thielepape, W., Ritter, W., Schäfer, H., Göring, G. (1963b). Zur Kenntnis von Hydrazin-Kaolinit. *Zeitschrift Für Anorganische Und Allgemeine Chemie*, *320*(1–4), 183–204.

Wiewióra, A., Brindley, G. W. (1969). Potassium acetate intercalation in kaolinite and its removal; effect of material characteristics. In: *Proceedings of the International Clay Conference, Tokyo* (Vol. 1, pp. 723–733).

Wojdyr, M. (2010). Fityk: a general-purpose peak fitting program. *Journal of Applied Crystallography*, *43*(5), 1126-1128.

WSolids1 ver. 1.21.3, K. Eichele, Universität Tübingen, 2015.

Yahiaoui, A., Belbachir, M., Hachemaoui, A. (2003) An acid exchanged montmorillonite clay-catalyzed synthesis of polyepichlorhydrin. *International Journal of Molecular Sciences*, *4*(10), 548-561.

Yang, H., Liu, M., Ouyang, J. (2010). Novel synthesis and characterization of nanosized γ-Al_2 O_3 from kaolin. *Applied Clay Science*, *47*(3), 438-443.

Yesinowski, J. P., Eckert, H. (1987). Hydrogen environments in calcium phosphates: proton MAS NMR at high spinning speeds. *Journal of the American Chemical Society*, *109*(21), 6274-6282.

Yesinowski, J. P., Eckert, H., Rossman, G. R. (1988). Characterization of hydrous species in minerals by high-speed proton MAS-NMR. *Journal of the American Chemical Society*, *110*(5), 1367-1375.

Yuan, G. D., Theng, B. K. G., Churchman, G. J., Gates, W. P. (2013). Chapter 5.1 - Clays and Clay Minerals for Pollution Control. In F. Bergaya, G. Lagaly (Eds.), *Handbook of Clay Science* (Vol. 5, pp. 587–644). Elsevier.

Zhou, B., Sherriff, B. L., Wang, T. (2009). ^{27}Al NMR spectroscopy at multiple magnetic fields and ab initio quantum modeling for kaolinite. *American Mineralogist*, *94*(7), 865-871.

Zhu, X., Zhu, Z., Lei, X., Yan, C. (2016). Defects in structure as the sources of the surface charges of kaolinite. *Applied Clay Science*, *124*, 127-136.